

---

# Effective field theory approaches for tensor potentials

---

Zur Erlangung des Grades eines Doktors der Naturwissenschaften (Dr. rer. nat.)  
genehmigte Dissertation von Maximilian Jansen aus Siegburg  
Tag der Einreichung: 18.10.2016, Tag der Prüfung: 14.11.2016  
Darmstadt 2016 — D 17

1. Gutachten: Prof. Dr. Hans-Werner Hammer
  2. Gutachten: Prof. Dr. Jens Braun
- 



TECHNISCHE  
UNIVERSITÄT  
DARMSTADT

Fachbereich Physik  
AG Hammer, Institut für Kernphysik

---

## **Effective field theory approaches for tensor potentials**

Genehmigte Dissertation von Maximilian Jansen aus Siegburg

1. Gutachten: Prof. Dr. Hans-Werner Hammer
2. Gutachten: Prof. Dr. Jens Braun

Tag der Einreichung: 18.10.2016

Tag der Prüfung: 14.11.2016

Darmstadt 2016 — D 17

---

## Erklärung zur Dissertation

---

Hiermit versichere ich, die vorliegende Dissertation ohne Hilfe Dritter nur mit den angegebenen Quellen und Hilfsmitteln angefertigt zu haben. Alle Stellen, die aus Quellen entnommen wurden, sind als solche kenntlich gemacht. Diese Arbeit hat in gleicher oder ähnlicher Form noch keiner Prüfungsbehörde vorgelegen. Eine Promotion wurde bisher noch nicht versucht.

Darmstadt, den 22. November 2016

---

(Maximilian Jansen)



---

## Abstract

---

Effective field theories are a widely used tool to study physical systems at low energies. We apply them to systematically analyze two and three particles interacting via tensor potentials. Two examples are addressed: pion interactions for  $\bar{D}^0 D^{*0}$  scattering to dynamically generate the  $X(3872)$  and dipole interactions for two and three bosons at low energies. For the former, the one-pion exchange and for the latter, the long-range dipole force induce a tensor-like structure of the potential. We apply perturbative as well as non-perturbative methods to determine low-energy observables.

The  $X(3872)$  is of major interest in modern high-energy physics. Its exotic characteristics require approaches outside the range of the quark model for baryons and mesons. Effective field theories represent such methods and provide access to its peculiar nature. We interpret the  $X(3872)$  as a hadronic molecule consisting of neutral  $D$  and  $D^*$  mesons. It is possible to apply an effective field theory with perturbative pions. Within this framework, we address chiral as well as finite volume extrapolations for low-energy observables, such as the binding energy and the scattering length. We show that the two-point correlation function for the  $D^{*0}$  meson has to be resummed to cure infrared divergences. Moreover, next-to-leading order coupling constants, which were introduced by power counting arguments, appear to be essential to renormalize the scattering amplitude.

The binding energy as well as the scattering length display a moderate dependence on the light quark masses. The  $X(3872)$  is most likely deeper bound for large light quark masses. In a finite volume on the other hand, the binding energy significantly increases. The dependence on the light quark masses and the volume size can be simultaneously obtained.

For bosonic dipoles we apply a non-perturbative, numerical approach. We solve the Lippmann-Schwinger equation for the two-dipole system and the Faddeev equation for three bosonic dipoles. Scattering amplitudes are ultraviolet divergent and have to be regularized. A single, isotropic  $S$ -wave operator is insufficient to properly renormalize and a linear combination of, in general anisotropic, short-range interactions has to be introduced.

Bound states can be classified by parity and projection of the orbital angular momentum on the dipole moment. Both quantum numbers are conserved. Moreover, binding energies can be divided into different sets characterized by multiple angular momentum quantum numbers. However, different sets couple among each other and the spectrum displays avoided level crossings whenever two of them come close.

We further determine the bound-state spectrum for three bosonic dipoles. The Faddeev equation decouples if the two-body threshold is dominated by a particular projection of orbital angular momentum. We solve it for the case of vanishing projection quantum number. It appears that bound states are universally determined by two-body low-energy observables and no explicit three-body forces have to be included to assure regulator independence.

Furthermore, we derive a reformulation of the Faddeev equation, which is numerically beneficial. For a proof of concept we implement it for the  $S$ -wave projected  $1/r^3$  potential.



---

## Kurzfassung

---

Effektive Feldtheorien finden Anwendung, um physikalische Systeme bei niedrigen Energien zu beschreiben. Wir untersuchen tensorartige Wechselwirkungen zwischen zwei und drei Teilchen mittels effektiver Formalismen. Zwei Beispiele werden in vorliegender Dissertation behandelt: Das  $X(3872)$  als  $\bar{D}^0 D^{*0}$ -Molekül mit expliziten Pionfreiheitsgraden und Bindungszustände zwischen zwei und drei bosonischen Dipolen. Für ersteres induzieren Pion austausche und für letzteres Dipol-Dipol-Wechselwirkungen ein tensorartiges Potential. Während für das  $X(3872)$  perturbative Ansätze verwendet werden können, setzen wir für Dipol-Rechnungen nicht-perturbative, numerische Methoden ein.

Das  $X(3872)$  ist eines der meist studierten exotischen Hadronen. Seine ungewöhnlichen Eigenschaften erfordern Beschreibungsansätze jenseits des Quarkmodells für Baryonen und Mesonen. Effektive Feldtheorien bieten hierfür einen geeigneten theoretischen Rahmen. Wir deuten das  $X(3872)$  als hadronisches Molekül, bestehend aus neutralen  $\bar{D}^0$ - und  $D^{*0}$ -Mesonen. Mittels einer effektiven Feldtheorie, in welcher Pionen explizit berücksichtigt und perturbativ eingebunden werden, berechnen wir Niederenergieobservablen wie beispielsweise die Bindungsenergie oder die Streulänge. Für diese stellen wir chirale Extrapolationen und endliche-Volumen Rechnungen auf. Wir zeigen, dass Zweipunktkorrelationsfunktionen resummiert werden müssen, um Infrarotdivergenzen zu beheben. Weiterhin sind Kontaktwechselwirkungen zu nächst führender Ordnung unerlässlich um Streuamplituden konsistent zu renormieren. Bindungsenergie und Streulänge zeigen eine moderate Abhängigkeit von den leichten Quarkmassen. Endliche-Volumen Korrekturen sind hingegen groß.

Um Observablen für Bosonen mit dominant dipolarer Wechselwirkung zu extrahieren, werden nicht-perturbative Methoden benötigt. Zwei-Dipol-Systeme können anhand der Lippmann-Schwinger-Gleichung untersucht werden. Messgrößen für drei Dipole folgen aus der Faddeev-Gleichung. Beide Gleichungen können mittels numerischer Verfahren gelöst werden. Wir zeigen, dass isotrope  $S$ -Wellen-Operatoren unzureichend sind, um Bindungsenergiespektren vollständig zu renormieren. Stattdessen müssen Linearkombinationen, im Allgemeinen anisotroper, kurzreichweitiger Wechselwirkungen eingeführt werden.

Resultierende Bindungszustände können anhand ihres Verhaltens unter Parität und der Projektion des orbitalen Drehimpulses auf das Dipolmoment klassifiziert werden. Eine weitere Unterteilung erfolgt durch Zuordnung mehrerer Bahndrehimpulsquantenzahlen. Diese sind jedoch nur näherungsweise erhalten und koppeln untereinander.

Darüber hinaus bestimmen wir Spektren für Bindungsenergien dreier, bosonischer Dipole. Wird die Zweikörperschwelle durch Beiträge mit bestimmter Projektion des Bahndrehimpulses dominiert, so entkoppelt die Faddeev-Gleichung. Wir lösen diese für verschwindende Projektionsquantenzahl und finden, dass Bindungszustände im Dreikörperbereich universell durch Niederenergieobservablen zweier Dipole bestimmt sind. Es folgt, dass keine expliziten Dreiteilchenkräfte eingebunden werden müssen, um Regulatorunabhängigkeit sicherzustellen.

Außerdem leiten wir eine alternative Formulierung der Faddeev-Gleichung her und demonstrieren am Beispiel des singulären  $1/r^3$ -Potentials numerische Vorteile.



<b>1. Introduction</b>	<b>1</b>
<b>2. Effective theories</b>	<b>9</b>
2.1. Renormalizability, symmetries and power counting	9
2.2. Pure contact theories	10
2.2.1. Short-distance operators	10
2.2.2. Renormalization schemes	10
2.2.3. Finite volume effects	14
2.3. Singular potentials	16
2.3.1. The $1/r^2$ potential	16
2.3.2. The $1/r^3$ potential	19
<b>3. Chiral extrapolations and finite volume effects for the <math>X(3872)</math></b>	<b>21</b>
3.1. An effective field theory for the $X(3872)$	21
3.1.1. Lagrangian of XEFT and Feynman rules	21
3.1.2. Pion exchanges between the $D$ mesons	22
3.1.3. Power counting	23
3.1.4. Charged $D$ meson contributions	23
3.2. Chiral extrapolations	24
3.2.1. $\bar{D}^0 D^{*0}$ transition amplitudes to next-to-leading order with bare propagators	24
3.2.2. Infrared divergences and full $D^{*0}$ propagator	26
3.2.3. Transition amplitudes to next-to-leading order with resummed $D^{*0}$ propagator	28
3.2.4. Renormalization of the scattering amplitude	28
3.2.5. The effective range expansion up to next-to-leading order	29
3.2.6. The binding energy to next-to-leading order	30
3.2.7. The imaginary part of the pole position	32
3.2.8. Chiral extrapolations and results	32
3.3. Finite volume effects	36
3.3.1. The leading-order amplitude	36
3.3.2. The $D^{*0}$ self-energy and mass shift	37
3.3.3. Next-to-leading-order corrections to the binding energy	37
3.3.4. Validity range of XEFT in the box	38
3.3.5. Effective range expansion for large $m_\pi$	39
3.3.6. Results	40
<b>4. Dipole-dipole interactions</b>	<b>43</b>
4.1. The two-dipole system	43
4.1.1. An effective theory for the dipole-dipole system	43
4.1.2. Dipole-dipole interaction potential	43
4.1.3. Partial wave expansions	45
4.1.4. Results	48
4.2. The three-dipole system	55
4.2.1. The Faddeev equation	55
4.2.2. Results	58
4.2.3. Alternative formulation of the Faddeev equation	59
<b>5. Conclusion and outlook</b>	<b>63</b>
<b>A. Calculations for the <math>X(3872)</math></b>	<b>67</b>
A.1. Infinite volume Feynman diagrams	67
A.1.1. Calculation of the $D^{*0}$ self-energy diagram	67
A.1.2. Calculation of $\mathcal{A}_0^{(I)}$	68
A.1.3. Calculation of $\mathcal{A}_0^{(II)}$	69
A.1.4. Calculation of $\mathcal{A}_0^{(III)}$	70
A.1.5. Calculation of $\mathcal{A}_0^{(IV)}$	70
A.2. Finite volume Feynman diagrams	72
A.2.1. Calculation of $\mathcal{A}_{0(IV)}^L$	72
A.3. Shift of the particle mass from a non-relativistic self-energy	73

---

<b>B. Dipole systems</b>	<b>75</b>
B.1. Fourier transform of the dipole-dipole potential . . . . .	75
B.2. Partial wave expansions . . . . .	76
B.2.1. Cylindrical coordinates . . . . .	76
B.2.2. Spherical coordinates . . . . .	77
B.2.3. Relation between spherical and cylindrical partial waves . . . . .	78
B.3. Numerical implementation . . . . .	80
B.4. Further unrenormalized two-dipole spectra . . . . .	81
B.4.1. Cutoff dependence for $m = 0, P = -$ . . . . .	81
B.5. Convergence of the partial wave expansion . . . . .	84
B.6. Partial wave projection of the Faddeev equation . . . . .	89
B.7. Numerical implementation . . . . .	90
B.8. Derivation of the modified Faddeev equation . . . . .	91
B.9. Partial wave projection of the modified Faddeev equation . . . . .	92

---

# 1 Introduction

---

Two peculiar characteristics of the strong force are confinement and asymptotic freedom. While the latter was thoroughly described already in 1973 [1, 2], a rigorous proof of the former is still pending. However, both phenomena are closely related. In quantum chromodynamics (QCD), both effects stem from self interactions of the gluons, the charge carriers of the strong force. For increasing energy, the interaction strength of QCD decreases and allows for a perturbative treatment at large energies. Conversely, at low energies, the strong coupling constant rapidly grows, demanding for non-perturbative approaches [3]. Examples are the quark model [4], lattice QCD [5] or effective field theories such as chiral perturbation theory [6, 7], which allowed for the prediction of numerous hadronic properties.

On the other hand, effective field theories play an increasingly important role in atomic physics [8]. With improved cooling techniques, the experimentally accessible temperatures for ultracold atomic gases continuously decreased over the past decades [9]. These achievements, in turn, created the possibility to prepare systems of atoms or molecules with typical de Broglie wavelengths larger than the average particle separation, such that quantum phenomena determine their characteristics [10]. Related experimental breakthroughs are, for example, the first realization of a Bose-Einstein condensate (BEC) in a dilute gas of rubidium atoms [11] and, shortly after, in a gas of sodium atoms [12] or the observation of an Efimov trimer [13, 14]. Ever since, the advance of quantitative, experimental investigations requires a precise determination of low-energy observables.

At first glance, it seems that hadronic physics and condensed matter theory for cold atoms do not have much in common. The typical energies, usually  $\sim \mathcal{O}(1 \text{ GeV})$  for the former and  $\sim \mathcal{O}(1 \text{ meV})$  for the latter, are separated by roughly twelve orders of magnitude. While colliders with dimensions  $\sim \mathcal{O}(10 \text{ km})$  are indispensable for hadronic experiments, table-top setups with sizes  $\sim \mathcal{O}(1 \text{ m})$  are state of the art in atomic physics. Nevertheless, within an effective field theory framework, both fields close ranks.

Similarities are evident, when taking a look at the effective potentials covered in this thesis. Anticipating Chaps. 3 and 4, the anisotropic parts of the one-pion-exchange (OPE) potential for neutral  $D^{(*)}$  mesons,  $V_{OPE}$ , and the effective interaction between two ideal dipoles,  $V_{dd}$ , bear close resemblance

$$V_{OPE}(\mathbf{q}) \sim \frac{(\boldsymbol{\varepsilon}_i \cdot \mathbf{q})(\boldsymbol{\varepsilon}_j^* \cdot \mathbf{q})}{q^2 - \mu^2}, \quad V_{dd}(\mathbf{q}) \sim \frac{(\mathbf{d}_1 \cdot \mathbf{q})(\mathbf{d}_2 \cdot \mathbf{q})}{q^2}. \quad (1.1)$$

Here,  $\mathbf{q}$  denotes the momentum transfer. Furthermore, the polarization vectors of the in- and outgoing  $D^{*0}$  ( $\bar{D}^{*0}$ ) mesons are  $\boldsymbol{\varepsilon}_i$  and  $\boldsymbol{\varepsilon}_j^*$  and the mass scale  $\mu \approx 44 \text{ MeV}$  is related to the hyperfine splitting of the neutral  $D^{(*)}$  mesons and the pion mass. The dipole moments of the interacting bosons are  $\mathbf{d}_1$  and  $\mathbf{d}_2$ . When factoring out the polarization vectors or the dipole moments, respectively, the tensor structure of both potentials becomes evident. Note that  $\mu$  is comparatively small, having in mind that typical momentum scales for hadrons are given by the pion mass  $\sim 135 \text{ MeV}$  [15]. Thus, an almost identical potential could result, when slightly increasing the pion mass away from its physical value, e.g., in future lattice simulations.

However, while the  $D^{*0}$  mesons have spin one and accordingly three polarization vectors have to be considered, the dipole moment is a classical degree of freedom and can be oriented arbitrarily in space. As described below, for a system of neutral  $D$  mesons, only the coupling between  $S$ - and  $D$ -waves of orbital angular momentum has to be taken into account. In contrast, for the dipolar system, for orbital angular momentum, all even and all odd partial waves couple among each other, respectively. Moreover, the fine tuning of the neutral  $DD^*$  system allows for a perturbative inclusion of pions after resummation of the lowest-order short-distance operator to all orders [16]. For the dipole-dipole system, on the other hand, we aim to understand the renormalization of the system. In particular, we also attempt to obtain spectra in absence of additional short-range interactions. Moreover, we aim to describe experiments with dominant dipole interaction. Therefore, a non-perturbative analysis is mandatory.

In addition, the dipole-dipole system can presumably be manipulated and allows for a tuning of certain low-energy observables [17]. Although lattice simulations offer the possibility to alter some parameters, experiments for the  $X(3872)$  are tied to the physical point.

As early as 1976, Voloshin et al. discussed the possibility of hidden-charmed dimeson states in the region of roughly 4 GeV [18]. It took almost thirty years until the discovery of the  $X(3872)$  [19], a state which can not be described as an ordinary meson or baryon. The mass of the  $X(3872)$  is in the region of charmonium states and various assignments were considered [20]. However, the description as a pure  $c\bar{c}$ -state is unfeasible due to isospin violations in  $X$  decays [21]. Unconventional states are thus mandatory and dominate the nature of the  $X(3872)$  [22, 23].

There are various interpretations for the  $X$ , e.g., as a tetraquark state [24, 25], a charmonium [26], a hadronic molecule

[27, 28, 29, 16] or a hybrid of a charmonium and a molecular state [30, 31]. For a recent review of exotic states and a more elaborate list of publications we refer to Ref. [32].

The signal for the first observation of the  $X$  by the Belle Collaboration is shown in Fig. 1.1. The decay chain proceeds as  $B^\pm \rightarrow K^\pm(X(3872) \rightarrow \pi^+\pi^-J/\psi)$ . The quantities  $M_{bc}$ ,  $M_{\pi^+\pi^-J/\psi}$  and  $\Delta E$  are defined as  $M_{bc} \equiv [(E_{\text{beam}}^{\text{CM}})^2 - (p_{\text{beam}}^{\text{CM}})^2]^{1/2}$ ,  $M_{\pi^+\pi^-J/\psi}$  as the invariant  $\pi^+\pi^-J/\psi$  mass and  $\Delta E \equiv E_B^{\text{CM}} - E_{\text{beam}}^{\text{CM}}$  with the beam energy in the CM system  $E_{\text{beam}}^{\text{CM}}$  and the  $B$  meson candidate's energy and momentum  $E_B^{\text{CM}}$  and  $p_{\text{beam}}^{\text{CM}}$ , respectively [19]. The central plot shows a clear signal at an energy of 3872 MeV belonging to the  $X$ . The  $X$  is extremely narrow and the width in Fig. 1.1 is exclusively determined by the detector's resolution. Choi et al. give as an upper limit with 90% confidence level  $\Gamma_X < 2.3$  MeV [19]. The current upper bound for the  $X$  is  $\Gamma_X < 1.2$  MeV [33].

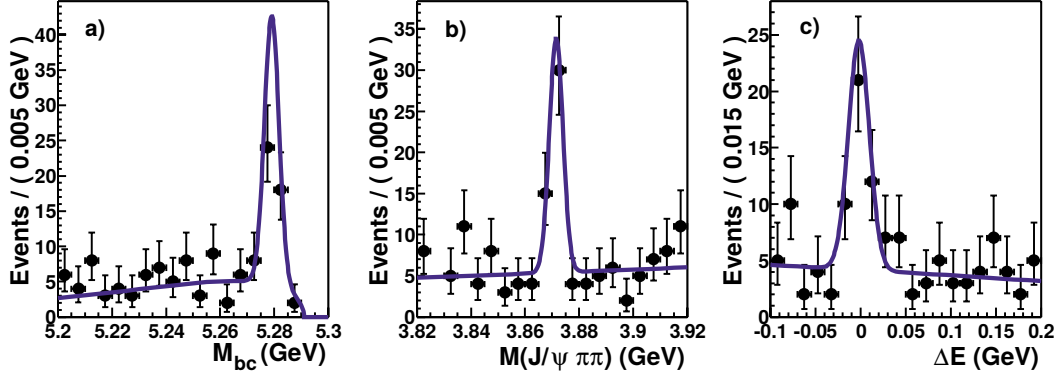


**Figure 1.1.:** Experimental evidence for a signal in the 3872 MeV region in  $B^\pm \rightarrow K^\pm \pi^+ \pi^- J/\psi$  decays reported by the Belle Collaboration. Adapted from “Observation of a narrow charmonium-like state in exclusive  $B^\pm \rightarrow K^\pm \pi^+ \pi^- J/\psi$  decays,” by S.K. Choi et al., Phys. Rev. Lett. **91**, 262001 (2003). Adapted with permission.

After the discovery of the  $X$  in 2003 by the Belle Collaboration [19] and its confirmation by the CDF Collaboration just about a month after [34], its quantum numbers remained uncertain for almost a decade [35]. First, its charge conjugation was determined to be  $C = +$  by its observed decays into  $J/\psi\gamma$  [21, 36]. For angular momentum and parity, all but two competing possibilities, namely  $J^{PC} = 1^{++}$  and  $J^{PC} = 2^{-+}$ , were ruled out in Ref. [37]. While some experimental data favored the  $J^{PC} = 2^{-+}$  hypothesis [38], other supported  $J^{PC} = 1^{++}$  [39]. However, in Ref. [40], the authors pointed out that the discrepancy between experiments is presumably overrated. One of the first (quenched) lattice simulations performed for the  $X$  preferred the  $J^{PC} = 1^{++}$  assignment [41]. It was not before 2013 that the LHCb Collaboration was able to finally determine angular momentum and parity to be  $J^{PC} = 1^{++}$  with a  $5\sigma$  significance [35].

In Fig. 1.2 we show the event distribution in the cosine of the helicity angle of the  $X$ ,  $\cos\theta_X$ , by the LHCb Collaboration. The top and bottom plot differ in the discrimination of events in the cosine of the helicity angle of the final-state pions,  $\cos\theta_{\pi\pi}$ . The data is compared to the outcome of a simulation for the different hypotheses  $J^{PC} = 1^{++}$  and  $J^{PC} = 2^{-+}$ .

The branching fractions of  $X$  decays into  $J/\psi\pi^+\pi^-$  [42] and  $J/\psi\pi^+\pi^-\pi^0$  [38] are of similar magnitude. Their ratio is given as [33]

$$\frac{\mathcal{B}[X \rightarrow J/\psi\pi^+\pi^-\pi^0]}{\mathcal{B}[X \rightarrow J/\psi\pi^+\pi^-]} = 0.8 \pm 0.3. \quad (1.2)$$

The decays to the two and three final state pions proceed predominantly via  $J/\psi\rho$  and  $J/\psi\omega$  intermediate states, respectively. While the  $\rho$  has isospin 1, the  $\omega$  has isospin 0 and thus, ratio (1.2) indicates a large violation of isospin in  $X$  decays. However, the authors of Ref. [43] pointed out that isospin violations could be enhanced due to phase space effects and therefore, estimates like (1.2) possibly overrate the isospin breaking. Nevertheless, isospin is clearly not preserved and hence, an interpretation of the  $X$  as pure charmonium state is implausible. A possible explanation is given by a delicate mass cancellation, when interpreting the  $X$  as a hadronic molecule of neutral  $\bar{D}D^*$  ( $D\bar{D}^*$ ) mesons.

The interpretation of the  $X$  as a hadronic molecule is appealing for several reasons. First of all, it naturally explains the proximity of the mass of the  $X$  to the neutral  $DD^*$  threshold. Using the latest values from the review of particle properties [33], we find for the mass difference

$$E_X \equiv m_D + m_{D^*} - m_X = (0.11 \pm 0.21) \text{ MeV}, \quad (1.3)$$

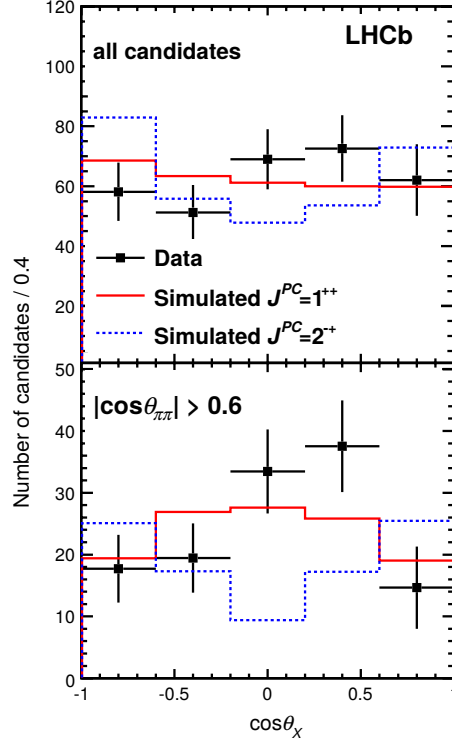


**Figure 1.2.:** Distribution of events in the cosine of the helicity angle of the  $X$ ,  $\cos \theta_X$ , for the decay channel  $B^+ \rightarrow K^+(X(3872) \rightarrow \pi^+ \pi^- J/\psi)$ . The analysis is performed for all  $X$  candidates (top) and those for which  $|\cos(\theta_{\pi\pi}) > 0.6|$  (bottom). The data is compared to simulated distributions for the hypotheses  $J^{PC} = 1^{++}$  and  $J^{PC} = 2^{-+}$ . Adapted from “Determination of the  $X(3872)$  meson quantum numbers,” by R. Aaij et al., Phys. Rev. Lett. **110**, 222001 (2013). Adapted with permission.

with  $m_D$ ,  $m_{D^*}$  and  $m_X$  being the masses of the  $D^0$  ( $\bar{D}^0$ ),  $D^{*0}$  ( $\bar{D}^{*0}$ ) and  $X$ , respectively. In the molecular picture expression (1.3) is the binding energy. Note that it is experimentally not excluded that the  $X$  is not bound but a resonance. The calculations presented in this thesis are also applicable to this scenario with minor modifications. However, for convenience, we assume that  $E_X > 0$  from now on and use  $E_X = 0.1$  MeV. The binding energy is extremely small compared to a typical energy scale set by one-pion exchange  $\sim m_\pi^2/2M_{DD^*} \approx 10$  MeV with the reduced  $\bar{D}^0 D^{*0}$  mass  $M_{DD^*}$ . Due to the small binding energy, the  $X$  displays universal properties. To lowest order it obeys the universal relation between the  $S$ -wave scattering length and the binding energy  $a_s = 1/\sqrt{2M_{DD^*}E_X}$  [8] from which we infer  $a_s \gtrsim 5$  fm. In Chap. 3.1, we introduce an effective field theory, called XEFT, which allows for a systematic calculation of corrections to universality [16].

The molecular interpretation further explains the isospin violations in  $X$  decays. The above mentioned nearness of the  $X$  mass to the neutral  $DD^*$  threshold induces a dominance of the neutral  $D^{(*)}$  mesons over the charged ones, which lie about 8 MeV above threshold. Due to this exceptional fine tuning, the  $X$  is not an eigenstate in isospin space, but an admixture with an  $I = 0$  and  $I = 1$  component. We further elaborate on charged states and consequential isospin violations in Chap. 3.1.4.

To obtain the correct behavior under charge conjugation, we need to superimpose<sup>1</sup>

$$X = \frac{1}{\sqrt{2}} (D^0 \bar{D}^{*0} + \bar{D}^0 D^{*0}). \quad (1.4)$$

The  $X$  is then eigenstate to the charge conjugation operator with eigenvalue +1. The  $X$  and the  $D^{*0}$  have spin one, whereas the  $D^0$  is a scalar particle. Consequently, the  $D^0$  and the  $D^{*0}$  can interact in an  $S$ -, a  $P$ - or a  $D$ -wave. The behavior under parity further restricts the allowed angular momenta. The intrinsic parity of the  $D$  mesons is  $-1$ . From the interaction we get another factor of  $(-1)^L$  and accordingly, to obtain a positive parity for the  $X$ , only  $S$ - or  $D$ -wave interactions contribute. In general, those are coupled. Since we are considering a low-energy theory,  $D$ -waves are strongly suppressed [44]. However, in the finite volume,  $D$ -waves might actually be enhanced, as already seen for nucleon-nucleon interactions [45]. A coupled-channel analysis by Garzon et al. [46] shows that for the volumes we regard in Sec. 3.3,  $D$ -waves are negligible.

<sup>1</sup> For shorthand notation we use  $\bar{D}^0 D^{*0}$  to refer to the  $X$  channel.

There are several approaches to treat the  $X$  in the molecular picture. In Ref. [22], Braaten and Kusunoki use an effective field theory in order to calculate effects of the unnaturally large scattering length of the  $\bar{D}^0 D^{*0}$  system on observables of the  $X$ . They use a Hamiltonian with contact interactions only and investigate the possibility of a fine-tuned  $P$ -wave charmonium to the  $\bar{D}^0 D^{*0}$  threshold to explain the unnaturally large scattering length. They further explain the absence of  $D^0 D^0 \bar{D}^{*0}$  Efimov states which, in principle, can occur in systems with unnaturally large scattering length [47]. In Refs. [48, 49], a non-perturbative approach is used to calculate line shapes for the  $X$  and the dependence of the binding energy on the light quark masses. The  $X$  is treated as a three-body  $D^0 \bar{D}^0 \pi$  system and the arising Faddeev equations are solved numerically. In particular, in Ref. [48], the authors investigate the effect when transitioning from a static pion approximation to a system with dynamic pions and found that the decay width decreases about a factor of two. However, for most observables, including the binding energy, a static pion approximation works well. Moreover, they confirmed the possibility of a perturbative treatment of pions used in Ref. [16]. The effective field theory of Ref. [16], called XEFT, with a consistent power counting, systematically derived from heavy hadron chiral perturbation theory, is used in this thesis to calculate chiral and finite volume extrapolations. We extensively discuss XEFT in Sec. 3.1. Braaten extended XEFT to a Galilean-invariant version [50], exploiting that mass is nearly conserved in decays of the  $D^{*0}$  to  $D^0 \pi^0$ . It enables the inclusion of the decay width of the  $D^{*0}$  to  $D^0 \gamma$  and further makes it possible to renormalize for variable quark masses at next-to-next-to-leading order (NNLO) and beyond. Starting from NNLO the effects of Galilean-invariant interactions and  $m_\pi/m_D$ -suppressed terms have to be considered, since they are in the same order as, for example, the two-pion exchange. Note, however, that at NNLO effects of relativistic pions might also be important as studied in detail in Ref. [51] for nucleon-nucleon scattering.

Moreover, in Ref. [52], XEFT is applied to the decays of  $X(3872) \rightarrow \chi_{cJ} \pi^0$  ( $J = 0, 1, 2$ ) and  $X(3872) \rightarrow \chi_{cJ} \pi^0 \pi^0$  ( $J = 0, 2$ ). The cross section for the breakup reaction when a charged pion is scattered off the  $X$ , i.e.  $\pi^+ X(3872) \rightarrow D^{*+} \bar{D}^{*0}$ , is calculated in Ref. [53].

In the above presented works on the  $X$ , the large spatial extent was exploited in order to construct the underlying effective field theories. Contrariwise, for lattice studies, the large length scales which govern the physics of the  $X$ , constitute a severe problem. Despite the above mentioned quenched lattice simulation [41], results of a full simulation were first available in 2013 [54]. With light quark masses at about four times the physical value and on a lattice with a spatial extent of about 2 fm, Prelovsek et al. found a candidate for the  $X$  about  $(11 \pm 7)$  MeV below the  $\bar{D}^0 D^{*0}$  threshold. However, due to the large light quark masses and in particular, the comparatively small volume, systematic errors are expected to be large. Subsequently published lattice studies use volumes and light quark masses of similar size [55, 56] and it is not to be expected to obtain results for physical light quark masses on volumes with a spatial extent much larger than typical length scales of the  $X$ , soon. Accordingly, chiral extrapolations and a systematic derivation of finite volume corrections are essential.

In this thesis, we provide chiral and finite volume extrapolations for the  $X$ . For two particles, Lüscher showed that finite volume observables are entirely determined by the infinite volume  $S$ -matrix elements [57, 58]. By implication, it is possible to extract meaningful results for physical observables from simulations performed in a finite volume. Beane et al. showed that this is also possible if the system has an unnaturally large scattering length [59]. But for  $\bar{D}^0 D^{*0}$  scattering, depending on the light quark mass, the  $D^{*0}$  meson can decay to  $D^0 \pi$  and on-shell  $D^0 \bar{D}^0 \pi$  intermediate states are present. To account for corresponding three-body effects, pion fields have to be included as explicit degrees of freedom. Three particles are at the frontier of current finite volume calculations. Just recently, proof was given that also for three particles in a box, the spectrum is determined by the infinite volume  $S$ -matrix elements [60, 61, 62]. Explicit calculations were performed, e.g., for the  $a_1(1260)$ , interpreted as  $\pi \rho$  resonance [63]. Moreover, triton properties were addressed in Ref. [64], based on foregoing work on the Efimov spectrum in a finite, cubic box in Ref. [65]. Also, implications for two-body bound states in a moving frame were investigated in Ref. [66]. An approach to obtain two-body energy spectra when inelastic channels are present utilizing the optical potential is introduced in Ref. [67]. Furthermore, an analytical expression for finite volume corrections to the binding energy of three particles interacting via a contact interaction in the unitary limit, is given in Ref. [68]. For the  $X$ , a finite volume, coupled-channel analysis without explicit pion fields was carried out in Ref. [46]. An investigation including pions was outstanding, however, and is one of the major subjects of this thesis.

Moreover, we present detailed studies for systems of two and three bosonic dipoles. A particularly appealing feature of the dipolar interaction is its anisotropic character. It presumably provides the opportunity to specifically manipulate systems of atoms and molecules at ultralow temperatures. Extending the current possibilities to fine-tune systems could enable to study interplays between different physical observables in greater detail and is thus of major interest in present experiments and theoretical explorations [10].

Nowadays, Feshbach resonances [69] are widely used to fine-tune low-energy observables [8]. They are quite well understood and were observed, for example, for systems of  $^{23}\text{Na}$  atoms [70], for  $^{133}\text{Cs}$  atoms [71] and for  $^6\text{Li}$  atoms [72]. In a subsequent experiment with (fermionic)  $^6\text{Li}$  atoms, it was possible to fine-tune the scattering length with

the aid of Feshbach resonances to form stable  ${}^6\text{Li}_2$  molecules and to observe Bose-Einstein condensation [73]. In the aforementioned gas of cesium atoms, Feshbach resonances were exploited to give the first experimental evidence for an Efimov resonance [13]. In particular, they were observed for an ultracold gas of  ${}^{52}\text{Cr}$  atoms [74], which have an exceptionally large magnetic dipole moment. In a subsequent experiment, it was possible to generate a BEC [75] with significant anisotropic dipolar character. A strongly dipolar BEC was reported in Ref. [76]. The strength of (long-range) dipolar interactions compared to short-range contributions to the potential can be estimated with the quantity [10]

$$\epsilon_{dd} \equiv \frac{Md^2}{3a_s}, \quad (1.5)$$

with particle mass  $M$ , dipole moment  $d$  and  $S$ -wave scattering length  $a_s$ . For  $\epsilon_{dd} > 1$ , the dipolar dominates over the short-range interaction and vice versa. For Ref. [76] the authors achieved  $\epsilon_{dd} \approx 1$  by reducing  $a_s$  using Feshbach resonances.

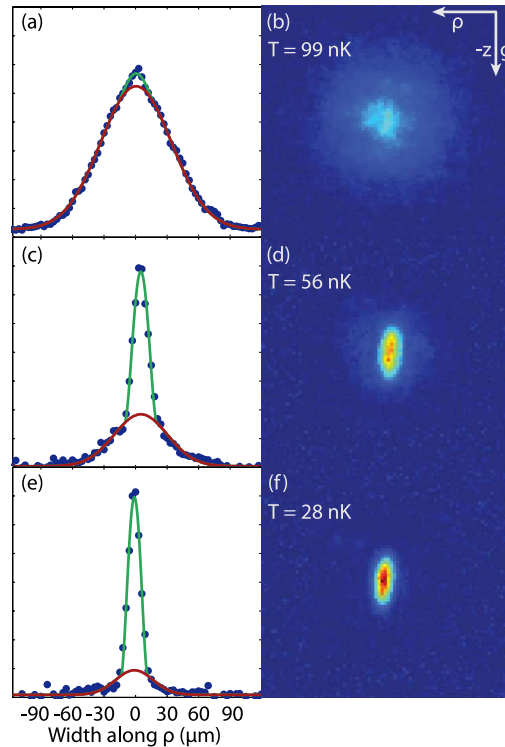


**Figure 1.3.:** Experimental evidence for a Bose-Einstein condensate of (strongly dipolar) dysprosium. Shown is the time-of-flight measurement for the radial extension of a dilute dysprosium condensate for three different temperatures. Adapted from “Strongly dipolar Bose-Einstein condensate of dysprosium,” by M. Lu et al., *Phys. Rev. Lett.* **107**, 190401 (2011). Adapted with permission.

The first BEC where  $\epsilon_{dd} > 1$  without an explicit tuning of  $a_s$ , was created by the authors of Ref. [77]. They used a dilute gas of dysprosium atoms, the element with the highest magnetic dipole moment [78], and found Bose-Einstein condensation for temperatures below  $T_c = 100 \pm 20$  nK. Figure 1.3 shows the momentum distribution of the condensate for various temperatures obtained from time-of-flight measurements. To describe a BEC of strongly dipolar atoms, the Gross-Pitaevskii equation [79, 80] can be extended to account for anisotropic interactions [81, 82]. It can be solved analytically in the Thomas-Fermi limit<sup>2</sup> and an inverted parabola is expected [83]. In Fig. 1.3, in addition to the parabolic momentum distribution, a Gaussian fit for the thermal background was performed and the inverted parabola is evident for  $T \lesssim T_c$ .

Optical lattices offer another opportunity to enhance the dipole-dipole interaction energy over motional and short-range interaction energies [84]. An optical lattice filled with bosonic erbium atoms, with large magnetic dipole moment, was experimentally realized [85] and theoretically described [86]. For fermionic potassium-rubidium molecules, it was possible to moderately tune the dipole-dipole interaction strength [87] by means of a lattice.

Moreover, plenty of universal phenomena are predicted to be present in a gas of ultracold polar molecules. For example in Refs. [88, 89] the authors analyze the dependence of the elastic scattering cross section on the scattering energy

<sup>2</sup> In the Thomas-Fermi limit the kinetic energy at zero-point is negligible compared to the trapping and interaction energy.

and find that results are independent of the details of the short-range interaction. Though, they are sensitive to the regulator used to remove ultraviolet divergences. The dependence on the radius of the hard-sphere regulator is studied in Ref. [88]. An analysis removing any influence of the regulator on physical observables has not been available. We thoroughly investigate and remove the regulator dependence within an effective-theory framework. In Ref. [90] two- and three-dipole systems are addressed. Also here, results depend on the radius of the hard-sphere regulator. However, the authors show that the dependence of the (two-body) binding energy on the  $S$ -wave scattering length is the same for all threshold resonances. Moreover, they determine the three-body recombination rate, i.e. the rate at which two of three polar molecules form a dimer and interact with the left over particle. They show that it is solely determined by two-body scattering length. In Ref. [91] three bosonic dipoles are studied within a hyperspherical formalism. It is found that the Efimov effect exists for polar molecules in the vicinity of a two-body resonance. The predicted three-body binding energies are exclusively determined by two-body observables, similar to Ref. [90]. However, a fully non-perturbative investigation of two- and three-dipole interactions, particularly with an emphasis on the renormalization of the two-dipole system has not been carried out and is provided in this thesis.

In all above mentioned analyses and in the here presented work, dipoles are assumed to be pointlike. In real experiments, deviations due to a finite spatial extension are small [90] but internal degrees of freedom and excitations coming along with those might play an important role. It is therefore desirable to prepare gases of atoms or molecules in their ground state in order to compare to theory. Moreover, a control over internal degrees of freedom is essential in order to be able to cool down a gas of atoms or molecules. While atoms are comprehended well, as earlier mentioned experiments demonstrate, molecules possess a much more sophisticated and less understood internal structure due to additional rotational, vibrational and hyperfine states.

First steps towards control over molecular gases have been taken. In Ref. [92] the authors report the preparation of a gas of highly dipolar potassium-bromide molecules in their ground state. Control over transitions between different excited states was recently achieved for potassium-sodium molecules in Ref. [93]. With the advance of cooling and controlling techniques, it should be possible to further manipulate and investigate gases of strongly polar molecules, opening new opportunities in the field of physics at ultralow temperatures.

This thesis is divided into three parts: about effective theories, the  $X(3872)$  and bosonic dipoles. Basics about effective theories are given in Chap. 2. We exemplify how to construct an effective theory starting from fundamental symmetry considerations. Different regularization techniques and renormalization schemes are introduced by means of a pure contact theory. Moreover, we elaborate on bound states in a finite volume and derive shifts for the binding energy. Subsequently, as an example for long-range interactions, the singular  $1/r^2$  and  $1/r^3$  potentials are discussed in an effective-theory framework.

Chapter 3 is dedicated to the  $X(3872)$ . At first, we elaborate on the phenomenology of the  $X(3872)$  and introduce the effective field theory we use in order to describe the  $X(3872)$  as a hadronic molecule, called XEFT. The Feynman rules, derived from the XEFT Lagrangian, are formulated and the power counting is discussed in detail. Furthermore, we elaborate on the role of pions. Their explicit inclusion is an essential feature of XEFT.

Chiral extrapolations for the  $X(3872)$  are derived in the second section of the third chapter. We calculate the scattering amplitude and cure emerging infrared divergences by resumming the  $D^{*0}$  self-energy. This procedure generates a width for the  $D^{*0}$  meson. After renormalizing at the physical point, we study chiral extrapolations for the binding energy and the  $\bar{D}^0 D^{*0}$   $S$ -wave scattering length. In particular, we describe a method on how to extract shifts for the binding energy from perturbative corrections to the scattering amplitude. We estimate for which quark masses XEFT is valid and present quantitative results subsequently.

Finite volume corrections to the binding energy are subject of the third and last section of Chap. 3. We rederive the transition amplitude for  $\bar{D}^0 D^{*0}$  mesons confined in a cubic box with periodic boundary conditions. Again, the  $D^{*0}$  meson's self-energy is of central importance and now induces a mass shift. A peculiarity of  $\bar{D}^0 D^{*0}$  scattering in the finite volume are on-shell three-body  $\bar{D}^0 D^0 \pi$  intermediate states which induce singularities. They have to be treated carefully and further restrict the range of validity of XEFT. Thereafter, we apply the above mentioned method, now to the finite volume amplitude, and extract the binding energy. In addition, we use a second approach based on the effective range expansion. It can be utilized for quark masses for which no on-shell three-body intermediate states exist. It serves to check our results for consistency. Eventually, we show our combined results for the volume and quark mass dependence of the binding energy.

Dipole-dipole interactions are covered in the fourth chapter. We establish an effective theory in order to describe non-relativistic dipoles. At its bottom is the long-range dipole-dipole potential. We shortly review the derivation of the potential and present a possible manipulation technique. Symmetries and consequential conservation laws are discussed in detail. To account for unresolved effects of physics beyond the scales integrated out of the effective theory, suitable

---

short-range operators are formulated. Moreover, a Gaussian cutoff regulator is used to remove ultraviolet divergences. The full potential is then projected on partial waves. We work in two different coordinate systems. On the one hand, we use cylindrical coordinates. They exploit the symmetry of the potential and the arising integral equations decouple completely. On the other hand, spherical coordinates increase the attainable accuracy, but come along with a coupled system of integral equations. The approaches complement one another and can be used to cross-check. At the end of the first section we present bound-state spectra for two bosonic dipoles for various quantum numbers and dipole tunings.

Three-dipole systems are addressed afterwards. The bound-state Faddeev equation is introduced and solved for the simpler case of a separable potential. For the non-separable dipole-dipole potential the Faddeev equation is projected on cylindrical partial waves. It can be simplified if the two-body threshold is dominated by a particular partial wave and the three dipoles are shallowly bound. We solve the Faddeev equation numerically and analyze the three-body spectrum. At the end of the fourth chapter, an alternative formulation of the Faddeev equation is presented, which is beneficial for numerical studies and can, for instance, be solved more cost-efficiently. For a proof of principle, we project it on spherical partial waves and solve it for the non-separable  $1/r^3$  potential.

In the appendix we derive the explicit expressions for selected Feynman amplitudes, for the infinite volume in App. A.1.1 and for the finite volume in App. A.2.1. Moreover, we calculate the mass shift induced by a non-relativistic self-energy diagram in App. A.3. For dipole interactions we Fourier transform the potential from coordinate to momentum space and vice versa in App. B.1. The partial wave expansions in a cylindrical as well as in a spherical basis are derived in Apps. B.2.1 and B.2.2, respectively. A relation between both representations is given subsequently in App. B.2.3. Details for the numerical implementation of the two-dipole problem are subject of App. B.3. Besides, we present various bound-state spectra for quantum numbers other than  $m = 0$  and  $P = +$  in App. B.4. A method to check for convergence in the truncation parameter, introduced for the Lippmann-Schwinger equation in a spherical coordinate system, can be found in App. B.5. Three-body dynamics are addressed in subsequent sections. The Faddeev amplitudes are projected on cylindrical partial waves in App. B.6. Afterwards, details on the numerical implementation are given. At the end, we derive an alternative formulation of the Faddeev equation in App. B.8 and project it on spherical partial waves in App. B.9.



---

## 2 Effective theories

---

Effective theories play a central role throughout this thesis. In this chapter we want to introduce fundamental concepts. We encourage the use of an effective theory description and discuss which requirements are at its basis. Moreover, we describe how to construct an effective theory. Explicit examples are given, beginning with pure contact interactions. In particular we discuss the regularization and renormalization following different approaches. Finite volume effects for contact theories are subject of the third section. Subsequently, we introduce long-range potentials, here the  $1/r^2$  and  $1/r^3$  potential, which can not be modeled with effective short-distance operators. The potentials are regularized and renormalized. Typical spectra are presented and discussed at the end.

For comparability reasons, we consistently utilize non-perturbative approaches, throughout this chapter and in Chap. 4 for two and three dipoles. We remark that for certain systems, for example for particles interacting via pure contact interactions or the  $X(3872)$ , it is also possible to calculate scattering amplitudes perturbatively [94, 16] (cf. Chap. 3).

---

### 2.1 Renormalizability, symmetries and power counting

---

Effective theories play a crucial role in all areas of physics and presumably all of presently used physical theories are in some sense an effective theory. For a detailed review about effective theories we refer to [95].

The basic idea is to exploit the fact that all physics experiments take place at a certain energy scale. Consider, for example, a collider experiment. An appropriate measure of the experiment's energy scale is the invariant mass. All particles with masses below the invariant mass and the correct quantum numbers can be created on-shell, can thus propagate and mediate non-local interactions. Particles with a mass much larger than the invariant mass of the collider can not exist on-shell and therefore their effect can be absorbed in local interactions [96].

Another example are atomic experiments. Here, the particles' kinetic energy can be used as an estimate for the experiment's typical energy. It is possible to assign a de Broglie wave length proportional to the square root of the inverse kinetic energy. The experiment's resolution is then limited by the de Broglie wave length. The effect of physics at smaller length scales or, equivalently, larger energies can again be included by a set of local operators. For each local operator a new low-energy constant appears, which has to be fitted to experiment or the underlying theory. We give an explicit example for the construction of an effective theory in Sec. 2.2.

The allowed short-distance operators are constrained by the symmetries of the underlying theory, e.g., the conservation of quantum numbers. It implies that when, for example, describing strong interactions with short-distance effective operators these have to conserve parity. Whereas for an effective theory for the weak interaction, four-point interaction vertices have to account for the parity-violating nature of the weak force [97].

Further principles which have to be fulfilled are analyticity and unitarity of the scattering amplitude together with the correct causality properties. These requirements narrow down the possible operators which may be included [98]. Nonetheless, there are infinitely many. In this sense, effective theories are non-renormalizable. In particular, when calculating  $n$ -point functions in an effective quantum field theory, all amplitudes are superficially ultraviolet divergent and infinitely many counterterms are required in order to absorb these divergences.

However, it is still possible to systematically include effective interactions into the theory by means of the *power counting*. A crucial feature of effective theories is a separation of scales [98]. It is possible to divide the theory into different energy regions as mentioned before. The low-energy scale,  $M_{lo}$ , at which a certain experiment takes place and the high-energy scale,  $M_{hi}$ , which is experimentally not accessible. Short-range operators can then be ordered in powers of the ratio of energy scales  $M_{lo}/M_{hi}$  and, depending on the desired precision, be included up to a maximum power of the ratio.

Considering weak decays, the low-energy scale is the difference of the mass of the decaying particle and its decay products. The high-energy scale, on the other hand, is the mass of the weak gauge bosons. Once the low-energy constants are determined from one decay process, e.g., the  $\beta^+$  decay of  $^{14}O \rightarrow ^{14}N^* + e^+ + \nu_e$ , it is possible to calculate low-energy observables such as decay widths for other  $\beta$  decays or for the  $\mu$  decay [97]. Considering the large mass of the weak gauge bosons ( $m_W \approx 80.39$  GeV,  $m_Z \approx 91.19$  GeV [33]) compared to typical released kinetic energies ( $\mathcal{O}(1$  MeV)), often just one low-energy constant is sufficient to describe the decay process accurately, known as Fermi's constant.

On the other hand, in a collider experiment with an invariant mass close to  $m_W$ , the weak gauge bosons have to be included explicitly as additional degrees of freedom and aforementioned effective field theory description fails. The high-energy scale can thus be interpreted as a breakdown scale of the effective theory or a scale above which new degrees of freedom become important.

---

## 2.2 Pure contact theories

---

In the following, we give an explicit example how to construct an effective theory using short-distance operators only. Since renormalization plays a central role in this thesis, we illustrate how to renormalize a pure contact theory in detail. Different renormalization schemes used in upcoming chapters are presented and fundamental techniques are introduced. We further explicitly calculate certain observables and exemplify how to embed an effective theory in a finite volume. It is worth mentioning that pure contact theories are by no means just toy models but find their application in different fields of physics and are a powerful tool in order to make predictions for experiments or computer simulations. Examples range from classical physics, where the kinetic gas theory is presumably the best known theory with contact operators only, to modern particle and condensed matter theory. For example, Bose-Einstein condensation can be described to great precision using short-distance degrees of freedom only [99]. Furthermore, Fermi's four-point interaction models the weak interaction at low energies to high accuracy [97] and pionless effective field theories are widely used in particle physics to mimic the real interaction between, e.g., nuclei [100] or  $D$  mesons [101], to name just a few.

---

### 2.2.1 Short-distance operators

---

We consider two pointlike and non-relativistic particles with mass  $M$ . The underlying theory we attempt to parametrize shall be invariant under rotations, i.e. conserves angular momentum. There are different approaches how to construct a suitable short-range interaction. Common examples are rectangular potential barriers [8] or a series of Dirac delta functions [96]. We use the latter parametrization since its representation in momentum space is particularly simple and does not suffer from oscillatory behavior.

We first write down a potential in coordinate space. The allowed terms are ordered by the typical momentum at which the calculations are carried out or experiments take place, respectively, over the momentum scale integrated out of the theory. Considering, for instance, a pionless theory for nucleon-nucleon scattering, the latter scale is the pion mass. An explicit potential takes the form [96]

$$U(\mathbf{r}) = c_0 \delta^{(3)}(\mathbf{r}) + \frac{c_2}{2} \nabla^2 \delta^{(3)}(\mathbf{r}) + \dots, \quad (2.1)$$

where the dots denote higher-order terms, compatible with the symmetries of the underlying theory and suppressed according to the power counting. The  $c_i$  are the coupling constants, coming with  $i$  derivatives. They have to be matched, either to the underlying theory or to experiment.

A common method is to match the coupling constants to an effective range expansion whose parameters are determined by experiment or to the outcome of a lattice calculation. The latter is an alternative approach to solve the underlying theory non-perturbatively. It will play an important role in Chap. 3. To match the coupling constants to an effective range expansion we follow Ref. [22].

We work in momentum space and thus need the Fourier transform of the potential (2.1). It reads, already projecting on  $S$ -waves

$$V(\ell, \ell') = c_0 + \frac{c_2}{2} (\ell^2 + \ell'^2) + \dots, \quad (2.2)$$

with the absolute values of the relative in- and outgoing momenta  $\ell$  and  $\ell'$ , respectively. As a next step, we solve the Lippmann-Schwinger (LS) equation, introduce different techniques to regularize ultraviolet divergences and match observables of the low-energy theory.

A completely equivalent approach to construct an effective theory is to use a Lagrangian formulation. We follow this approach in Chap. 3 for the  $X(3872)$ .

---

### 2.2.2 Renormalization schemes

---

We consider  $S$ -wave scattering in the non-relativistic limit. The LS equation for scattering at energy  $E$  then only depends on the absolute values of the external momenta and reads

$$T(E, \ell, \ell') = -V(\ell, \ell') + \int \frac{d^3k}{(2\pi)^3} V(\ell, k) \frac{1}{E - k^2/M + i\epsilon} T(E, k, \ell'). \quad (2.3)$$

We already performed the contour integration over the zeroth component of the momentum. Furthermore, the potential is separable in the in- and outgoing momenta. From now on, we omit any higher-order terms in our effective theory expansion for convenience. Considering on-shell scattering only, we can simplify Eq. (2.3)

$$\begin{aligned} T(p^2) &= -c_0 - c_2 p^2 - MT(p^2) \int \frac{d^3k}{(2\pi)^3} \frac{1}{k^2 - p^2 - i\epsilon} \left( c_0 + \frac{c_2}{2} (p^2 + k^2) \right) \\ &= -c_0 - c_2 p^2 - MT(p^2) \left( c_0 I_0(p^2) + \frac{c_2}{2} p^2 I_0(p^2) + \frac{c_2}{2} I_2(p^2) \right), \end{aligned} \quad (2.4)$$

with  $ME = p^2 = \ell^2 = \ell'^2$ . The loop integrals  $I_0(p^2)$  and  $I_2(p^2)$  are defined as

$$I_0(p^2) \equiv \int \frac{d^3k}{(2\pi)^3} \frac{1}{k^2 - p^2 - i\epsilon}, \quad (2.5)$$

$$I_2(p^2) \equiv \int \frac{d^3k}{(2\pi)^3} \frac{k^2}{k^2 - p^2 - i\epsilon} \quad (2.6)$$

and are divergent. The divergences are of ultraviolet type, i.e. come from the integration over high momenta, where the effective theory breaks down. There are different approaches how to regularize such divergences and in the following, we introduce two which will be used in latter parts of this thesis.

---

### Cutoff regularization

---

An intuitive and straightforward way to regularize ultraviolet (UV) divergences is to introduce a cutoff for high momenta, i.e. a regulator  $f^R(\ell)$  for which holds

$$f^R(\ell) \rightarrow \begin{cases} 1, & \ell \rightarrow 0, \\ 0, & \ell \rightarrow \infty. \end{cases} \quad (2.7)$$

The cutoff regularization is motivated by the circumstance that the effective theory is only valid up to a certain momentum scale. The momentum at which the theory breaks down is determined by the scale integrated out of the theory, e.g., the pion mass in case of the pionless effective field theory. The idea is then to mimic the effects of physics at high-momentum scales by tuning the short-range operators as introduced in Eq. (2.1) or Eq. (2.2), respectively, to reproduce a chosen set of low-energy observables. However, it has several disadvantages as well. On the one hand, it suffers from a violation of gauge and Galilean invariance. On the other hand, expressions tend to be lengthier than for dimensional regularization. To implement the cutoff, we rewrite the potential

$$V(\ell, \ell') \equiv f^R(\ell)V^R(\ell, \ell')f^R(\ell') \quad (2.8)$$

and we obtain the regularized LS equation for the regularized  $T$ -matrix,  $T^R(p^2)$ , which reads, starting from Eq. (2.4)

$$\begin{aligned} T^R(p^2) &= -c_0 - c_2 p^2 - M T^R(p^2) \int \frac{d^3k}{(2\pi)^3} \frac{f^R(k^2)}{k^2 - p^2 - i\epsilon} \left( c_0 + \frac{c_2}{2}(p^2 + k^2) \right) \\ &= -c_0 - c_2 p^2 - M T^R(p^2) \left( c_0 I_0^R(p^2) + \frac{c_2}{2} p^2 I_0^R(p^2) + \frac{c_2}{2} I_2^R(p^2) \right). \end{aligned} \quad (2.9)$$

Note that, since our ansatz to regularize is separable, the regularized  $T$ -matrix still depends on the energy only. For illustration we use a particularly simple choice for the regulator

$$f^R(\ell) \equiv \theta(\lambda - \ell), \quad (2.10)$$

where  $\theta(x)$  is the Heaviside function.<sup>1</sup> We introduced the cutoff parameter  $\lambda$ . The loop integrals are now divergence free but depend on  $\lambda$ . They read

$$I_0^R(p^2) = \int_0^\lambda \frac{dk}{2\pi^2} \frac{k^2}{k^2 - p^2 - i\epsilon} = \frac{1}{2\pi^2} \left( \lambda - \sqrt{-p^2 - i\epsilon} \operatorname{atan} \left( \frac{\lambda}{\sqrt{-p^2 - i\epsilon}} \right) \right), \quad (2.11)$$

$$I_2^R(p^2) = \frac{1}{2\pi^2} \frac{\lambda^3}{3} + p^2 I_0^R(p^2). \quad (2.12)$$

The cutoff parameter characterizes the momentum scales integrated out of the theory. We do not expect that our theory remains valid for energies  $p^2 \gtrsim \lambda^2$ . We therefore assume  $p^2 \ll \lambda^2$  and it is justified to expand the atan to obtain

$$I_0^R(p^2) = \frac{1}{2\pi^2} \left( \lambda - \frac{\pi}{2} \sqrt{-p^2 - i\epsilon} - \frac{p^2}{\lambda} \right) + \mathcal{O} \left( \frac{p^4}{\lambda^3} \right) \quad (2.13)$$

---

<sup>1</sup> We remark that the choice of a sharp cutoff regulator might be disadvantageous in certain cases and a Gaussian cutoff is preferable. First of all, a Gaussian cutoff is globally differentiable. Furthermore, using, e.g., spherical and cylindrical coordinates, as done in Sec. 4.1, a Gaussian regulator has the advantage of coinciding in both coordinate systems. Moreover, the Fourier transform to coordinate space of a potential with a sharp cutoff might be oscillatory.

and likewise for the regularized loop integral  $I_2^R(p^2)$ . The regularized  $T$ -matrix is then given as

$$T^R(p^2) = \frac{4\pi}{M} \frac{-c_0 - c_2 p^2}{\frac{4\pi}{M} + (c_0 + c_2 p^2) \left( \frac{2}{\pi} \lambda - \frac{2}{\pi} \frac{p^2}{\lambda} + ip \right) + c_2 \frac{2}{\pi} \lambda^3}. \quad (2.14)$$

To eliminate the dependence on the cutoff parameter we use the leftover degrees of freedom, namely the coupling constants  $c_0$  and  $c_2$ . To match the coupling constants we use the effective range expansion [102]. For the on-shell scattering amplitude holds

$$ip + \frac{4\pi}{M} \frac{1}{T^R(p^2)} = -\frac{1}{a_s} + \frac{1}{2} r_s p^2 + \mathcal{O}(p^4), \quad (2.15)$$

with the  $S$ -wave scattering length  $a_s$  and the  $S$ -wave effective range  $r_s$ . Expanding  $T^R(p^2)$  in powers of  $p$  we obtain for the coupling constants

$$c_0 = \frac{4\pi}{M} \frac{1}{\frac{1}{a_s} - \frac{2}{\pi} \lambda} + \frac{c_2 \lambda^3}{3\pi} \frac{1}{\frac{1}{a_s} - \frac{2}{\pi} \lambda}, \quad (2.16)$$

$$c_2 = \frac{4\pi}{M} \frac{r_s/2 - 2/\pi\lambda}{\left( \frac{1}{a_s} - \frac{2}{\pi} \lambda \right)^2 - \frac{r_s/2 - 2/\pi\lambda}{3\pi} \lambda^3}. \quad (2.17)$$

We are now in the position to write down the renormalized<sup>2</sup> scattering amplitude up to  $\mathcal{O}(p^4)$ . It is given as

$$T^R(p^2) = \frac{4\pi}{M} \frac{1}{-\frac{1}{a_s} + \frac{r_s}{2} p^2 - ip + \mathcal{O}(p^4)}. \quad (2.18)$$

Equation (2.18) is in agreement with the general expression for the  $S$ -wave scattering amplitude

$$T^R(p^2) = \frac{4\pi}{M} \frac{1}{p \cot \delta_s(p) - ip}. \quad (2.19)$$

For the  $S$ -wave scattering phase shift  $\delta_s(p)$  applies a similar effective range expansion as in Eq. (2.15).

The effective range parameters  $a_s$  and  $r_s$  account for the effects of short-range physics not accessible in the experiment of interest. They are coming from the high-momentum region and are thus of order  $\sim 1/M_{hi}$ . On the other hand,  $p$  is in the order of the typical momentum scale and therefore  $\sim M_{lo}$ . Considering the denominator of the transition amplitude in Eq. (2.18), we can confirm the power counting, i.e. the expansion in the ratio of the low- over the high-momentum scale. The term proportional to the  $S$ -wave effective range is suppressed by  $(M_{lo}/M_{hi})^2$  compared to the first term  $\sim 1/a_s$ . It first occurs when the  $c_2 p^2$  vertex is embedded and hence we conclude that  $c_2$  accounts for higher-order effects.

We remark that the suppression of the  $c_2 p^2$  vertex compared to the  $c_0$  vertex is already manifest in Eqs. (2.16) and (2.17), when assuming that the cutoff is large compared to  $p$ . Then, the  $c_0$  vertex behaves  $\sim 1/\lambda$ , whereas  $c_2 p^2 \sim p^2/\lambda^3$  and hence is suppressed with  $p^2/\lambda^2$ . However, we emphasize that this suppression is not to be confused with the power counting which does not depend on the cutoff scale  $\lambda$ .

We further consider a scenario in which the scattering length is unnaturally large, i.e.  $a_s \gg r_s$ . The scattering amplitude has a pole at a binding energy of<sup>3</sup>

$$\begin{aligned} E_B &= \frac{2}{Mr_s^2} \left( 1 - \frac{r_s}{a_s} - \sqrt{1 - 2\frac{r_s}{a_s}} \right) \\ &= \frac{1}{Ma_s^2} \left( 1 + \frac{r_s}{a_s} + \mathcal{O}\left(\frac{r_s}{a_s}\right)^2 \right). \end{aligned} \quad (2.20)$$

<sup>2</sup> Renormalized means that the amplitude is UV finite and does not depend on the cutoff scale anymore, i.e. that all cutoff dependence is absorbed in the coupling constants and that the theory is already matched to reproduce a set of low-energy observables.

<sup>3</sup> We point out the existence of a second pole at an energy of

$$E_B = \frac{2}{Mr_s^2} \left( 1 - \frac{r_s}{a_s} + \sqrt{1 - 2\frac{r_s}{a_s}} \right) = \frac{4}{Mr_s^2} \left( 1 - \frac{r_s}{a_s} + \mathcal{O}\left(\frac{r_s}{a_s}\right)^2 \right).$$

However, since  $r_s$  is counted  $\sim 1/M_{hi}$ , this pole is in the high-momentum region and therefore clearly out of the range of applicability of our effective theory.

For  $r_s \rightarrow 0$  or  $a_s \rightarrow \infty$  we acquire the universal<sup>4</sup> relation

$$E_B \rightarrow 1/Ma_s^2. \quad (2.21)$$

The limit of  $a_s \rightarrow \infty$  is also known as the resonant limit, whereas the limit of all other effective range parameters going to zero (here only the effective range) is known as scaling limit [8]. In both limits, Eq. (2.21) can also be obtained from scaling symmetry. Corrections of order  $r_s/a_s$  are thus also known as scaling violations.

In the resonant or scaling limit, just one coupling constant is required, here  $c_0$ . The corresponding contact operator comes with a  $\delta$ -distribution and the interacting particles are treated as if they were pointlike. Note that for  $a_s \rightarrow \infty$  we find  $E_B \rightarrow 0$  and the scattering amplitude has a pole at threshold. Physically, at threshold the de Broglie wavelength goes to infinity and no internal structure of the particles is resolved. Moving away from threshold, the de Broglie wavelength decreases and higher-order contact terms have to be included to account for deviations from perfect pointlike particles. Going to higher orders in the effective theory, the error can be systematically decreased, usually in powers of  $M_{lo}/M_{hi}$ . But each new coupling constant has to be matched with a low-energy observable. The next term in the expansion comes with four derivatives or a momentum to the fourth power, respectively. A suitable low-energy observable would be the  $S$ -wave shape parameter occurring as the coefficient for the  $p^4$ -term in the effective range expansion. For further discussions, we refer to the literature [8, 103, 104].

---

### Power divergence subtraction scheme

---

We present another regularization scheme, namely the power divergence subtraction (PDS). It was introduced for nucleon-nucleon scattering [94] and is a dimensional regularization scheme. It allows for a consistent and manifest power counting for systems with an unnaturally large scattering length. For calculations considering the  $X(3872)$ , it enables to perturbatively include pions (cf. Chap. 3) and systematically expand the scattering amplitude when considering  $\bar{D}^0 D^{*0}$  scattering. We follow Ref. [94] to convey the general idea. Details and the methodology how to include pions perturbatively are discussed in more detail in Chap. 3. In combination with the cutoff regularization discussed in the previous section, the authors of Ref. [59] developed a method how to calculate observables of a two-particle system with unnaturally large scattering length in a finite volume. The method is subject of the upcoming section.

We begin with the regularization of the loop integrals introduced in Eqs. (2.5) and (2.6). First, the integration measure is replaced with a  $d$ -dimensional one to obtain for the loop integrals

$$I_0^d(p^2) \equiv \left(\frac{\Lambda}{2}\right)^{3-d} \int \frac{d^d k}{(2\pi)^d} \frac{1}{k^2 - p^2 - i\epsilon}, \quad (2.22)$$

$$I_2^d(p^2) \equiv \left(\frac{\Lambda}{2}\right)^{3-d} \int \frac{d^d k}{(2\pi)^d} \frac{k^2}{k^2 - p^2 - i\epsilon}. \quad (2.23)$$

We introduced the PDS renormalization scale  $\Lambda$ , which ensures that the dimension of coupling constants is unchanged [105]. The contour integration has been performed already and we are left with an Euclidean metric. The integrals read

$$I_0^d(p^2) = (-p^2 - i\epsilon)^{\frac{d-2}{2}} \Gamma\left[\frac{2-d}{2}\right] \frac{(\Lambda/2)^{3-d}}{(4\pi)^{d/2}}, \quad (2.24)$$

$$I_2^d(p^2) = p^2 I_0^d(p^2), \quad (2.25)$$

where we used that in dimensional regularization scaleless integrals vanish. Both loop integrals are finite in  $d = 3$  space dimensions, but have a pole in  $d = 2$ . In contrast to the  $MS$  scheme, where only poles in  $d = 3$  are subtracted, in PDS poles in both dimensions,  $d = 3$  and  $d = 2$ , are removed. Eventually, the scattering amplitude is independent of the renormalization scale. The consequence of such a subtraction scheme, however, is that diagrams of higher orders are manifestly suppressed even for unnaturally large scattering length. As opposed to the  $MS$  scheme, the suppression is evident already when regarding the coupling constants, similar to the cutoff regularization.

We proceed with the evaluation and regularization of the loop integrals (2.24) and (2.25). Using PDS and taking the limit  $d \rightarrow 3$  afterwards, we obtain

$$I_0(p^2) \xrightarrow{\text{PDS}} \frac{1}{4\pi} \left(\Lambda - \sqrt{-p^2 - i\epsilon}\right), \quad (2.26)$$

$$I_2(p^2) \xrightarrow{\text{PDS}} \frac{1}{4\pi} p^2 \left(\Lambda - \sqrt{-p^2 - i\epsilon}\right). \quad (2.27)$$

---

<sup>4</sup> Universal means that relations are not dependent on the precise form of the interaction itself but on low-energy observables only.

Note the similarity to the cutoff regularized loop integral  $I_0(p^2)$  in Eq. (2.13). The abundance of the term  $\sim \Lambda^3$  makes expressions particularly simple for the coupling constants  $c_0$  and  $c_2$  in PDS. We match the transition amplitude in PDS,

$$T^R(p^2) = \frac{4\pi}{M} \frac{-c_0 - c_2 p^2}{\frac{4\pi}{M} + (c_0 + c_2 p^2)(\Lambda + ip)}, \quad (2.28)$$

to the effective range expansion in Eq. (2.15) and obtain expression (2.18). The PDS renormalized coupling constants read

$$c_0 = \frac{4\pi}{M} \frac{1}{\frac{1}{a_s} - \Lambda}, \quad (2.29)$$

$$c_2 = \frac{4\pi}{M} \frac{r_s/2}{\left(\frac{1}{a_s} - \Lambda\right)^2}. \quad (2.30)$$

Again, there is a close similarity to the cutoff-renormalized expressions for  $c_0$  and  $c_2$  when omitting the  $\lambda^3$  terms. In this sense, PDS is a dimensional regularization scheme which restores the linear divergences occurring in cutoff regularization.

The  $MS$  regularized expressions for the coupling constants coincide with Eqs. (2.29) and (2.30) when letting  $\Lambda \rightarrow 0$ . Note that in  $MS$   $c_0 \sim a_s$  and  $c_2 \sim a_s^2/M_{hi}$ . When going to higher orders with interactions  $\sim c_{2n}p^{2n}$ , one finds  $c_{2n} \sim a_s^{n+1}/M_{hi}^n$  [94] (see also Ref. [51] for an explicit expression of  $c_4$ ). For large scattering length,  $MS$  regularization suggests that coupling constants of higher orders are enhanced and the effective theory is valid over a very narrow momentum range only. Using PDS on the other hand,  $\Lambda$  can be used to tune the coupling constants to be of natural size even in the limit of  $a_s \rightarrow \infty$ . Choosing  $\Lambda \sim M_{lo}$ , we find for the coupling constants  $c_0 \sim 1/M_{lo}$ ,  $c_2 p^2 \sim 1/M_{hi}$  and  $c_4 p^4 \sim M_{lo}^2/M_{hi}^3$ . This suppression of higher-order terms is confirmed when looking at the renormalized scattering amplitude. The next term in the effective range expansion can be used to estimate the systematic error made by truncating. It is proportional to the  $S$ -wave shape parameter,  $P_s$ , which is counted  $\sim 1/M_{hi}^3$ . Therefore, its contribution is suppressed with  $(M_{lo}/M_{hi})^2$  compared to the effective range term, which is the same suppression for the  $c_4 p^4$  compared to the  $c_2 p^2$  vertex using PDS. Hence, for unnaturally large scattering length, PDS reflects the correct suppression of higher-order terms already in the expressions for the coupling constants. It thus makes the justification of the perturbative inclusion of higher-order interactions manifest. A method on how to extract shifts for the binding energy from perturbative amplitudes will be given in Sec. 3.2.6.

---

### 2.2.3 Finite volume effects

---

A major topic of this thesis is the investigation of finite volume effects. Quantifying the errors due to finite volume effects in a controlled way is essential since lattice simulations play an increasingly important role in modern particle physics. Of special interest are systems with large length scales since the numerical treatment of those is particularly difficult. The  $X(3872)$  represents such a system and is addressed in Chap. 3, where we calculate shifts up to NLO for its binding energy. In particular, finite volume effects for the  $X(3872)$  are subject of Sec. 3.3.

In this section, we want to present fundamental relations and techniques for scattering in a finite volume. It was Lüscher who first derived the volume dependence of the energy spectrum for two stable particles in a finite box with large spatial extent [57, 58]. For two non-relativistic particles interacting with large scattering length Beane et al. [59] developed a method to obtain scattering observables in a finite volume. Here, we follow their derivation. The authors pointed out that a lattice does not have to be large compared to the scattering length of the system to extract meaningful results. In this section, we consider two-body scattering. When three-body intermediate states are present, a more generalized approach has to be used, which we introduce in Sec. 3.2.6 and particularly in 3.3.

We consider a spatial, cubic box with side length  $L$  and periodic boundary conditions. At the same time, we keep the time interval infinite. This assumption is justified since lattice simulations are usually performed with significantly larger time than spatial interval length and effects due to the finite time interval are thus much smaller. The infinite time interval allows performing contour integrations over the zeroth component of momenta. Discretization effects are not part of this thesis, i.e. space and time shall be continuous.

We first consider a one-dimensional plane wave with momentum  $\ell$  on an interval of length  $L$  with periodic boundary conditions. The periodicity implies

$$e^{i\ell x} \doteq e^{i\ell(x+L)}, \quad (2.31)$$

constraining the allowed momenta to be integer multiples of  $2\pi/L$ . Going to three dimensions, relation (2.31) has to hold in all three directions and therefore, momenta are an integer vector times  $2\pi/L$ . Further, loop integrals over continuous, infinite volume loop momenta have to be replaced with discrete sums. The rule for replacement reads [57]

$$\int \frac{d^3k}{(2\pi)^3} \xrightarrow{V \rightarrow L^3} \frac{1}{L^3} \sum_{\mathbf{k} = \frac{2\pi}{L} \mathbf{n}}, \quad \mathbf{n} \in \mathbb{Z}^3. \quad (2.32)$$

To calculate finite volume corrections, we use the results of the previous section. The infinite volume transition amplitude follows from Eq. (2.4). Using the  $d$ -dimensional expressions for the loop integrals (2.22), (2.23) and (2.24), (2.25), respectively, the  $T$ -matrix reads

$$T(p^2) = \frac{-c_0 - c_2 p^2}{1 + (c_0 + c_2 p^2) M I_0(p^2)}. \quad (2.33)$$

Short-distance physics is unchanged and we expect the ultraviolet behavior to be the same as in the infinite volume. On the one hand, it follows that the coupling constants, parameterizing the high-momentum region integrated out of the effective theory, are unchanged when transitioning to the finite volume [57]. On the other hand, the UV divergences are the same as in the infinite volume. To regularize the finite volume loop integral using PDS, the authors of Ref. [59] add and subtract the infinite volume loop integral at zero energy. One infinite volume integral is regularized using PDS, yielding the dependence on the PDS renormalization scale  $\Lambda$ . For the other one, as well as for the finite volume loop integral, a momentum cutoff is introduced. Taking the limit  $\lambda \rightarrow \infty$  for the sum subsequently, the UV finite part of the finite volume loop integral is obtained. It follows for  $I_0$

$$\begin{aligned} I_0(p^2) \xrightarrow{V \rightarrow L^3} I_0^{R,L}(p^2) &= \lim_{\lambda \rightarrow \infty} \left[ \frac{1}{L^3} \sum_{\mathbf{k} = \frac{2\pi}{L} \mathbf{n}}^{\|\mathbf{k}\| < \lambda} \frac{1}{k^2 - p^2} - \int \frac{d^3\mathbf{k}}{(2\pi)^3} \frac{\theta(\lambda - |\mathbf{k}|)}{k^2} \right] + \frac{\Lambda}{4\pi} \\ &= \frac{1}{4\pi} \left( \Lambda + \frac{1}{\pi L} S \left( \left( \frac{Lp}{2\pi} \right)^2 \right) \right), \end{aligned} \quad (2.34)$$

where the quantity  $S(x)$  is defined as

$$S(x) \equiv \lim_{\lambda_n \rightarrow \infty} \left[ \sum_{\mathbf{n}}^{\|\mathbf{n}\| < \lambda_n} \frac{1}{n^2 - x} - 4\pi\lambda_n \right] \quad (2.35)$$

and  $\lambda_n \equiv L\lambda/2\pi$ . In general, the sum runs over all integer three-vectors and has to be evaluated numerically. However, it is possible to expand the sum around certain values of the energy to obtain analytical expansions. In particular, for negative energies far away from threshold, it is possible to use the Poisson summation formula<sup>5</sup>

$$\frac{1}{L^3} \sum_{\mathbf{k} = \frac{2\pi}{L} \mathbf{n}} f(\mathbf{k}) = \int \frac{d^3k}{(2\pi)^3} f(\mathbf{k}) + \sum_{\mathbf{n} \neq 0} \int \frac{d^3k}{(2\pi)^3} f(\mathbf{k}) e^{iL\mathbf{k}\cdot\mathbf{n}}. \quad (2.37)$$

The second term then gives the difference between finite and infinite volume quantities. For negative energies, it is exponentially suppressed.

The renormalized finite volume transition amplitude is just expression (2.33) with  $I_0(p^2)$  replaced with  $I_0^{R,L}(p^2)$ . The criteria for a pole of the transition matrix reads

$$1 + (c_0 + c_2 p^2) M I_0^{R,L}(p^2) \doteq 0, \quad (2.38)$$

determining the energy levels of the two-particle system in a finite volume. The coupling constants are given by Eqs. (2.29) and (2.30), respectively. The finite volume amplitude is independent of the PDS renormalization scale  $\Lambda$ .

In general, there are solutions to Eq. (2.38) for negative and positive energies. The negative-energy solutions approach

<sup>5</sup> The Poisson summation formula is a direct consequence of the Fourier representation of the Dirac comb

$$\frac{(2\pi)^3}{L^3} \sum_{\mathbf{n} \in \mathbb{Z}^3} \delta^{(3)}(\mathbf{k} - \frac{2\pi}{L} \mathbf{n}) = \sum_{\mathbf{n} \in \mathbb{Z}^3} e^{iL\mathbf{k}\cdot\mathbf{n}}. \quad (2.36)$$

bound states in the infinite volume. The positive-energy solutions, however, do not have a one-to-one counterpart. They originate from the particles being in resonance with the finite box, in other words, they occur when the extent of the box is a multiple of the particles de Broglie wavelength. For the  $X(3872)$  we focus on the negative-energy solutions. Depending on the parity of the state considered, the two particles are either deeper (positive parity) or weaker (negative parity) bound [106]. The results of this section are applicable to both scenarios: finite volume, two-particle scattering with a scattering length much larger than the side length of the box and systems for which  $L \gg |a_s|$ . The latter limit reproduces Lüscher's formula (here for  $c_2 = 0$ ) [57, 59]

$$E_B = \frac{1}{M a_s^2} \left[ 1 + \frac{12 a_s}{L} e^{-L/a_s} + \dots \right], \quad (2.39)$$

where the dots represent terms suppressed with higher powers of the exponential.

---

## 2.3 Singular potentials

---

The previous section is concerned with short-distance physics, which can not be resolved due to a finite de Broglie wavelength at low energies. In addition to such a short-range potential, which can be parametrized using, e.g., delta-distributions, long-range potentials might be present. These long-distance degrees of freedom can not be replaced by a series of tunable short-range operators since the energies of the considered experiments are sufficient to resolve details of the long-range interaction. They have to be included explicitly. For illustrative purposes we use isotropic, inverse power-law potentials, i.e. potentials of the type  $U(r) = 1/r^n$  with  $n \geq 2$  and  $r$  being the two-body separation. Potentials of this type are known as singular potentials since they diverge at  $r = 0$  and do not necessarily possess a unique solution to the Schrödinger equation (see [107, 108] and references therein).

Applications can be found, for instance, in atomic and molecular physics, where dipole-dipole interactions have a  $1/r^3$  proportion [109]. Moreover, in hadronic and nuclear physics, the OPE potentials obey a similar behavior [110]. Both potentials are subject of this thesis. As another example,  $1/r^6$  potentials correspond to van der Waals forces and find a wide range of application when looking at the low-energy scattering of atoms [8, 111]. In this section, we examine the  $1/r^3$  potential since it is relevant to latter chapters, and the  $1/r^2$  potential, as it possesses a discrete scale invariance [107] and is closely related to a system of three bosons interacting with unnaturally large scattering length [112], discussed in Sec. 4.2.1. Fundamental techniques are introduced and effects are discussed. They are also of interest in latter parts of this thesis, especially in Sec. 4.1. We begin with the  $1/r^2$  potential.

---

### 2.3.1 The $1/r^2$ potential

---

A study of the  $1/r^2$  potential in momentum space can be found in Ref. [107]. The authors use a renormalization group approach to investigate the bound-state spectrum of the attractive  $1/r^2$  potential. They use a momentum cutoff as a regulator and parametrize short-distance degrees of freedom using delta distributions. We follow their derivation but solve the LS equation solely numerically, introducing techniques used in upcoming chapters.

In addition to the short-range operators of the previous section (we set  $c_2 = 0$  and keep the  $c_0$  term only), we introduce a long-range part of the potential

$$U_l(r) = \frac{c}{M} \frac{1}{r^2}, \quad c = -\frac{1}{4} - \nu^2. \quad (2.40)$$

In contrast to the one- or two-dimensional case, in three dimensions, the attractive  $1/r^2$  potential has to have a minimum strength in order to possess a bound state [107] (also cf. [113] for other kinds of potentials). The constant  $c$  is the strength of the long-range potential and is chosen such that a bound state exists for real valued  $\nu$ . A Fourier transform can be defined in  $d$  dimensions, taking the limit  $d \rightarrow 3$  subsequently [107]. We further project on  $S$ -waves. The full potential is the sum of the short- and the long-range degrees of freedom. The momentum space representation for the  $S$ -wave projected potential reads

$$V(\ell, \ell') = c_0 + 2\pi^2 \frac{c}{M} \left( \frac{\theta(\ell - \ell')}{\ell} + \frac{\theta(\ell' - \ell)}{\ell'} \right). \quad (2.41)$$

Note that the potential is not separable and a simplification like in Eq. (2.4) is not applicable anymore. We therefore have to use the full LS equation (2.3).

When calculating loop contributions to the  $T$ -matrix, these are again divergent. We therefore proceed in analogy to the previous section and introduce a momentum cutoff to regularize. However, we do not evaluate integrals analytically but use a numerical approach to solve the LS equation.

Further, we focus on bound states, i.e. on poles of the  $T$ -matrix. The inhomogeneous part of the LS equation, i.e. the potential term in Eq. (2.3), can then be neglected. Moreover, it can be shown that the  $T$ -matrix separates in the region of a bound state [114]. A common ansatz is to use

$$T^R(E, \ell, \ell') = \frac{\chi(E, \ell)\chi^\dagger(E, \ell')}{E + E_B + i\epsilon}, \quad (2.42)$$

at binding energy  $E_B$  and with the bound-state wave function  $\chi$ . Equation (2.42) still holds for angular dependent  $T$ -matrices, i.e. for  $\ell \rightarrow \ell$  ( $\ell' \rightarrow \ell'$ ).

The LS equation simplifies to the bound-state equation

$$\chi(E, \ell) = \int_0^\lambda \frac{dk}{2\pi^2} V(\ell, k) \frac{k^2}{E - k^2/M + i\epsilon} \chi(E, k), \quad (2.43)$$

which is particularly advantageous when using numerical approaches to determine binding energies. A widely used approach is to discretize the integrals, e.g., by using a Newton-Cotes or a Gaussian quadrature. The LS equation reduces to a system of linear equations. For the bound-state equation an eigenvalue problem is left to solve. We obtain explicitly, using weights  $\{w_i\}$

$$\chi(E, y_i) = \sum_{j=0}^{N-1} \underbrace{\frac{w_j}{2\pi^2} V(y_i, y_j)}_{K_{ij}} \frac{y_j^2}{E - y_j^2/M} \chi(E, y_j), \quad (2.44)$$

where the sampling points  $\{y_i\} \in [0, \lambda]$  are distributed depending on the quadrature used. Equation (2.44) has a solution if the kernel matrix  $(K_{ij})$  has an eigenvalue equals one. The (negative) energies fulfilling this criteria are binding energies of the potential. Again, the coupling constant  $c_0$  has to absorb the dependence on the cutoff parameter  $\lambda$ . It needs to be tuned until a given bound state has the correct binding energy determined, e.g., by experiment. It can be shown that the LS equation for the  $1/r^2$  potential can be rescaled such that the only left over dimensionful constant is  $Mc_0$ . Since  $Mc_0$  is determined by tuning such that a certain binding energy is reproduced, useful units can only be given *after* renormalization. All dimensionful quantities, such as the cutoff or the remaining bound states of the spectrum, are then expressed in units of the bound state renormalized onto.

We use the  $1/r^2$  potential to demonstrate how to renormalize non-perturbatively with long-range degrees of freedom. We begin with an unrenormalized spectrum, i.e. with  $c_0 = 0$ . The spectrum's dependence on the cutoff is shown in Fig. 2.1.

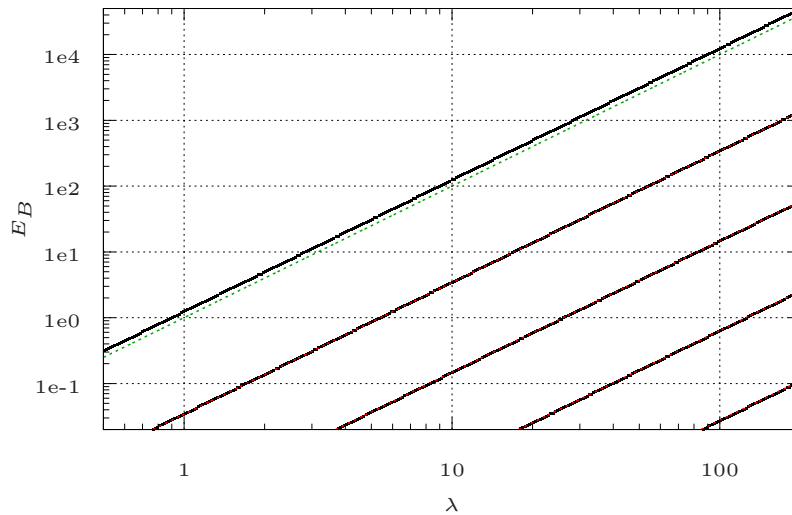


**Figure 2.1.:** Unrenormalized bound-state spectrum for two non-relativistic particles interacting at low energies via a  $1/r^2$  potential. The numerical results are shown as black squares, the red, dashed lines are analytical results taken from Ref. [107]. The green, dashed line belongs to  $E_B(\lambda) = \lambda^2/M$ , i.e. the energy scale at which the effective theory is expected to break down.

The black squares belong to the numerical results obtained by solving Eq. (2.44). We compare with the analytical results, taken from Ref. [107], shown with red, dashed lines. The authors find a series of bound states with binding energies

$$\log(E_B^{(n)}) = b_1 - n \frac{2\pi}{\nu} + 2 \log(\lambda), \quad n \in \mathbb{N}^{\geq 0}. \quad (2.45)$$

The deepest bound state is labeled with  $n = 0$  and  $b_1$  is a constant which needs to be fitted. The spectrum displays the discrete scale invariance of the  $1/r^2$  potential. If  $E_B^{(0)}$  is a binding energy for fixed cutoff, then  $E_B^{(n)} = \sigma_0^{2n} E_B^{(0)}$  also is a binding energy of the spectrum for the same cutoff. The dimensionless quantity  $\sigma_0$  is called discrete scaling factor. Here, it is given as  $\sigma_0 = e^{\pi/\nu}$ . Moreover, if  $E_B$  is a solution to Eq. (2.44) for a given cutoff  $\lambda_*$ , then it is also a solution for the cutoff  $\sigma_0^n \lambda_*$ . The integer powers for  $\sigma_0$  follow from dimensional analysis. Momenta scale proportional to  $\sigma_0$  and energies to  $\sigma_0^2$ , according to the non-relativistic dispersion relation. Further, discrete scale invariance implies for the binding energies that there is an accumulation point at threshold, i.e. at threshold bound states lie arbitrarily close to each other.

The upper bound for the spectrum is given by the scales integrated out of the theory. For momenta this scale is  $\lambda$ , for energies it is  $\lambda^2/M$ . The dashed, green curve belongs to the upper energy scale. The deepest state is above this upper bound. It does not fit into the series of bound states as the factor with which it is separated from its adjacent bound state is greater than for the others. Numerically, there is a lower bound as well coming from the finite resolution due to a finite number of sampling points used for approximating the integrals. We proceed with the renormalization of the bound-state

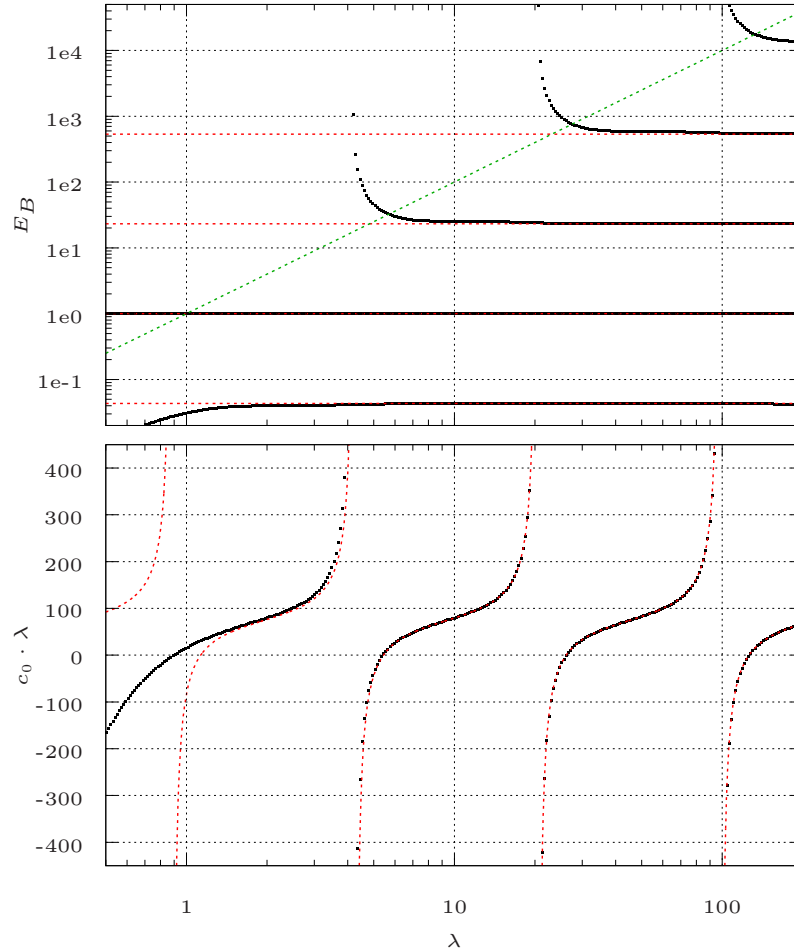


**Figure 2.2.:** Renormalized bound-state spectrum for two non-relativistic particles acting via a  $1/r^2$  potential is shown in the upper plot. The coupling constant in dependence on the cutoff scale  $\lambda$  is depicted below. We multiply with the cutoff scales to keep the inflection points at a constant value. The notation is the same as in Fig. 2.1. The analytical solution from Ref. [107] in Eq. (2.46) does not account for effects coming from a finite cutoff  $\lambda$ . This restriction explains the deviations for the coupling constants for small values of  $\lambda$ . For  $\lambda \rightarrow \infty$ , the spectrum as well as the coupling constant converge towards the analytically expected outcome.

spectrum. We tune the coupling constant to renormalize one of the bound states to a binding energy of  $E_B = 1$ . The outcome is shown in Fig. 2.2. The notation is the same as before. The black squares belong to numerical results and the red, dashed lines to the analytically expected binding energies taken from Ref. [107]. The evolution of the coupling constant is shown in the lower plot.

In the limit of  $\lambda \rightarrow \infty$ , the analytical expectation is that infinitely many binding energies exist in the spectrum, separated by the scaling factor  $\sigma_0$ . For finite  $\lambda$ , binding energies which belong to scales integrated out of the theory do not appear in the spectrum. When increasing the cutoff, i.e. bringing back in scales integrated out before, bound states join the spectrum from above, asymptotically approaching the analytical solutions for  $\lambda \rightarrow \infty$ . The dashed, green line, again belonging to the energy  $\lambda^2/M$ , indicates nicely beyond which cutoff the numerical solution coincides with the analytically

expected result for  $\lambda \rightarrow \infty$ . Since for the lowest values of the cutoff shown in the plot this upper bound is greater than one, the bound states with binding energies less than one join the analytical solutions from below. For the coupling constant, the analytical result reads [107]

$$\lambda c_0 = 2\pi^2 \frac{c}{M} \frac{1 - 2\nu \tan(\nu \log(\lambda))}{1 + 2\nu \tan(\nu \log(\lambda))}. \quad (2.46)$$

It is valid in the limit  $\lambda \rightarrow \infty$ , which explains the deviations between the numerical result and Eq. (2.46). Every time a new bound state appears in the spectrum, the coupling constant has a pole. Further, the coupling constant has a log-periodic behavior as expected from the discrete scale invariance of the theory. If for given cutoff  $\lambda_*$   $c_0$  renormalizes to a binding energy of  $E_B = 1$ , then it also does for the rescaled cutoff  $\sigma^n \lambda_*$ .

### 2.3.2 The $1/r^3$ potential

As another example for a singular potential, we consider the  $1/r^3$  potential. As in the previous section, we solve the bound-state LS equation in momentum space numerically. The dipole-dipole potential has a  $1/r^3$  proportion [109], but is more sophisticated due to couplings between channels with different angular momentum. Nonetheless, we expect that spectra for both potentials display similarities.

The long-range part of the potential in coordinate space is given by

$$U_l(r) = \frac{c}{M} \frac{1}{r^3}, \quad (2.47)$$

where the coupling strength  $c$  now has dimension of length. In contrast to the  $1/r^2$  potential, dimensions of quantities are expressed in terms of  $c$  and  $M$ . Momenta come in units of  $1/c$  and energies in units of  $1/Mc^2$ . A peculiarity of the  $1/r^3$  potential is that its Fourier transform is ill defined. The problem stems from the short-distance region where we do not expect the long-range potential to be valid. We do thus use the short-range potential to absorb divergences. Again, the Fourier transform can be defined as the  $d \rightarrow 3$  limit of the  $d$  dimensional expression

$$\begin{aligned} V(q) &\equiv \lim_{d \rightarrow 3} \left[ c_0 + r_0^{3-d} \int d^d r e^{i\mathbf{q}\cdot\mathbf{r}} U_l(r) \right] \\ &= \lim_{d \rightarrow 3} \left[ c_0 + \frac{c}{M} \frac{\pi^2}{2} \left( \frac{2}{d-3} - (\gamma_E - \log(4\pi)) - \log((r_0 q)^2) + \mathcal{O}(d-3) \right) \right], \end{aligned} \quad (2.48)$$

with the momentum transfer  $q = |\ell - \ell'|$ . The quantity  $r_0$  with dimension of length ensures that the potential keeps the correct dimension. The long-range potential's dependence on  $r_0$  can actually completely be compensated with  $c_0$ . Before taking the limit  $d \rightarrow 3$ , we remove the divergent part by redefining the coupling constant  $c_0$ . Further, we absorb renormalization constants, such as the Euler-Mascheroni constant and the logarithm of  $4\pi$ . After projecting on  $S$ -waves we obtain for the full potential

$$V(\ell, \ell') = c_0 + \frac{c}{M} \frac{\pi^2}{2} \left( 1 + \frac{(\ell - \ell')^2}{4\ell\ell'} \log(r_0^2(\ell - \ell')^2) - \frac{(\ell + \ell')^2}{4\ell\ell'} \log(r_0^2(\ell + \ell')^2) \right). \quad (2.49)$$

The unrenormalized spectrum is shown in Fig. 2.3, i.e. the spectrum for  $c_0 = 0$  in dependence on the momentum cutoff  $\lambda$ . In the foregoing section, the  $1/r^2$  potential possessed bound states for arbitrary momentum cutoff as long as  $\nu \in \mathbb{R}$  (cf. Eq. (2.40) and below).<sup>6</sup> In contrast to this, for the  $1/r^3$  potential, independent of its strength, there always exists a critical cutoff below which no bound states exist. For the chosen strength of  $c = -1$  no bound states exist below  $\lambda \approx 3/c$ . Moreover, the binding energies grow faster than for the  $1/r^2$  potential. In the limit of  $\lambda \rightarrow \infty$  the bound states align parallel and increase  $\sim \lambda^3$ . Furthermore, the frequency of occurrence and the density of states grows for increasing cutoff. There neither is a fixed scaling factor nor an accumulation point as for the  $1/r^2$  potential.

The renormalized spectrum is shown in Fig. 2.4. To renormalize, we tune the coupling constant and demand that a state with  $E_B = 1$  exists. When increasing the cutoff, states join the spectrum from above similar to the  $1/r^2$  potential. However, an oscillatory behavior is present. Whenever a new state appears, all states with lower binding energy decrease in energy. The sensitivity to deeply bound states is lower for states close to threshold. The breakdown energy scale  $\lambda^2/M$  is depicted with a green, dashed line. Above, states are strongly dependent on the cutoff. Below, they quickly converge towards a constant.

The coupling constant is shown in the lower plot. We divide it by the logarithm of the cutoff scale to keep the inflection points at a constant value. The coupling constant diverges whenever a new state appears. The factor with which poles are separated decreases for increasing cutoff.

<sup>6</sup> The actual values for the binding energies did depend on the size of  $\lambda$ , though.

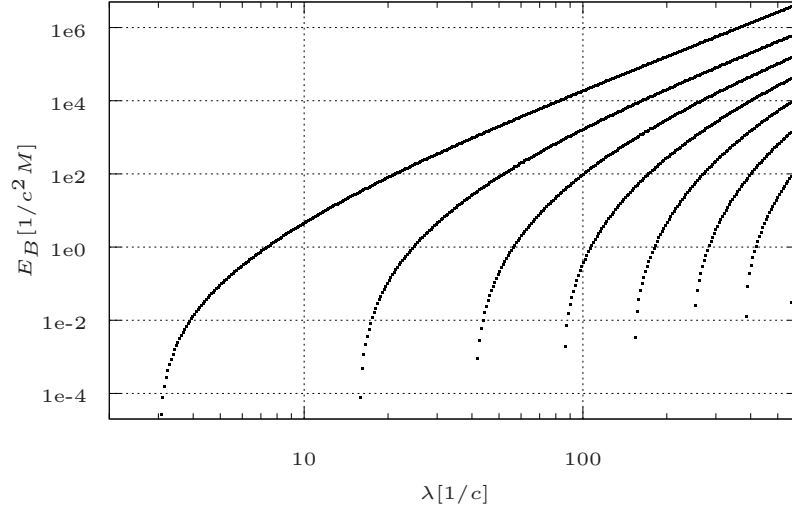


**Figure 2.3.:** Unrenormalized bound-state spectrum for two non-relativistic particles interacting at low energies via an  $1/r^3$  potential. The spectrum is obtained by solving the bound-state LS equation (2.44) numerically.

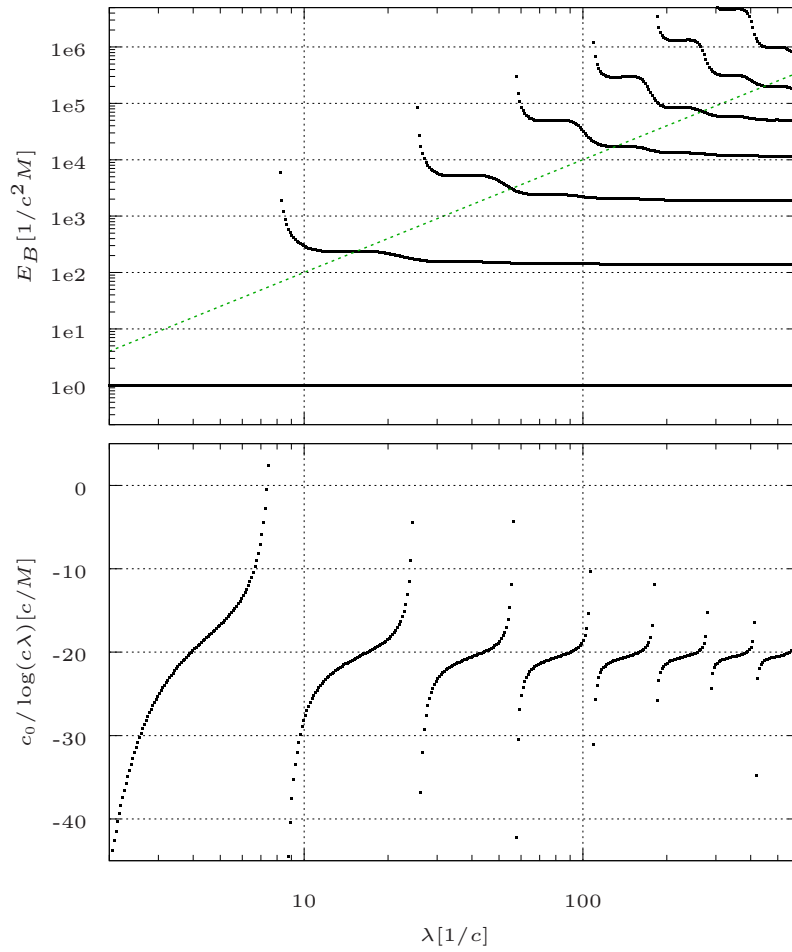


**Figure 2.4.:** Renormalized bound-state spectrum and evolution of the coupling constant for the  $1/r^3$  potential. The upper plot shows the bound-state spectrum. The binding energies converge quickly towards a constant binding energy. The breakdown energy scale  $\lambda^2/M$  belongs to the diagonal, dashed, green line. The lower plot shows the dependence of the coupling constant  $c_0$  on the cutoff scale  $\lambda$ . We divide by the logarithm of the cutoff to keep the inflection points at a constant value.

### 3 Chiral extrapolations and finite volume effects for the $X(3872)$

In this chapter, we present our results for the chiral extrapolations and finite volume effects for the  $X(3872)$ . We closely follow the lines of our publications [115] and [116], with few, minor modifications.

The light quark mass dependence and pion mass dependence can be interchangeably used due to the Gell-Mann-Oakes-Renner relation [117]

$$m_\pi^2 = -(m_u + m_d)\langle 0|\bar{u}u + \bar{d}d|0\rangle/f^2 \quad (3.1)$$

with the pion decay constant  $f \approx 130$  MeV and the light quark condensate  $\langle 0|\bar{u}u|0\rangle = \langle 0|\bar{d}d|0\rangle = (-283(2) \text{ MeV})^3$  in the  $\overline{MS}$  scheme at 2 GeV [118].

#### 3.1 An effective field theory for the $X(3872)$

In order to describe the  $X$  we use a non-relativistic effective field theory, called XEFT, which was derived by Fleming et al. in Ref. [16] starting from heavy meson chiral perturbation theory. In XEFT, the  $X(3872)$  is described as an  $S$ -wave hadronic molecule. It is generated by  $\bar{D}^0 D^{*0}$  scattering in the  $C = +1$  channel. In this framework, we can evaluate the center-of-momentum  $\bar{D}^0 D^{*0}$  scattering diagrams. From these, we can eventually extract the light quark mass dependence of the scattering length and binding energy of the  $X$  and the dependence of the binding energy on the size of a finite volume.

##### 3.1.1 Lagrangian of XEFT and Feynman rules

The Lagrangian of XEFT contains non-relativistic fields for the  $D^0$ ,  $D^{*0}$ ,  $\bar{D}^0$ , and  $\bar{D}^{*0}$  mesons as well as non-relativistic pion fields. The interaction between the  $D$  and  $D^*$  mesons is given by pion exchange and by contact interactions. States containing charged  $D^{(*)}$  mesons, such as  $D^{*+} D^-$ , are integrated out since they lie about 8 MeV above the threshold for neutral  $D$  mesons (cf. Sec. 3.1.4). The Lagrangian reads

$$\begin{aligned} \mathcal{L} = & D^\dagger \left( i\partial_0 + \frac{\overleftrightarrow{\nabla}^2}{2m_{D^*}} \right) D + D^\dagger \left( i\partial_0 + \frac{\overleftrightarrow{\nabla}^2}{2m_D} \right) D \\ & + \bar{D}^\dagger \left( i\partial_0 + \frac{\overleftrightarrow{\nabla}^2}{2m_{D^*}} \right) \bar{D} + \bar{D}^\dagger \left( i\partial_0 + \frac{\overleftrightarrow{\nabla}^2}{2m_D} \right) \bar{D} + \pi^\dagger \left( i\partial_0 + \frac{\overleftrightarrow{\nabla}^2}{2m_\pi} + \delta \right) \pi \\ & + \frac{g}{\sqrt{2}f} \frac{1}{\sqrt{2m_\pi}} \left( D D^\dagger \cdot \overleftrightarrow{\nabla} \pi + \bar{D}^\dagger \bar{D} \cdot \overleftrightarrow{\nabla} \pi^\dagger \right) + \text{h.c.} \\ & - \frac{C_0}{2} (\bar{D} D + D \bar{D})^\dagger \cdot (\bar{D} D + D \bar{D}) \\ & + \frac{C_2}{16} (\bar{D} D + D \bar{D})^\dagger \cdot (\bar{D} \overleftrightarrow{\nabla}^2 D + D \overleftrightarrow{\nabla}^2 \bar{D}) + \text{h.c.} \\ & - \frac{D_2 \mu^2}{2} (\bar{D} D + D \bar{D})^\dagger \cdot (\bar{D} D + D \bar{D}) + \dots \end{aligned} \quad (3.2)$$

Here,  $\overleftrightarrow{\nabla} \equiv (\overrightarrow{m} \overleftarrow{\nabla} - \overleftarrow{m} \overrightarrow{\nabla})/(\overleftarrow{m} + \overrightarrow{m})$  is the Galilean-invariant derivative,  $\overleftarrow{m}$  ( $\overrightarrow{m}$ ) the mass of the left- (right-) hand field and the ellipsis denote higher-order interactions. The pion,  $D^0$  and  $D^{*0}$  fields are labeled by  $\pi$ ,  $D$  and  $D$  and their masses are  $m_\pi$ ,  $m_D$  and  $m_{D^*}$ , respectively. Furthermore,  $g$  is the  $D$  meson axial-coupling constant,  $f$  the pion decay constant and  $\Delta \equiv m_{D^*} - m_D$  the hyperfine splitting of the  $D$  mesons. The mass scales  $\mu$  and  $\delta$  are defined as  $\mu^2 \equiv \Delta^2 - m_\pi^2$  and  $\delta \equiv \Delta - m_\pi$ . The coupling constants  $C_0$ ,  $C_2$  and  $D_2$  parametrize short-range physics not explicitly included in XEFT and are discussed below. Note that this Lagrangian has no exact Galilean invariance. The  $D^0 D^{*0} \pi$  coupling is given by the leading term in the chiral limit and only the leading terms in expansion in  $m_\pi/m_D$  and  $\delta/m_\pi$  are kept in the calculated observables (cf. Sec. 3.1.2). Further particle properties are summarized in Tab. 3.1 at the end of this section.

Moreover, we give the Feynman rules in Fig. 3.1 following from the Lagrangian in Eq. (3.2). The propagators are on the left, the interaction vertices on the right. The energies and momenta of the propagators are denoted by  $k_0$  and  $\mathbf{k}$ , respectively. From top to bottom we show the particle and antiparticle  $D^0$ ,  $D^{*0}$  and the  $\pi$  propagators. Whenever required, arrows for particles point to the right, arrows for antiparticles to the left. The pion propagator comes with the additional mass scale  $\delta$  in the denominator accounting for the excess energy when a  $D^{*0}$  decays to  $D^0 \pi$ . The  $D^{*0}$  ( $\bar{D}^{*0}$ )

**Figure 3.1.:** Feynman rules for XEFT up to NLO. The propagators for the  $D^0$  and  $\bar{D}^0$  mesons are denoted with single, the propagators for the  $D^{*0}$  and  $\bar{D}^{*0}$  mesons with double and pion propagators with dashed lines. There are one LO and two NLO contact interactions, denoted with a dot, square and triangle vertex, respectively. Together with the pion coupling to the  $D$  mesons, they represent the XEFT interactions up to NLO.

is a spin 1 vector meson and is polarized. We denote its incoming and outgoing polarizations in all diagrams with  $\epsilon_i$  and  $\epsilon_j^*$ , respectively. For the propagator the polarization vectors need to be contracted implying its proportionality to a Kronecker delta.

For the vertices we use ingoing momenta  $\ell$  and  $-\ell$  and outgoing momenta  $\ell'$  and  $-\ell'$  for the  $D^{*0}$  ( $\bar{D}^{*0}$ ) and  $D^0$  ( $\bar{D}^0$ ) mesons. From top left to bottom right we show the  $D^0 D^{*0} \pi$  interaction as well as the LO and NLO contact interactions. The  $D$  mesons couple to the pion in a  $P$ -wave. The interaction vertex is proportional to the contraction of the polarization vector and the momentum transfer  $\mathbf{q} \equiv \ell - \ell'$ . For each external pion an additional factor of  $\sqrt{2m_\pi}$  is required due to the non-relativistic normalization of the pion fields. Since we are interested in  $S$ -wave scattering, a pion-exchange diagram has to be  $S$ -wave projected (cf. Sec. 3.2.1). Moreover,  $S$ -wave scattering implies that all contact interaction vertices are proportional to a Kronecker delta.

### 3.1.2 Pion exchanges between the $D$ mesons

In its structure, XEFT is similar to the Kaplan-Savage-Wise theory (KSW) for nucleon-nucleon ( $NN$ ) scattering, which makes use of the power divergence subtraction (PDS) [94]. PDS has proven to be well suited for systems with an unnaturally large scattering length. In the KSW counting, the pion exchanges are included perturbatively. Although the perturbative treatment of the pion exchanges was shown to fail in the  $NN$  sector at NNLO because of large contributions from the nuclear tensor force [51], it is expected to work well for  $\bar{D}^0 D^{*0}$  scattering in XEFT due to a significantly smaller expansion parameter [16].

By means of naive dimensional analysis, the two-pion exchange (TPE) is suppressed compared to the one-pion exchange by a factor of

$$\frac{g^2 M_{DD^*} \mu}{4\pi f^2} \approx \frac{1}{20}, \quad (3.3)$$

which serves as an approximation for the expansion parameter [16]. It is about one order of magnitude smaller than the expansion parameter in KSW. Note, however, that expression (3.3) is quark mass dependent and also depends on the size of the volume when embedding XEFT in a finite volume. We will use it to estimate the range of validity of XEFT.

Beside, we expand all graphs in powers of the mass ratios  $m_\pi/m_D \approx 0.07$  and  $\delta/m_\pi \approx 0.04$ , which are of the same order as the expansion parameter in Eq. (3.3). Hence, diagrams including a pion with an additional suppression factor of  $m_\pi/m_D$  or  $\delta/m_\pi$  are in the same order of magnitude as the two-pion-exchange graph which is of NNLO and can be neglected at the order we are working.<sup>1</sup>

Furthermore, a pion exchange changes the flavor of the considered states. In Fig. 3.2 we show the one-pion exchange for ingoing  $\bar{D}^0 D^{*0}$  and outgoing  $D^0 \bar{D}^{*0}$  mesons. However, due to charge conjugation symmetry the conjugated diagram with ingoing  $D^0 \bar{D}^{*0}$  and outgoing  $\bar{D}^0 D^{*0}$  mesons gives the same contribution. When evaluating transition matrix elements for neutral  $DD^*$  scattering in the  $X$  channel, only the sum of both channels has to be considered. Moreover, contact interactions are introduced for the  $X$  channel and therefore, are invariant under charge conjugation by construction. Thus, we do not use any arrows in the scattering diagrams for the  $D$  mesons and always refer to the sum of both channels.

<sup>1</sup> Note that for the calculation of the decay width of the  $X(3872)$ , neglecting  $m_\pi/m_D$  terms is not a good approximation. We discuss this issue in Sec. 3.2.7.

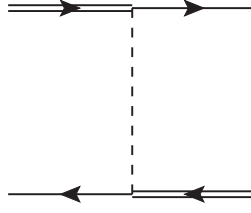


**Figure 3.2.:** One-pion-exchange diagram with ingoing  $\bar{D}^0 D^{*0}$  and outgoing  $D^0 \bar{D}^{*0}$  mesons. The double lines indicate  $D^{*0}$  ( $\bar{D}^{*0}$ ), the single lines  $D^0$  ( $\bar{D}^0$ ) mesons. Arrows to the right belong to particles, arrows to the left to antiparticles.

### 3.1.3 Power counting

Effective field theories are non-renormalizable and, in general, infinitely many terms are compatible with the underlying symmetries. Thus, an essential demand on every meaningful effective field theory is a systematic power counting. XEFT provides a consistent power counting, which allows for an estimate of the relevance of different contributions to the  $\bar{D}^0 D^{*0}$  scattering amplitude. In XEFT power counting, the binding momentum, the  $D^0$  ( $\bar{D}^0$ ) and  $D^{*0}$  ( $\bar{D}^{*0}$ ) mesons' as well as the pion's typical momentum and the scale  $\mu$  are counted as order  $Q$ , defining the typical momentum scale of XEFT. At LO, which is  $Q^{-1}$  in XEFT power counting, there is one contact interaction with coupling constant  $C_0$ .

Since XEFT is a non-relativistic field theory, all propagators are of order  $Q^{-2}$  and loop integrations are of order  $Q^5$  [16]. Therefore, a loop, consisting of a loop integration ( $Q^5$ ), two propagators (each  $Q^{-2}$ ) and a LO contact interaction ( $Q^{-1}$ ) is counted as order  $Q^0$ . Appending such a loop to any diagram leaves the order of the diagram unchanged. On the one hand, this implies that the LO contact interaction has to be resummed to all orders. On the other hand, the higher-order contributions have to be dressed in all possible ways by LO amplitudes.

At NLO, which is  $Q^0$ , three more interactions have to be considered: two NLO contact interactions with coupling constants  $C_2$  and  $D_2$  and the  $D^0 D^{*0} \pi$  coupling. The coupling constants are of order  $Q^{-2}$  [94, 16]. In the XEFT Lagrangian (3.2), they come with two derivatives ( $C_2$ ) or a factor of  $\mu^2$  ( $D_2$ ). Note that this is different from the factor  $m_\pi^2$  in KSW counting because in XEFT, the typical momenta of the  $D^{(*)}$  mesons are of order  $\mu \ll m_\pi$ . It follows that vertices including  $C_2$  or  $D_2$  are of order  $Q^0$ . For each pion exchange there are two  $D^0 D^{*0} \pi$  axial couplings, each of order  $Q^1$ , and one pion propagator of order  $Q^{-2}$  resulting in order  $Q^0$ , too.

### 3.1.4 Charged $D$ meson contributions

Charged  $D^{(*)}$  mesons are integrated out of XEFT. They lie about 8 MeV above the neutral  $\bar{D}^0 D^{*0}$  threshold. Accordingly, typical momenta of charged mesons are of the order 120 MeV, being much larger than the typical momenta of the neutral mesons, which are in the order of the binding momentum of order 15 MeV for  $E_X = 0.1$  MeV. In general, the charged mesons can be integrated out if one is interested in the energy range of a few MeV around the threshold for neutral  $D$  mesons. Of course, this does not mean that the effects of charged mesons are unimportant. They are included implicitly via short-range contact interactions. If the charged mesons are explicitly included in the theory, they contribute first at NNLO in the XEFT power counting [16]. Note that coupled-channel effects arising from the explicit inclusion of the charged states could be volume dependent, requiring a coupled channel analysis. Such volume-dependent coupled-channel effects were indeed found in the case of the  $X(3872)$ , but the effect becomes less important as  $L$  increases [46]. For  $L \gtrsim 5$  fm it is rather small. In the finite volume analysis in Sec. 3.3, we focus on the region  $L \gtrsim 5$  fm where the perturbative expansion in XEFT is well behaved. Thus, volume-dependent coupled-channel effects can be neglected in this work. Other states close to the  $X$  mass are, e.g.,  $J/\psi \omega$ , also about 8 MeV above threshold and  $J/\psi \rho$  only about 1.2 MeV above threshold. For the latter, one has to take the  $\rho$  width into account, which induces an energy scale  $\sim \Gamma_\rho/2 = 73$  MeV and therefore, can be integrated out as well [16]. It is this dominance of neutral  $D$  meson states, which can explain the isospin violations in the molecular picture. The isospin doublets for the  $D$  mesons are determined by

$$\begin{pmatrix} D^+ \\ D^0 \end{pmatrix}, \begin{pmatrix} \bar{D}^0 \\ D^- \end{pmatrix}, \begin{pmatrix} D^{*+} \\ D^{*0} \end{pmatrix}, \begin{pmatrix} -\bar{D}^{*0} \\ -D^{*-} \end{pmatrix}, \quad (3.4)$$

using the sign conventions of Ref. [48]. The combination of neutral  $D$  mesons thus is an admixture of isospin eigenstates with  $I = 0$  and  $I = 1$ . Since charged  $D$  mesons barely contribute to the scattering amplitude for the  $X$ , the  $X$  can be properly described as a superposition of neutral  $D$  mesons (cf. Eq. (1.4)). Accordingly, it can decay in the isospin  $I = 0$  and in the  $I = 1$  channel. Note that isospin symmetry for the  $D$  mesons is fulfilled to high precision. Deviations of masses in the isospin doublets are in the order of 1 per mill. It is the cancellation of the  $X$  mass and the neutral  $\bar{D}^0 D^{*0}$  threshold and the consequential dominance of the neutral  $D$  mesons which causes the violation of isospin invariance in  $X$  decays.

	$m$ [MeV]	$J^{P(C)}$	$I(I_3)$	Quarks
$D^0$	1864.84(5)	$0^-$	$\frac{1}{2} (-\frac{1}{2})$	$c\bar{u}$
$D^{*0}$	2006.97(8)	$1^-$	$\frac{1}{2} (-\frac{1}{2})$	$c\bar{u}$
$\pi^0$	134.98(0)	$0^{++}$	$1 (0)$	$(u\bar{u} + d\bar{d})/\sqrt{2}$
$D^+$	1869.61(9)	$0^-$	$\frac{1}{2} (\frac{1}{2})$	$c\bar{d}$
$D^{*+}$	2010.27(5)	$1^-$	$\frac{1}{2} (\frac{1}{2})$	$c\bar{d}$
$\pi^+$	139.57(0)	$0^-$	$\frac{1}{2} (\frac{1}{2})$	$u\bar{d}$
$X$	3871.69(17)	$1^{++}$		

**Table 3.1.:** Properties of the most relevant particles referred to. All values are taken from the review of particle properties [33]

## 3.2 Chiral extrapolations

We present our findings for the quark mass dependence of the binding energy and the scattering length. We begin with the calculation of the transition amplitude using bare  $D^{*0}$  propagators, discuss the occurrence of infrared divergences and how to treat these. Furthermore, we introduce methods which we also employ in order to calculate finite volume corrections to the binding energy in the upcoming section. The results are presented at the end of this section.

### 3.2.1 $\bar{D}^0 D^{*0}$ transition amplitudes to next-to-leading order with bare propagators

Since we treat the  $X(3872)$  as an  $S$ -wave hadronic molecule, the total angular momentum is given by the  $D^{*0}$  meson's spin. From angular momentum conservation follows that the polarizations of the incoming and outgoing  $D^{*0}$  mesons have to coincide. Using spin indices  $i$  and  $j$ , the spin dependence of the transition amplitude is of the form

$$\hat{\mathcal{A}}_{ij} = \delta_{ij} \mathcal{A}. \quad (3.5)$$

For the discussion of the binding energy and scattering length it is sufficient to consider the scalar amplitude  $\mathcal{A}$ .

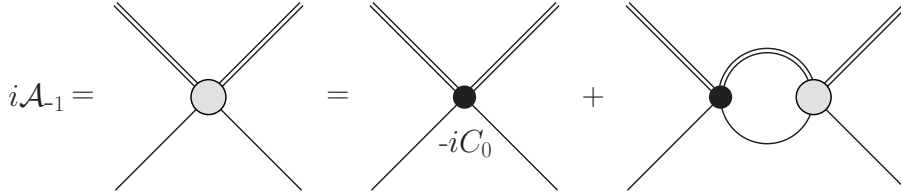


**Figure 3.3.:** Leading-order contribution to the  $\bar{D}^0 D^{*0}$  scattering amplitude. The  $\bar{D}^0$  and the  $D^{*0}$  mesons are indicated by single and double lines, respectively.

We begin with the LO amplitude. Following XEFT power counting, the  $C_0$  vertex has to be resummed to all orders. Using the power divergence subtraction procedure [94] to regularize the linear divergence of the loop integral in Fig. 3.3

$$I_0 = \int \frac{d^3\mathbf{k}}{(2\pi)^3} \frac{1}{k^2 - 2M_{DD^*}E - i\epsilon} \xrightarrow{\text{PDS}} \frac{1}{4\pi} (\Lambda - \sqrt{-2M_{DD^*}E - i\epsilon}), \quad (3.6)$$

the LO amplitude at energy  $E$  for  $\bar{D}^0 D^{*0}$  scattering in the  $C = +1$  channel is given as

$$i\mathcal{A}_{-1} = \frac{2\pi i}{M_{DD^*}} \frac{1}{-\frac{2\pi}{M_{DD^*}C_0(\Lambda)} - 4\pi I_0} = \frac{2\pi i}{M_{DD^*}} \frac{1}{-\gamma + \sqrt{-2M_{DD^*}E - i\epsilon}}, \quad (3.7)$$

where  $M_{DD^*}$  is the reduced mass of the  $\bar{D}^0$  and  $D^{*0}$  mesons. The quantity  $\gamma$  is defined as

$$\gamma \equiv \frac{2\pi}{M_{DD^*}C_0(\Lambda)} + \Lambda, \quad (3.8)$$

with the PDS renormalization scale  $\Lambda$ . Taking  $\Lambda$  of order  $Q$ , we see that the LO amplitude indeed scales as  $Q^{-1}$ . It has a pole at the LO binding energy  $E_X^{\text{LO}} = \gamma^2 / (2M_{DD^*})^2$ .<sup>2</sup> Hence,  $\gamma$  can be identified with the LO binding momentum.

At NLO in XEFT power counting we have to include the NLO contact interactions with coupling constants  $C_2$  and  $D_2$  and the pion exchange (cf. Sec. 3.1.3). Appending the LO amplitude in all possible ways to the NLO interactions we end up with the five diagrams shown in Fig. 3.4, similar to the diagrams for  $NN$  scattering in KSW theory.

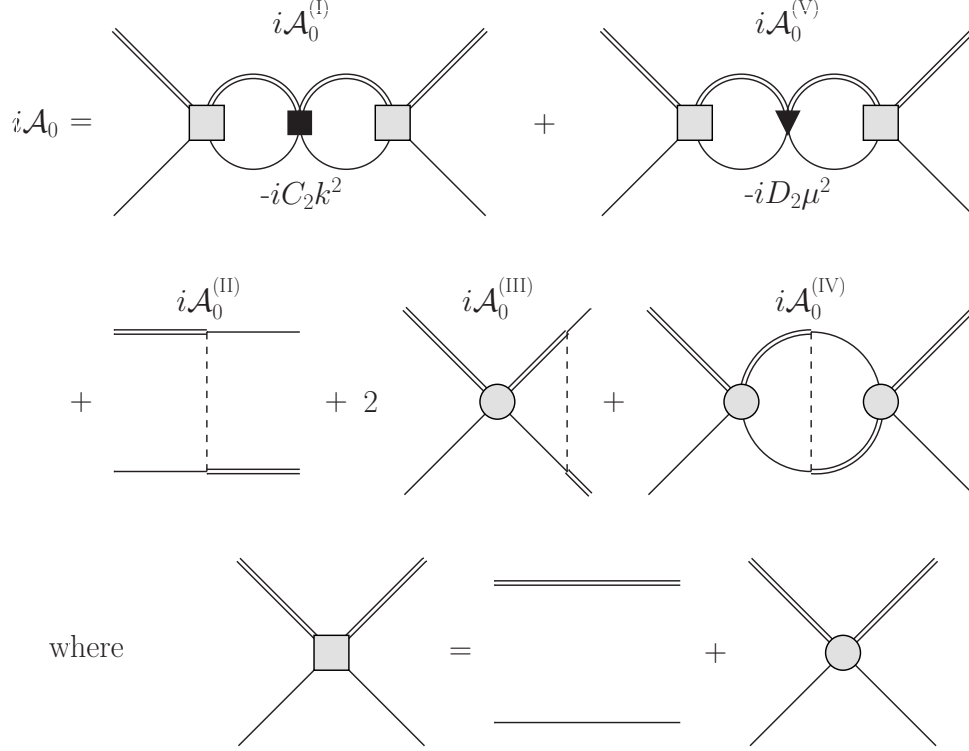


**Figure 3.4.:** Next-to-leading-order contributions to the  $\bar{D}^0 D^{*0}$  scattering amplitude. The pions, the  $\bar{D}^0$  and the  $D^{*0}$  mesons are indicated by dashed lines, solid lines and double lines, respectively.

A novel feature of XEFT is the occurrence of a sixth diagram,  $\mathcal{A}_0^{(\text{VI})}$ , depicted in Fig. 3.5. The transition amplitude

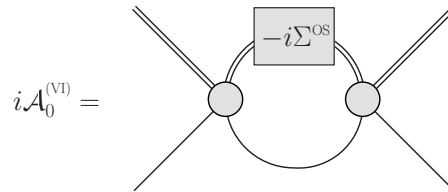


**Figure 3.5.:** Next-to-leading-order contribution from  $D^{*0}$  self-energy. The notation is the same as in Fig. 3.4.

$\mathcal{A}_0^{(\text{VI})}$  comes from the self-energy diagram for the  $D^{*0}$  shown in Fig. 3.6. It does not occur in KSW theory due to the different kinematics for nucleons. Since pions are always off-shell for the  $NN$  system, the bare self-energy diagram is purely imaginary and removed by the counterterm in the on-shell renormalization scheme. A more detailed discussion can be found in Sec. 3.2.2 and App. A.1.1. We denote the external incoming momenta in the center-of-momentum frame of the  $\bar{D}^0$  and  $D^{*0}$  mesons  $\ell$  and  $-\ell$  and the outgoing  $\ell'$  and  $-\ell'$ , respectively. In this section, we evaluate at the on-shell point, i.e.  $E = p^2 / 2M_{DD^*}$  for  $|\ell| = |\ell'| = p$ . For the loop integrals we apply a multiplicative renormalization scheme for

<sup>2</sup> After the inclusion of pions, the pole position of the scattering amplitude becomes complex and will be denoted by  $B$ . The binding energy,  $E_X$ , is then given as the real part of  $B$ .

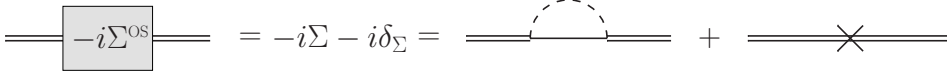


Figure 3.6.: Self-energy graph and counterterm for the  $D^{*0}$ . We use the same notation like in Fig. 3.4.

which UV divergent integrals are regularized separately. We begin with the contributions of the NLO contact interactions,  $\mathcal{A}_0^{(I)}$  and  $\mathcal{A}_0^{(V)}$ , respectively. Similar to the  $NN$  case [94], we obtain

$$i\mathcal{A}_0^{(I)} = \frac{-iC_2 p^2}{C_0^2} \mathcal{A}_{-1}^2, \quad (3.9a)$$

$$i\mathcal{A}_0^{(V)} = \frac{-iD_2 \mu^2}{C_0^2} \mathcal{A}_{-1}^2. \quad (3.9b)$$

The OPE transition amplitude  $\hat{\mathcal{A}}_0^{(II)}{}_{ij}$  is given as

$$i\hat{\mathcal{A}}_0^{(II)}{}_{ij} = \frac{ig^2}{2f^2} \frac{(\boldsymbol{\varepsilon}_i \cdot \mathbf{q})(\boldsymbol{\varepsilon}_j^* \cdot \mathbf{q})}{q^2 - \mu^2 - i\epsilon}, \quad (3.10)$$

where  $\mathbf{q} = \boldsymbol{\ell} - \boldsymbol{\ell}'$  is the momentum transfer and  $\boldsymbol{\varepsilon}_i$  and  $\boldsymbol{\varepsilon}_j^*$  are the polarization vectors of the  $D^{*0}$  mesons. Projecting  $\hat{\mathcal{A}}_0^{(II)}{}_{ij}$  on the  $X$  channel and factoring out the spin dependence like in Eq. (3.5), we end up with

$$i\mathcal{A}_0^{(II)} = \frac{ig^2}{6f^2} \left[ 1 + \frac{\mu^2}{4p^2} \log \left( 1 - \frac{4p^2}{\mu^2} \right) \right]. \quad (3.11)$$

For the one- and two-loop diagrams with one-pion exchange,  $\mathcal{A}_0^{(III)}$  and  $\mathcal{A}_0^{(IV)}$ , we acquire

$$i\mathcal{A}_0^{(III)} = \frac{ig^2}{3f^2} \left[ (ip + \Lambda) + i\mu^2 \frac{1}{2p} \log \left( 1 + \frac{2p}{\mu} \right) \right] \frac{M_{DD^*}}{2\pi} \mathcal{A}_{-1}, \quad (3.12a)$$

$$i\mathcal{A}_0^{(IV)} = \frac{ig^2}{6f^2} \left[ (ip + \Lambda)^2 + \mu^2 \left( \log \left( \frac{\Lambda}{-2ip - i\mu} \right) + \frac{1}{2} + R \right) \right] \left( \frac{M_{DD^*}}{2\pi} \right)^2 \mathcal{A}_{-1}^2, \quad (3.12b)$$

with  $R \equiv \frac{1}{2}(-\gamma_E + \log(\pi))$ . Since  $\mathcal{A}_0^{(IV)}$  depends logarithmically on  $\Lambda$ , it is required to include the  $\mu^2$ -dependent vertex proportional to  $D_2$  to ensure that physical results are renormalization scale independent [94].

### 3.2.2 Infrared divergences and full $D^{*0}$ propagator

Before we come to the calculation of diagram  $\mathcal{A}_0^{(VI)}$  in Fig. 3.5, we consider the renormalized  $D^{*0}$  self-energy shown in Fig. 3.6.<sup>3</sup> Explicit calculations for the bare self-energy diagram and  $\mathcal{A}_0^{(VI)}$  can be found in App. A.1.1. We use the on-shell renormalization scheme. It ensures that the real part of the  $D^{*0}$  propagator's pole position is at the on-shell point  $k_0 = k^2/2m_{D^*}$ , with  $k_0$  being the energy and  $\mathbf{k}$  the momentum of the  $D^{*0}$  ( $k = |\mathbf{k}|$ ).

Under the PDS regularization<sup>4</sup>, the bare self-energy reads

$$-i\Sigma = \frac{ig^2}{24\pi f^2} (i\mu^3 + \Lambda\mu^2). \quad (3.13)$$

The second term in parentheses has a linear divergence in the renormalization scale  $\Lambda$ , is real valued for arbitrary pion mass and analytic in the quark masses. The counterterm,  $-i\delta_\Sigma$ , is chosen to cancel it.

The first term is purely imaginary as long as the  $D^{*0}$  can decay into  $D^0\pi$ , i.e. for pion masses smaller than the hyperfine splitting. In this case, it induces a finite decay width. For pion masses greater than the hyperfine splitting, it is real valued and the self-energy implies a finite mass shift for the  $D^{*0}$ , denoted by  $\Delta_{m_{D^*}}$  (see also App. A.3). Since the rest mass

<sup>3</sup> The self-energy of the  $D^0$  meson is determined by a similar diagram with a  $D^{*0}\pi$  loop. However, in this case, the particles in the loop are off-shell by  $\sim m_\pi + \Delta$ . Thus, this contribution is strongly suppressed and will not be included.

<sup>4</sup> Note that the additional term occurring in PDS, proportional to the renormalization scale  $\Lambda$ , is subtracted again due to the use of the on-shell renormalization scheme.

is subtracted in the non-relativistic propagators, this mass shift is included in the chiral extrapolation (cf. Eq. (3.40b) below) and not in the non-relativistic  $D^{*0}$  self-energy. In summary we have

$$-i\delta_\Sigma = -\frac{ig^2}{24\pi f^2}\Lambda\mu^2, \quad (3.14)$$

$$\Delta_{m_{D^*}} = \begin{cases} 0, & m_\pi < \Delta, \\ -\frac{g^2}{24\pi f^2}i\mu^3, & m_\pi \geq \Delta. \end{cases} \quad (3.15)$$

We point out that the mass scale  $\mu$  is purely imaginary above the  $D^{*0}$  decay threshold and hence,  $\Delta_{m_{D^*}}$  is real valued for all pion masses.

As soon as pions can not go on-shell, the on-shell renormalized self-energy yields zero and thus,  $\mathcal{A}_0^{(VI)}$  vanishes, too. Note that pions in  $NN$  scattering are always off-shell, implying that the diagram in Fig. 3.5 does not contribute in KSW theory. However, for the  $X$  and  $m_\pi < \Delta$  the on-shell renormalized self-energy is finite and we obtain for diagram  $\mathcal{A}_0^{(VI)}$

$$i\mathcal{A}_0^{(VI)} = \frac{i}{p} 2\pi(-i\Sigma^{\text{OS}}) \left(\frac{M_{DD^*}}{2\pi}\right)^2 \mathcal{A}_{-1}^2, \quad (3.16)$$

which is infrared divergent ( $p^2 = 2M_{DD^*}E$ ). The divergence occurs due to an inappropriate expansion at low energies.

$$iG = \text{---} = \text{====} + \text{====} \boxed{-i\Sigma^{\text{OS}}} \text{---}$$

**Figure 3.7.:** The full  $D^{*0}$  propagator. The free  $D^{*0}$  propagator is denoted by a double line, the full  $D^{*0}$  propagator by a thick, single line.

To trace the origin of the infrared divergence, let us consider the full  $D^{*0}$  propagator with resummed self-energy shown in Fig. 3.7

$$iG = \frac{i}{k_0 - k^2/2m_{D^*} + i\epsilon} (1 - i\Sigma^{\text{OS}}iG) = \frac{i}{k_0 - k^2/2m_{D^*} - \Sigma^{\text{OS}} + i\epsilon}. \quad (3.17)$$

For pion masses  $m_\pi < \Delta$ ,  $\Sigma^{\text{OS}}$  is purely imaginary and is related to the decay width of the  $D^{*0}$ ,  $\Gamma_*$ , by  $\Sigma^{\text{OS}} = -i\Gamma_*/2$ . Hence, the full propagator takes the non-zero decay width of the  $D^{*0}$  into account.

Now, we use Eq. (3.17) to evaluate  $\mathcal{A}_0^{(VI)}$  with full instead of free  $D^{*0}$  propagators. To avoid double counting, we replace one of the two free  $D^{*0}$  propagators in the loop in Fig. 3.5 by the full one. We obtain the resummed amplitude  $(\mathcal{A}_0^{(VI)})^{\text{res}}$

$$\begin{aligned} i(\mathcal{A}_0^{(VI)})^{\text{res}} &= \frac{-2ip - 2\sqrt{-p^2 - i\kappa^2 - i\epsilon}}{i\kappa^2} 2\pi(-i\Sigma^{\text{OS}}) \left(\frac{M_{DD^*}}{2\pi}\right)^2 \mathcal{A}_{-1}^2 \\ &= \frac{-2 + 2\sqrt{1 + i\kappa^2/p^2}}{i\kappa^2/p^2} \cdot \frac{i}{p} 2\pi(-i\Sigma^{\text{OS}}) \left(\frac{M_{DD^*}}{2\pi}\right)^2 \mathcal{A}_{-1}^2, \end{aligned} \quad (3.18)$$

with  $i\kappa^2 = -2M_{DD^*}\Sigma^{\text{OS}}$ . As can be seen from the first line, the resummed transition amplitude is infrared finite for all values of  $m_\pi$ . Let us expand the first factor in the second line of Eq. (3.18) around  $\kappa^2/p^2 = 0$ , which is equivalent to expanding the full  $D^{*0}$  propagator. At zeroth order we reproduce Eq. (3.16). It is clear that this expansion is invalid for momenta  $p \lesssim |\kappa| \approx 5$  MeV and we have to use the full  $D^{*0}$  propagator instead of the expanded one. Figuratively speaking, at energies close to the  $\bar{D}^0 D^{*0}$  threshold, the main contribution to the loop integral comes from the low-energy regime, where the virtual  $D^{*0}$  meson can propagate much longer than the virtual  $D^{*0}$ 's average lifetime. Therefore, it is not justified to treat its decay in perturbation theory anymore.

When dressing the  $D^{*0}$  propagators in diagrams  $\mathcal{A}_0^{(I)}$  to  $\mathcal{A}_0^{(V)}$  with pion loops, similar infrared divergences occur. Hence, for consistency, we have to use the full  $D^{*0}$  propagator for all these diagrams as well as for the LO amplitude  $\mathcal{A}_{-1}$ . Note that in XEFT power counting  $\kappa^2$  is counted as  $Q^3$ , i.e. it is suppressed compared to the other terms  $\sim Q^2$  occurring in the denominator of the full  $D^{*0}$  propagator. Consequentially, the full  $D^{*0}$  propagator is still of order  $Q^{-2}$ , i.e. the power counting remains unaltered (see also App. A.1.1).

### 3.2.3 Transition amplitudes to next-to-leading order with resummed $D^{*0}$ propagator

As seen in the previous section, amplitudes containing a  $D^{*0}$  propagator dressed with a pion loop exhibit infrared divergences. Therefore, considering the low-energy regime, we have to reexpress the LO and NLO amplitudes  $\mathcal{A}_{-1}$  and  $\mathcal{A}_0^{(I)}$  to  $\mathcal{A}_0^{(V)}$  with full  $D^{*0}$  propagators. Note that the LO amplitude  $\mathcal{A}_{-1}$  with the  $D^{*0}$  propagator dressed to all orders already includes the amplitude  $\mathcal{A}_0^{(VI)}$ , which thus must not be taken into account separately to avoid double counting. For in- and outgoing momenta  $\ell$  and  $\ell'$ , respectively, the full off-shell amplitudes with resummed  $D^{*0}$  propagators read

$$i\mathcal{A}_{-1} = \frac{2\pi i}{M_{DD^*}} \frac{1}{-\gamma + \eta}, \quad (3.19a)$$

$$i\mathcal{A}_0^{(I)} = -i \frac{C_2}{2} (\ell^2 + \ell'^2) - 2i \frac{C_2}{2} \left( \frac{1}{2} (\ell^2 + \ell'^2) - \eta^2 \right) (-\eta + \Lambda) \frac{M_{DD^*}}{2\pi} \mathcal{A}_{-1} \\ - i \frac{C_2}{2} (-2\eta^2) (-\eta + \Lambda)^2 \left( \frac{M_{DD^*}}{2\pi} \right)^2 (\mathcal{A}_{-1})^2, \quad (3.19b)$$

$$i\mathcal{A}_0^{(II)} = \frac{ig^2}{6f^2} \left( 1 + \frac{\mu^2}{4|\ell||\ell'|} \log \left( 1 - \frac{4|\ell||\ell'|}{\mu^2 - (\ell^2 - \ell'^2)} \right) \right), \quad (3.19c)$$

$$i\mathcal{A}_0^{(III)} = \frac{ig^2}{3f^2} \left( (-\eta + \Lambda) + \frac{i\mu^2}{2} \left( \frac{1}{2|\ell|} \log \left( 1 + \frac{2|\ell|}{i\eta + \mu - |\ell|} \right) + |\ell| \leftrightarrow |\ell'| \right) \right) \frac{M_{DD^*}}{2\pi} \mathcal{A}_{-1}, \quad (3.19d)$$

$$i\mathcal{A}_0^{(IV)} = \frac{ig^2}{6f^2} \left( (-\eta + \Lambda)^2 + \mu^2 \left( \log \left( \frac{\Lambda}{2\eta - i\mu} \right) + \frac{1}{2} + R \right) \right) \left( \frac{M_{DD^*}}{2\pi} \right)^2 (\mathcal{A}_{-1})^2, \quad (3.19e)$$

$$i\mathcal{A}_0^{(V)} = \frac{-iD_2\mu^2}{(C_0)^2} (\mathcal{A}_{-1})^2, \quad (3.19f)$$

with  $\eta$  defined as  $\eta \equiv \sqrt{-2M_{DD^*}(E - \Sigma^{os}) - i\epsilon} = \sqrt{-p^2 - i\kappa^2 - i\epsilon}$ . All diagrams are finite for  $\eta \rightarrow 0$  and all values of  $m_\pi$ . For  $m_\pi > \Delta$ , i.e.  $\Sigma^{os} \rightarrow 0$ ,  $\eta \rightarrow -ip$  and the results for the diagrams with the free  $D^{*0}$  propagator are reproduced.<sup>5</sup> The LO diagram  $\mathcal{A}_{-1}$  has a pole at

$$-E = B^{\text{LO}} = \frac{\gamma^2}{2M_{DD^*}} - \Sigma^{os}, \quad (3.20)$$

which is complex for  $m_\pi < \Delta$ . The binding energy is given as the real part of the pole position and can be tuned with  $C_0$  through  $\gamma$  for renormalization.<sup>6</sup> To LO, we can relate the imaginary part with the decay width of the  $X$ . As shown in App. A.1.1, the  $X$  decay width coincides with the  $D^{*0}$  meson's decay width up to  $\beta^2$  suppressed terms.

Our result for the LO transition amplitude  $\mathcal{A}_{-1}$  is in agreement with the results from Ref. [119], where the authors obtained the  $\bar{D}^0 D^{*0}$  transition amplitude to LO by analytically continuing the parameters of a threshold-resonance form for two stable particles to the complex plane.

### 3.2.4 Renormalization of the scattering amplitude

The scattering amplitude  $\mathcal{A}_{-1} + \mathcal{A}_0 = \mathcal{A}_{-1} + \mathcal{A}_0^{(I)} + \dots + \mathcal{A}_0^{(V)}$  has to be renormalization scale independent up to NLO. We rewrite the coupling constants  $C_2$  and  $D_2$

$$C_2 = \frac{M_{DD^*}}{2\pi} \frac{r_0}{2} (C_0)^2 \equiv c_2 (C_0)^2, \quad (3.21a)$$

$$D_2 = \frac{g^2}{6f^2} \left( \frac{M_{DD^*}}{2\pi} \right)^2 \left( d_2 + \log \left( \frac{\Lambda}{\mu^{\text{ph}}} \right) + R \right) (C_0)^2, \quad (3.21b)$$

in analogy to Refs. [94] and [16]. Here and in the following, the superscript ph denotes the physical value of a quantity, i.e. at the physical pion mass. The quantity  $r_0$  with dimension of length can be identified with the effective range in the pionless theory. We further absorbed the constant  $R$ , which occurs in PDS, in the coupling constant  $D_2$ . Following the arguments of [16], we use  $r_0 \in [0, 1/100\text{MeV}]$ , i.e. the maximum value of  $r_0$  is inversely proportional to the momentum scales integrated out of the theory. For the dimensionless parameter  $d_2$ , we use that the numerical value of the terms in the parentheses with  $\mu^2$  as prefactor in Eq. (3.12b) is  $\mathcal{O}(1)$  evaluated at the physical pion mass with  $\Lambda \sim \mu^{\text{ph}}$ . We therefore take  $d_2 \in [-1, 1]$  as an estimate for a natural size. In the future, it should be possible to determine  $C_2$  and  $D_2$  from lattice calculations.

<sup>5</sup> Except that now, the  $D^{*0}$  obtains an additional mass shift,  $\Delta_{m_{D^*}}$ .

<sup>6</sup> Since we are not considering inelastic channels like, for example,  $X \rightarrow J/\Psi \pi^+ \pi^-$ , the LO binding momentum,  $\gamma$ , is real valued [119]. Further, the LO binding momentum is an observable only to LO. At NLO it obtains a shift  $\gamma \rightarrow \gamma + \frac{g^2 M_{DD^*}}{12\pi f^2} (\gamma - \Lambda)^2$ , i.e. depends on the renormalization scale  $\Lambda$ . After matching, for example to the experimentally observed binding energy, it also depends on the NLO coupling constants.

### 3.2.5 The effective range expansion up to next-to-leading order

In the previous sections we presented results for the scattering amplitudes. We now turn to the calculation of the scattering length. We attempt to employ the effective range expansion [102]. It is a low-energy expansion for the  $S$ -matrix, which is related to the scattering amplitude  $\mathcal{A}$  by

$$S - 1 = e^{2i\delta} - 1 = i \frac{p M_{DD^*}}{\pi} \mathcal{A}, \quad (3.22)$$

with the scattering phase shift  $\delta(p)$ . The  $S$ -matrix, though, is defined for large times, i.e. for asymptotic initial- and final-state particles [105]. Unstable particles, on the other hand, decay in finite times. Therefore, the  $D^{*0}$  is not the asymptotic state, but its decay products, i.e., in XEFT, the  $D^0$  and  $\pi$  (cf. Fig. 3.8). However, the effective range expansion is defined for two-particle scattering.

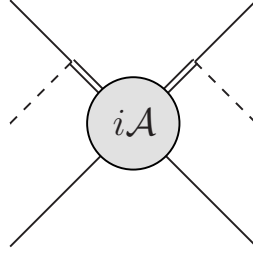


Figure 3.8.: Scattering diagram for the asymptotic states  $D^0 \bar{D}^0 \pi$ .

We therefore modify the on-shell point of the  $D^{*0}$  particle to be at complex energy, defined by the zero of the denominator of the  $D^{*0}$  meson's propagator. For a  $D^{*0}$  meson with momentum  $\mathbf{p}$ , we use as on-shell energy  $E_{D^*} = p^2/2m_{D^*} - i\Gamma_*/2$ . It implies for the  $\bar{D}^0 D^{*0}$  scattering amplitude that the on-shell energy is now given as  $E = p^2/2M_{DD^*} + \Sigma^{0S}$  or equivalently  $\eta^2 = -p^2$ . This procedure is similar to the complex mass scheme [120, 121] or the complex on-shell scheme [50]. Equation (3.22) can then be rewritten and expanded at low energies in  $p^2$  as

$$p \cot \delta_s(p) = ip + \frac{2\pi}{M_{DD^*} \mathcal{A}} = -\frac{1}{a_s} + \frac{1}{2} r_s p^2 + \dots \quad (3.23)$$

The quantity  $r_s$  is called  $S$ -wave effective range and  $a_s$  is the  $S$ -wave scattering length. In the pionless theory, the effective range  $r_s$  coincides with  $r_0$  in Eq. (3.21a). However, after the inclusion of pions, the effective range expansion gives valuable insight only up to order  $p^0$  for  $m_\pi < \Delta$  ( $\mu^2 > 0$ ). This circumstance can be understood by taking a closer look at the Fourier transform of the one-pion exchange in potential approximation

$$\frac{g^2}{2f^2} \frac{(\boldsymbol{\varepsilon}_i \cdot \mathbf{q})(\boldsymbol{\varepsilon}_j^* \cdot \mathbf{q})}{q^2 - \mu^2 - i\epsilon} \xrightarrow{\text{FT.}} \frac{g^2}{8\pi f^2} (\boldsymbol{\varepsilon}_i \cdot \boldsymbol{\varepsilon}_j^* - 3(\boldsymbol{\varepsilon}_i \cdot \hat{\mathbf{r}})(\boldsymbol{\varepsilon}_j^* \cdot \hat{\mathbf{r}})) \frac{\cos(\mu r) + \mu r \sin(\mu r)}{r^3} + \dots, \quad (3.24)$$

occurring in all diagrams involving pions. In contrast to the exponentially decreasing potential for the one-pion exchange as an effective, Yukawa-like  $NN$  interaction, the potential (3.24) is oscillatory with just a power-law suppression [122]. The oscillatory behavior originates in the open decay channel of the  $D^{*0} \rightarrow D^0 \pi$ , i.e. on-shell three-particle intermediate states, implying the negative sign of  $\mu^2$  in Eq. (3.24).

For potentials which decay like  $1/r^n$  all partial waves with angular momentum  $L > (n-2)/2$  contribute at the same order and approach zero like  $p^{n-2}$  [8]. Hence, for the potential (3.24) with  $n = 3$  beginning from the  $P$ -wave, all partial waves have contributions linear in  $p$ . Effects of the  $S$ -wave effective range are therefore not the dominating contribution at order  $p^2$ . Nevertheless, the  $S$ -wave scattering length can be calculated as the zero energy limit of the on-shell scattering amplitude. To take the inelastic channel  $\bar{D}^0 D^{*0} \rightarrow \bar{D}^0 D^0 \pi$  into account, we allow the scattering phase shift and accordingly the scattering length to be complex. For the NLO amplitudes (3.19) we take the limit  $\eta \rightarrow 0$  and simultaneously  $\ell, \ell' \rightarrow 0$  to obtain for the scattering length at NLO

$$a_s = \frac{1}{\gamma} + \frac{1}{\gamma^2} \frac{g^2}{6f^2} \frac{M_{DD^*}}{2\pi} \left[ (\gamma + i\mu)^2 + \mu^2 \left( d_2 + \frac{1}{2} - \log \left( \frac{i\mu^{\text{ph}}}{\mu} \right) \right) \right]. \quad (3.25)$$

The scattering length is complex for  $m_\pi < \Delta$  accounting for the inelastic contributions as mentioned above. It becomes real as soon as the hyperfine splitting of the  $D^0$  and  $D^{*0}$  mesons is smaller than the neutral pion mass, i.e. when the  $D^{*0}$

is stable. As soon as  $m_\pi > \Delta$ , the mass scale  $\mu$  is purely imaginary and the cos and sin in Eq. (3.24) decay exponentially. The effective range can then be calculated and we acquire, using that  $\mu = i|\mu|$  for  $m_\pi > \Delta$

$$r_s = r_0 \left[ 1 - \frac{2}{\gamma} \frac{g^2}{6f^2} \frac{M_{DD^*}}{2\pi} \left( (\gamma - |\mu|)^2 - |\mu|^2 \left( d_2 + \frac{1}{2} - \log \left( \frac{\mu^{\text{ph}}}{|\mu|} \right) \right) \right) \right] - \frac{g^2}{6f^2} \frac{M_{DD^*}}{2\pi} 2 \left( 1 - \frac{8}{3} \frac{\gamma}{|\mu|} + 2 \frac{\gamma^2}{|\mu|^2} \right). \quad (3.26)$$

Note that for pion masses only slightly larger than the hyperfine splitting, convergence of the effective range expansion might not be certain. The radius of convergence of the effective range expansion is limited to energies  $|p^2| \lesssim |\mu^2|/4$  [123, 124]. Using  $\gamma^2$  as a typical energy at which the scattering amplitude is evaluated, we find  $m_\pi \gtrsim 145$  MeV as a constraint for the pion mass. If one is interested in larger energies, the lower bound for the pion mass might be greater.

### 3.2.6 The binding energy to next-to-leading order

For an unstable  $D^{*0}$  meson, the OPE potential is oscillatory and not Yukawa-like [122]. The effective range expansion breaks down at NLO and the effective range is not defined. Hence, the binding energy can not be extracted from effective range parameters. In this section, we present an alternative method to access the binding energy up to NLO, employing the two-body scattering amplitudes, regardless of whether examining stable or unstable particles. It will further be possible to employ the presented method in order to extract the binding energy to NLO in the finite volume.

First, we note that the sum of the NLO scattering amplitudes,  $\mathcal{A}_0^{(1)}, \dots, \mathcal{A}_0^{(V)}$ , can be collected in powers of the LO amplitude

$$\mathcal{A}_0 = \mathcal{A}_0^{(1)} + \dots + \mathcal{A}_0^{(V)} = s_0 + s_1 \mathcal{A}_{-1} + s_2 (\mathcal{A}_{-1})^2. \quad (3.27)$$

We remark at this point that the coefficients are energy and momentum dependent, i.e.  $s_0 \equiv s_0(E, |\ell|, |\ell'|)$ ,  $s_1 \equiv s_1(E, |\ell|, |\ell'|)$  and  $s_2 \equiv s_2(E)$ . For convenience, we skip the dependence for a moment, but will come back to it later. Furthermore, we expand the LO amplitude around the LO pole position

$$\mathcal{A}_{-1} \equiv \frac{Z_{-1}}{E + B^{\text{LO}}} + \dots, \quad (3.28)$$

where the dots denote terms being finite at  $E = -B^{\text{LO}}$  and  $Z_{-1}$  is the residue

$$(Z_{-1})^{-1} = \left[ i \frac{\partial}{\partial E} \frac{1}{i \mathcal{A}_{-1}} \right]_{E=-B^{\text{LO}}} = \frac{-(M_{DD^*})^2}{2\pi} \frac{1}{\gamma}. \quad (3.29)$$

Accordingly, the full amplitude up to NLO, expanded around the LO pole position, can be written as

$$\mathcal{A} = \mathcal{A}_{-1} + \mathcal{A}_0 = \frac{Z_{-1} + s_1 Z_{-1}}{E + B^{\text{LO}}} + \frac{s_2 (Z_{-1})^2}{(E + B^{\text{LO}})^2} + \dots. \quad (3.30)$$

Moreover, we consider a generic, non-perturbative expression for the amplitude with shifted pole position,  $B = B^{\text{LO}} + \Delta B$ , and shifted residue,  $Z = Z_{-1} + \Delta Z$ , and expand it around the LO pole position

$$\mathcal{A}^{\text{np}} = \frac{Z}{E + B} + \dots = \frac{Z_{-1} + \Delta Z}{E + B^{\text{LO}}} - \frac{Z \Delta B}{(E + B^{\text{LO}})^2} + \dots. \quad (3.31)$$

Utilizing expressions (3.30) and (3.31), the NLO shifts for the residue,  $Z_{-1}$ , and the LO pole position,  $B^{\text{LO}}$ , can be read off by equating coefficients

$$\Delta Z^{\text{NLO}} = s_1(E, |\ell|, |\ell'|) Z_{-1} \Big|_{E=-B^{\text{LO}}}, \quad (3.32a)$$

$$\Delta B^{\text{NLO}} = - \frac{s_2(E)}{1 + s_1(E, |\ell|, |\ell'|)} Z_{-1} \Big|_{E=-B^{\text{LO}}}, \quad (3.32b)$$

where we reintroduced the dependence on the energy and the momenta of the coefficients again. At NLO, the field strength renormalization depends on the absolute value of the external momenta  $\ell$  and  $\ell'$ . Further, the expression for the shift of the binding energy also does, seemingly posing a problem since it must not depend on scattering variables. To resolve this issue, we first note that the dimensionless coefficient  $s_1$  derives from the NLO amplitudes and is thus

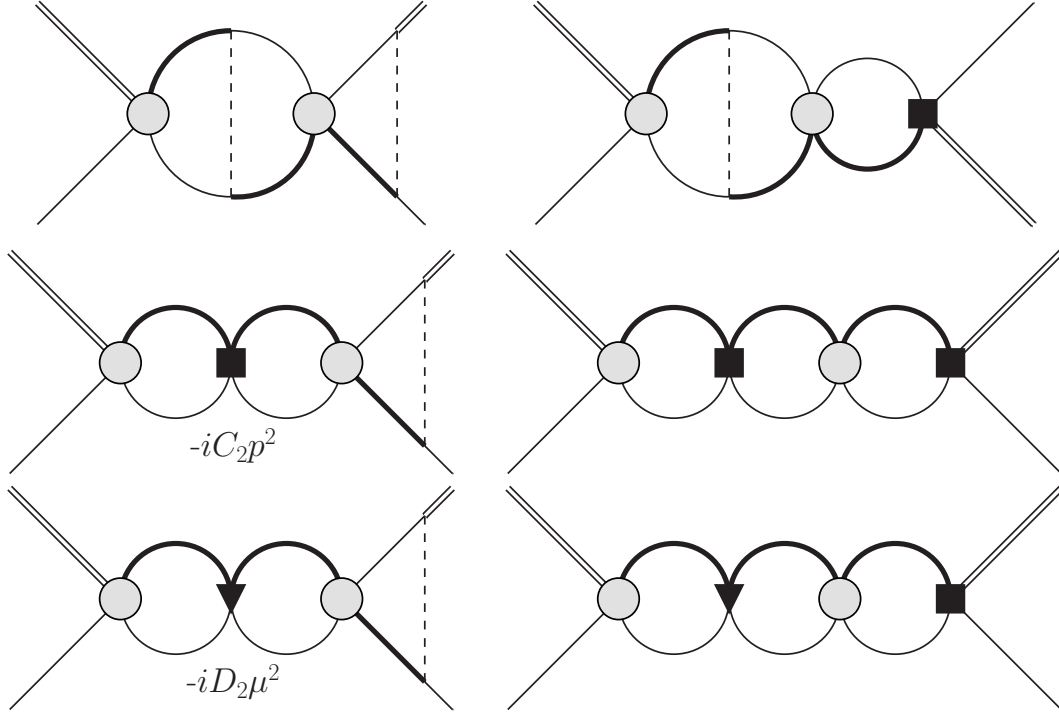


**Figure 3.9.:** Scattering amplitudes shifting the coefficient  $s_2$  in Eq. (3.27) at NNLO and causing a cancellation in Eq. (3.32b).

expected to be much smaller than 1. Hence, we expand the overall factor  $1/(1+s_1)$  in Eq. (3.32b) as a geometrical series and obtain

$$\Delta B^{\text{NLO}} = -Z_{-1} (s_2 - s_1 s_2 + \mathcal{O}(s_1^2 s_2)). \quad (3.33)$$

Taking into account that  $s_2$  derives from NLO amplitudes as well, we anticipate that terms proportional to  $s_1 s_2$  are actually of NNLO. In fact, at NNLO there are exactly six diagrams which depend on the external momenta and are proportional to the LO amplitude squared, depicted in Fig. 3.9. These lead to a momentum dependent NNLO shift for the coefficient  $s_2$

$$\Delta s_2^{\text{NNLO} (1)}(E, |\ell|, |\ell'|) = s_1(E, |\ell|, |\ell'|) s_2(E), \quad (3.34)$$

where coefficients without a superscript are of NLO. Here, we used that amplitudes are separable at resummed LO vertices. Further shifts for  $s_2$  at NNLO which do not depend on the external momenta, are denoted by  $\Delta s_2^{\text{NNLO} (2)}(E)$  and we obtain

$$\begin{aligned} s_2(E) &\xrightarrow{\text{NNLO}} s_2(E) + \Delta s_2^{\text{NNLO} (1)}(E, |\ell|, |\ell'|) + \Delta s_2^{\text{NNLO} (2)}(E) = s_2(E) + s_1(E, |\ell|, |\ell'|) s_2(E) + \Delta s_2^{\text{NNLO} (2)}(E) \\ &\Rightarrow \frac{1}{1 + s_1(E, |\ell|, |\ell'|)} s_2(E) \xrightarrow{\text{NNLO}} s_2(E) + \Delta s_2^{\text{NNLO} (2)}(E) + \mathcal{O}(s_1^2 s_2), \end{aligned}$$

implying that now, any momentum dependence occurs first at  $\text{N}^3\text{LO}$ . Since we work to NLO only, we skip the momentum dependent factor of  $1/(1+s_1)$  and use for the shift of the binding energy

$$\Delta B^{\text{NLO}} = -s_2(E) Z_{-1} \Big|_{E=-B^{\text{LO}}}, \quad (3.35)$$

with

$$s_2(E) \Big|_{E=-B^{\text{LO}}} = c_2 \gamma^2 + \frac{g^2}{6f^2} \left( \frac{M_{DD^*}}{2\pi} \right)^2 \mu^2 \left( -d_2 + \log \left( \frac{\mu^{\text{ph}}}{2\gamma - i\mu} \right) + \frac{1}{2} \right). \quad (3.36)$$

### 3.2.7 The imaginary part of the pole position

The imaginary part of the pole position's NLO shift,  $\text{Im}[\Delta B^{\text{NLO}}]$ , derives from the imaginary part of the coefficient  $s_2$  since  $Z_{-1}$  is real valued. It can be obtained by applying cuts to the diagrams in Fig. 3.4.<sup>7</sup> Consider, for example, the cut diagram shown in Fig. 3.10. Applying the cut by replacing all cut propagators with appropriate delta distributions and keeping all  $m_\pi/m_D$  suppressed terms [105], the expressions for the imaginary parts coincide with the decay diagrams in Ref. [119] at energy  $E_X$ . In Ref. [16], the authors pointed out that dropping  $m_\pi/m_D$  terms is equivalent to treating

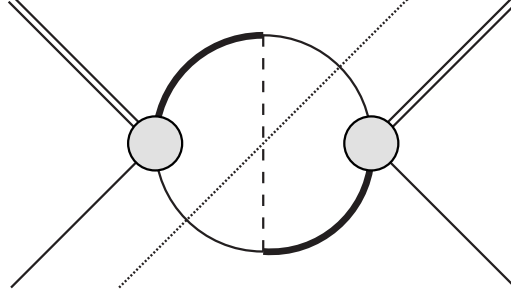


**Figure 3.10.:** Example for a cut diagram, determining a contribution to the imaginary part of the pole position  $B$ . The notation is the same as in the previous figures. The cuts through the pion,  $D^0$  and  $\bar{D}^0$  meson propagators are indicated by dotted lines.

pions in potential approximation.<sup>8</sup> But for the decay diagrams, the pions in the final state are on-shell and the potential approximation is invalid. Hence, for the calculation of the imaginary part of the pole position, which is related to the decay width by  $\text{Im}[B] = \Gamma[X \rightarrow D^0 \bar{D}^0 \pi]/2$ , all  $m_\pi/m_D$  suppressed terms have to be kept and the remaining three-body phase space integral has to be evaluated numerically. We do not expect that the decay width is well approximated when treating the final state pions in potential approximation. Further discussions can be found in Refs. [126, 16, 119].

### 3.2.8 Chiral extrapolations and results

To determine the quark mass dependence of the  $X(3872)$ 's binding energy, we need the chiral extrapolations of the pion decay constant, the  $D$  meson axial coupling constant and the  $D^0$  and  $D^{*0}$  mesons' masses, respectively. We use a superscript (0) to denote the chiral limit value of a quantity. We take the  $m_\pi$  dependence of the pion decay constant from Ref. [6]

$$f = f^{(0)} \left[ 1 - \frac{1}{4\pi^2 f^{(0)2}} m_\pi^2 \log\left(\frac{m_\pi}{m_\pi^{\text{ph}}}\right) + \frac{\bar{l}_4}{8\pi^2 f^{(0)2}} m_\pi^2 \right], \quad (3.37)$$

with the low-energy constant  $\bar{l}_4 = 4.4$  and  $f^{(0)} = 124$  MeV, implying  $f^{\text{ph}} = 132$  MeV [6, 127]. For the  $D$  meson axial coupling constant, we use the lattice results from Ref. [128]. The chiral extrapolation reads

$$g = g^{(0)} \left[ 1 - \frac{1 + 2g^{(0)2}}{4\pi^2 f^{(0)2}} m_\pi^2 \log\left(\frac{m_\pi}{\mu_{\text{lat}}}\right) + \alpha m_\pi^2 \right], \quad (3.38)$$

with the parameters [128]

$$g^{(0)} = 0.46, \quad \alpha = -0.16 \text{ GeV}^{-2}, \quad \mu_{\text{lat}} = 1 \text{ GeV}. \quad (3.39)$$

Evaluated at the physical pion mass, the physical value of the  $D$  meson axial coupling constant is  $g^{\text{ph}} = 0.5$ . The value for  $g^{\text{ph}}$  is consistent with an estimate in Ref. [50]. There the decay width of the  $D^{*+} \rightarrow D^0 \pi^+$ ,  $D^+ \pi^0$  [129] was used as an input and furthermore, isospin symmetry to determine the  $D$  meson axial coupling constant.

For the quark mass dependence of the  $D$  meson masses and hence, the hyperfine splitting  $\Delta$ , we use the results of [130] and add the mass shift (3.15) for the  $D^{*0}$  meson

$$m_D = m_D^{\text{ph}} + \frac{h_1}{m_D^{\text{ph}}} \left( m_\pi^2 - (m_\pi^{\text{ph}})^2 \right), \quad (3.40a)$$

$$m_{D^*} = m_{D^*}^{\text{ph}} + \frac{h_1}{m_{D^*}^{\text{ph}}} \left( m_\pi^2 - (m_\pi^{\text{ph}})^2 \right) + \Delta_{m_{D^*}}, \quad (3.40b)$$

<sup>7</sup> The scattering diagrams in Fig. 3.4 still involve bare  $D^{*0}$  propagators, which have to be replaced with the full ones first.

<sup>8</sup> For potential pions, the kinetic energy is much smaller than the pion momentum [125]. Dropping  $m_\pi/m_D$  terms implies that the kinetic energy of the pions is neglected and thus, pions are treated in potential approximation.

with  $h_1 = 0.42$  [130].

In the KSW theory for  $NN$  scattering, the relative size of the two-pion-exchange and OPE graphs is about  $1/2$ . Due to NNLO coefficients of order  $5 \sim 6$  being much greater than the expansion parameter in KSW theory, contributions at NLO and NNLO are of comparable magnitude and the perturbative treatment of pions fails [51]. In XEFT, the two-pion exchange is suppressed more strongly. However, the estimate of the suppression based on expression (3.3) depends on the quark mass, dominantly through the mass scale  $\mu$ . To determine a region of validity for XEFT we use a rather conservative estimate for the upper bound of the expansion parameter and require that the absolute value of expression (3.3) is smaller than 0.15. Even though unnaturally large NNLO coefficients of similar size as in KSW occur, expression (3.3) is expected to be small enough to compensate for those, such that the perturbative inclusion of pions remains valid. A plot for the expansion factor is shown in Fig. 3.11. For the lower bound we consider that pions are treated non-

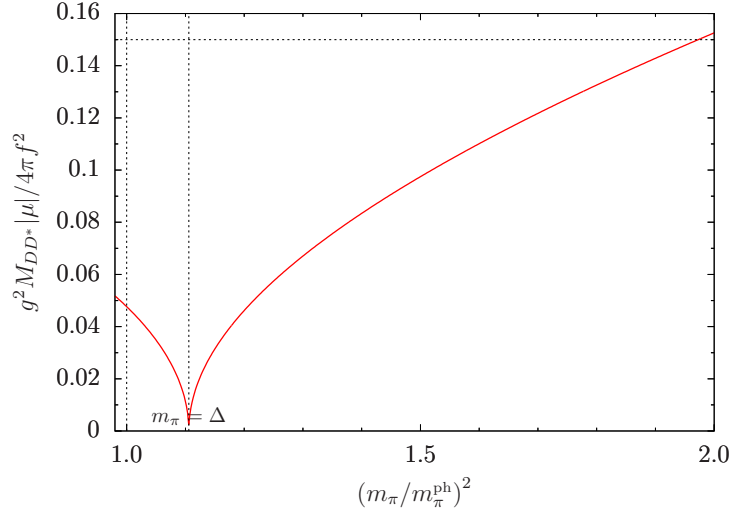


**Figure 3.11:** Expansion parameter for the perturbative inclusion of pions in XEFT. We use the absolute value of  $\mu$  since it is completely imaginary for  $m_\pi > \Delta$ . The horizontal dashed line belongs to 0.15 which we take as an upper bound to have a clear suppression even if NNLO contributions are unnaturally large.

relativistically in XEFT. We require for the maximum pion velocity  $v_\pi \approx \mu/m_\pi \lesssim 0.35$ .<sup>9</sup> These conditions are fulfilled for  $0.98 (m_\pi^{\text{ph}})^2 \lesssim m_\pi^2 \lesssim 2 (m_\pi^{\text{ph}})^2$ . Since the coupling constants  $c_2$  and  $d_2$  are undetermined, unnaturally large corrections to the LO amplitude might occur at NLO. We will come to this issue when discussing the scattering length below.

In Fig. 3.12, the quark mass dependence of the binding energy of the  $X$  is shown. We plot against the squared pion mass, which is proportional to the light quark masses at LO in chiral perturbation theory [117]. In XEFT power counting  $\Lambda \gtrsim Q$  and thus, we use  $\Lambda = 50$  MeV. As described in the introduction in Chap. 1, we fix the binding energy at the physical value of the pion mass  $m_\pi^{\text{ph}}$  and use  $E_X^{\text{ph}} = 0.1$  MeV. The  $m_\pi$ -dependent and independent contact interactions at NLO can be tuned by modifying the parameters  $d_2$  and  $r_0$  defined in Eqs. (3.21b, 3.21a), respectively. For  $d_2 = 0$  and  $r_0 = 0$ , the  $D$  mesons interact via the LO contact interaction and pion exchanges only, corresponding to the solid, thick curve in Fig. 3.12.<sup>10</sup> We see that for increasing pion mass the binding energy first moves towards the threshold with an inflection point at  $m_\pi = \Delta$ . Shortly after the inflection point, the sign of the slope reverses and the binding energy increases for increasing quark masses. Tuning the strengths of the NLO contact interactions via the parameters  $d_2$  and  $r_0$  can either imply that the slope of the binding energy of the  $X$  enlarges or decreases. The lower bound for the binding energy is acquired for  $d_2 = -1$  and  $r_0 = 0.01/\text{MeV}$ . For this scenario, the binding energy remains below the physical one for pion masses  $(m_\pi^{\text{ph}})^2 < m_\pi^2 < 2(m_\pi^{\text{ph}})^2$ . Contrariwise, assuming positive values for  $d_2$  and small values for  $r_0$ , the binding energy of the  $X$  steeply rises for pion masses beyond the inflection point. The upper bound belongs to  $d_2 = 1$  and  $r_0 = 0$ . The dominating contribution to the shift of the binding energy at NLO is the quark mass dependent contact interaction. Considering, e.g., a negative coupling constant  $d_2$  with enhanced magnitude, it is possible that the bound state of the  $X$  vanishes for large quark masses. Such a scenario is represented by the dashed curve in Fig. 3.12 belonging to  $d_2 = -2$  and  $r_0 = 0$ .

Before addressing the chiral extrapolation of the scattering length over the whole range of validity, we take a closer look at its behavior around  $m_\pi = \Delta$ , i.e. where the pion mass is close to the hyperfine splitting of the  $D^0$  and  $D^{*0}$ . At LO the scattering length reads  $a^{\text{LO}} = 1/\gamma$  and fulfills the universal relation  $E_X = 1/2M_{DD^*} a_s^2$ .

<sup>9</sup> Due to small coefficients in the non-relativistic expansion, greater pion velocities are probably compatible with a non-relativistic treatment.

<sup>10</sup> The NLO contact interaction with vertex  $D_2\mu^2$  is still needed to subtract the logarithmic dependence on the renormalization scale.

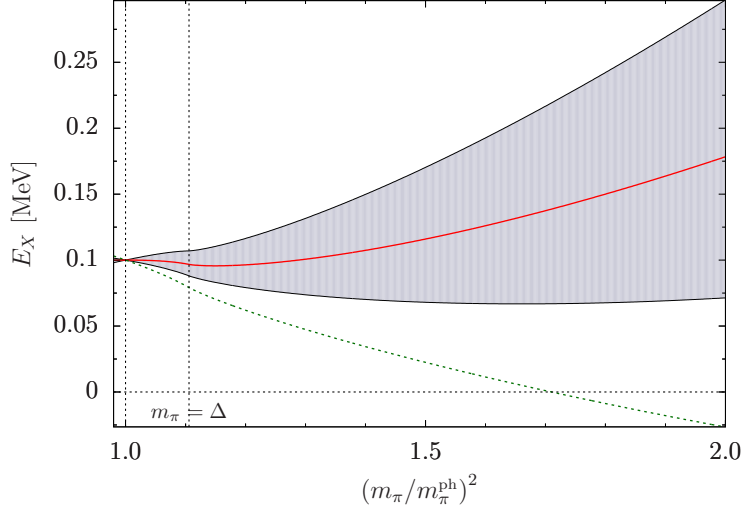


**Figure 3.12.:** Binding energy of the  $X(3872)$  in dependence on the light quark masses. The solid, thick curve belongs to  $d_2 = 0$  and  $r_0 = 0$ , i.e. considering the LO contact interaction and pion exchanges only. For  $d_2 = -1$  and  $r_0 = 0.01/\text{MeV}$  we acquire the lower bound and for  $d_2 = 1$  and  $r_0 = 0$  the upper bound for the binding energy. The dashed curve corresponds to  $d_2 = -2$ .

At NLO, the scattering length is given in Eq. (3.25). The scattering length is continuous but not differentiable at  $m_\pi = \Delta$ . We consider the derivative of the scattering length with respect to  $m_\pi$  around  $m_\pi = \Delta$  ( $\mu = 0$ ). It has two divergent terms, one proportional to  $\log(i\mu^{\text{ph}}/\mu)$  and another one proportional to  $-i/\mu$ . The first one implies a logarithmic divergence for the real part of the derivative of  $a_s$  to  $+\infty$ , for both limits  $m_\pi \nearrow \Delta$  and  $m_\pi \searrow \Delta$ . The second term diverges  $\sim -i/\sqrt{\Delta - m_\pi}$ . On the one hand, this implies a divergence of  $\text{Im}[\partial a_s/\partial m_\pi] \rightarrow -\infty$  for  $m_\pi \nearrow \Delta$ . On the other hand, the real part of the derivative of the scattering length goes to  $-\infty$  for  $m_\pi \searrow \Delta$ . Furthermore, the imaginary part vanishes for  $m_\pi > \Delta$ . In conclusion, for the derivative of the scattering length we find

$$\text{Re}\left[\frac{\partial a_s}{\partial m_\pi}\right] \rightarrow \begin{cases} +\infty, & m_\pi \nearrow \Delta, \\ -\infty, & m_\pi \searrow \Delta, \end{cases} \quad (3.41a)$$

$$\text{Im}\left[\frac{\partial a_s}{\partial m_\pi}\right] \rightarrow \begin{cases} -\infty, & m_\pi \nearrow \Delta, \\ 0, & m_\pi \searrow \Delta \end{cases} \quad (3.41b)$$

and therefore, we expect a cusp effect for the real as well as the imaginary part of the scattering length. The real and imaginary part of the scattering length in dependence on the light quark masses are shown in Fig. 3.13. We see the expected negative correlation between the real part of the scattering length and the binding energy, i.e. the scattering length decreases for increasing binding energy and vice versa. Again the solid, thick curve belongs to the case where  $d_2 = 0$  and  $r_0 = 0$ , i.e. when only the LO contact interaction and the pion exchanges are considered. The inset on the left shows the cusp for the real part at  $m_\pi = \Delta$  in more detail. The lower and upper bounds are obtained by varying  $d_2$  and  $r_0$  in the natural ranges  $r_0 \in [0, 1/100\text{MeV}]$ ,  $d_2 \in [-1, 1]$  and maximizing the width of the error band. The scattering length can be compared to the effective range from Eq. (3.26), depicted in Fig. 3.14. The effective range is plotted for  $m_\pi > 145 \text{ MeV}$  (cf. Sec. 3.2.5). Over the whole range for the light quark masses considered, the scattering length is larger than the effective range. Although, there are certain combinations of  $r_0$  and  $d_2$  for which scattering length and effective range are of comparable magnitude, the most likely scenario is that the scattering length is unnaturally large and universal phenomena dominate. We therefore expect that XEFT power counting remains valid for pion masses beyond the physical one.

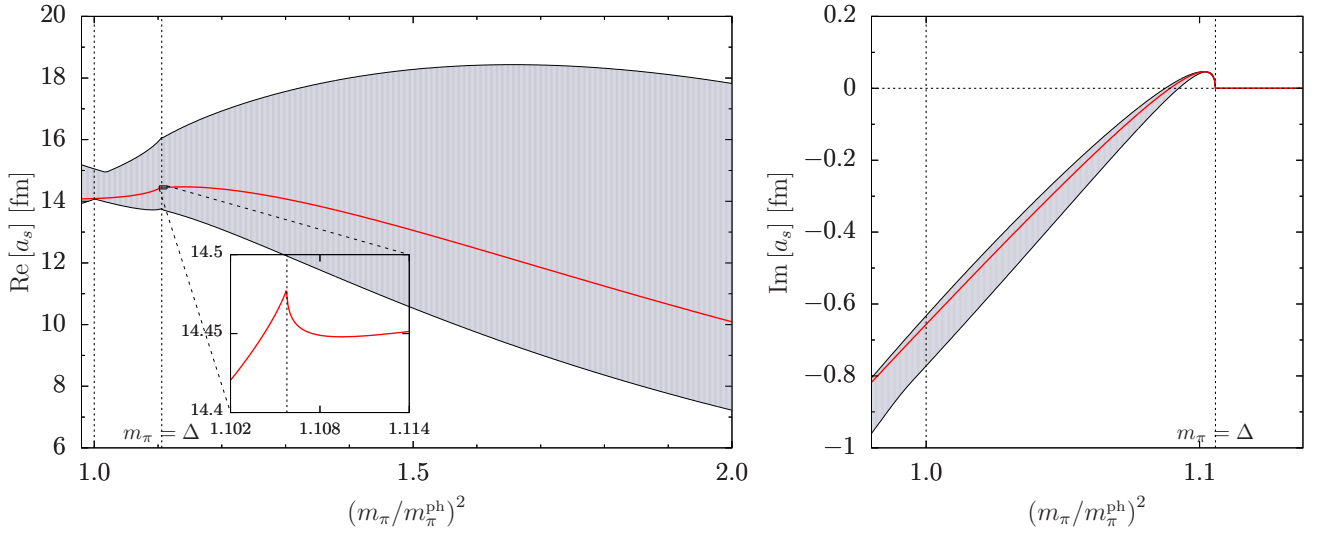


**Figure 3.13.:** The quark mass dependence of the real (left) and imaginary (right) part of the  $X(3872)$ 's scattering length. The solid, thick curve belongs to  $d_2 = 0$  and  $r_0 = 0$ . The bounds are acquired by varying  $d_2$  and  $r_0$  in their natural ranges  $r_0 \in [0, 1/100\text{MeV}]$  and  $d_2 \in [-1, 1]$  and maximizing the width of the error band.

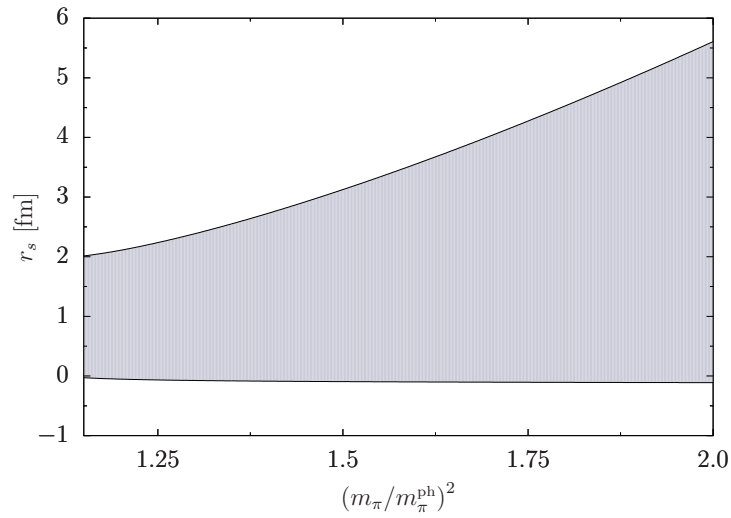


**Figure 3.14.:** The quark mass dependence of the  $X(3872)$ 's  $S$ -wave effective range for  $m_\pi^2 \geq 1.15(m_\pi^{\text{ph}})^2$ . The bounds are acquired by varying  $d_2$  and  $r_0$  in their natural ranges  $r_0 \in [0, 1/100\text{MeV}]$  and  $d_2 \in [-1, 1]$  and maximizing the width of the error band.

### 3.3 Finite volume effects

We consider the  $\bar{D}^0 D^{*0}$  system in a box with side length  $L$  and periodic boundary conditions. The allowed lattice momenta are then given by integer vectors times  $2\pi/L$  (cf. Sec. 2.2.3). Integrals occurring in calculations for the binding energy in the infinite volume have to be replaced by discrete sums over the quantized lattice momenta. Since we are interested in  $\bar{D}^0 D^{*0}$  bound states with even parity, we expect that the binding energy obtains a positive shift. We distinguish between two different regions. One, where the  $D^{*0}$  is unstable, i.e. for pion masses  $m_\pi < \Delta$  and a second region where the  $D^{*0}$  is stable, i.e.  $m_\pi \geq \Delta$ . Whereas in the first case explicit XEFT calculations have to be carried out due to three-body  $D\bar{D}\pi$  intermediate states, in the latter case one can alternatively use a two-body approach introduced in Ref. [59], which serves as a consistency check. All quantities which differ in the finite volume are tagged by a superscript  $L$ .

#### 3.3.1 The leading-order amplitude

Let us begin with the explicit XEFT calculations, which can be utilized in both regions. To LO, the amplitude in the finite volume reads

$$i\mathcal{A}_{-1}^L = \frac{2\pi i}{M_{DD^*}^L} \frac{1}{-\frac{2\pi}{M_{DD^*}^L c_0} - 4\pi I_0^L}, \quad (3.42)$$

where the finite volume quantity  $I_0^L$  is given by

$$I_0^L \equiv \frac{1}{L^3} \sum_{\mathbf{k}=\frac{2\pi}{L}\mathbf{n}} \frac{1}{k^2 - 2M_{DD^*}^L E}, \quad \mathbf{n} \in \mathbb{Z}^3. \quad (3.43)$$

Since the mass of the  $D^{*0}$  meson obtains a shift in the finite volume as given below, the reduced mass depends on the box size, too. Like the loop integral (3.6) in the infinite volume,  $I_0^L$  is linearly ultraviolet divergent since short-distance properties of the theory remain unchanged in the finite volume. We regularize the loop integrals following [59] (cf. Sec. 2.2.3): first, we introduce a sharp momentum cutoff,  $\lambda$ , for the sum and then add and subtract the infinite volume loop integrals evaluated at zero energy. One of the loop integrals is regularized using PDS, the other one using a momentum cutoff, which coincides with the cutoff in the sum. Finally, the limit  $\lambda \rightarrow \infty$  is taken. We obtain

$$I_0^L \xrightarrow{\text{PDS}} \lim_{\lambda \rightarrow \infty} \left[ \frac{1}{L^3} \sum_{\mathbf{k}=\frac{2\pi}{L}\mathbf{n}}^{|k|<\lambda} \frac{1}{k^2 - p^2} - \int \frac{d^3\mathbf{k}}{(2\pi)^3} \frac{\theta(\lambda - |\mathbf{k}|)}{k^2} \right] + \frac{\Lambda}{4\pi}, \quad (3.44)$$

with  $E = p^2/2M_{DD^*}^L$ . Plugging Eq. (3.44) into Eq. (3.42) and using the definition for the LO binding momentum in the infinite volume (Eq. (3.8)), we acquire

$$i\mathcal{A}_{-1}^L = \frac{-2\pi i}{M_{DD^*}^L} \frac{1}{\gamma + \frac{1}{\pi L} S\left(\left(\frac{Lp}{2\pi}\right)^2\right)}, \quad (3.45)$$

with

$$S(x) = \lim_{\lambda_n \rightarrow \infty} \left[ \sum_{\mathbf{n}}^{|n|<\lambda_n} \frac{1}{n^2 - x} - 4\pi\lambda_n \right], \quad (3.46)$$

where  $\lambda_n \equiv L\lambda/(2\pi)$ . The energy levels of the  $\bar{D}^0 D^{*0}$  system to LO in the finite volume can be obtained from Eq. (3.45). Note that they are fully determined by the infinite volume quantity  $\gamma$ .<sup>11</sup> Here, we are interested in the solution with negative energy, i.e. the solution which approaches the infinite volume LO binding energy for  $L \rightarrow \infty$ . We denote the corresponding LO binding momentum by  $\gamma^L$ , defined by

$$\gamma + \frac{1}{\pi L} S\left(-\left(\frac{L\gamma^L}{2\pi}\right)^2\right) = 0. \quad (3.47)$$

<sup>11</sup> We expect that even if three-particle intermediate states exist that is after the inclusion of NLO contributions and for  $m_\pi < \Delta$ , finite volume observables are still determined by the infinite volume S-matrix as demonstrated in Refs. [60, 61, 62].

### 3.3.2 The $D^{*0}$ self-energy and mass shift

We proceed with the  $D^{*0}$  self-energy and mass shift. The calculation is carried out similarly to the one of the LO amplitude. Using PDS and cutoff regularization we obtain for the bare self-energy

$$-i\Sigma^L = \frac{ig^2}{24\pi(f^L)^2}(\mu^L)^2 \left( \frac{1}{\pi L} S \left( \left( \frac{L\mu^L}{2\pi} \right)^2 \right) + \Lambda \right). \quad (3.48)$$

Independent of the pion mass, we do not receive any imaginary contributions for the bare self-energy in the box. However, since the finite volume itself cuts off low-frequency modes, we do not expect the occurrence of any infrared divergences.

Again, we use the on-shell renormalization scheme and subtract the second term proportional to the PDS renormalization scale  $\Lambda$ . Hence, the counterterms in the finite and infinite volume coincide up to corrections to  $f$  and  $\mu$ . The shift for the  $D^{*0}$  mass is different though,

$$\Delta_{m_{D^*}}^L = -\frac{g^2}{24\pi(f^L)^2}(\mu^L)^2 \frac{1}{\pi L} S \left( \left( \frac{L\mu^L}{2\pi} \right)^2 \right). \quad (3.49)$$

Note that even for physical pion mass, the  $D^{*0}$  meson in a box receives a finite mass shift.

### 3.3.3 Next-to-leading-order corrections to the binding energy

Now we implement the corrections due to the NLO amplitudes. In analogy to the infinite volume we find for the NLO contact interactions, i.e. the amplitudes  $\mathcal{A}_{0(\text{I})}^L$  and  $\mathcal{A}_{0(\text{V})}^L$

$$i\mathcal{A}_{0(\text{I})}^L = \frac{-iC_2 p^2}{(C_0)^2} (\mathcal{A}_{-1}^L)^2, \quad (3.50a)$$

$$i\mathcal{A}_{0(\text{V})}^L = \frac{-iD_2(\mu^L)^2}{(C_0)^2} (\mathcal{A}_{-1}^L)^2. \quad (3.50b)$$

For the pion-exchange diagrams we do not project onto the  $S$ -waves. Whereas the infinite volume is rotationally invariant, the lattice is only invariant under transformations of the cubic group. In principle, it is possible to decompose quantities transforming according to an irreducible representation of the cubic group into spherical harmonics [131, 65]. However, we keep the sums over integer vectors since convergence of the partial wave expansion is not certain. The OPE amplitude  $\mathcal{A}_{0(\text{II})}^L$  is then given as

$$i\hat{\mathcal{A}}_{0(\text{II})ij}^L = \frac{ig^2}{2(f^L)^2} \frac{(\boldsymbol{\varepsilon}_i \cdot (\boldsymbol{\ell} - \boldsymbol{\ell}'))(\boldsymbol{\varepsilon}_j^* \cdot (\boldsymbol{\ell} - \boldsymbol{\ell}'))}{|\boldsymbol{\ell} - \boldsymbol{\ell}'|^2 - (\mu^L)^2}, \quad (3.51)$$

with the incoming (outgoing) relative momentum  $\boldsymbol{\ell}$  ( $\boldsymbol{\ell}'$ )<sup>12</sup>. For  $\mathcal{A}_{0(\text{III})}^L$  we find

$$i\hat{\mathcal{A}}_{0(\text{III})ij}^L = \mathcal{A}_{-1}^L \frac{M_{DD^*}^L}{2\pi} \frac{ig^2}{2(f^L)^2} \left( \frac{1}{\pi L} S_{ij}^{(\text{III})} \left( \frac{L\boldsymbol{\ell}}{2\pi}, \left( \frac{L\mu^L}{2\pi} \right)^2 \right) + \frac{\delta_{ij}}{3} \Lambda \right) + \boldsymbol{\ell} \longleftrightarrow \boldsymbol{\ell}', \quad (3.52)$$

where the quantity  $S_{ij}^{(\text{III})}$  is defined as

$$S_{ij}^{(\text{III})}(\mathbf{m}, \mathbf{x}) \equiv \lim_{\lambda_n \rightarrow \infty} \left[ \sum_{\mathbf{n}}^{\|\mathbf{n}\| < \lambda_n} \frac{1}{n^2 - m^2} \frac{\boldsymbol{\varepsilon}_i \cdot (\mathbf{n} + \mathbf{m}) \boldsymbol{\varepsilon}_j^* \cdot (\mathbf{n} + \mathbf{m})}{|\mathbf{n} + \mathbf{m}|^2 - x} - \frac{\delta_{ij}}{3} 4\pi\lambda_n \right]. \quad (3.53)$$

The amplitudes  $\hat{\mathcal{A}}_{0(\text{II})ij}^L$  and  $\hat{\mathcal{A}}_{0(\text{III})ij}^L$  imply a coupling between channels with different angular momentum. Considering the  $A_1$  representation of the cubic group, the lowest angular momenta coupled are with  $l = 0, 4, 6, 8, \dots$ . On the other hand, we can use a tensor decomposition for the amplitude  $\hat{\mathcal{A}}_{0(\text{IV})ij}^L$  and it appears that  $\hat{\mathcal{A}}_{0(\text{IV})ij}^L = \delta_{ij} \mathcal{A}_{0(\text{IV})}^L$ . A detailed derivation is given in App. A.2.1. We obtain for the scalar amplitude

$$i\mathcal{A}_{0(\text{IV})}^L = (\mathcal{A}_{-1}^L)^2 \left( \frac{M_{DD^*}^L}{2\pi} \right)^2 \frac{ig^2}{6(f^L)^2} \left[ \left( \frac{1}{\pi L} S \left( \left( \frac{Lp}{2\pi} \right)^2 \right) + \Lambda \right)^2 + (\mu^L)^2 \left( \frac{1}{(2\pi^2)^2} S_{(\text{IV})} \left( \left( \frac{Lp}{2\pi} \right)^2, \left( \frac{L\mu^L}{2\pi} \right)^2 \right) + \log \left( \frac{\Lambda}{|\mu^L|} \right) + \frac{1}{2} + R \right) \right], \quad (3.54)$$

<sup>12</sup> Note that the energy dependence of the pion propagators occurring in the OPE amplitudes is suppressed by  $m_\pi/m_D$ . Thus, only potential pions contribute to the order we are working at.

where<sup>13</sup>

$$S^{(IV)}(x, y) \equiv \lim_{\lambda_n \rightarrow \infty} \left[ \sum_{\mathbf{n}, \mathbf{n}'}^{|\mathbf{n}|, |\mathbf{n}'| < \lambda_n} \frac{1}{n^2 - x} \frac{1}{n'^2 - x} \frac{1}{|\mathbf{n} + \mathbf{n}'|^2 - y} - 2\pi^4 \left( \log \left( \frac{\lambda_n^2}{|y|} \right) - 1 \right) \right]. \quad (3.55)$$

Due to the coupling between different angular momenta, the finite volume amplitudes  $\mathcal{A}_{0(\text{II})ij}^L$  and  $\mathcal{A}_{0(\text{III})ij}^L$  do not factorize into a scalar amplitude and a function of the incoming and outgoing  $D^{*0}$  mesons' spins, in particular,  $\mathcal{A}_{0(\text{II}),(\text{III})ij}^L \neq \delta_{ij} \mathcal{A}_{0(\text{II}),(\text{III})}^L$ . This property implies a non-trivial dependence of the coefficients  $s_0$  and  $s_1$  in Eq. (3.27) on the polarization vectors  $\boldsymbol{\epsilon}_i$  and  $\boldsymbol{\epsilon}_j^*$  and hence, of the NLO shift for the field strength renormalization constant,  $\Delta Z^{\text{NLO}}$ . However, since the amplitudes  $\mathcal{A}_{0(\text{I})ij}^L$ ,  $\mathcal{A}_{0(\text{IV})ij}^L$  and  $\mathcal{A}_{0(\text{V})ij}^L$  do factorize<sup>14</sup> and therefore  $s_2$  as well, it is sufficient to consider the scalar amplitudes  $\mathcal{A}_{0(\text{I})}^L$ ,  $\mathcal{A}_{0(\text{IV})}^L$  and  $\mathcal{A}_{0(\text{V})}^L$  to calculate the shift for the binding energy.

The dependence of the loop integrals on the PDS renormalization scale  $\Lambda$  is the same as for the infinite volume. Accordingly, the NLO coupling constants coincide with the ones given in Eqs. (3.21a) and (3.21b) up to finite volume corrections to scales large compared to  $Q$  (for example, to the quantities  $m_{D^*}$  or  $f$ ). Again, to obtain error bands, we vary the coupling constants within their natural ranges. For the binding energy we employ the results of Sec. 3.2.6. The quantities  $Z_{-1}$  and  $s_2$  have to be reevaluated in the box. We find for the residue

$$(Z_{-1}^L)^{-1} = \left[ i \frac{\partial}{\partial E} \frac{1}{i \mathcal{A}_{-1}^L} \right]_{E=E_{X,\text{LO}}^L} = \frac{-\left(\frac{LM_{DD^*}^L}{2\pi}\right)^2}{2\pi} \frac{2}{\pi L} S' \left( -\left(\frac{L\gamma^L}{2\pi}\right)^2 \right), \quad (3.56)$$

where  $E_{X,\text{LO}}^L \equiv (\gamma^L)^2 / 2M_{DD^*}^L$  and

$$S'(x) \equiv \partial_x S(x) = \sum_{\mathbf{n}} \frac{1}{(n^2 - x)^2}. \quad (3.57)$$

For the coefficient  $s_2^L$  we obtain, already inserting expressions (3.21a) and (3.21b) for the coupling constants,

$$s_2^L = c_2 (\gamma^L)^2 + \frac{g^2}{6(f^L)^2} \left( \frac{M_{DD^*}^L}{2\pi} \right)^2 (\mu^L)^2 \left( -d_2 + \log \left( \frac{\mu^{L,\text{ph}}}{|\mu^L|} \right) + \frac{1}{2} + \frac{1}{4\pi^4} S^{(IV)} \left( -\left(\frac{L\gamma^L}{2\pi}\right)^2, \left(\frac{L\mu^L}{2\pi}\right)^2 \right) \right). \quad (3.58)$$

### 3.3.4 Validity range of XEFT in the box

In the infinite volume, the range of applicability of XEFT is constrained by two demands. On the one hand, we require that pions can be included perturbatively, determining the boundary for large pion masses. On the other hand, treating pions non-relativistically settles the low- $m_\pi$  boundary. In summary, we have in the infinite volume  $0.98(m_\pi^{\text{ph}})^2 \lesssim m_\pi^2 \lesssim 2(m_\pi^{\text{ph}})^2$  [115].

However, for three particles in the finite volume, singularities occur as soon as three-body propagators can go on-shell, a behavior which was already investigated, e.g., in Refs. [60] and [61]. In XEFT, this manifests in the last term of Eq. (3.58). For pion masses smaller than the hyperfine splitting, where the  $D^{*0} \rightarrow D^0 \pi$  decay channel is open,  $(\mu^L)^2 S^{(IV)}$  possesses singularities for values of  $(L\mu^L/2\pi)^2$  being the absolute value of an integer vector squared, greater than or equal to one. So for certain values of  $m_\pi$  and  $L$ , the perturbative treatment fails clearly. Since the  $D^{*0} \rightarrow D^0 \pi$  decay proceeds via a  $P$ -wave interaction,  $s_2^L$  is finite for  $(L\mu^L/2\pi)^2 = 0$ . To obtain a region of validity for XEFT in dependence on the volume and the pion mass, we take a look at the quantity

$$\epsilon_\pi^L \equiv \frac{g^2 M_{DD^*}^L}{4\pi(f^L)^2} \left| \frac{1}{\pi L} S \left( \left(\frac{L\mu^L}{2\pi}\right)^2 \right) + \frac{1}{\pi L} \left( \frac{2\pi}{L\mu^L} \right)^2 \right|, \quad (3.59)$$

which explicitly accounts for the singularities of  $(\mu^L)^2 S^{(IV)}$  for  $m_\pi < \Delta$  and approaches the infinite volume XEFT expansion parameter for  $m_\pi > \Delta$  and  $L \rightarrow \infty$ . It is further motivated by the additional (finite volume) loop integral occurring, when comparing the TPE to the OPE and possesses the same pole structure. The second term in Eq. (3.59) ensures that  $\epsilon_\pi^L$  is finite for  $\mu^L \rightarrow 0$ . A density plot is shown in Fig. 3.15. We restrict our analysis on regions where  $\epsilon_\pi^L < 0.15$  such that it is small enough to compensate for unnaturally large NNLO coefficients of similar size as in KSW. For physical pion mass it follows that a perturbative treatment of pions is justified for  $5 \text{ fm} \lesssim L \lesssim 20 \text{ fm}$ . We point out that the NLO parameters  $c_2$  and  $d_2$  coincide in the finite and infinite volume and, once determined from lattice calculations, one can utilize the infinite volume formulas to extrapolate to  $L \rightarrow \infty$ .

<sup>13</sup> In the expression for  $S^{(IV)}$  given here, we drop all terms suppressed with powers of  $1/\lambda_n$ . For numerical evaluations, however, it often is advantageous to keep those terms to improve numerical convergence.

<sup>14</sup> The amplitudes  $\mathcal{A}_{0(\text{I})ij}^L$ ,  $\mathcal{A}_{0(\text{IV})ij}^L$  and  $\mathcal{A}_{0(\text{V})ij}^L$  factorize since they contain the momentum- and angular-independent LO amplitude  $\mathcal{A}_{-1}^L$  on both sides and thus are momentum and angular independent by themselves.

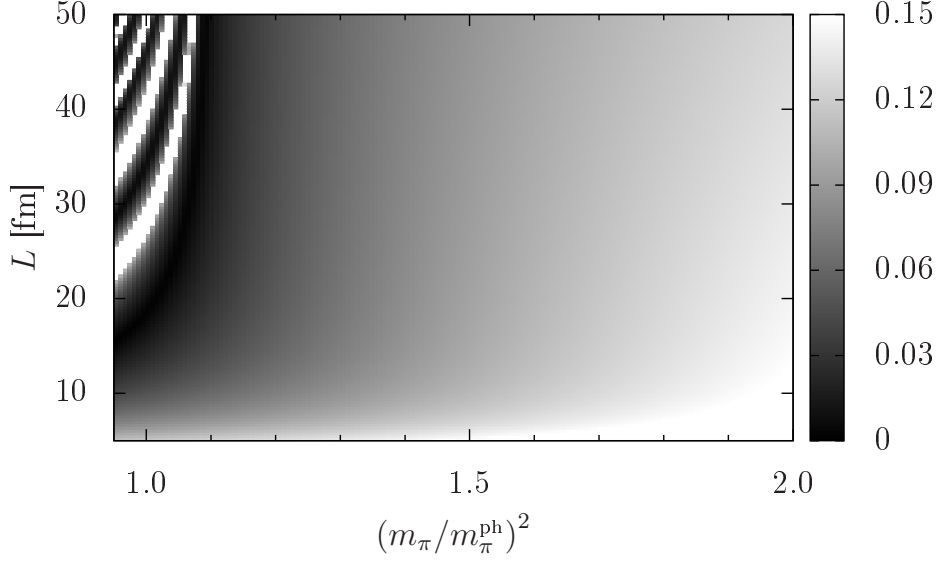


**Figure 3.15.:** Density plot for the expansion parameter  $\epsilon_\pi^L$ . White regions belong to values of  $L$  and  $m_\pi$  where the perturbative inclusion of pions breaks down. For pion masses close to the physical value, there are several narrow bands of hyperbolic shape due to on-shell three-body propagators.

### 3.3.5 Effective range expansion for large $m_\pi$

The preceding analysis is valid for all pion masses. Now we focus on the region where the  $D^{*0}$  is stable, i.e. for  $m_\pi > \Delta$ . It is then possible to apply the effective range expansion for the infinite volume amplitude, analytically continue it to negative energies and apply the procedure established in Ref. [59]. We use the expressions for the  $S$ -wave scattering length and effective range from Eqs. (3.25) and (3.26) for pion masses greater than the hyperfine splitting

$$\frac{1}{a_s} = \gamma - \frac{g^2}{6f^2} \frac{M_{DD^*}}{2\pi} \left( (\gamma - |\mu|)^2 - |\mu|^2 \left( d_2 + \frac{1}{2} - \log \left( \frac{\mu^{\text{ph}}}{|\mu|} \right) \right) \right), \quad (3.60a)$$

$$r_s = r_0 \left[ 1 - \frac{2}{\gamma} \frac{g^2}{6f^2} \frac{M_{DD^*}}{2\pi} \left( (\gamma - |\mu|)^2 - |\mu|^2 \left( d_2 + \frac{1}{2} - \log \left( \frac{\mu^{\text{ph}}}{|\mu|} \right) \right) \right) \right] - \frac{g^2}{6f^2} \frac{M_{DD^*}}{2\pi} 2 \left( 1 - \frac{8}{3} \frac{\gamma}{|\mu|} + 2 \frac{\gamma^2}{|\mu|^2} \right). \quad (3.60b)$$

Let us briefly consider an effective theory in the infinite volume, where pion interactions are not included explicitly but via modified LO and NLO coupling constants. It holds a similar renormalization condition like in Eq. (3.21a) but with  $r_0$  replaced by  $r_s$  in Eq. (3.60b). The criteria for a bound state follows from Eq. (3.23) and reads, applying Eq. (3.23) and neglecting higher-order shape parameters,

$$\frac{1}{a_s} + \frac{1}{2} r_s \gamma_*^2 - \gamma_* = 0, \quad (3.61)$$

where  $\gamma_*$  is the binding momentum incorporating NLO contributions. For the binding energy up to NLO follows (cf. Sec. 2.2)

$$\begin{aligned} E_{X,\text{NLO}}^\infty &= \frac{1}{2M_{DD^*}} \frac{2}{r_s^2} \left( 1 - \frac{r_s}{a_s} - \sqrt{1 - 2 \frac{r_s}{a_s}} \right) \\ &= \frac{1}{2M_{DD^*} a_s^2} \left( 1 + \frac{r_s}{a_s} + \mathcal{O} \left( \frac{r_s}{a_s} \right)^2 \right). \end{aligned} \quad (3.62)$$

Using the same effective theory but now accounting for NLO corrections by applying the strategy described in Eqs. (3.27) through (3.32), we obtain the same result as in the second line of Eq. (3.62) except that no terms of order  $r_s^2/a_s^2$  occur. Hence, as long as the  $S$ -wave scattering length is significantly larger than the  $S$ -wave effective range, both methods deliver consistent results.

Using a pionless effective field theory in the finite volume, the amplitude can be calculated in analogy to Sec. 3.3.1 and the result is given by Eq. (3.45) with  $\gamma$  replaced by  $-p \cot \delta_s(p)$  (cf. Eq. (3.23)). The criteria for a bound state looks similar to Eqs. (3.47) and (3.61) (cf. Ref. [59])

$$\frac{1}{a_s} + \frac{1}{2} r_s (\gamma_*^L)^2 + \frac{1}{\pi L} S \left( - \left( \frac{L \gamma_*^L}{2\pi} \right)^2 \right) = 0. \quad (3.63)$$

Here,  $\gamma_*^L$  is the finite volume binding momentum including NLO corrections. Equation (3.63) approaches Eq. (3.61) in the limit  $L \rightarrow \infty$ . As for the infinite volume, we expect that the results from the two different methods agree as long as  $a_s \gg r_s$ .

### 3.3.6 Results

To determine the finite volume and quark mass dependence of the binding energy, we first consider the extrapolations for the pion decay constant, the  $D$  meson axial coupling constant and the  $D^0$  and  $D^{*0}$  mesons' masses, respectively. The  $D$  meson axial coupling constant does not receive any corrections in the finite volume and we can use expression (3.38) for all volumes. For the pion decay constant we employ the results given in Ref. [132] obtained from chiral perturbation theory to one loop

$$f^L = f \left[ 1 - \frac{m_\pi}{2\pi f^{(0)2}} \frac{1}{\pi L} \sum_{\mathbf{n}}^{|n| \geq 1} \frac{K_1(|\mathbf{n}| m_\pi L)}{|\mathbf{n}|} \right], \quad (3.64)$$

with  $K_1$  being the modified Bessel function of second kind and  $f$  being the chiral extrapolation of the pion decay constant in the infinite volume in Eq. (3.37). The chiral and finite volume extrapolations for the  $D^0$  and  $D^{*0}$  mesons' masses can be summarized as

$$m_D^L = m_D = m_D^{\text{ph}} + \frac{h_1}{m_D^{\text{ph}}} (m_\pi^2 - (m_\pi^{\text{ph}})^2), \quad (3.65)$$

$$m_{D^*}^L = m_{D^*}^{\text{ph}} + \frac{h_1}{m_{D^*}^{\text{ph}}} (m_\pi^2 - (m_\pi^{\text{ph}})^2) + \Delta_{m_{D^*}}^L, \quad (3.66)$$

with  $h_1 = 0.42$  [130]. In the finite volume, the mass of the  $D^{*0}$  obtains a shift,  $\Delta_{m_{D^*}}^L$ , given in Eq. (3.49). In the limit  $L \rightarrow \infty$ ,  $\Delta_{m_{D^*}}^L$  from Eq. (3.49) has to be inserted instead.

In Fig. 3.16, we plot the dependence of the binding energy on the side length of the box,  $L$ , to compare the two approaches described in Sec. 3.3. The pion masses are fixed at values of  $m_\pi = 145$  MeV and  $m_\pi = 160$  MeV, respectively.

The infinite volume results are shown by solid lines. For both, the infinite and the finite volume results, the upper bounds corresponds to values of the NLO parameters of  $d_2 = 1$  and  $r_0 = 0.01/\text{MeV}$  and the lower bounds to  $d_2 = -1$  and  $r_0 = 0$ .

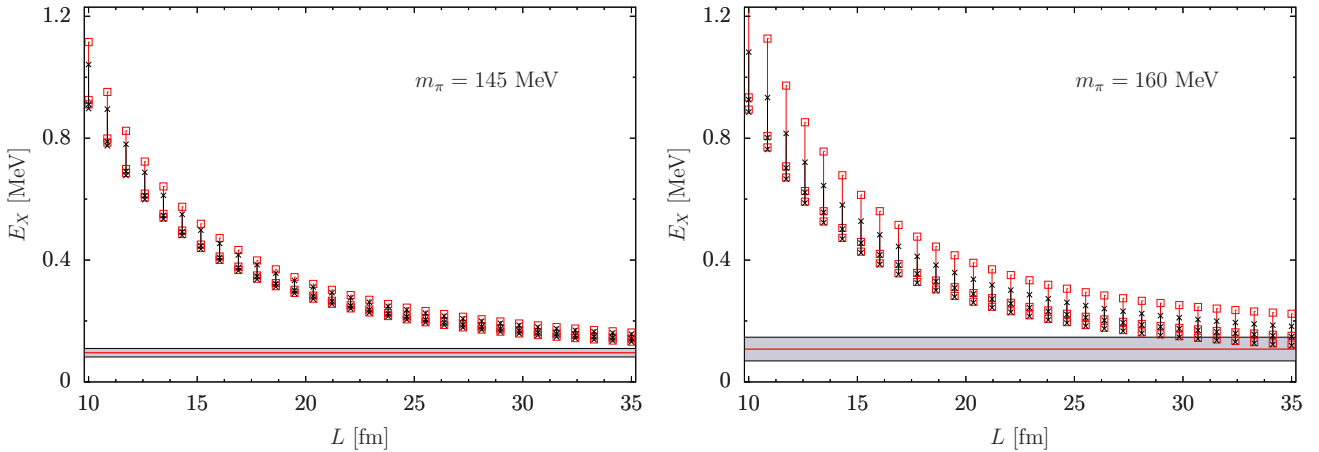


**Figure 3.16.:** Comparison of the two methods to obtain the binding energy to NLO described in Secs. 3.2.6 and 3.3. We keep the pion mass fixed at values of  $m_\pi = 145$  MeV (left) and  $m_\pi = 160$  MeV (right). The binding energy in the infinite volume is represented by solid lines. The band is obtained by varying the NLO parameters  $d_2$  and  $r_0$  within their natural ranges. The thick, central curve belongs to  $d_2 = 0$  and  $r_0 = 0$ . The finite volume results correspond to crosses for the explicit XEFT calculations and to empty squares for the results obtained from an effective range expansion. The central crosses and squares belong to  $d_2 = 0$  and  $r_0 = 0$ .

Whereas the lower bounds and central values coincide well using the two different strategies and deviations are clearly smaller than the NLO shifts, there is some discrepancy for the upper bounds. The difference can be understood from the considerations in Sec. 3.3.5. Results are consistent as long as the  $S$ -wave scattering length is much larger than the

S-wave effective range. For  $d_2 = 1$  and  $r_0 = 0.01/\text{MeV}$ , however,  $a_s$  and  $r_s$  are similar in size and the error induced by approximating the root in Eq. (3.62) is  $\sim 5\% - 10\%$ . This error is in the order of the NLO corrections and explains the deviation for the upper bounds in Fig. 3.16. We point out that effective range and scattering length are of comparable magnitude for a very limited range of the NLO parameters only.

So far we have looked at pion masses above the hyperfine splitting of the  $D$  mesons. We now consider the region where the  $D^{*0}$  can decay into  $D^0\pi$ . The binding energy in a finite volume for physical pion mass is depicted in Fig. 3.17. We plot for box lengths between 5 and 20 fm where the expansion parameter in Eq. (3.59) is clearly smaller than 0.15 as can be read off from Fig. 3.15.

The result for  $d_2 = 0$  and  $r_0 = 0$  is not shown as it almost coincides with the lower bound. This coincidence can be understood by noting that the only difference of the central values and the lower bound is the value of  $d_2$ . Since  $\mu$  is rather insensitive to effects of the finite volume, the NLO contact interaction with vertex  $-iD_2\mu^2$  barely differs in a finite box. The renormalization to  $E_X = 0.1$  MeV at physical pion mass then explains the similarity of the outcome for  $d_2 = 0$  and  $d_2 = -1$ . The renormalization condition further explains why there is no error band for the binding energy in the infinite volume for  $m_\pi = 135$  MeV. The contribution of the NLO contact interaction with coupling constant  $C_2$ , on the other hand, is proportional to  $(\gamma^L)^2$  and since finite volume corrections to  $\gamma$  are significantly greater than those to  $\mu$ , the error band for physical pion mass is predominantly determined by  $r_0$ . Instead of the results with  $d_2 = 0$  and  $r_0 = 0$ , we show the LO result, i.e. the outcome if neither pion nor NLO contact interactions are included.

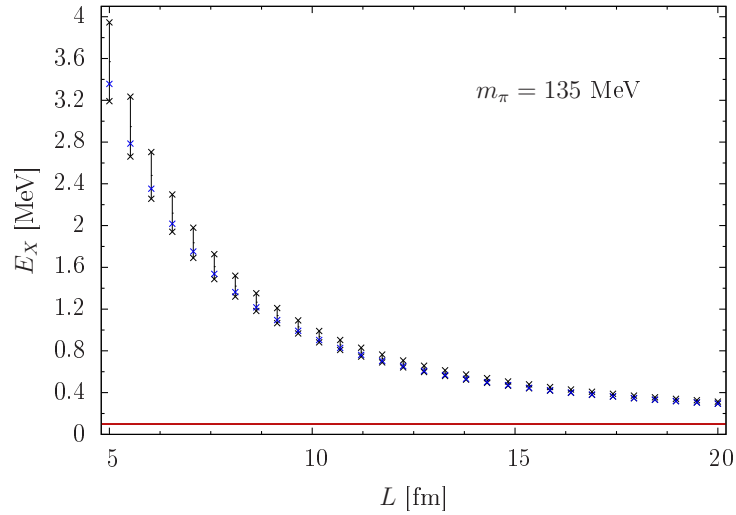


**Figure 3.17.:** Volume dependence of the binding energy for physical quark masses. The notation is the same as in Fig. 3.16. The LO result belongs to the blue central crosses. The effective range expansion breaks down for pion masses below 142 MeV and hence, effective range results are not included. Furthermore, we renormalized the binding energy in the infinite volume to 0.1 MeV and thus, the infinite volume result is represented by a single line.

The binding energy is, as expected, increasing for decreasing box size and approaches the infinite volume value for large volumes. However, even at  $L = 20$  fm, finite volume contributions are still  $\sim 100\%$ . To obtain useful results from simulations performed on such lattices a precise understanding of finite volume corrections is essential. The  $X$  is significantly deeper bound for small box lengths and finite volume corrections yield the dominating contribution to the binding energy. The total of pion and NLO contact interactions can be both, repulsive and attractive, depending on the parameters  $d_2$  and  $r_0$ .

Besides the demand that pions can be included perturbatively, it is required that the binding momentum does not exceed the scales integrated out, which are at the order of the pion mass. For a volume with  $L \gtrsim 5$  fm,  $E_X \lesssim 4$  MeV corresponding to binding momentum  $\lesssim 90$  MeV, we expect that XEFT describes the dynamics of the  $X$  properly.

The chiral extrapolations for fixed box size of  $L = 10$  fm,  $L = 15$  fm and  $L = \infty$  are shown in Fig. 3.18. The infinite volume results are again depicted by solid lines. The NLO parameters for the bounds coincide with the ones for Fig. 3.16. As in the infinite volume, the binding energy in a finite box shows only a moderate sensitivity to the light quark masses. The central values of the finite volume belong to  $d_2 = 0$  and  $r_0 = 0$  and approach the lower bound for physical pion mass for reasons explained above.

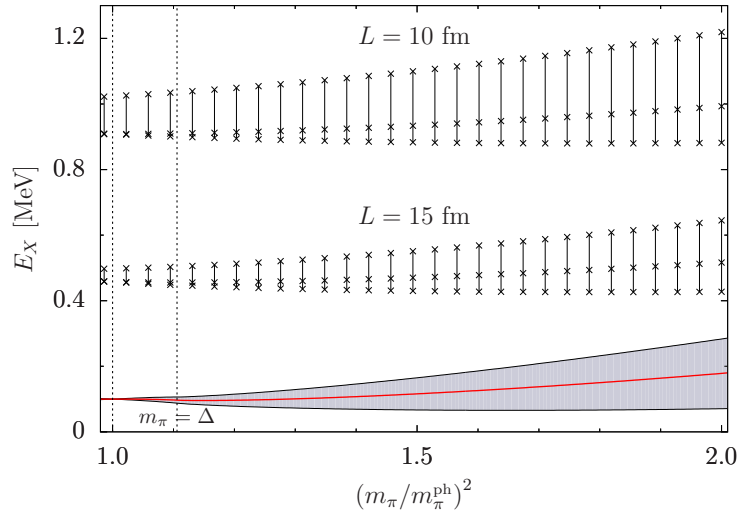


**Figure 3.18.:** Quark mass dependence of the binding energy for various box lengths. From top to bottom, box lengths of  $L = 10$  fm,  $L = 15$  fm and  $L = \infty$  are considered. The notation is the same as in Fig. 3.16. Again, no effective range results are included since these are not valid over the whole range of the quark masses.

---

## 4 Dipole-dipole interactions

---

In the chapter at hand, we present our results for systems of two and three bosonic dipoles. We refer to electric dipoles, but our results are directly applicable to systems of magnetic dipoles as well. We begin with the two-dipole system and introduce the dipole-dipole-interaction potential. We discuss phenomenological aspects and introduce the momentum space representation. We further project on partial waves in a cylindrical as well as a spherical coordinate system. Details about the numerical implementation to solve the Lippmann-Schwinger equation can be found in App. B.3. At the end of the first part of this chapter, we present our results for two bosonic dipoles with a focus on universal relations and the renormalization of the system. Subsequently, we proceed with the three-dipole system. The bound-state Faddeev equation is introduced and projected on partial waves in a cylindrical basis. We solve it numerically in a next step and discuss implications for the three-dipole system, again attaching importance to the renormalization. Moreover, a reformulation of the Faddeev equation is introduced, which is numerically advantageous. First investigations, considering the three-body bound-state spectrum for the  $1/r^3$  potential are discussed.

Parts of this chapter were already presented in my master's thesis "Bound states of two and three bosonic dipoles" [133]. There, a discussion of the phenomenology can be found. Further, partial wave projections were already performed. However, here, we work with a representation of the partial wave amplitudes specifically adapted to a system of aligned dipoles. Moreover, in my master's thesis, derivations of the Lippmann-Schwinger and Faddeev equation were given and first findings for the spectra of two and three dipoles were presented. An analysis for the complete spectra, in particular using spherical coordinates, was still pending.

---

### 4.1 The two-dipole system

---

We begin with the two-dipole system. Fundamental properties and relations for the interaction between two bosonic dipoles are presented. We elaborate on the Fourier transform of the potential and its partial wave projections on different basis functions of the underlying coordinate systems. Moreover, detailed results for various sets of quantum numbers and dipole tunings are given.

---

#### 4.1.1 An effective theory for the dipole-dipole system

---

In order to describe the two-dipole system at low energies, we employ a non-relativistic, effective theory. The emerging equation is the Lippmann-Schwinger equation. It reads in momentum space for two identical bosons with mass  $M$

$$T(E, \ell, \ell') = -V(\ell, \ell') + \int d^3k V(\ell, \mathbf{k}) \frac{1}{E - k^2/M + i\epsilon} T(E, \mathbf{k}, \ell'), \quad (4.1)$$

with in- and outgoing relative momenta  $\ell$  and  $\ell'$  in the center of momentum frame. The potential is denoted by  $V$  and contains long- as well as short-range degrees of freedom as explained below. The LS equation can be solved numerically to obtain the scattering amplitude  $T$ . The scattering amplitude contains information about scattering observables, such as binding energies and scattering lengths. We remark that we use a different normalization than before.<sup>1</sup> It is beneficial for the numerical implementation since less factors of, e.g.,  $\pi$  occur. However, when calculating observables like the scattering length, the normalization has to be taken into account.

---

#### 4.1.2 Dipole-dipole interaction potential

---

We want to investigate two identical, point-like, aligned, bosonic dipoles. The potential can be obtained starting from the Coulomb potential for two particles with charges of opposite sign,  $\pm q$ , separated by  $\delta$ . The multipole expansion [109] can then be employed to isolate the dipolar contribution. We examine a system of ideal dipoles, i.e. the limit  $|\delta| \rightarrow 0$ ,  $q \rightarrow \infty$  while keeping the dipole moment  $q \cdot \delta \equiv \mathbf{d}$  constant. All multipole contributions higher than the dipolar vanish.

---

<sup>1</sup> In, for example, the LS equation, no factors of  $(2\pi)^3$  occur.

Placing a second ideal dipole in the potential of the first one, we obtain the dipole-dipole potential in coordinate space for dipoles with the dipole separation  $\mathbf{r}$  and dipole moments  $\mathbf{d}_1$  and  $\mathbf{d}_2$ <sup>2</sup>

$$U_{dd}(\mathbf{r}) = \frac{\mathbf{d}_1 \cdot \mathbf{d}_2 r^2 - 3(\mathbf{d}_1 \cdot \mathbf{r})(\mathbf{d}_2 \cdot \mathbf{r})}{r^5}. \quad (4.2)$$

An outstanding feature of the potential of two dipoles is its tunability. Following Ref. [17], it should be possible to tune the interaction by applying external electric fields. First, a static, homogeneous electric field,  $\mathbf{E}_z$ , is applied. The dipoles align parallel and since we regard identical particles, the dipole moments coincide,  $\mathbf{d}_1 = \mathbf{d}_2 = \mathbf{d}$ . We choose the  $z$ -axis parallel to the dipole moment. A second, perpendicular field,  $\mathbf{E}_{xy}$ , rotating in the  $xy$ -plane is applied to tune the potential. The dipole moments align parallel to the sum of the external fields and become time dependent. Since we attempt to establish a low-energy theory, it is possible to choose the rotation frequency large compared to the average collision frequency.<sup>3</sup> It follows that the time between two interactions is large compared to the time of a single rotation. It is therefore justified to average the potential over time to obtain the effective and tuned interaction potential [17]

$$\langle U_{dd}^{\text{tuned}}(\mathbf{r}, t) \rangle_t = U_{dd}(\mathbf{r})\alpha(\varphi), \quad (4.3)$$

with the tuning parameter  $\alpha(\varphi)$  given as

$$\alpha(\varphi) \equiv (3 \cos^2(\varphi) - 1)/2 \in [-\frac{1}{2}, 1], \quad \tan(\varphi) = E_{xy}/E_z. \quad (4.4)$$

The tuning parameter depends on the ratio of the external field strengths  $\tan(\varphi)$  only. It can take positive and negative values and vanishes for  $\varphi = \arccos(1/\sqrt{3})$ . For antiparallel dipoles, the potential (4.2) has the opposite sign. Therefore, tuning the external fields such that  $\alpha(\varphi) < 0$  is equivalent to antiparallel dipole scattering. We thus also refer to parallel dipoles for  $\alpha(\varphi) > 0$  and to antiparallel dipoles for  $\alpha(\varphi) < 0$ .

Since we work in momentum space we need the Fourier transform of Eq. (4.3). A detailed derivation is given in App. B.1, where we also elaborate on the Gaussian regulator introduced later on. The Fourier transformed potential reads

$$V_{dd}(\mathbf{q}) = D \frac{-q^2 + 3(\hat{\mathbf{e}}_z \cdot \mathbf{q})^2}{q^2} = D(-1 + 3 \cos^2(\theta_q)) = D \sqrt{\frac{16\pi}{5}} Y_{20}(\Omega_q), \quad (4.5)$$

with the momentum transfer  $\mathbf{q} \equiv \ell - \ell'$ . The angle between  $\mathbf{q}$  and the unit vector in  $z$ -direction,  $\hat{\mathbf{e}}_z$ , is denoted by  $\theta_q$ . Moreover,  $\Omega_q = (\theta_q, \phi_q)$ , with the azimuthal angle  $\phi_q$ . We further adopted the shorthand notation  $D \equiv 4\pi\alpha(\varphi)d^2/3$ .

In addition to the long-range interaction given by the dipole-dipole potential, a short-range interaction is required. To parametrize the short-distance degrees of freedom we use contact interactions. It turns out that a single, isotropic  $S$ -wave interaction is insufficient in order to fully renormalize the dipole-dipole system. Thus, we employ a series of short-range interactions, also including anisotropic operators

$$V_s(\ell, \ell') \equiv \sum_{l,m} g_{lm} Y_{lm}(\Omega_\ell) Y_{lm}^*(\Omega_{\ell'}), \quad (4.6)$$

with  $\Omega_\ell = (\theta_\ell, \phi_\ell)$  ( $\Omega_{\ell'} = (\theta_{\ell'}, \phi_{\ell'})$ ) being the angular coordinates of  $\ell$  ( $\ell'$ ) and coupling constants  $g_{lm}$ . The sets over which the  $l$  and  $m$  are summed are determined depending on the quantum numbers of the considered states. Here, cylindrical symmetry was taken into account by constraining the dependence on the azimuthal angles of the in- and outgoing relative momenta. Moreover, the short-distance operators conserve orbital angular momentum. The interaction further is Galilean invariant and separable. Also, the partial waves of the short-range potential can be read off immediately.

We further introduce a Gaussian cutoff with cutoff scale  $\lambda$ , in order to regularize UV divergences emerging in loop contributions to the transition matrix. The Gaussian regulator has the advantage of being smooth and monotonic in momentum and coordinate space and coincides in cylindrical and spherical coordinates. In summary, the potential  $V$  reads

$$V(\ell, \ell') = (V_s(\ell, \ell') + V_{dd}(\ell, \ell')) e^{-(\ell^2 + \ell'^2)/\lambda^2}. \quad (4.7)$$

Subsequently, the short-range potential is tuned by means of the coupling constants in order to obtain cutoff independent observables.

<sup>2</sup> We remark that when performing integrations over the the electric field of a dipole or the dipole-dipole potential, an additional delta distribution must be included. For a detailed discussion we refer to the literature [109, 83]. See also App. B.1 for the precise expression. For finite  $\mathbf{r}$ , however, the delta distribution does not contribute and the potential is given by Eq. (4.2).

<sup>3</sup> The rotation frequency is limited by the demand that no inner degrees of freedom of the dipoles get excited.

The cutoff of high-momentum contributions corresponds to a regularization in the short-range regime in coordinate space. Short-distance degrees of freedom are integrated out by introducing a regulator which tends to zero for  $r \rightarrow 0$  and to one for  $r \rightarrow \infty$ , with  $r$  being the relative distance between the dipoles. Physical observables eventually must not depend on the precise form of the regulator and the choice is in general arbitrary. In Ref. [134], the authors regularized short-distance physics by introducing an infinite box potential with radius  $r_c$ , fixing the boundary conditions of the wave function. The radius  $r_c$  then corresponds to an inverse momentum cutoff. However, results still depend on the radius  $r_c$ . To ensure that observables are independent of the regulator, one could replace the infinite with a finite box potential. The height of the potential represents an additional degree of freedom corresponding to a coupling constant and can be used to tune the isotropic proportion of the potential to reproduce a given low-energy observable.

To determine the dimension of quantities, we exploit that the dimension of the potential is  $[V] = [D]$  (cf. Eq. (4.5)) and so is the dimension of the scattering amplitude. Hence, we can rewrite  $V = D\tilde{V}$  and further,  $T = D\tilde{T}$ . The LS equation for the dimensionless transition amplitude  $\tilde{T}$  reads

$$\tilde{T}(E, \underline{\ell}, \underline{\ell}') = -\tilde{V}(\underline{\ell}, \underline{\ell}') + MD \int d^3k \tilde{V}(\underline{\ell}, \mathbf{k}) \frac{1}{ME - k^2 + i\epsilon} \tilde{T}(E, \mathbf{k}, \underline{\ell}'). \quad (4.8)$$

The integral has the dimension of momentum and we can read off  $\underline{\ell} = \tilde{\ell}/MD$  and  $E = \tilde{E}/M^3D^2$ , where all quantities with a tilde are now dimensionless. Rewriting Eq. (4.8) using  $\tilde{\ell}$  and so on, it does not depend on any dimensionful entity, i.e. neither on  $M$  nor on  $D$ . It is sufficient to solve the dimensionless LS equation and multiply observables with appropriate powers of  $MD$  and  $M^3D^2$  afterwards in order to obtain meaningful results.

### 4.1.3 Partial wave expansions

When rewriting the potential in cylindrical or spherical coordinates, the cylindrical symmetry implies a dependence on the difference of the azimuthal angles of the in- and outgoing relative momenta, only. It is thus eligible to expand in cylindrical waves depending on the azimuthal angle of  $\underline{\ell}$  and  $\underline{\ell}'$ ,  $\phi_\ell$  and  $\phi_{\ell'}$ , respectively. The LS equation then becomes a system of two-dimensional integral equation. The expansion significantly reduces the numerical costs and improves computational performance. To further decrease the LS equation to a one-dimensional (but coupled) integral equation, it is useful to further expand in the polar angles  $\theta_\ell$  and  $\theta_{\ell'}$ . Also, spherical partial waves provide a more profound physical understanding. As shown below, the LS equation completely decouples with respect to the projection of orbital angular momentum,  $m$ , and parity,  $P$ . Therefore, we use parity,  $P$ , and projection,  $m$ , as quantum numbers in order to label states. Details of the derivations for the partial wave projections are given in App. B.2.1.

The cylindrical partial wave expansion can be obtained using the ansatz

$$V(\mathbf{q}) = \sum_{m=-\infty}^{\infty} v_m(\underline{\ell}, \underline{\ell}') y_m(\phi_\ell) y_m^*(\phi_{\ell'}), \quad (4.9)$$

with orthonormal cylindrical basis functions

$$y_m(\phi) \equiv e^{im\phi} / \sqrt{2\pi}. \quad (4.10)$$

It is then possible to act with projection operators on the potential to extract the partial waves

$$v_m^s(\underline{\ell}, \underline{\ell}') = \left[ v_m^s(\underline{\ell}, \underline{\ell}') + 2\pi D \left( -\delta_{m0} + \frac{3c_2(\underline{\ell}, \underline{\ell}')}{\sqrt{1 - c_1^2(\underline{\ell}, \underline{\ell}')}} \frac{1}{c_1^{|m|}(\underline{\ell}, \underline{\ell}')} \left(1 - \sqrt{1 - c_1^2(\underline{\ell}, \underline{\ell}')} \right)^{|m|} \right) \right] e^{-(\ell^2 + \ell'^2)/\lambda^2}. \quad (4.11)$$

We defined

$$c_1(\underline{\ell}, \underline{\ell}') \equiv \frac{2\ell_\rho \ell'_\rho}{(\ell_z - \ell'_z)^2 + \ell_\rho^2 + \ell'_\rho^2}, \quad c_2(\underline{\ell}, \underline{\ell}') \equiv \frac{(\ell_z - \ell'_z)^2}{(\ell_z - \ell'_z)^2 + \ell_\rho^2 + \ell'_\rho^2}, \quad (4.12)$$

depending on the cylindrical two-momentum  $\underline{\ell} \equiv (\ell_\rho, \ell_z)$  ( $\underline{\ell}' \equiv (\ell'_\rho, \ell'_z)$ ) with the radial- and z-components  $\ell_\rho$  and  $\ell_z$  ( $\ell'_\rho$  and  $\ell'_z$ ) of the relative ingoing (and outgoing) momentum  $\underline{\ell}$  ( $\underline{\ell}'$ ). Using that  $\cos(\theta_\ell) = \ell_z/\ell$  ( $\cos(\theta_{\ell'}) = \ell'_z/\ell'$ ), the partial wave projected short-range potential reads

$$v_m^s(\underline{\ell}, \underline{\ell}') = \sum_l g_{lm} \frac{2l+1}{2} \frac{(l-m)!}{(l+m)!} P_l^m(\ell_z/\ell) P_l^m(\ell'_z/\ell'), \quad (4.13)$$

with the associated Legendre polynomials  $P_l^m$ . The dipole-dipole interaction conserves parity. This property can be seen noting that the potential depends on  $(\ell_z - \ell'_z)^2$  and  $\phi_\ell - \phi_{\ell'}$  only, i.e. is invariant under a simultaneous transformation of  $\ell_z \rightarrow -\ell_z$ ,  $\ell'_z \rightarrow -\ell'_z$ ,  $\phi_\ell \rightarrow \phi_\ell + \pi$ ,  $\phi_{\ell'} \rightarrow \phi_{\ell'} + \pi$ .

For the transition matrix we use a similar approach like for the potential and obtain a system of decoupled, two-dimensional integral equations for the LS equation

$$t_m(E, \underline{\ell}, \underline{\ell}') = -v_m(\underline{\ell}, \underline{\ell}') + \int d^2k v_m(\underline{\ell}, \underline{\mathbf{k}}) \frac{k_\rho}{E - k^2/M + i\epsilon} t_m(E, \underline{\mathbf{k}}, \underline{\ell}'), \quad (4.14)$$

where the integration measure is given as  $d^2k \equiv dk_\rho dk_z$ .

With the transformation property of the associated Legendre polynomials

$$P_l^{-m}(\ell_z/\ell) = (-1)^m \frac{(l-m)!}{(l+m)!} P_l^m(\ell_z/\ell), \quad (4.15)$$

follows that the short-range potential is invariant under  $m \rightarrow -m$ . The same holds true for the long-range part of the potential. Together with Eq. (4.14) we obtain for the transition matrix

$$t_m(\underline{\ell}, \underline{\ell}') = t_{-m}(\underline{\ell}, \underline{\ell}'). \quad (4.16a)$$

It is therefore sufficient to solve the LS equation for  $m \geq 0$ . In analogy to Sec. 2.3.1, we use that the transition matrix separates in the vicinity of a bound state [114] and we can write

$$t_m(E, \underline{\ell}, \underline{\ell}') \equiv \frac{\chi_m(E, \underline{\ell}) \chi_m^\dagger(E, \underline{\ell}')}{E + E_d + i\epsilon}. \quad (4.17)$$

It follows for the bound-state equation

$$\chi_m(E, \underline{\ell}) = \int d^2k v_m(\underline{\ell}, \underline{\mathbf{k}}) \frac{k_\rho}{E - k^2/M + i\epsilon} \chi_m(E, \underline{\mathbf{k}}). \quad (4.18)$$

**The spherical partial wave expansion** can be carried out analogously, using spherical harmonics depending on  $\Omega_\ell$  and  $\Omega_{\ell'}$  as basis functions. The potential takes the form

$$V(\mathbf{q}) = \sum_{l_1, l_2=0}^{\infty} \sum_m v_m^{l_1, l_2}(\ell, \ell') Y_{l_1, m}(\Omega_\ell) Y_{l_2, m}^*(\Omega_{\ell'}), \quad (4.19)$$

where the sum over  $m$  runs from minus to plus  $\min(l_1, l_2)$ . We find for the partial waves

$$v_m^{l_1, l_2}(\ell, \ell') = \left( \delta_{l_1, l_2} g_{l_1 m} + 4\pi D \sqrt{24} \sum_{n=0}^2 \sum_{s=-n}^n \sum_{\sigma=0}^{\infty} \frac{(-1)^{n+s}}{\sqrt{(2n)!(4-2n)!}} \frac{1}{\sqrt{(2l_1+1)(2l_2+1)}} z^{1-n} \alpha_\sigma(z) \right. \\ \left. \times \begin{bmatrix} n & 2-n & 2 \\ s & -s & 0 \end{bmatrix} \begin{bmatrix} n & \sigma & l_1 \\ 0 & 0 & 0 \end{bmatrix} \begin{bmatrix} n & \sigma & l_1 \\ s & m-s & m \end{bmatrix} \begin{bmatrix} 2-n & \sigma & l_2 \\ 0 & 0 & 0 \end{bmatrix} \begin{bmatrix} 2-n & \sigma & l_2 \\ s & m-s & m \end{bmatrix} \right) e^{-(\ell^2 + \ell'^2)/\lambda^2}, \quad (4.20)$$

with [...] being Clebsch-Gordan coefficients and  $\alpha_\sigma$  defined as

$$\alpha_\sigma(z) \equiv \frac{2\sigma+1}{2} \int_{-1}^1 dx \frac{P_\sigma(x)}{\frac{1}{2}(z + \frac{1}{z}) - x}. \quad (4.21)$$

Note that the partial waves do only depend on the ratio of  $\ell$  and  $\ell'$ ,  $z \equiv \ell'/\ell$ , as expected from dimensional analysis. The short-range partial waves can be read off immediately

$$v_s^{m, l_1, l_2} = \delta_{l_1, l_2} g_{l_1 m}. \quad (4.22)$$

Also here, parity conservation of the potential is evident since even and odd partial waves do not couple, i.e.  $v_m^{l, l+2n+1}(\ell, \ell') = 0$ ,  $n \in \mathbb{Z}$ . Furthermore, the potential is non-vanishing only for adjacent even or adjacent odd partial waves, for example,  $v_0^{04}(\ell, \ell') = 0$ . By implication, coupling between non-adjacent states is always indirect and therefore suppressed. Beside, for all  $l_1, l_2$  and  $m$ , only the partial waves  $v_0^{02}(z)$  and  $v_0^{20}(z)$  have a constant proportion

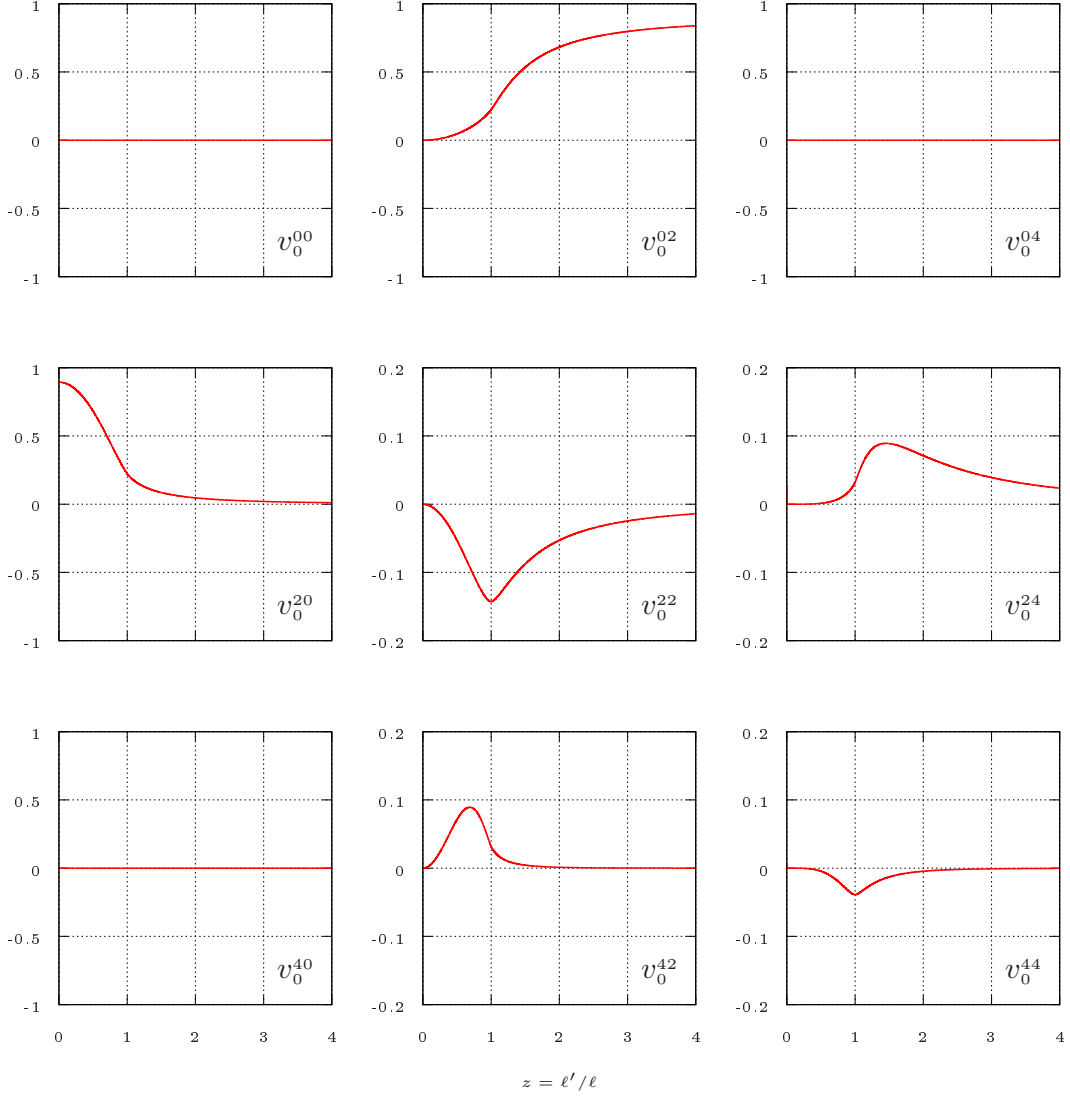


**Figure 4.1.:** Partial wave projections for the long-range dipole-dipole potential for vanishing projection of orbital angular momentum  $m = 0$  and even parity in dependence on the momentum ratio  $z \equiv \ell'/\ell$ . From left to right we increase  $l_1$  and from top to bottom  $l_2$  for  $v_0^{l_1 l_2}(z)$ . Note the different co-domain for higher partial waves.

and thus dominate when considering interactions in the  $m = 0, P = +$  channel. Finally, it can be shown with Eq. (4.20) that

$$v_m^{l_1, l_2}(\ell, \ell') = v_m^{l_2, l_1}(\ell', \ell), \quad (4.23)$$

implying that partial waves with  $l_1 = l_2$  are invariant under  $z \rightarrow 1/z$ .

We show the partial waves for  $m = 0$  and even  $l_1$  and  $l_2$ , i.e. for positive parity, in dependence on the momentum ratio  $z = \ell'/\ell$  in Fig. 4.1. For  $m = 1$  an analogous plot can be found in App. B.2.2 in Fig. B.2. From left to right  $l_1$  and from top to bottom  $l_2$  increases for  $v_m^{l_1 l_2}(\ell, \ell') = v_m^{l_1 l_2}(z)$ . The partial wave  $v_0^{00}(z) = 0$  as can be seen, using the orthogonality for the spherical harmonics and  $Y_{00}(\Omega_\ell)Y_{00}(\Omega'_\ell) = Y_{00}(\Omega_q)/\sqrt{4\pi}$  together with the third equality in Eq. (4.5).

We also expand the transition matrix in spherical harmonics and project the LS equation

$$t_m^{l_1, l_2}(E, \ell, \ell') = -v_m^{l_1, l_2}(\ell, \ell') + \int dk \frac{k^2}{E - k^2/M + i\epsilon} \sum_{n=0}^{\infty} v_m^{l_1, n}(\ell, k) t_m^{n, l_2}(E, k, \ell'). \quad (4.24)$$

So after expanding, one-dimensional integral equations are left to solve, decoupled in  $m$  but with a coupling between channels with different orbital angular momentum,  $l$ . Therefore, a truncation with respect to orbital angular momentum,  $L_{\max}$ , has to be applied. Again, the transition matrix separates when evaluated at a binding energy  $E_d$

$$t_m^{l_1, l_2}(E, \ell, \ell') \equiv \frac{\chi_m^{l_1}(E, \ell) \chi_m^{l_2 \dagger}(E, \ell')}{E + E_d + i\epsilon} \quad (4.25)$$

and we find for the bound-state equation

$$\chi_m^l(E, \ell) = \int dk \frac{k^2}{E - k^2/M + i\epsilon} \sum_{n=0}^{\infty} v_m^{l, n}(\ell, k) \chi_m^n(E, k). \quad (4.26)$$

**The relation between partial waves** in cylindrical and spherical coordinates is derived in App. B.2.3. We obtain for the transition amplitudes (and for the potentials)

$$t_m(E, \underline{\ell}, \underline{\ell}') = \sum_{l_1, l_2=|m|}^{\infty} t_m^{l_1, l_2}(E, \ell, \ell') \xi_m^{l_1, l_2} P_{l_1}^m(\ell_z/\ell) P_{l_2}^m(\ell'_z/\ell'), \quad (4.27a)$$

$$t_m^{l_1, l_2}(E, \ell, \ell') = \xi_m^{l_1, l_2} \int \frac{d\ell_z}{\ell} \int \frac{d\ell'_z}{\ell'} t_m(E, \underline{\ell}, \underline{\ell}') P_{l_1}^m(\ell_z/\ell) P_{l_2}^m(\ell'_z/\ell'), \quad (4.27b)$$

with the geometrical quantity

$$\xi_m^{l_1, l_2} \equiv \sqrt{\frac{(2l_1 + 1)(2l_2 + 1)(l_1 - m)!(l_2 - m)!}{2 \cdot 2 \cdot (l_1 + m)!(l_2 + m)!}}. \quad (4.27c)$$

Relations between both partial wave amplitudes serve as a powerful tool to check results for convergence and consistency. In particular, Eq. (4.27a) can be used to examine whether results obtained in a cylindrical basis are converged with respect to the number of sampling points. Or Eq. (4.27b) to assure that observables in a spherical basis are converged with respect to the amount of partial waves included (see also Sec. B.5).

**The scattering lengths** in different channels of  $l_1$  and  $l_2$  can be calculated as zero energy limit of the (on-shell) spherical scattering amplitude. To extract a particular scattering length from the cylindrical amplitude, relation (4.27b) can be used to project on the corresponding channel. With our normalization holds

$$a_m^{l_1, l_2} = -\pi \lim_{\ell \rightarrow 0} t_m^{l_1, l_2}(E = \ell^2/M, \ell, \ell). \quad (4.28)$$

---

#### 4.1.4 Results

---

Here, we present our results for vanishing projection quantum number and positive parity ( $m = 0, P = +$ ). We consider different tunings of the long-range dipole-dipole interaction, i.e. parallel ( $D > 0$ ) and antiparallel ( $D < 0$ ) dipoles. For non-vanishing angular momentum projections and odd parity unrenormalized spectra can be found in App. B.4. Details on the numerical implementation are given in App. B.3.

---

##### Parallel dipoles ( $D > 0$ )

---

We begin with the unrenormalized spectrum. In order to determine the dependence of the spectrum on the cutoff parameter, we set all coupling constants  $g_{lm} = 0$ , i.e. exclusively include the regularized long-range potential. The result for parallel dipoles with projection  $m = 0$  and positive parity is shown in Fig. 4.2.

We expanded in a spherical basis. The convergence in the number of partial waves included was checked with a comparison to the outcome of a cylindrical algorithm (cf. Sec. B.5). We plot the binding energies as well as the scattering length  $a_0^{00}$ . All dimensionful quantities are given in dipole units, i.e. momenta in  $1/MD$ , lengths in  $MD$  and energies in  $1/M^3D^2$ .

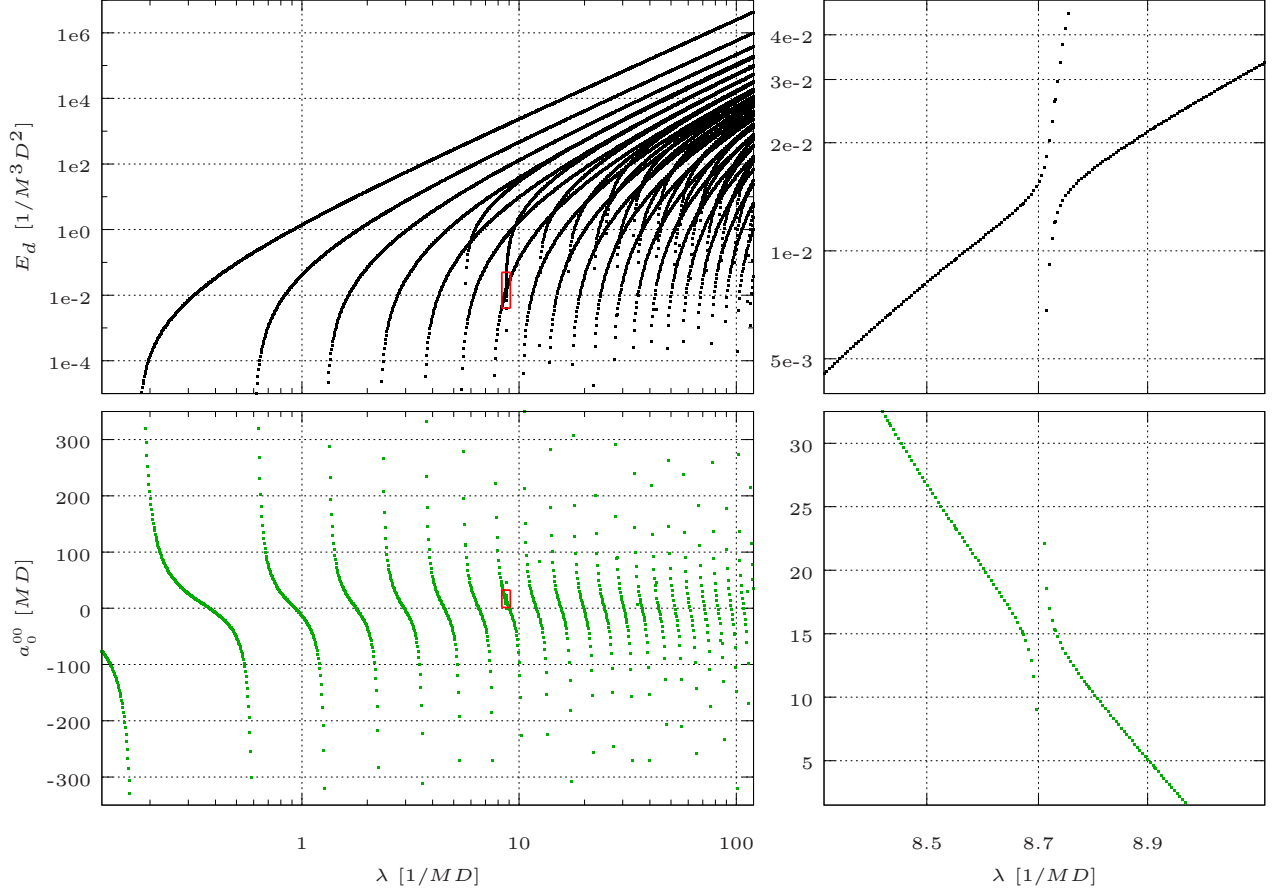


**Figure 4.2.:** Unrenormalized spectrum of bound states and the scattering length  $a_0^{00}$  for  $D > 0$ ,  $m = 0$  and  $P = +$ . The dependence of the binding energies on the cutoff scale  $\lambda$  is shown in the upper left. For cutoff scales  $8.3/MD < \lambda < 9.1/MD$  the avoided level crossing can be seen in the upper right plot. The result for the scattering length  $a_0^{00}$  in dependence on  $\lambda$  is depicted in the lower plots. Again, the plot on the right shows results for restricted values of the cutoff.

For a cutoff below about  $0.2/MD$ , no bound states exist. Accordingly, the scattering length is strictly negative. For  $\lambda \gtrsim 0.2/MD$  first bound states appear. We point out the similarity of the deepest few bound states to the spectrum of the  $1/r^3$  potential, accounting for the  $1/r^3$  proportion of the dipole-dipole potential.

With increasing cutoff, the frequency of occurrence of bound states grows and the states align parallel. For each new state, a pole of the scattering length  $a_0^{00}$  is evident. We conclude that the first occurring states can be assigned to a set which is  $S$ -wave dominated<sup>4</sup>. Increasing the cutoff further, a second set of bound states of similar shape and structure shows up. The second set with the same quantum numbers  $m = 0$  and  $P = +1$  respectively, overlays the first. In the region where two bound states of different sets come close, an avoided level crossing takes place. This behavior can better be seen in the upper right plot, showing the region in the red rectangle of the upper left plot. Further increasing the cutoff, a third set appears, again of similar structure. New sets of states also occur for higher cutoffs and we expect this behavior to persist for  $\lambda \rightarrow \infty$ . All level crossings are avoided since the only conserved quantum numbers are  $m$  and  $P$ , which are the same for all sets. But we can further classify sets of states by means of the orbital angular momentum. Though, transitions between all different angular momentum states are allowed, the sets of bound states are dominated by certain sets of angular momenta  $\{l\}$ . States belonging to the same  $\{l\}$ -set couple predominantly among themselves and hardly to states of other sets. Not orbital angular momentum itself but the sets of orbital angular momentum  $\{l\}$  are an almost conserved quantum number.

For the first set we find a dominance of  $\{l\} = \{0, 2\}$ , for the second  $\{l\} = \{4\}$  and for the third  $\{l\} = \{6, 8\}$ . We use two approaches in order to determine the angular momentum sets. One option is to include short-distance operators and to vary the corresponding coupling constants to check to which operators of definite angular momentum the sets are sensitive. We come back to this method when renormalizing the spectrum. Another option is to vary the highest partial

<sup>4</sup> It is worth mentioning that the potential  $v_0^{00}(l, l') \equiv 0$  and  $S$ -wave components are predominantly induced by the off-diagonal elements  $v_0^{02}(l, l')$  and  $v_0^{20}(l, l')$ . Also, the set of states has a significant  $D$ -wave component. We give a further classification of sets of bound states below.

wave included. We increment the truncation parameter  $L_{\max}$  and compare to the bound-state spectrum obtained in a cylindrical basis. It shows up that, for example, states of the  $\{6, 8\}$ -set first appear for  $L_{\max} = 6$  and further states for the same set for  $L_{\max} = 8$ . When including partial waves with  $L_{\max} \geq 10$ , the distance between states slightly changes, but no new states appear. The latter method is illustrated in App. B.5.

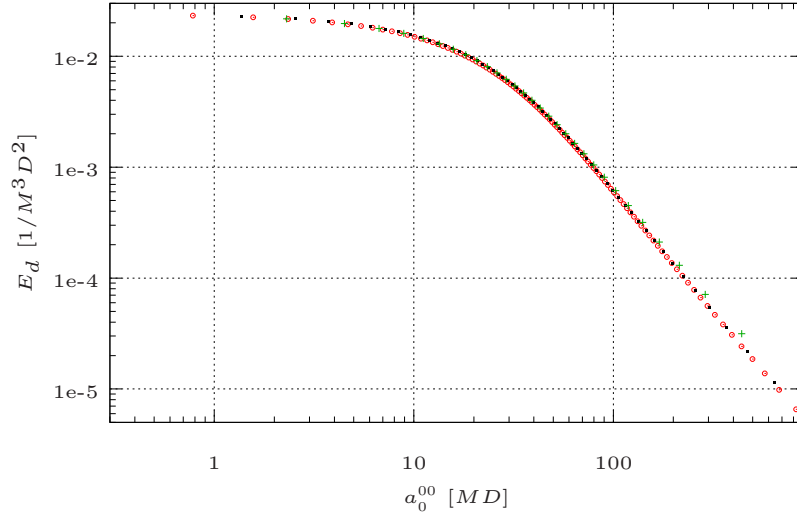


**Figure 4.3.:** Binding energies in dependence on the scattering length  $a_0^{00}$ . We show the first (red circles), second (black squares) and fifth (green crosses) bound state of the  $\{0, 2\}$ -set. The binding energies show a typical power-law behavior  $E_d \sim (a_0^{00})^{-2}$  for  $a_0^{00} \rightarrow \infty$  [8] and saturate for  $a_0^{00} \rightarrow 0$ .

Moreover, we show the binding energy in dependence on the scattering length  $a_0^{00}$  in Fig. 4.3. Depicted are the first, second and fifth state of the lowest set of bound states in dependence on  $a_0^{00}$ . We can confirm the result of Ref. [90] that the shape is the same for all states, up to some minor numerical deviations. Not only do the bound states coincide for large scattering length as one expects from the general universal relations for regions where the S-wave scattering length is large (cf. Ref. [8] and Sec. 2.2), but also for  $a_0^{00} < MD$ . Note that full convergence for the outcome shown in Fig. 4.3 is achieved already for  $L_{\max} = 2$ . A more profound analysis is given in App. B.5.

---

### Antiparallel dipoles ( $D < 0$ )

---

For antiparallel dipoles less sets of states exist and the spectrum appears to be less complex. It is shown in Fig. 4.4. Since antiparallel dipoles correspond to  $D < 0$ , the absolute value of  $D$  is implied when expressing any units.

Each set of bound states is similar in shape to the sets for parallel dipoles. Further, the cutoff scale  $\lambda$  above which first states appear is approximately the same. As before, all level crossings are avoided. We proceed analogously to the preceding analysis and determine the dominating angular momentum contributions by including short-distance operators, on the one hand and varying  $L_{\max}$ , on the other hand. Again, the first set is mainly sensitive to  $\{l\} = \{0, 2\}$ . The other set is comparable to the third set for parallel dipoles and belongs to  $\{l\} = \{6, 8\}$ . It also appears for similar cutoffs and is comparably deeply bound. The  $\{4\}$ -set, however, is completely missing.

Due to the absence of the  $\{l\} = \{4\}$ -set, the coupling between the sets with  $\{l\} = \{6, 8\}$  and  $\{l\} = \{0, 2\}$  is weaker. Therefore, classifying states with sets of orbital angular momentum works particularly well for  $m = 0$ ,  $P = +$  and  $D < 0$ . Moreover, the weak coupling implies that the distance between states in regions of avoided level crossings is much smaller. This circumstance simplifies the renormalization since the coupling constants can be tuned independently almost everywhere. The independent tuning fails wherever an avoided level crossing takes place.

The lowest-order scattering length,  $a_0^{00}$ , again is sensitive to all bound states, the pole, though, is more narrow when a  $\{6, 8\}$ -state appears, confirming the weak coupling between sets of different  $\{l\}$ .

We illustrate how to renormalize the spectrum of antiparallel dipoles properly. We begin with the  $\{0, 2\}$ -set of bound states and use as a short-distance operator  $V_s(\ell, \ell') = g_{00} Y_{00}(\Omega_\ell) Y_{00}^*(\Omega_{\ell'})$ . The coupling constant  $g_{00}$  is determined such that the fourth lowest state is bound with the dipole binding energy  $E_d = 100/M^3 D^2$ . The actual value we chose is arbitrary but could in principle be determined from future experiments. The outcome is shown in Fig. 4.5. The cutoff lies within the interval  $5/MD < \lambda < 120/MD$ . For increasing cutoff scale, the three lowest bound states align parallel to the renormalized state. Furthermore, degrees of freedom which were previously integrated out by regulating and introducing a cutoff enter from above and also align parallel to the renormalized state. All states but the fourth lowest oscillate when entering the spectrum, but converge quickly towards a constant value. The oscillations can possibly be

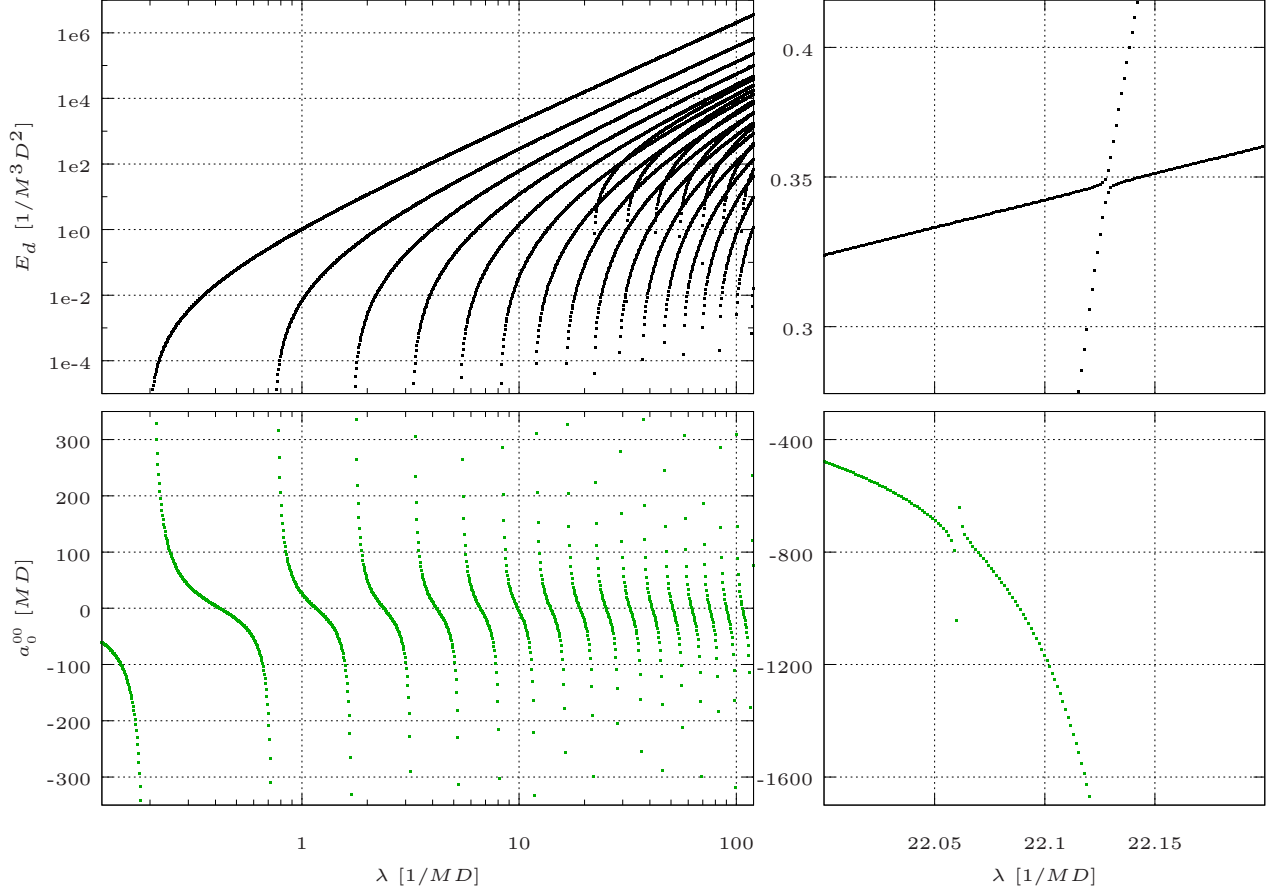


**Figure 4.4.:** Unrenormalized spectrum of bound states and the scattering length  $a_0^{00}$  for  $D < 0$ ,  $m = 0$  and  $P = +$ . The dependence on the cutoff scale for the binding energies and the scattering length  $a_0^{00}$  is shown in the upper and lower half, respectively. The right side corresponds to  $22.0/M D < \lambda < 22.2/M D$ . Avoided level crossings take place wherever two binding energies come close. Opposed to Fig. 4.2, we do not show the area magnified in the left plots as it is significantly smaller and would appear as a single dot. Since  $D < 0$ , we refer to the absolute value when expressing dimensional quantities in dipole units.

explained in analogy to the  $1/r^3$  spectrum. States of the same set couple among each other. Additional oscillations might occur since the  $\{0, 2\}$ -set is not a pure  $S$ -wave, but also has a significant  $D$ -wave contribution. Oscillations can possibly be reduced by introducing a linear combination of an  $S$ - and a  $D$ -wave short-distance operator.

The second  $\{l\} = \{6, 8\}$ -set is barely sensitive to the chosen short-distance operator. Note, however, that all level crossings are still avoided and in the region where bound states of different sets are of the same order, the short-distance  $S$ -wave operator does influence the  $\{6, 8\}$ -set.

To renormalize the states of the  $\{6, 8\}$ -set, anisotropic operators have to be utilized. We use  $V_s(\ell, \ell') = g_{80} Y_{80}(\Omega_\ell) Y_{80}^*(\Omega_{\ell'})$ . We renormalize the lowest state of the set to a binding energy  $E_d = 100/M^3 D^2$ . The situation is now reversed. The  $\{0, 2\}$ -set of states is barely sensitive to the short-distance operator and only affected when level crossings are avoided. Increasing the cutoff, states of higher energy enter the spectrum since degrees of freedom are brought back into the theory. The oscillations of those states have amplitudes with significantly larger magnitude and die off more slowly than for the  $\{0, 2\}$ -set.<sup>5</sup> For the second lowest  $\{6, 8\}$ -bound state we plotted the amplitude of the first oscillation as a blue band. The second oscillation already lies clearly within the band. We conclude that it is to be expected that in the limit  $\lambda \rightarrow \infty$  all states approach a constant value. This expectation is further supported by the analogous behavior of the  $\{0, 2\}$ -set when renormalizing with  $S$ -wave operators.

From a practical point of view, for higher cutoffs even more sets of bound states appear, complicating the identification of single states. However, exploiting that, given a desired accuracy, sets of bound states are sensitive to a finite number of orbital angular momentum contributions one can prevent new sets to enter the spectrum by keeping the truncation parameter  $L_{\max}$  fixed.

Moreover, spurious states of parabolic shape (in double logarithmic plots) occur at low energies when introducing the

<sup>5</sup> The larger amplitude of the oscillations can possibly be explained, taking into account that the  $\{6, 8\}$ -set couples stronger to other partial waves.

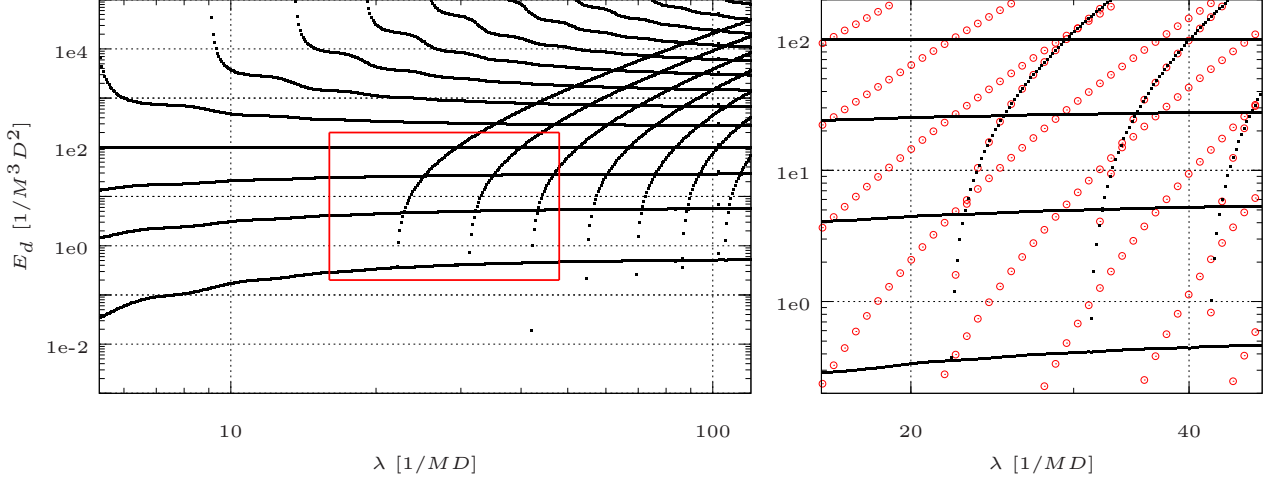


**Figure 4.5.:** Partially renormalized spectrum for antiparallel dipoles. The fourth lowest state of the  $\{0, 2\}$ -set of bound states is renormalized to a binding energy of  $E_d = 100/M^3 D^2$ . We use a short-distance operator  $\sim Y_{00}(\Omega_\ell)Y_{00}^*(\Omega_{\ell'})$ . The plot on the right shows the region in the red rectangle, which is for  $16/MD < \lambda < 48/MD$ . Additionally, the unrenormalized spectrum is shown with red circles. The  $\{6, 8\}$ -set is barely sensitive to the chosen short-distance operator and coincides well with the corresponding unrenormalized set.

short-range potential. These are of much smaller binding energy, though, and vanish shortly after their first appearance. Besides, the maximum in binding energy decreases for higher cutoffs.

It is further possible to combine the preceding operators, i.e. to use  $V_s(\ell, \ell') = g_{00}Y_{00}(\Omega_\ell)Y_{00}^*(\Omega_{\ell'}) + g_{80}Y_{80}(\Omega_\ell)Y_{80}^*(\Omega_{\ell'})$ , in order to renormalize the full spectrum. The outcome is shown in Fig. 4.7. For a clear separation between the renormalized states, we use  $E_d = 10/M^3 D^2$  for the second lowest state of the  $\{0, 2\}$ -set. The lowest state of the  $\{6, 8\}$ -set is still at  $E_d = 100/M^3 D^2$ . The fully renormalized spectrum is a combination of the previous spectra. In the region of avoided level crossings, renormalization might fail numerically, causing data points to scatter. In particular, this happens for the lowest  $\{6, 8\}$ -state for which  $E_d \neq 100/M^3 D^2$  for certain values of  $\lambda$ . Note that we determined the coupling constants separately to reduce computational costs. A full, two-dimensional analysis can fix this problem in future calculations. This behavior can also be seen regarding the coupling constants. They are shown below in dependence on the cutoff. The black squares belong to  $g_{00}$ , the red circles to  $g_{80}$ . For each newly appearing state of a set, the corresponding coupling constant diverges. For cutoffs for which the bare dipole-dipole interaction does not possess any  $\{6, 8\}$ -state,  $g_{80}$  is strictly negative and thus, the short-range interaction attractive.

Finally, Fig. 4.8 shows the universal dependence of the binding energy on the scattering length for parallel and antiparallel dipoles, respectively. Independent of the sign of  $D$ ,  $E_d(a_0^{00})$  coincide for large as well as for small scattering length.

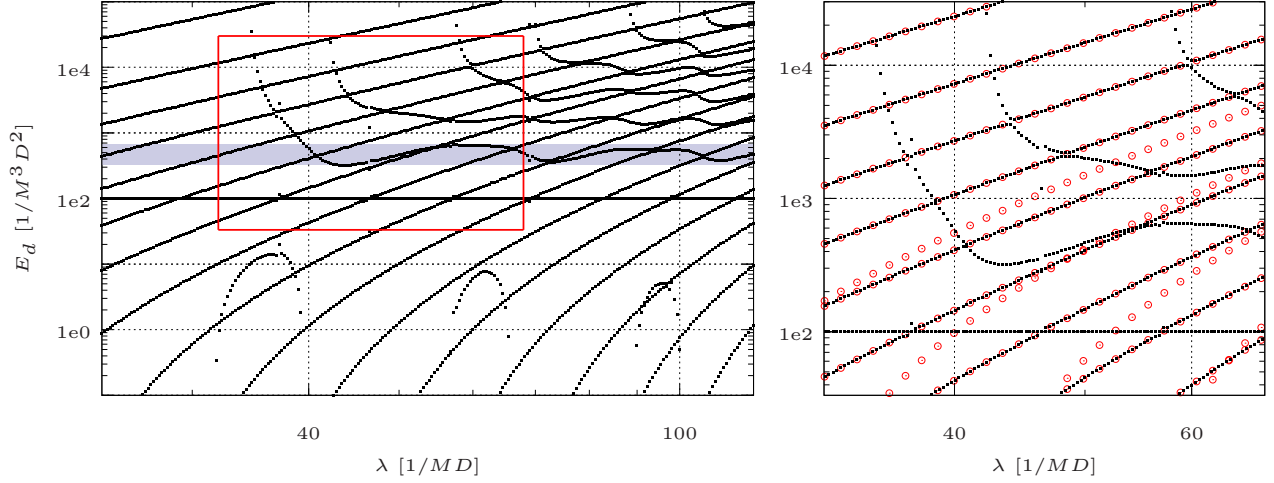


**Figure 4.6.:** Partially renormalized spectrum for antiparallel dipoles. The lowest state of the  $\{6, 8\}$ -set is renormalized to a binding energy of  $E_d = 100/M^3 D^2$ . We use a short-distance operator  $\sim Y_{80}(\Omega_\ell)Y_{80}^*(\Omega_{\ell'})$ . The plot on the right shows the region in the red rectangle, which is for  $32/MD < \lambda < 68/MD$ . The unrenormalized spectrum is shown with red circles. The situation is reversed compared to Fig. 4.5 - the  $\{0, 2\}$ -set is barely sensitive to the included short-distance operator. The blue band shows the amplitude of the first oscillation.

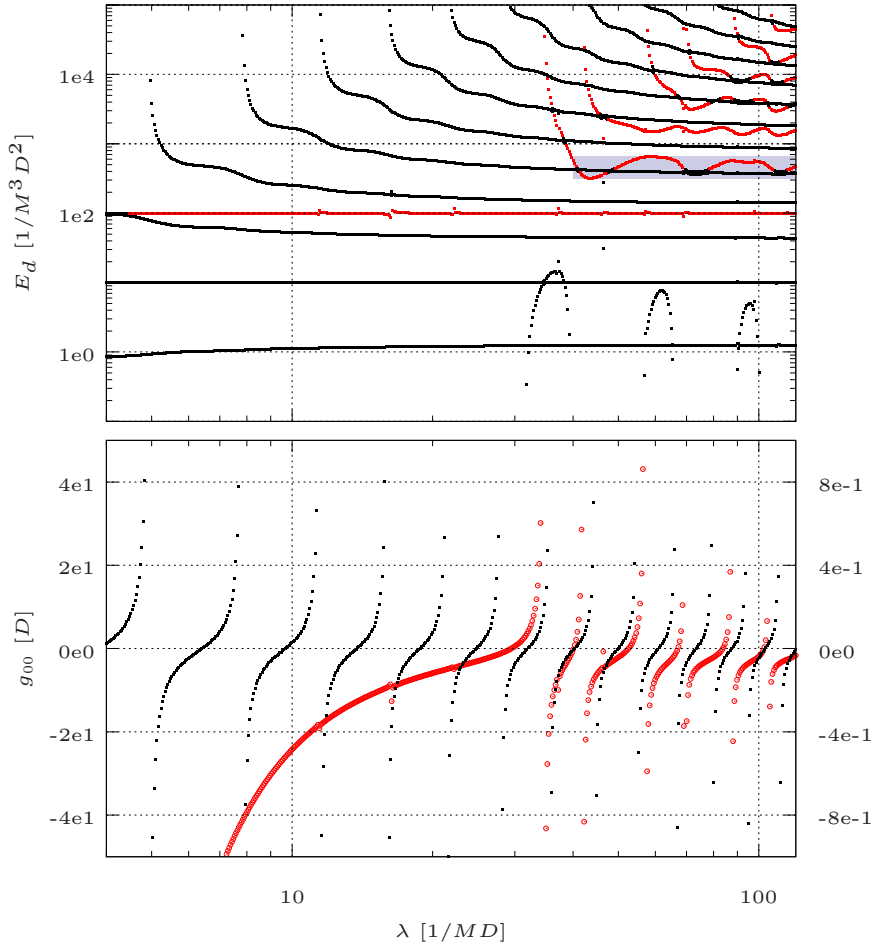


**Figure 4.7.:** Fully renormalized spectrum for two antiparallel dipoles and the evolution of the coupling constants. The short-range operator  $V_s(\ell, \ell') = g_{00}Y_{00}(\Omega_\ell)Y_{00}^*(\Omega_{\ell'}) + g_{80}Y_{80}(\Omega_\ell)Y_{80}^*(\Omega_{\ell'})$  has been used for renormalization. The lowest  $\{6, 8\}$ -state is still renormalized to a binding energy of  $E_d = 100/M^3 D^2$ , whereas the second lowest  $\{0, 2\}$ -state is now at  $E_d = 10/M^3 D^2$  to clearly separate the fixed states. We plot for  $4/MD < \lambda < 120/MD$ . For certain values of  $\lambda$ , the lowest  $\{6, 8\}$ -state is not accurately renormalized since coupling constants have been determined independently to reduce computational costs. Binding energies which can be clearly assigned to the  $\{6, 8\}$ -set are colored in red. In the lower plot,  $g_{00}$  belongs to black squares and  $g_{80}$  to red circles. Black circles belong to the left, red circles to the right y-axis.

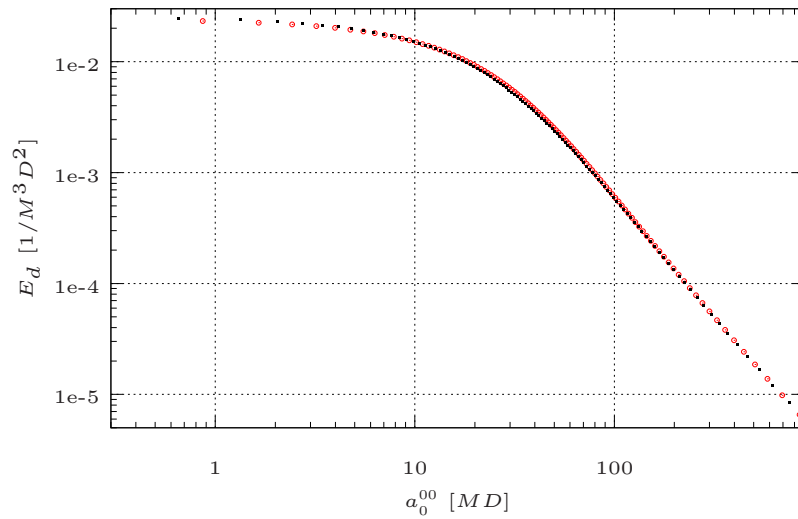


**Figure 4.8.:** Binding energies for parallel and antiparallel dipoles in dependence on the scattering length  $a_0^{00}$ . We show the first bound state of the  $\{0, 2\}$ -set for  $D > 0$  (red circles) and for  $D < 0$  (black squares).

## 4.2 The three-dipole system

In this section, our results for three non-relativistic, bosonic dipoles are presented. We investigate the low-energy regime and calculate binding energies. In particular, the cutoff dependence of the system and the question whether a three-body short-range operator is required in order to renormalize the bound-state spectrum is addressed. To calculate observables we utilize the Faddeev equation. At the end of this section we present an alternative formulation of the Faddeev equation which is numerically advantageous.

### 4.2.1 The Faddeev equation

The Faddeev equation can be employed in order to determine low-energy observables for three non-relativistic particles. Since we are interested in the bound-state spectrum, we focus on the (homogeneous) Faddeev bound-state equation. Note that for bound states  $E < 0$  and therefore, no  $i\epsilon$  prescription is required in the emerging propagators. Here, we project on cylindrical partial waves. An analysis in a spherical basis to improve precision in the infrared is still outstanding. However, the analysis presented here gives valuable information about the cutoff dependence and on the shape of three-body binding energies. For a thorough derivation of the Faddeev equation, we refer to the literature, e.g., Ref. [135], where it is derived from the three-body Schrödinger equation.

We denote the particles momenta  $\ell_1$ ,  $\ell_2$  and  $\ell_3$ , respectively, and introduce the Jacobi momenta

$$\begin{aligned}\mathbf{p} &\equiv \frac{1}{2}(\ell_2 - \ell_3), \\ \mathbf{q} &\equiv \frac{2}{3}(\ell_1 - \frac{1}{2}(\ell_2 + \ell_3)).\end{aligned}\quad (4.29)$$

The Faddeev equation in momentum space is then given as

$$\begin{aligned}\psi(E, \mathbf{p}, \mathbf{q}) &= -g_0(p^2, q^2) \int d^3k \left\{ T(E - \frac{3}{4}q^2/M, \mathbf{p}, \mathbf{k}) g_0(k^2, q^2) T_{3c}(E) \psi(E, \mathbf{k}, \mathbf{q}) \right. \\ &\left. + (1 + g_0(k^2, q^2) T_{3c}(E)) \cdot [T(E - \frac{3}{4}q^2/M, \mathbf{p}, \boldsymbol{\pi}_1) \psi(E, -\boldsymbol{\pi}_2, \mathbf{k}) + T(E - \frac{3}{4}q^2/M, \mathbf{p}, -\boldsymbol{\pi}_1) \psi(E, \boldsymbol{\pi}_2, \mathbf{k})] \right\},\end{aligned}\quad (4.30)$$

where we introduced the shifted momenta  $\boldsymbol{\pi}_1$  and  $\boldsymbol{\pi}_2$ , depending on the Jacobi momentum  $\mathbf{q}$  and the loop momentum  $\mathbf{k}$

$$\begin{aligned}\boldsymbol{\pi}_1(\mathbf{k}, \mathbf{q}) &\equiv \mathbf{k} + \frac{1}{2}\mathbf{q}, \\ \boldsymbol{\pi}_2(\mathbf{k}, \mathbf{q}) &\equiv \frac{1}{2}\mathbf{k} + \mathbf{q}.\end{aligned}\quad (4.31)$$

The quantity  $g_0(p^2, q^2)$  is defined as

$$g_0 \equiv (E - (p^2 + \frac{3}{4}q^2)/M)^{-1}.\quad (4.32)$$

Moreover,  $T_{3c}(E)$  is the three-body contact transition amplitude and fulfills the LS equation for three-body contact interactions. The solution to Eq. (4.30),  $\psi$ , is called Faddeev component and is directly related to the three-body wave function following from the Schrödinger equation. The binding energies  $E_B^{(3)} > E_B$  for which Eq. (4.30) has a solution, determine the spectrum for three particles, with the two-body binding energies  $E_B$ . If dipolar interactions display a universal behavior, i.e. if the entire three-dipole spectrum is solely determined by two-body low-energy observables, no three-body forces are required [8]. In case of pure two-body contact interactions, the three-body spectrum is determined by, for example, the two-body scattering length,  $a_s$ , up to one degree of freedom. If no three-body force is included, the three-particle binding energies are dependent on the cutoff scale,  $\lambda$ , but they also display a discrete scale invariance in the limit of  $a_s \rightarrow \infty$  and  $\lambda \rightarrow \infty$ .<sup>6</sup> The discrete scale invariance implies that as soon as one three-body binding energy is fixed, e.g., by experiment, the complete spectrum is set. We attempt to identify possible universal behavior for the dipole system. It is sufficient to check whether the binding energies of the three-particle spectrum show a cutoff dependence in absence of three-body forces, i.e. for  $T_{3c}(E) \equiv 0$ . The Faddeev equation simplifies to

$$\psi(E, \mathbf{p}, \mathbf{q}) = -g_0(p^2, q^2) \int d^3k \left\{ T(E - \frac{3}{4}q^2/M, \mathbf{p}, \boldsymbol{\pi}_1) \psi(E, -\boldsymbol{\pi}_2, \mathbf{k}) + T(E - \frac{3}{4}q^2/M, \mathbf{p}, -\boldsymbol{\pi}_1) \psi(E, \boldsymbol{\pi}_2, \mathbf{k}) \right\}.\quad (4.33)$$

<sup>6</sup> For finite cutoff there is, as for the two interacting particles, a maximal three-body binding energy  $\sim \lambda^2/M$ .

The sum of Faddeev components  $\psi(E, \mathbf{p}, \mathbf{q})$ , with cyclic permutations of the particles momenta  $\ell_1, \ell_2$  and  $\ell_3$  in Eq. (4.29), is a solution to the three-body Schrödinger equation.

Before addressing the dipole-dipole interaction, we solve Eq. (4.33) for a simpler potential, namely for a pure two-body contact interaction. It will provide some insight into dynamics of a three-body system and allows to classify different scenarios. For a detailed review for three particles interacting at low energies through pure contact interactions we refer to the literature [8, 136].

**The Faddeev equation for a separable potential** can be further simplified, using that the two-body transition matrix is separable. For isotropic interactions the potential depends on the absolute value of the momenta only and we use

$$V(\ell, \ell') = g_2 v_1(\ell) v_2(\ell'). \quad (4.34)$$

We can then make the ansatz

$$T(E, \ell, \ell') \equiv \tau(E) v_1(\ell) v_2(\ell') \quad (4.35)$$

and it is straightforward to show that  $\tau(E)$  obeys the LS equation

$$\tau(E) = -g_2 + 4\pi g_2 \tau(E) \int dk \frac{k^2 v_1(k) v_2(k)}{E - k^2/M + i\epsilon}. \quad (4.36)$$

In our case the only momentum dependence comes from the regulator. We use a Gaussian regulator function, i.e.  $f^R(\ell^2) = e^{-\ell^2/\lambda^2}$ . Plugging expression (4.35) into the Faddeev equation (4.33) yields

$$\psi(E, \mathbf{p}, \mathbf{q}) = -g_0(p^2, q^2) \tau(E - \frac{3}{4}q^2/M) f^R(p^2) \int d^3k f^R(\pi_1^2) \{\psi(E, -\pi_2, \mathbf{k}) + \psi(E, \pi_2, \mathbf{k})\}. \quad (4.37)$$

It can be solved with the ansatz [136]

$$\psi(E, \mathbf{p}, \mathbf{q}) = g_0(p^2, q^2) f^R(p^2) F(E, q), \quad (4.38)$$

which reduces the Faddeev equation to an integral equation in one variable

$$F(E, q) = -\tau(E - \frac{3}{4}q^2/M) 4\pi \int dk k^2 \int_{-1}^1 dx f^R(\pi_1^2) g_0(\pi_2^2, k^2) f^R(\pi_2^2) F(E, k). \quad (4.39)$$

We plot the three-body spectrum for an isotropic two-body contact interaction characterized by one coupling constant  $g_2$  and in the absence of three-body forces in Fig. 4.9. The left side shows the evolution of the three-body bound-state spectrum in dependence on the cutoff scale  $\lambda$ . The coupling constant is determined by the demand that the two-body binding energy is renormalized to one. Actual experimental input could assign physical units to the two- and three-body binding energies.

For increasing cutoff, the number of bound states grows. They become deeper bound and align parallel to each other. It is evident that a three-body interaction is indispensable in order to obtain renormalization scale independence. An analytical solution can be found, e.g., in Refs. [137, 138], where the authors use a renormalization group approach. The three-boson system has a discrete scaling symmetry. This feature is known as Efimov effect [47, 112], which is undergoing intense theoretical and experimental studies in current research.<sup>7</sup> In the limit of  $\lambda \rightarrow \infty$  and  $a_s \rightarrow \infty$ , the scaling factor is  $\sigma_0 = 22.7$ .

The discrete scaling symmetry is similar to the one we found for the  $1/r^2$  potential in Sec. 2.3.1. Using hyperspherical coordinates [8], three bosons interacting with large scattering length obey a Schrödinger equation similar to the radial Schrödinger equation for the  $1/r^2$  potential [107, 112]. The discrete scale invariance implies that if  $E_{(3)B}^{(0)}$  is a binding energy, then  $E_{(3)B}^{(n)} = \sigma_0^{2n} E_{(3)B}^{(0)}$  also is a binding energy of the spectrum. For finite cutoff, the binding energy of the deepest bound state is  $\lesssim \lambda^2/M$  implying an upper bound for the spectrum. Moreover, the finite numerical precision ultimately limits the number of resolved bound states. In Fig. 4.9 three bound states appear for the cutoff range and number of sampling points chosen. On the right of the three-particle spectrum, we show the ratio of adjacent bound states. In the limit of  $\lambda \rightarrow \infty$  the ratios approach the analytically expected value of  $\sigma_0^2 \approx 515$ .

<sup>7</sup> Efimov further predicted a system with short-range interactions to be a Borromean system, i.e. that three-body bound states exist even in the absence of bound dimers.

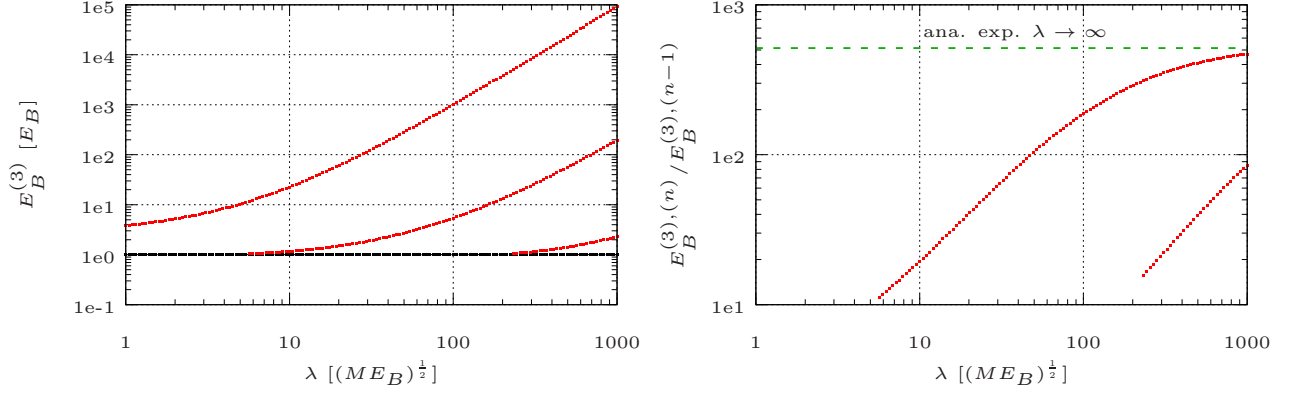


**Figure 4.9.:** Spectrum for three bosons acting via a two-body contact potential. No explicit short-range three-body forces are included. We show the unrenormalized spectrum of binding energies in the left plot. The plot on the right-hand side depicts the ratio of adjacent binding energies. The analytically expected limit for  $\lambda \rightarrow \infty$  and  $a_s \rightarrow \infty$  is shown with a green, dashed line. For both plots, all dimensionful quantities are given in units of the two-body binding energy  $E_B$ .

**The three-dipole Faddeev equation** can not be simplified like in Eq. (4.37), since the two-body potential and transition matrix are non-separable. We first consider the most general case and use the full partial wave expansion for the two-body transition amplitude

$$T(E, \ell, \ell') = \sum_{m=-\infty}^{\infty} t_m(E, \underline{\ell}, \underline{\ell}') y_m(\phi_\ell) y_m^*(\phi_{\ell'}), \quad (4.40)$$

where the amplitudes  $t_m$  are determined by Eq. (4.14). We further expand the Faddeev components using the general ansatz

$$\psi(E, \mathbf{p}, \mathbf{q}) = \sum_{m_1, m_2=-\infty}^{\infty} \psi_{m_1 m_2}(E, \underline{\mathbf{p}}, \underline{\mathbf{q}}) y_{m_1}(\phi_p) y_{m_2}^*(\phi_q) \quad (4.41)$$

and plug Eqs. (4.40) and (4.41) into the Faddeev equation (4.33). We find for the partial wave projected Faddeev components

$$\begin{aligned} \psi_{m_1 m_2}(E, \underline{\mathbf{p}}, \underline{\mathbf{q}}) = & -g_0(p^2, q^2) \int d^2k \int_0^{2\pi} d\phi \left\{ t_{m_1}(E - \frac{3}{4}q^2/M, \underline{\mathbf{p}}, \underline{\boldsymbol{\pi}}_1(\phi)) \right. \\ & \times \sum_{m_3, m_4} \sum_{n_1, n_3=0}^{m_1, m_3} D_{n_1 n_3}^{m_1 m_3}(q_\rho, k_\rho, \phi) \frac{y_{m_4+n_1-n_3}^*(\phi)}{\sqrt{2\pi}} (-1)^{m_3} \delta_{m_1-m_3, m_2-m_4} \psi_{m_3 m_4}(-\underline{\boldsymbol{\pi}}_2(\phi), \underline{\mathbf{k}}) + \pi_{1,2} \leftrightarrow -\pi_{1,2} \left. \right\}, \end{aligned} \quad (4.42)$$

where the quantity  $D_{n_1 n_3}^{m_1 m_3}$  is defined as

$$D_{n_1 n_3}^{m_1 m_3}(q_\rho, k_\rho, \phi) \equiv \binom{|m_1|}{|n_1|} \binom{|m_3|}{|n_3|} \left(\frac{1}{2}\right)^{|m_1|-|n_1|+|n_3|} \frac{(k_\rho)^{|n_1|+|n_3|} (q_\rho)^{|m_1|+|m_3|-(|n_1|+|n_3|)}}{(\pi_1^\rho(\phi))^{|m_1|} (\pi_2^\rho(\phi))^{|m_3|}}, \quad (4.43)$$

with binomial coefficients  $\binom{|m_1|}{|n_1|}$  and  $\binom{|m_3|}{|n_3|}$ . We give a detailed derivation in App. B.8. Note that the interchange  $\pi_{1,2} \leftrightarrow -\pi_{1,2}$  in Eq. (4.42) also implies that  $(-1)^{m_3}$  has to be replaced with  $(-1)^{m_1}$  (cf. App. B.8). The  $\rho$ - and  $z$ -component of the shifted momenta  $\underline{\boldsymbol{\pi}}_1 \equiv (\pi_1^\rho, \pi_1^z)^T$  and  $\underline{\boldsymbol{\pi}}_2 \equiv (\pi_2^\rho, \pi_2^z)^T$  are given as

$$\underline{\boldsymbol{\pi}}_1 \equiv \begin{pmatrix} \sqrt{k_\rho^2 + \frac{1}{4}q_\rho^2 + k_\rho q_\rho \cos(\phi_k - \phi_q)} \\ k_z + \frac{1}{2}q_z \end{pmatrix}, \quad (4.44a)$$

$$\underline{\boldsymbol{\pi}}_2 \equiv \begin{pmatrix} \sqrt{\frac{1}{4}k_\rho^2 + q_\rho^2 + k_\rho q_\rho \cos(\phi_k - \phi_q)} \\ \frac{1}{2}k_z + q_z \end{pmatrix}. \quad (4.44b)$$

The minus sign in front of the shifted momenta only applies to the  $z$ -component, i.e.  $-\underline{\boldsymbol{\pi}} \equiv (\pi^\rho, -\pi^z)^T$ .

There is a simplification we can apply if the deepest two-body bound state with particular  $\bar{m}_1$  is clearly separated from bound states with different angular momentum projection. Then, for energies in the vicinity of the greatest two-body binding energy, the transition amplitude,  $T$ , is dominated by its partial wave  $t_{\bar{m}_1}$  and we can approximate

$$T(E, \ell, \ell') \approx t_{\bar{m}_1}(E, \underline{\ell}, \underline{\ell}') y_{\bar{m}_1}(\phi_\ell) y_{\bar{m}_1}^*(\phi_{\ell'}). \quad (4.45)$$

We expect this approximation to work particularly well for three-body binding energies close to the two-body threshold. For the partial wave amplitudes in Eq. (4.40) follows

$$t_m(E, \underline{\ell}, \underline{\ell}') = \delta_{m\bar{m}_1} t_{\bar{m}_1}(E, \underline{\ell}, \underline{\ell}'). \quad (4.46)$$

The Faddeev equation then decouples and we find

$$\begin{aligned} \psi_{\bar{m}_1 m_2}(E, \underline{\mathbf{p}}, \underline{\mathbf{q}}) = & -g_0(p^2, q^2) \int d^2k \int_0^{2\pi} d\phi \left\{ t_{\bar{m}_1}(E - \frac{3}{4}q^2/M, \underline{\mathbf{p}}, \underline{\boldsymbol{\pi}}_1(\phi)) \right. \\ & \times \sum_{n_1, n_3=0}^{\bar{m}_1} D_{n_1 n_3}^{\bar{m}_1 \bar{m}_1}(q_\rho, k_\rho, \phi) \frac{Y_{m_2+n_1-n_3}^*(\phi)}{\sqrt{2\pi}} (-1)^{\bar{m}_1} \psi_{\bar{m}_1 m_2}(-\underline{\boldsymbol{\pi}}_2(\phi), \underline{\mathbf{k}}) + \pi_{1,2} \leftrightarrow -\pi_{1,2} \left. \right\}. \end{aligned} \quad (4.47)$$

For  $\bar{m}_1 = m_2 = 0$  we obtain from Eq. (4.47)

$$\psi_{00}(E, \underline{\mathbf{p}}, \underline{\mathbf{q}}) = -g_0(p^2, q^2) \int d^2k \int_0^{2\pi} \frac{d\phi}{2\pi} \left\{ t_0(E - \frac{3}{4}q^2/M, \underline{\mathbf{p}}, \underline{\boldsymbol{\pi}}_1(\phi)) \psi_{00}(-\underline{\boldsymbol{\pi}}_2(\phi), \underline{\mathbf{k}}) + \pi_{1,2} \leftrightarrow -\pi_{1,2} \right\}. \quad (4.48)$$

We illustrate how to solve Eq. (4.48) in App. B.7 numerically. In the next section we present our results for the bound-state spectrum of three interacting, bosonic dipoles.

## 4.2.2 Results

We present our results for three bosonic dipoles acting via two-body interactions only. We constrain our analysis to regions where the  $T$ -matrix is dominated by one particular angular momentum projection, i.e. where condition (4.45) is fulfilled. For the here presented analysis we use  $m = 0$  and  $D < 0$ . The spectrum is shown in Fig. 4.10. All dimensionful quantities are expressed in dipole units. We use a Lanczos algorithm as described in App. B.7. It is a Krylov subspace algorithm which are particularly useful for sparse kernel matrices inducing comparatively inexpensive matrix-vector multiplications. We use  $N = 15$  and  $2N - 1 = 29$  sampling points for the  $\rho$ - and  $z$ -components of the momenta, respectively. The cutoff is varied between  $\lambda = 1 \dots 20/M D$  and the short-range operator is an isotropic  $S$ -wave operator. For the whole range of the cutoff, just one set of bound states is present and, e.g., avoided level crossings do not occur. The lowest bound state is renormalized to  $E_d = 0.1/M^3 D^2$ .

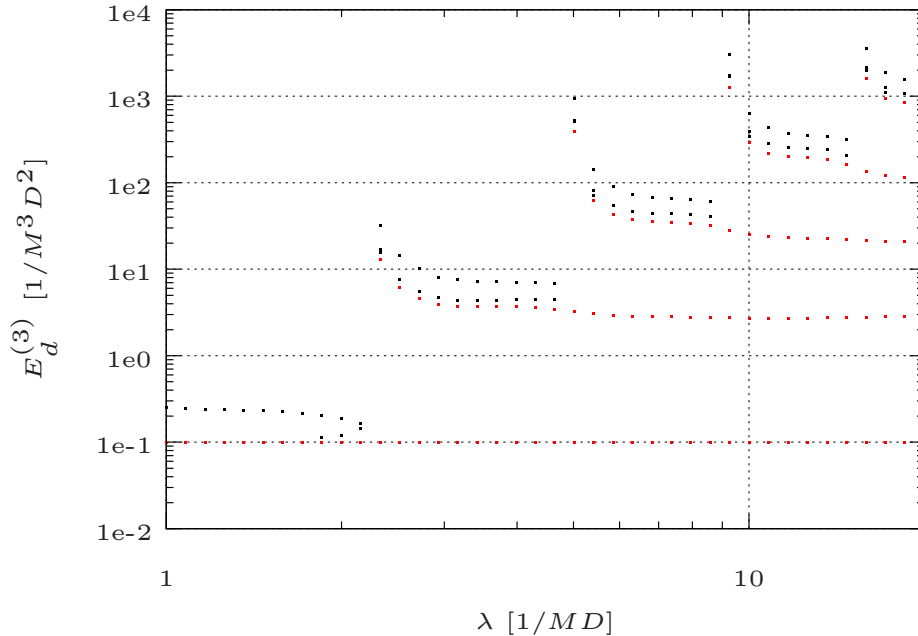


**Figure 4.10.:** Bound-state spectrum for three bosonic dipoles. We plot the binding energies in dependence on the cutoff. Green squares belong to two-body bound states and red squares to the three-body spectrum. The deepest two-body bound state is renormalized to  $E_d = 0.1/M^3 D^2$ .

Three-dipole bound states are present for the whole range of the cutoff. To avoid poles of the two-body  $T$ -matrix, we constrain the three-body spectrum to energies  $E_d^{(3)} \geq 1.1E_d$ . This confinement explains why only one bound state is found

for  $\lambda \lesssim 1.8/MD$ . Moreover, the shallowest three-body bound state is always deeper bound than the deepest two-dipole state, since otherwise it was energetically favorable for the three-body state to decay into a two-body bound state and a free particle. Thus, every time a two-body bound state joins the spectrum from above, the three-body bound states align parallel to it.

It appears that the three-body spectrum shows barely any sensitivity to the cutoff as soon as the deepest two-body bound state has converged. We conclude that no three-body short-range operators are required in order to renormalize the spectrum, which is in agreement with the findings in Ref. [91]. The three-dipole bound-state spectrum appears to be universally determined by two-body low-energy observables.

For most cutoffs, two bound states of the three-body spectrum are present. A third one only occurs for values of the cutoff where the deepest two- and three-body bound states are not converged yet. Due to the absence of a fully converged third state, we could not confirm Efimov physics, predicted in Ref. [91]. In the future, it should be possible to go to higher precision. An implementation in spherical coordinates presumably allows for a larger number of sampling points, increasing the achieved resolution. Furthermore, it is desirable to search for three-body binding energies closer to the two-dipole threshold. A reformulation of the Faddeev equation presented in the upcoming section allows to obtain the three-body spectrum arbitrarily close to the two-body threshold without encountering poles of the transition matrix. It further reduces the numerical expenses significantly.

### 4.2.3 Alternative formulation of the Faddeev equation

As described in App. B.7, the Faddeev equation for bound states can be discretized and reduced to an eigenvalue problem. Negative energies for which the kernel possesses eigenvalue one are binding energies of the system. Root-finding algorithms might necessitate many function evaluations, in particular, when many three-body bound states are present. Each function evaluation comes with the cost of finding the eigenvalues of the kernel. Furthermore, when, e.g., using a bisection, the interval on which the roots are determined is finite and hence particular solutions might not be found. Moreover, root-finding algorithms come with a finite precision with which the binding energies are determined and thus increase the error of the binding energies. Algorithm with a faster convergence, on the other hand, might suffer from a lower robustness.

It is therefore desirable to find an alternative approach, similar to the modified bound-state equation for the two-body system (cf. App. B.3). Then, the eigenvalues have to be determined just once in order to determine the complete spectrum. We derive such a reformulation of the Faddeev equation in App. B.8, which can also be utilized for non-separable potentials. The modified Faddeev equation without explicit three-body forces reads

$$E\psi(\mathbf{p}, \mathbf{q}) = \frac{1}{M} \left( \frac{3}{4}q^2 + p^2 \right) \psi(\mathbf{p}, \mathbf{q}) + \int d^3k V(\mathbf{p}, \mathbf{k}) \psi(\mathbf{k}, \mathbf{q}) + \int d^3k \{V(\mathbf{p}, \boldsymbol{\pi}_1) \psi(-\boldsymbol{\pi}_2, \mathbf{k}) + V(\mathbf{p}, -\boldsymbol{\pi}_1) \psi(\boldsymbol{\pi}_2, \mathbf{k})\}. \quad (4.49)$$

On the right-hand side of Eq. (4.49) only energy independent quantities appear. In particular, in the last term, the potential occurs instead of the transition matrix (cf. Eq. (4.33)). While the transition matrix depends on three momenta ( $\mathbf{q}$ ,  $\mathbf{p}$  and  $\boldsymbol{\pi}_1$ ) and the energy, the potential depends on two momenta only. Thus, the required memory in order to store the kernel matrix is reduced by one order<sup>8</sup>. Moreover, for the determination of the transition matrix, for instance, when regarding dipole-dipole interactions, matrix inversions are required, whereas the potential follows from direct function evaluations. It is hence expected that numerical expenses for the determination of the kernel matrix are clearly reduced when employing Eq. (4.49). Also, close to the two-body threshold, the transition matrix possesses poles. The poles restrict the domain on which binding energies are determined and brings additional risk that numerical evaluations fail. Ultimately, we aim to apply Eq. (4.49) to the three-dipole system using a spherical basis in order to increase numerical precision. A full implementation is still outstanding. However, we give a proof of concept considering a simpler potential, namely the  $1/r^3$  potential. It is non-separable but angular momentum channels do not couple when projecting on partial waves. We derive the partial wave projection of Eq. (4.49) in App. B.9. The projection of the third term can be conducted in complete analogy to the partial wave projection of the Faddeev equation in Eq. (4.33), which can be found in the literature (e.g. in Ref. [135]). As a basis for the expansion, we use bipolar spherical harmonics. They are defined as

$$\mathcal{Y}_{l\lambda}^{LM}(\Omega_p, \Omega_q) \equiv \sum_{m, \mu} \begin{bmatrix} l & \lambda & L \\ m & \mu & M \end{bmatrix} Y_{lm}(\Omega_p) Y_{\lambda\mu}(\Omega_q), \quad (4.50)$$

where  $m$  and  $\mu$  run over  $-l, \dots, l$  and  $-\lambda, \dots, \lambda$ , respectively. The bipolar spherical harmonics are orthonormal and complete w.r.t.  $\Omega_\ell \otimes \Omega_{\ell'}$ . We can expand the Faddeev components of Eq. (4.49)

$$\psi(\mathbf{p}, \mathbf{q}) = \sum_{L, M, l, \lambda} \psi_{l\lambda}^{LM}(p, q) \mathcal{Y}_{l\lambda}^{LM}(\Omega_p, \Omega_q), \quad (4.51)$$

<sup>8</sup> Using  $N$  sampling points for all momenta, for fixed energy  $E$ ,  $N^3$  array entries have to be stored for the  $T$ -matrix, while for the potential  $N^2$  are sufficient.

where  $L, l$  and  $\lambda$  run from zero to infinity and  $M = -L \dots L$ . We abbreviate the indices of the Faddeev components

$$\alpha \equiv \begin{pmatrix} L & M \\ l & \lambda \end{pmatrix} \quad (4.52)$$

and find for the partial wave amplitudes

$$E\psi_\alpha(p, q) = \frac{1}{M} \left( \frac{3}{4}q^2 + p^2 \right) \psi_\alpha(p, q) + \sum_{\alpha'} \int dk k^2 \mathcal{V}_{\alpha\alpha'}(p, k) \psi_{\alpha'}(k, q) + \sum_{\alpha', \alpha''} \int dk k^2 \int_{-1}^1 dx \frac{\mathcal{V}_{\alpha\alpha'}(p, \pi_1(q, k, x))}{(\pi_1(q, k, x))^{l'}} G_{\alpha'\alpha''}(q, k, x) \frac{\psi_{\alpha''}(\pi_2(q, k, x), k)}{(\pi_2(q, k, x))^{l''}}, \quad (4.53)$$

where [...] represent Clebsch-Gordan coefficients. The potential  $\mathcal{V}_{\alpha\alpha'}$  can be expressed in terms of the two-body potential  $v_m^{ll'}$

$$\mathcal{V}_{\alpha\alpha'}(p, k) \equiv \delta_{\lambda\lambda'} \delta_{MM'} \sum_{m=-M}^M \begin{bmatrix} l & \lambda & L \\ m & M-m & M \end{bmatrix} \begin{bmatrix} l' & \lambda & L' \\ m & M-m & M \end{bmatrix} v_m^{ll'}(p, k). \quad (4.54)$$

The absolute values of the shifted momenta are denoted by  $\pi_1$  and  $\pi_2$ , respectively, and read

$$\pi_1(q, k, x) \equiv \sqrt{\frac{1}{4}q^2 + k^2 + qkx}, \quad (4.55a)$$

$$\pi_2(q, k, x) \equiv \sqrt{q^2 + \frac{1}{4}k^2 + qkx}. \quad (4.55b)$$

The recoupling coefficient  $G_{\alpha'\alpha''}$  is defined as

$$G_{\alpha'\alpha''}(q, k, x) \equiv \sum_{n=0}^{\infty} P_n(x) \sum_{\substack{l'_1+l'_2=l' \\ l''_1+l''_2=l''}} q^{l'_2+l''_2} k^{l'_1+l''_1} \cdot g_{\alpha'\alpha''}^{n l'_1 l'_2 l''_1 l''_2}, \quad (4.56)$$

with the geometrical quantity

$$g_{\alpha'\alpha''}^{n l'_1 l'_2 l''_1 l''_2} \equiv \delta_{L'L''} \delta_{M'M''} ((-1)^{l'} + (-1)^{l''}) \left( \frac{1}{2} \right)^{l'_2+l''_2+1} [n] \sqrt{[l'] [\lambda'] [l''] [\lambda'']} \sqrt{\frac{[l']!}{(2l'_1)!(2l'_2)!}} \sqrt{\frac{[l'']!}{(2l''_1)!(2l''_2)!}} \times \sum_{f', f''=0}^{\infty} \begin{bmatrix} l'_2 & \lambda' & f' \\ 0 & 0 & 0 \end{bmatrix} \begin{bmatrix} l''_2 & \lambda'' & f'' \\ 0 & 0 & 0 \end{bmatrix} \begin{bmatrix} n & l'_1 & f' \\ 0 & 0 & 0 \end{bmatrix} \begin{bmatrix} n & l''_1 & f'' \\ 0 & 0 & 0 \end{bmatrix} \left\{ \begin{matrix} l'_1 & l'_2 & l' \\ \lambda' & L' & f' \end{matrix} \right\} \left\{ \begin{matrix} l''_1 & l''_2 & l'' \\ \lambda'' & L'' & f'' \end{matrix} \right\} \left\{ \begin{matrix} f' & l'_1 & L' \\ f'' & l''_1 & n \end{matrix} \right\}, \quad (4.57)$$

where, for instance,  $[n] \equiv 2n + 1$  and  $\{\dots\}$  denote Wigner's 6- $j$  symbols.

We solve Eq. (4.53) for an  $S$ -wave projected  $1/r^3$  potential. The recoupling coefficient becomes particularly simple, namely  $G_{\alpha'\alpha''}(q, k, x) = 1$  and we obtain

$$E\psi_{00}^{00}(p, q) = \frac{1}{M} \left( \frac{3}{4}q^2 + p^2 \right) \psi_{00}^{00}(p, q) + \int dk k^2 v_0^{00}(p, k) \psi_{00}^{00}(k, q) + \int dk k^2 \int_{-1}^1 dx v_0^{00}(p, \pi_1(q, k, x)) \psi_{00}^{00}(\pi_2(q, k, x), k). \quad (4.58)$$

The projection of the potential is given in Eq. (2.49) and reads

$$v_0^{00}(p, k) = c_0 + \frac{c}{M} \frac{\pi^2}{2} \left( 1 + \frac{(p-k)^2}{4pk} \log(r_0^2(p-k)^2) - \frac{(p+k)^2}{4pk} \log(r_0^2(p+k)^2) \right). \quad (4.59)$$

As explained below Eq. (2.48), the dependence on  $r_0$  can be completely absorbed in the coupling constant  $c_0$ . We further use  $c_0$  to renormalize the two-body spectrum. The modified Faddeev equation for the  $1/r^3$  potential is then solved numerically. The three-body spectrum is shown on the left of Fig. 4.11. The shallowest two-body binding energy is renormalized to  $E_B = 1/c$ . The spectrum bears close resemblance to the three-dipole spectrum in Fig. 4.10. Also here it appears that three-body binding energies are fully determined by two-body observables.

We further compare to the spectrum obtained by solving the Faddeev equation (4.33) also projected on  $S$ -waves. The spectra agree well within numerical precision. Note that in order to find three-body binding energies using the Faddeev equation in its original formulation, the domain for the root search has to be restricted, as described above. The restriction explains the absence of the three-body bound state close to the two-body threshold for  $\lambda \lesssim 40/c$ . The runtime comparison on the right is performed for fixed cutoff  $\lambda = 50/c$  and manifests the computational advantage of Eq. (4.58). For the same number of sampling points, an algorithm employing Eq. (4.58) outperforms a similar algorithm with Eq. (4.30) at its basis by a factor of roughly 50. This factor presumably further increases when more three-body bound states are present.

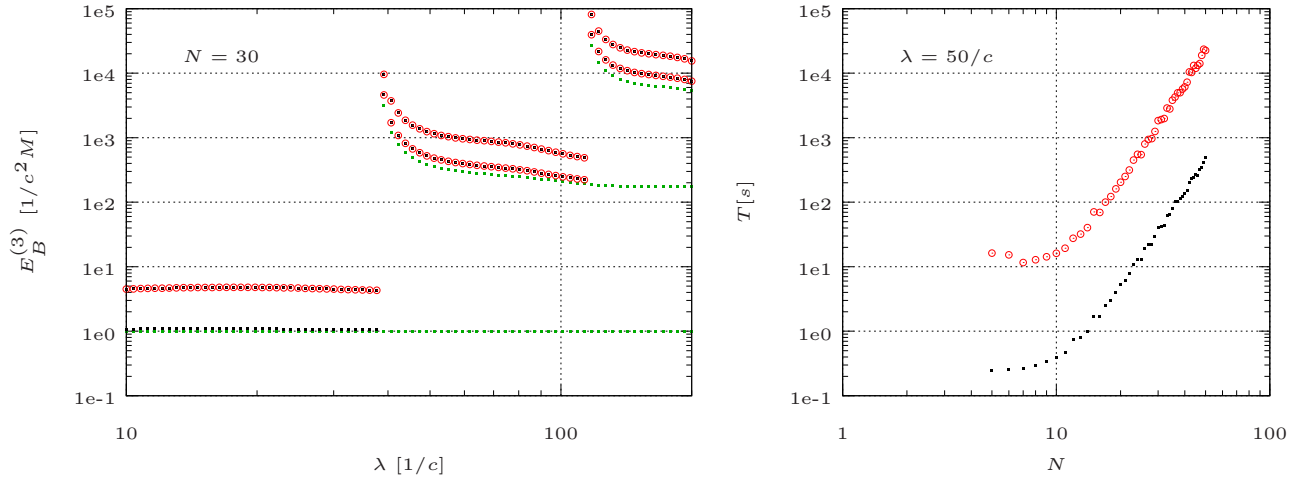


**Figure 4.11.:** Three-body bound-state spectrum and runtime comparison for the  $1/r^3$  potential. The three-body spectra are shown on the left. The green squares belong to the two-body binding energies, the black squares to the numerical solution of the S-wave projected, modified Faddeev equation (4.58). The red circles represent the spectrum obtained by solving the S-wave projection of Eq. (4.33). For the spectra on the left,  $N = 30$  sampling points were used. The right-hand side shows the dependence of the runtime of both algorithms for fixed cutoff  $\lambda = 50/c$  on the number of sampling points. Black squares again belong to the modified Faddeev equation, red circles to its original formulation.



---

## 5 Conclusion and outlook

---

In the presented thesis we studied few-body systems with tensor interactions. We focused on two examples. On the one hand, the  $X(3872)$  was thoroughly investigated. We extrapolated low-energy observables, such as the binding energy and the scattering length, to unphysical light quark masses and finite volumes. It appears that the  $X(3872)$  is most likely deeper bound for large quark masses and small volumes. Our results can also be used vice versa to extrapolate lattice results to the physical point. On the other hand, we analyzed interactions between two and three bosonic dipoles. Bound-state spectra as well as scattering lengths were presented and analyzed for various quantum numbers and dipole tunings. Dipole spectra display a rich variety of states and in comparison to pure  $S$ -wave potentials, short-range operators with anisotropic proportions have to be implemented in order to properly renormalize.

In Chap. 1 we introduced the phenomenology as well as the physical context relevant to this thesis. We further motivated the presented investigations and gave an outline.

Effective theories were subject of Chap. 2. We discussed presuppositions required to establish an effective theory. The explicit construction was demonstrated by means of various examples. We began with pure contact theories, which provide a relatively simple though widely applicable framework to describe low-energy experiments. A suitable set of short-distance operators was formulated and we discussed two methods to remove emerging ultraviolet divergences: the cutoff regularization as well as the power divergence subtraction scheme. Subsequently, the coupling constants were tuned to match to the effective range expansion. Finite volume corrections were applied afterwards. We derived an explicit expression for the shift of the binding energy when placing the before discussed system in a cubic box with periodic boundary conditions. Singular potentials possess long-range tails and can not be parametrized using contact operators. The  $1/r^2$  and  $1/r^3$  potentials represent such singular potentials. We solved the corresponding Lippmann-Schwinger equation numerically and discussed and renormalized their bound-state spectra.

A thorough analysis of chiral and finite volume extrapolations for the  $X(3872)$  was provided in Chap. 3. First, we discussed the effective field theory employed. The Lagrangian was introduced and the Feynman rules were deduced. We elaborated on the role of pions and discussed the power counting and the relevance of charged  $D$  mesons in detail. Chiral extrapolations for the binding energy and the scattering length were given in Sec. 3.2. We interpreted the  $X(3872)$  as a bound, hadronic molecule and applied the effective field theory to  $\bar{D}^0 D^{*0}$  scattering. The scattering amplitudes were calculated up to next-to-leading order and peculiarities due to on-shell pions were analyzed. We renormalized the theory at the physical point, estimated natural ranges for unknown coupling constants and provided chiral extrapolations for the binding energy and the scattering length. Our main results can be summarized as follows.

- The scattering amplitude to NLO with bare propagators is infrared divergent. A careful analysis revealed that divergences stem from on-shell pion self-energy diagrams for the  $D^{*0}$  meson. They could be cured by resumming the pion contributions to the  $D^{*0}$  propagator to all orders, inducing a finite decay width for the  $D^{*0}$ .
- Next-to-leading order contact interactions, required by power counting, are crucial to ensure a consistent renormalization.
- The effective range expansion for  $\bar{D}^0 D^{*0}$  scattering breaks down for unstable  $D^{*0}$  since constituent states are not asymptotic. The scattering length could still be usefully defined after shifting the on-shell point to complex energy. The effective range could be calculated for large light quark masses.
- The binding energy to NLO followed from a comparison to a non-perturbative expression for the scattering amplitude. A supposed momentum dependence cancels at NNLO.
- Scattering length and binding energy were obtained for light quark masses up to about twice their physical value. The  $X(3872)$  is most likely deeper bound for increasing quark masses. Moreover, the scattering length displays a cusp effect.

Section 3.3 addresses finite volume effects for the  $X(3872)$ . In addition to the light quark mass dependence, we analyzed the dependence of the binding energy on the side length of the box. We found for the  $X(3872)$  in a cubic box:

- Aforementioned infrared divergences do not occur in the finite volume since low-frequency modes are cut off, but contributions from low-energy regimes can still be large and the self-energy has to be resummed. The resummation induces a finite mass shift. Short-distance physics, on the other hand, remains unchanged.

- The range of validity of XEFT is further restricted due to on-shell three-body intermediate states. XEFT can still be applied over a wide range of light quark masses and box sizes.
- The binding energy can still be obtained with the method applied before. Moreover, an alternative approach utilizing the effective range expansion for large pion masses could be used to check for consistency.
- The  $X(3872)$  is significantly deeper bound for small volumes over the whole range of analyzed light quark masses.

In the fourth chapter we examined bosonic dipoles at ultralow temperatures. We reviewed the effective theory used to describe dipoles interacting at low energies. At its bottom is the long-range dipole-dipole interaction potential. We discussed symmetries and conservation laws of the potential and established a set of suitable quantum numbers to classify states. Opportunities to tune the interaction strength were described. Moreover, we set up suitable short-range operators. Furthermore, we regularized ultraviolet divergences and projected the potential on partial waves in cylindrical as well as spherical coordinates. Arising integral equations were solved numerically. The central results we found are:

- After projecting on cylindrical partial waves, two-dimensional, decoupled integral equations are left to solve to determine the transition amplitude.
- In a spherical coordinate system, a greater precision in the low-energy regime can be achieved since integration measures are one-dimensional. Partial waves in different channels of angular momentum couple strongly but sets of angular momentum, which dominate certain bound states, can be assigned. We established a method to determine according sets and to check for convergence.
- Whenever a new state appears, the scattering length diverges. The scattering length further reflects the coupling between channels with different angular momentum. We confirmed that the binding energy shows a universal behavior when plotting in dependence on the scattering length.
- To fully renormalize the spectrum, a linear combination of, in general, anisotropic short-distance operators has to be implemented. For each set of angular momentum, one coupling constant had to be tuned until a certain bound state was reproduced.

Afterwards, we considered non-relativistic three-body systems and particularly focused on the renormalization. To determine bound states, we solved the Faddeev equation numerically. First, for a simple example, namely for a separable potential to discuss different scenarios. Afterwards, we projected the Faddeev equation for three dipoles on cylindrical partial waves. We solved it for dipoles interacting via two-body potentials only. The main findings are

- The Faddeev equation couples different projections of angular momentum. However, if the deepest two-body bound state is dominated by a particular projection quantum number, the Faddeev equation decouples.
- The shallowest three-dipole bound states are always below two-body threshold. Whenever a new two-body bound state joins the spectrum from above, the three-dipole spectrum possesses a discontinuity.
- The three-dipole spectrum is universally determined by two-body low-energy observables. All three-body bound states align parallel to the two-body threshold.

At the end of Chap. 4 we presented a reformulation of the Faddeev equation which is numerically beneficial. For a proof of concept we applied it to the singular  $1/r^3$  potential. Similar to the dipole-dipole interactions, also for particles interacting via a  $1/r^3$  potential, the three-body spectrum is universally determined by two-body observables. We demonstrated that the modified Faddeev equation is indeed favorable when considering three-body bound-state spectra for non-separable two-body interactions.

Due to their distinct characteristics, tensor potentials display a wide variety of peculiar features which attract considerable attention, both experimentally and theoretically. Various questions are worthwhile to be addressed in future analyses.

Studies of the  $X(3872)$  within fully Galilean-invariant effective field theories are subject of ongoing work. On the one hand with a focus on chiral extrapolations utilizing analytical methods [139] and on the other hand with an emphasis on three-body  $D^0\bar{D}^0\pi$  dynamics within a numerical framework [140]. Moreover, a precise quantification of coupled channel effects for charged and neutral  $D$  mesons could further clarify the importance of charged  $D$  meson contributions. Furthermore, the inclusion of  $S$ - $D$ -wave couplings could serve as a preparation for NNLO calculations for the  $X(3872)$ . However, to improve predictions for observables by including explicit NNLO contributions to the  $\bar{D}^0D^{*0}$  scattering amplitude, it is essential to determine the next-to-leading order XEFT coupling constants. To extract them from lattice calculations, simulations performed at smaller light quark masses and larger volume are desirable. Of particular importance are precise

---

experimental determinations of the  $X$  mass and its width. The PANDA experiment [141] promises to improve currently available data for the  $X(3872)$ .

For dipolar interactions, a plausible extension is to develop a framework to describe four and more particles. But also in the two-body sector, improvement is desirable. The numerical precision of bound-state spectra for two bosonic dipoles is mainly limited by the convergence in the momentum cutoff. Modified regulator functions on the one hand and more sophisticated short-range operators, affecting multiple angular momentum channels, on the other hand, might decrease the sensitivity to the momentum cutoff. For three-dipole systems, an implementation in a spherical coordinate system, preferably with the alternative formulation of the Faddeev equation at its basis, presumably increases the resolution with which bound states are determined. For example, Efimov-like phenomena could then be quantitatively described to high precision. Moreover, coupled channel effects might play an important role if the two-body threshold is not dominated by a single angular momentum projection quantum number. Their influence on three-body dynamics might reveal new effects for three dipoles. Condensates of molecules are at the frontier of current experimental research. In particular, molecules with large electric dipole moment promise to open an entirely new field in the area of ultracold gases. Their continuous and precise tuning could allow for the observation of yet unknown quantum phenomena for many-body systems.



## A Calculations for the $X(3872)$

### A.1 Infinite volume Feynman diagrams

We derive expressions of selected Feynman diagrams. We begin with the Feynman diagrams for the infinite volume scattering amplitude.

#### A.1.1 Calculation of the $D^{*0}$ self-energy diagram

In this section we show the explicit calculations for the bare  $D^{*0}$  self-energy diagram depicted in Fig. 3.6. At the beginning we keep all spin indices and  $m_\pi/m_D$ -suppressed terms. The self-energy reads, using spin indices  $i$  and  $j$

$$-i\hat{\Sigma}_{ij}(p_0, \mathbf{p}) = \left(\frac{\Lambda}{2}\right)^{4-D} \int \frac{d^D k}{(2\pi)^D} \frac{-g^2}{2f^2} \frac{1}{2m_\pi} \frac{i}{-k_0 - k^2/2m_D + i\epsilon} \frac{i(\boldsymbol{\varepsilon}_i \cdot (\mathbf{p} + \mathbf{k}))(\boldsymbol{\varepsilon}_j^* \cdot (\mathbf{p} + \mathbf{k}))}{p_0 + k_0 - (\mathbf{p} + \mathbf{k})^2/2m_\pi + \delta + i\epsilon}. \quad (\text{A.1})$$

Performing the contour integration for  $k_0$  we obtain

$$-i\hat{\Sigma}_{ij} = \frac{-ig^2}{2f^2} \frac{1}{2m_\pi} \left(\frac{\Lambda}{2}\right)^{3-d} \int \frac{d^d k}{(2\pi)^d} \frac{(\boldsymbol{\varepsilon}_i \cdot (\mathbf{p} + \mathbf{k}))(\boldsymbol{\varepsilon}_j^* \cdot (\mathbf{p} + \mathbf{k}))}{p_0 - k^2/2m_D - (\mathbf{p} + \mathbf{k})^2/2m_\pi + \delta + i\epsilon}, \quad (\text{A.2})$$

where  $d = D - 1$ . Using a tensor decomposition for Eq. (A.2), we can replace

$$\boldsymbol{\varepsilon}_i \cdot (\mathbf{p} + \mathbf{k}) \boldsymbol{\varepsilon}_j^* \cdot (\mathbf{p} + \mathbf{k}) = (\mathbf{p} + \mathbf{k})_i \cdot (\mathbf{p} + \mathbf{k})_j \rightarrow \frac{\delta_{ij}}{3} (\mathbf{p} + \mathbf{k})^2 \quad (\text{A.3})$$

in the integral and obtain for the self-energy diagram

$$-i\hat{\Sigma}_{ij} = \frac{-ig^2}{2f^2} \frac{\delta_{ij}}{3} \left(\frac{\Lambda}{2}\right)^{3-d} \int \frac{d^d k}{(2\pi)^d} \frac{(\mathbf{p} + \mathbf{k})^2}{2m_\pi p_0 - k^2 m_\pi/m_D - (\mathbf{p} + \mathbf{k})^2 + 2m_\pi \delta + i\epsilon}. \quad (\text{A.4})$$

Though the energy as well as the momentum dependence of Eq. (A.4) is  $m_\pi/m_D$  suppressed, we first keep all terms in order to make the suppression explicit. Similar to Eq. (3.5) we utilize  $-i\hat{\Sigma}_{ij} = -\delta_{ij}i\Sigma$  and obtain

$$-i\Sigma = \frac{ig^2}{6f^2} \frac{m_{D\pi}}{m_\pi} \left(\frac{\Lambda}{2}\right)^{3-d} \frac{1}{(4\pi)^{d/2}} \left[ \frac{d}{2} \Gamma\left[\frac{-d}{2}\right] \left( p^2 \frac{m_{D\pi}}{m_\pi} \left(1 - \frac{m_{D\pi}}{m_\pi}\right) - 2m_{D\pi}(p_0 + \delta) - i\epsilon \right)^{\frac{d}{2}} \right. \\ \left. + p^2 \left(1 - \frac{m_{D\pi}}{m_\pi}\right)^2 \Gamma\left[1 - \frac{d}{2}\right] \left( p^2 \frac{m_{D\pi}}{m_\pi} \left(1 - \frac{m_{D\pi}}{m_\pi}\right) - 2m_{D\pi}(p_0 + \delta) - i\epsilon \right)^{\frac{d}{2}-1} \right], \quad (\text{A.5})$$

where  $m_{D\pi}$  is the reduced mass of the pion and the  $D^0$  meson.<sup>1</sup> We keep all terms linear in  $\beta \equiv m_\pi/m_D$

$$-i\Sigma = \frac{ig^2}{6f^2} \frac{(\Lambda/2)^{3-d}}{(4\pi)^{d/2}} \frac{d}{2} \Gamma\left[-\frac{d}{2}\right] (1-\beta)(\beta p^2 - (1-\beta)2m_\pi(p_0 + \delta) - i\epsilon)^{\frac{d}{2}}. \quad (\text{A.6})$$

Using PDS and on-shell renormalization where

$$\text{Re}\left[G^{-1}(p_0, \mathbf{p})\right]_{p_0=p^2/2m_{D^*}} = 0, \quad (\text{A.7})$$

we obtain for the on-shell counterterm

$$-i\delta_\Sigma = \frac{-ig^2}{24\pi f^2} (1-2\beta)2m_\pi \delta \Lambda + \mathcal{O}(\beta^2) = \frac{-ig^2}{24\pi f^2} \mu^2 \Lambda + \mathcal{O}(\beta), \quad (\text{A.8})$$

<sup>1</sup> We remark that  $m_{D\pi}$  differs from  $m_\pi$  only by  $m_\pi/m_D$ -suppressed terms.

where we used that  $\delta/m_\pi = \mathcal{O}(\beta)$ . Going to higher orders in  $\beta$ , momentum dependent terms have to be subtracted as well. A more thorough analysis shows that these terms first occur at  $\mathcal{O}(\beta^3)$ . Note that the first expression in Eq. (A.8) is non-analytic in the light quark masses. Counterterms as in the first equality of Eq. (A.8) can only be subtracted for fixed pion mass. Neglecting NLO terms linear in  $\beta$ , as done in the second expression, the counterterm is analytic and might be subtracted for variable quark masses, too. Since we work up to NLO and  $\beta$  suppressed NLO terms are of NNLO, we use the second expression of Eq. (A.8) as an on-shell counterterm for the  $D^{*0}$  self-energy.

Note that when going on-shell, the terms in parentheses proportional to  $p^2$  and  $p_0$  cancel each other up to order  $\beta^2$ . This cancellation implies that the decay width of the  $X$  to LO with resummed  $D^{*0}$  propagator differs from the  $D^{*0}$  meson's decay width only by  $\beta^2$  suppressed terms. Further, in the limit of the scattering length going to infinity, the  $X$  decay width coincides exactly with the  $D^{*0}$  meson's decay width.

In XEFT power counting, the self-energy counts as  $Q^3$ , coming from one loop integration, two propagators and two  $D^0 D^{*0} \pi$  couplings. When resumming the  $D^{*0}$  propagator, the self-energy comes along with energy and momentum squared, i.e. order  $Q^2$  and thus is suppressed by one order of  $Q$ . The power counting for  $D^{*0}$  propagators is therefore unaltered after resumming.

If one is interested only up to  $\mathcal{O}(\beta^0)$ , i.e. when calculating in XEFT up to NLO, the  $\beta$ -dependence of the self-energy can be dropped already in Eq. (A.4) in the denominator of the reduced propagator. The integral in Eq. (A.4) simplifies and we obtain

$$\begin{aligned} -i\Sigma &\approx \frac{ig^2}{6f^2} \left(\frac{\Lambda}{2}\right)^{3-d} \int \frac{d^d k}{(2\pi)^d} \frac{(\mathbf{p}+\mathbf{k})^2}{(\mathbf{p}+\mathbf{k})^2 - \mu^2 - i\epsilon} \\ &= \frac{ig^2}{6f^2} \left(\frac{\Lambda}{2}\right)^{3-d} \frac{1}{(4\pi)^{d/2}} \frac{d}{2} \Gamma\left[\frac{-d}{2}\right] (-\mu^2 - i\epsilon)^{\frac{d}{2}}. \end{aligned} \quad (\text{A.9})$$

We also used that the energy of the  $D^{*0}$  meson is of order  $p^2/2m_{D^*}$ . The counterterm is determined by the second expression in Eq. (A.8). We eventually obtain for the on-shell renormalized self-energy of the  $D^{*0}$  meson

$$-i\Sigma^{\text{OS}} = \begin{cases} -\frac{ig^2}{24\pi f^2} i\mu^3 & , m_\pi < \Delta, \\ 0 & , m_\pi \geq \Delta. \end{cases} \quad (\text{A.10})$$

---

### A.1.2 Calculation of $\mathcal{A}_0^{(1)}$

---

There are four Feynman diagrams belonging to the momentum dependent contact interaction contributing to the NLO  $\bar{D}^0 D^{*0}$  scattering amplitude, depicted in Fig. A.1. The tree level contribution is given by the Feynman rule in Fig. 3.1

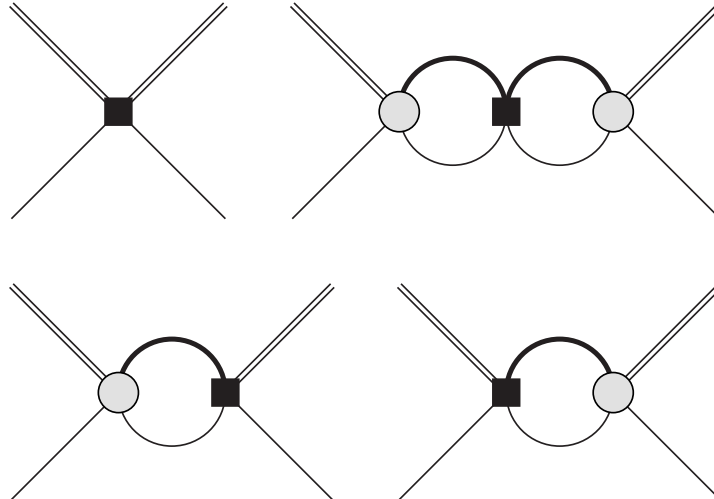


**Figure A.1.:** Momentum dependent NLO contact interaction. The notation is the same as in Fig. 3.4. In addition, the thick lines denote resummed  $D^{*0}$  propagators.

$$-i \frac{G_2}{2} (\ell^2 + \ell'^2), \quad (\text{A.11})$$

skipping the Kronecker delta for convenience. The one-loop contributions below are related to each other by exchanging the in- and outgoing relative momenta. Applying the Feynman rules and performing the contour integration in the usual fashion, we find for the sum of both diagrams

$$\begin{aligned}
& \left(\frac{\Lambda}{2}\right)^{4-D} \int \frac{d^D k}{(2\pi)^D} \frac{-iC_2}{2} (k^2 + \ell'^2) \frac{i}{E + k_0 - k^2/2m_{D^*} - \Sigma^{\text{OS}} + i\epsilon} \frac{i}{-k_0 - k^2/2m_D + i\epsilon} i\mathcal{A}_{-1} + \ell \leftrightarrow \ell' \\
&= -i \frac{C_2}{2} 2M_{DD^*} \mathcal{A}_{-1} \left(\frac{\Lambda}{2}\right)^{3-d} \int \frac{d^d k}{(2\pi)^d} \frac{2k^2 + \ell^2 + \ell'^2}{k^2 + \eta^2} \\
&= -2i \frac{C_2}{2} \left(\frac{1}{2}(\ell^2 + \ell'^2) - \eta^2\right) (-\eta + \Lambda) \frac{M_{DD^*}}{2\pi} \mathcal{A}_{-1}.
\end{aligned} \tag{A.12}$$

The expressions for  $\mathcal{A}_0^{(1)}$  simplify when going on-shell after including the two-loop contribution in Fig. A.1. The two-loop diagram does not depend on the external momenta but only on the energy through the quantity  $\eta$

$$\begin{aligned}
i\mathcal{A}_{-1} \left(\frac{\Lambda}{2}\right)^{8-2D} \int \frac{d^D k}{(2\pi)^D} \int \frac{d^D k'}{(2\pi)^D} \frac{i}{E + k_0 - k^2/2m_{D^*} - \Sigma^{\text{OS}} + i\epsilon} \frac{i}{-k_0 - k^2/2m_D + i\epsilon} \frac{-iC_2}{2} (k^2 + k'^2) \\
\times \frac{i}{E + k'_0 - k'^2/2m_{D^*} - \Sigma^{\text{OS}} + i\epsilon} \frac{i}{-k'_0 - k'^2/2m_D + i\epsilon}.
\end{aligned} \tag{A.13}$$

We use that the interaction is separable and obtain the same contribution to the transition amplitude twice

$$-i \frac{C_2}{2} (-2\eta^2) (-\eta + \Lambda)^2 \left(\frac{M_{DD^*}}{2\pi}\right)^2 (\mathcal{A}_{-1})^2. \tag{A.14}$$

Going on-shell, i.e. regarding the limit  $\ell, \ell' \rightarrow p$  and  $\eta^2 \rightarrow -p^2$  with  $2M_{DD^*}E = p^2$ , the four contributions add up to the short and simple expression

$$i\mathcal{A}_0^{(1)} = -\frac{iC_2 p^2}{C_0^2} (\mathcal{A}_{-1})^2. \tag{A.15}$$

### A.1.3 Calculation of $\mathcal{A}_0^{(II)}$

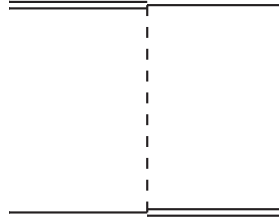


**Figure A.2.:** Tree level OPE contribution to the NLO amplitude. The notation is the same as in Fig. 3.4.

For the one-pion exchanges we begin with the tree level diagram shown in Fig. A.2. When applying the Feynman rules, expression (3.10) is obtained

$$i\hat{\mathcal{A}}_{0ij}^{(II)} = \frac{ig^2}{2f^2} \frac{(\boldsymbol{\varepsilon}_i \cdot \mathbf{q})(\boldsymbol{\varepsilon}_j^* \cdot \mathbf{q})}{q^2 - \mu^2 - i\epsilon}. \tag{A.16}$$

Since we aim to obtain the  $S$ -wave scattering amplitude, we apply the projection operator

$$\frac{1}{2} \int_{-1}^1 d(\cos \theta_{\ell\ell'}) \tag{A.17}$$

from the left, with  $\theta_{\ell\ell'}$  being the angle between the in- and outgoing relative momenta  $\ell$  and  $\ell'$ . We obtain for the  $S$ -wave projected, tree-level one-pion-exchange amplitude

$$\begin{aligned}
i\hat{\mathcal{A}}_{0ij}^{(II)} &= \frac{ig^2}{2f^2} \frac{1}{2} \int_{-1}^1 dx \frac{(\ell - \ell')_i (\ell - \ell')_j}{\ell^2 + \ell'^2 + 2\ell\ell'x - \mu^2 - i\epsilon} \\
&= \frac{\delta_{ij}}{3} \frac{ig^2}{2f^2} \left(1 + \frac{\mu^2}{4|\ell||\ell'|} \log\left(1 - \frac{4|\ell||\ell'|}{\mu^2 - (\ell^2 - \ell'^2)}\right)\right),
\end{aligned} \tag{A.18}$$

where we used substitution (A.3) to obtain the second line.

### A.1.4 Calculation of $\mathcal{A}_0^{(\text{III})}$

Here, we show the explicit calculation for the one-loop pion-exchange graphs summed up in the amplitude  $\mathcal{A}_0^{(\text{III})}$ . The diagrams are shown in Fig. A.3.

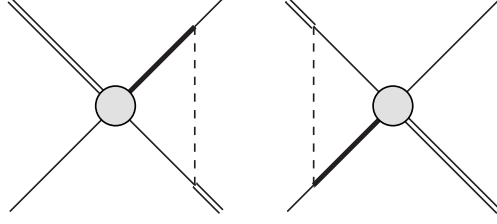


**Figure A.3.:** One-loop pion-exchange contribution to the NLO amplitude. The notation is the same as, e.g., in Fig. 3.4. In addition, the thick line denotes a resummed  $D^{*0}$  propagator.

Applying the Feynman rules, we obtain

$$i\hat{\mathcal{A}}_{0ij}^{(\text{III})} = i\mathcal{A}_{-1} \left(\frac{\Lambda}{2}\right)^{4-D} \int \frac{d^D k}{(2\pi)^D} \frac{-g^2}{2f^2} \frac{1}{2m_\pi} \frac{i}{E + k_0 - k^2/2m_{D^*} - \Sigma^{\text{OS}} + i\epsilon} \frac{i}{-k_0 - k^2/2m_D + i\epsilon} \frac{i}{E + k_0 + \ell_0 - (\ell + \mathbf{k})^2/2m_\pi + \delta + i\epsilon} + \ell \leftrightarrow \ell' \quad (\text{A.19})$$

As a next step, we perform the contour integration, use the substitution (A.3) and drop  $m_\pi/m_D$  and  $\delta/m_\pi$ -suppressed terms. Taking into account that  $E \sim \ell_0 \sim k_0 \sim Q^2/2m_D$ , we get for the scalar amplitude

$$i\mathcal{A}_0^{(\text{III})} = i\mathcal{A}_{-1} 2M_{DD^*} \frac{g^2}{6f^2} \left(\frac{\Lambda}{2}\right)^{3-d} \int \frac{d^d k}{(2\pi)^d} \frac{1}{k^2 - 2M_{DD^*}(E - \Sigma^{\text{OS}}) - i\epsilon} \left(1 + \frac{\mu^2}{(\ell + \mathbf{k})^2 - \mu^2 - i\epsilon}\right) + \ell \leftrightarrow \ell' \quad (\text{A.20})$$

with  $d = D - 1$ . We use PDS to regularize UV divergences. Evaluating the first term in parentheses results in  $I_0$  from Eq. (3.6) with  $E$  replaced with  $E - \Sigma^{\text{OS}}$ . For the second term, we use Feynman parameters

$$\begin{aligned} T^{(\text{III})}(\eta^2, |\ell|, \mu^2) &\equiv \left(\frac{\Lambda}{2}\right)^{3-d} \int \frac{d^d k}{(2\pi)^d} \frac{1}{k^2 + \eta^2} \frac{1}{(\ell + \mathbf{k})^2 - \mu^2 - i\epsilon} \\ &= \frac{1}{8\pi} \int_0^1 dx [x(1-x)\ell^2 + (1-x)\eta^2 - x\mu^2 - i\epsilon]^{-\frac{1}{2}} \\ &= \frac{1}{8\pi} \frac{i}{|\ell|} \log\left(1 + \frac{2|\ell|}{i\eta + \mu - |\ell|}\right) \end{aligned} \quad (\text{A.21})$$

and eventually obtain for the NLO scattering amplitude  $\mathcal{A}_0^{(\text{III})}$

$$i\mathcal{A}_0^{(\text{III})} = \frac{ig^2}{3f^2} \left( (-\eta + \Lambda) + \mu^2 \left( \frac{i}{4|\ell|} \log\left(1 + \frac{2|\ell|}{i\eta + \mu - |\ell|}\right) + \ell \leftrightarrow \ell' \right) \right) \frac{M_{DD^*}}{2\pi} \mathcal{A}_{-1}. \quad (\text{A.22})$$

### A.1.5 Calculation of $\mathcal{A}_0^{(\text{IV})}$

The two-loop pion-exchange contribution to the NLO amplitude is depicted in Fig. A.4.

We use the Feynman rules to acquire

$$i\hat{\mathcal{A}}_{0ij}^{(\text{IV})} = i\mathcal{A}_{-1} \left(\frac{\Lambda}{2}\right)^{8-2D} \int \frac{d^D k}{(2\pi)^D} \int \frac{d^D k'}{(2\pi)^D} \frac{-g^2}{2f^2} \frac{1}{2m_\pi} \frac{i}{E + k_0 - k^2/2m_{D^*} - \Sigma^{\text{OS}} + i\epsilon} \frac{i}{-k_0 - k^2/2m_D + i\epsilon} \frac{i}{E + k_0 + k'_0 - (\mathbf{k} + \mathbf{k}')^2/2m_\pi + \delta + i\epsilon} \frac{i}{E + k'_0 - k'^2/2m_{D^*} - \Sigma^{\text{OS}} + i\epsilon} \frac{i}{-k'_0 - k'^2/2m_D + i\epsilon} i\mathcal{A}_{-1}. \quad (\text{A.23})$$

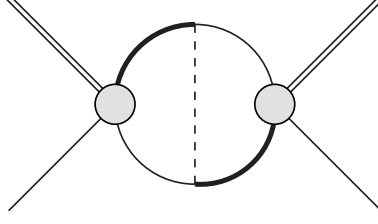


**Figure A.4.:** Two-loop pion-exchange contribution to the NLO amplitude. The notation is the same as in Fig. 3.4. In addition, the thick lines denote resummed  $D^{*0}$  propagators.

We proceed in analogy to Sec. A.1.4, i.e. perform the contour integrations, factor out the spin dependence and drop  $m_\pi/m_D$  suppressed terms. The scalar amplitude reads

$$i\mathcal{A}_0^{(\text{IV})} = \frac{ig^2}{6f^2} (2M_{DD^*})^2 (\mathcal{A}_{-1})^2 \left(\frac{\Lambda}{2}\right)^{6-2d} \int \frac{d^d k}{(2\pi)^d} \int \frac{d^d k'}{(2\pi)^d} \frac{1}{k^2 + \eta^2} \frac{1}{k'^2 + \eta^2} \left(1 + \frac{\mu^2}{(\mathbf{k} + \mathbf{k}')^2 - \mu^2 - i\epsilon}\right). \quad (\text{A.24})$$

The reduced  $\bar{D}^0 D^{*0}$  propagators separate in  $|\mathbf{k}|$  and  $|\mathbf{k}'|$  and the integrals can be evaluated independently, resulting in a contribution of  $I_0^2$ , again with  $E$  replaced with  $E - \Sigma^{\text{OS}}$ . For the second term, we separate the UV divergent part

$$\begin{aligned} T^{(\text{IV})}(\eta, \mu) &\equiv \left(\frac{\Lambda}{2}\right)^{6-2d} \int \frac{d^d k}{(2\pi)^d} \int \frac{d^d k'}{(2\pi)^d} \frac{1}{k^2 + \eta^2} \frac{1}{k'^2 + \eta^2} \frac{1}{(\mathbf{k} + \mathbf{k}')^2 - \mu^2 - i\epsilon} \\ &= \underbrace{T^{(\text{IV})}(\eta, \mu) - T^{(\text{IV})}(\eta, 0)}_{\text{UV finite}} + \underbrace{T^{(\text{IV})}(\eta, 0)}_{\text{UV divergent}}. \end{aligned} \quad (\text{A.25})$$

We begin with the evaluation of  $T^{(\text{IV})}(\eta, 0)$

$$\begin{aligned} T^{(\text{IV})}(\eta, 0) &= \left(\frac{\Lambda}{2}\right)^{6-2d} \int \frac{d^d k}{(2\pi)^d} \int \frac{d^d k'}{(2\pi)^d} \frac{1}{k^2 + \eta^2} \frac{1}{k'^2 + \eta^2} \frac{1}{(\mathbf{k} + \mathbf{k}')^2 - i\epsilon} \\ &= \left(\frac{\Lambda}{2}\right)^{6-2d} \frac{\Gamma[3-d]}{(4\pi)^d} (\eta^2)^{d-3} \int_0^1 dx (x(1-x))^{1-\frac{d}{2}} \int_0^1 dy y^{\frac{d}{2}-2} \\ &\xrightarrow{d \rightarrow 3} \frac{1}{(4\pi)^2} \frac{1}{2} \left(1 + \log\left(\frac{\pi}{4}\right) - \gamma_E + \log\left(\frac{\Lambda^2}{\eta^2}\right)\right) \end{aligned} \quad (\text{A.26})$$

and further obtain for the UV finite part, already taking the limit  $d \rightarrow 3$  ( $D \rightarrow 4$ )

$$\begin{aligned} T^{(\text{IV})}(\eta, \mu) - T^{(\text{IV})}(\eta^2, 0) &= \int \frac{d^3 k}{(2\pi)^3} \int \frac{d^3 k'}{(2\pi)^3} \frac{1}{k^2 + \eta^2} \frac{1}{k'^2 + \eta^2} \left(\frac{1}{(\mathbf{k} + \mathbf{k}')^2 - \mu^2 - i\epsilon} - \frac{1}{(\mathbf{k} + \mathbf{k}')^2 - i\epsilon}\right) \\ &= \int \frac{d^3 k}{(2\pi)^3} \frac{\mu^2}{k^2 - \mu^2 - i\epsilon} \frac{1}{k^2} \int_0^1 dx \frac{\Gamma[\frac{1}{2}]}{(4\pi)^{\frac{3}{2}}} [x(1-x)k^2 + \eta^2 - i\epsilon]^{-\frac{1}{2}} \\ &= \frac{1}{(2\pi)^3} \int_0^\infty dq \frac{\mu^2}{q^2 - \mu^2 - i\epsilon} \frac{1}{q} \text{acot}\left(\frac{2\eta}{q}\right) \\ &= \frac{1}{(4\pi)^2} \frac{1}{2} \left(\log(4) + \log\left(\frac{\eta^2}{(2\eta - i\mu)^2}\right)\right). \end{aligned} \quad (\text{A.27})$$

Combining Eqs. (A.26) and (A.27), the result for  $T^{(\text{IV})}(\eta, \mu)$  reads

$$T^{(\text{IV})}(\eta, \mu) = \frac{1}{(4\pi)^2} \left(\frac{1}{2} + \frac{1}{2}(\log(\pi) - \gamma_E) + \log\left(\frac{\Lambda}{2\eta - i\mu}\right)\right) \quad (\text{A.28})$$

and we obtain for the scalar amplitude  $\mathcal{A}_0^{(\text{IV})}$

$$\begin{aligned} i\mathcal{A}_0^{(\text{IV})} &= \frac{ig^2}{6f^2} (2M_{DD^*})^2 (\mathcal{A}_{-1})^2 \left( (I_0(E - \Sigma^{\text{OS}}))^2 + \mu^2 T^{(\text{IV})}(\eta, \mu) \right) \\ &= \frac{ig^2}{6f^2} \left(\frac{M_{DD^*}}{2\pi}\right)^2 (\mathcal{A}_{-1})^2 \left( (-\eta + \Lambda)^2 + \mu^2 \left(\frac{1}{2} + R + \log\left(\frac{\Lambda}{2\eta - i\mu}\right)\right) \right), \end{aligned} \quad (\text{A.29})$$

with  $R \equiv (\log(\pi) - \gamma_E)/2$ .

## A.2 Finite volume Feynman diagrams

Here, we derive the explicit expression for the finite volume Feynman diagram  $\mathcal{A}_{0(\text{IV})}^L$ .

### A.2.1 Calculation of $\mathcal{A}_{0(\text{IV})}^L$

The OPE amplitude  $\mathcal{A}_0^{(\text{IV})}$  is depicted in Fig. 3.4. We begin with the unregularized expression in the infinite volume

$$i\mathcal{A}_{0ij}^{(\text{IV})} = -i\mathcal{A}_{-1}^2 \frac{g^2}{2f^2} \frac{1}{2m_\pi} \int \frac{dk_0}{2\pi i} \int \frac{dk'_0}{2\pi i} \int \frac{d^3\mathbf{k}}{(2\pi)^3} \int \frac{d^3\mathbf{k}'}{(2\pi)^3} \frac{1}{E+k_0-k^2/2m_{D^*}+i\epsilon} \frac{1}{k_0+k^2/2m_D-i\epsilon} \frac{\boldsymbol{\varepsilon}_i \cdot (\mathbf{k}+\mathbf{k}') \boldsymbol{\varepsilon}_j^* \cdot (\mathbf{k}+\mathbf{k}')}{E+k_0+k'_0-|\mathbf{k}+\mathbf{k}'|^2/2m_\pi+\delta+i\epsilon} \frac{1}{E+k'_0-k'^2/2m_{D^*}+i\epsilon} \frac{1}{k'_0+k'^2/2m_D-i\epsilon}. \quad (\text{A.30})$$

To transition to the finite volume we replace the spatial integrations by sums over the allowed lattice momenta

$$\int \frac{d^3\mathbf{k}}{(2\pi)^3} \xrightarrow{V \rightarrow L^3} \frac{1}{L^3} \sum_{\mathbf{k}=\frac{2\pi}{L}\mathbf{n}}. \quad (\text{A.31})$$

At the same time we keep the contour integration over the time component since lattice simulations are usually performed with significantly larger time than spatial interval. We acquire

$$i\mathcal{A}_{0(\text{IV})ij}^L = i(\mathcal{A}_{-1}^L)^2 \frac{g^2}{2(f^L)^2} \frac{1}{L^3} \sum_{\mathbf{k}=\frac{2\pi}{L}\mathbf{n}} \frac{1}{L^3} \sum_{\mathbf{k}'=\frac{2\pi}{L}\mathbf{n}'} \frac{1}{E-k^2/2M_{DD^*}^L} \frac{1}{E-k'^2/2M_{DD^*}^L} \frac{\boldsymbol{\varepsilon}_i \cdot (\mathbf{k}+\mathbf{k}') \boldsymbol{\varepsilon}_j^* \cdot (\mathbf{k}+\mathbf{k}')}{|\mathbf{k}+\mathbf{k}'|^2 - 2m_\pi \delta^L - 2m_\pi E - \frac{m_\pi}{m_D}(k^2+k'^2)}. \quad (\text{A.32})$$

As a next step, we evaluate at an energy  $E = p^2/2M_{DD^*}^L$ , neglect terms proportional to  $m_\pi/m_D$  and  $\delta^L/m_\pi$ , respectively, use a tensor decomposition to replace

$$\boldsymbol{\varepsilon}_i \cdot (\mathbf{k}+\mathbf{k}') \boldsymbol{\varepsilon}_j^* \cdot (\mathbf{k}+\mathbf{k}') \rightarrow \frac{\delta_{ij}}{3} |\mathbf{k}+\mathbf{k}'|^2 \quad (\text{A.33})$$

and express the lattice momenta  $\mathbf{k}$  and  $\mathbf{k}'$  in terms of  $\mathbf{n}$  and  $\mathbf{n}'$ . We get for the scalar amplitude

$$i\mathcal{A}_{0(\text{IV})}^L \approx i(\mathcal{A}_{-1}^L)^2 \frac{g^2}{6(f^L)^2} \left(\frac{M_{DD^*}^L}{2\pi}\right)^2 \frac{1}{(\pi L)^2} \sum_{\mathbf{n}, \mathbf{n}'} \frac{1}{n^2 - \left(\frac{Lp}{2\pi}\right)^2} \frac{1}{n'^2 - \left(\frac{Lp}{2\pi}\right)^2} \frac{|\mathbf{n}+\mathbf{n}'|^2}{|\mathbf{n}+\mathbf{n}'|^2 - \left(\frac{L\mu^L}{2\pi}\right)^2}. \quad (\text{A.34})$$

To renormalize, we introduce a cutoff  $\lambda_n$  for the sum, add and subtract the infinite volume loop integrals evaluated at zero energy, one regularized using a cutoff and the other one using PDS and take the limit  $\lambda_n \rightarrow \infty$

$$i\mathcal{A}_{0(\text{IV})}^L = i(\mathcal{A}_{-1}^L)^2 \frac{g^2}{6(f^L)^2} \left(\frac{M_{DD^*}^L}{2\pi}\right)^2 \left[ \left( \frac{1}{\pi L} S\left(\left(\frac{Lp}{2\pi}\right)^2\right) + \Lambda \right)^2 + (\mu^L)^2 \left( \frac{1}{(2\pi^2)^2} S^{(\text{IV})}\left(\left(\frac{Lp}{2\pi}\right)^2, \left(\frac{L\mu^L}{2\pi}\right)^2\right) + \log\left(\frac{\Lambda}{|\mu^L|}\right) + \frac{1}{2} + R \right) \right]. \quad (\text{A.35})$$

The quantity  $S(x)$  is defined in Eq. (3.46) and  $S_{(\text{IV})}(x, y)$  is given as

$$S^{(\text{IV})}(x, y) \equiv \lim_{\lambda_n \rightarrow \infty} \left[ \sum_{\mathbf{n}, \mathbf{n}'}^{|\mathbf{n}|, |\mathbf{n}'| < \lambda_n} \frac{1}{n^2 - x} \frac{1}{n'^2 - x} \frac{1}{|\mathbf{n}+\mathbf{n}'|^2 - y} - 2\pi^4 \left( \log\left(\frac{\lambda_n^2}{|y|}\right) - 1 + \mathcal{O}\left(\log\left(\frac{\lambda_n^2}{|y|}\right) \cdot \frac{|y|}{\lambda_n^2}\right) \right) \right]. \quad (\text{A.36})$$

For the cutoff regularized integral, we expanded in  $\mu/\lambda$

$$\begin{aligned} & \int d^3\mathbf{k} \int d^3\mathbf{k}' \frac{\theta(\lambda - |\mathbf{k}|)}{k^2} \frac{\theta(\lambda - |\mathbf{k}'|)}{k'^2} \frac{1}{|\mathbf{k} + \mathbf{k}'|^2 - \mu^2 - i\epsilon} \\ &= \log\left(\frac{\lambda^2}{\mu^2}\right) \left( I_0^{(1)} + I_1^{(1)} \frac{\mu}{\lambda} + I_2^{(1)} \frac{\mu^2}{\lambda^2} + \mathcal{O}\left(\frac{\mu^3}{\lambda^3}\right) \right) + I_0^{(2)} + I_1^{(2)} \frac{\mu}{\lambda} + I_2^{(2)} \frac{\mu^2}{\lambda^2} + \mathcal{O}\left(\frac{\mu^3}{\lambda^3}\right) \end{aligned} \quad (\text{A.37})$$

and found for the coefficients

$$\begin{aligned} I_0^{(1)} &= 2\pi^4, & I_0^{(2)} &= 2\pi^4(-1 + i\pi), \\ I_1^{(1)} &= 0, & I_1^{(2)} &= -8i\pi^3, \\ I_2^{(1)} &= -2\pi^2, & I_2^{(2)} &= -2\pi^2(1 + i\pi + \log(4)). \end{aligned} \quad (\text{A.38})$$

### A.3 Shift of the particle mass from a non-relativistic self-energy

Comparing the Feynman-diagram in Fig. A.5 with non-relativistic, bare propagators  $G_0^{nr}$  to the one with relativistic, bare propagators  $G_0^r$  in the non-relativistic limit, we get the relations

$$G_0^r \approx \frac{1}{2m} G_0^{nr} \quad \text{and} \quad M^2 \approx 2m\Sigma, \quad (\text{A.39})$$

with the relativistic self-energy  $M^2$ , the non-relativistic self-energy  $\Sigma$  and the particle mass  $m$ .

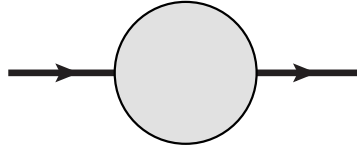


Figure A.5.: Lowest-order self-energy insertion.

We obtain the relativistic, full propagator,  $iG^r$ , by resumming

$$iG^r = iG_0^r + iG_0^r(-iM^2)iG^r = \frac{i}{p^2 - m^2 - M^2 + i\epsilon}. \quad (\text{A.40})$$

The denominator reads

$$\left( p_0^r - \sqrt{m^2 + p^2 + 2m\Sigma_r + 2m\Sigma_i} + i\epsilon \right) \left( p_0^r + \sqrt{m^2 + p^2 + 2m\Sigma_r + 2m\Sigma_i} \right) \equiv t_1 \cdot t_2, \quad (\text{A.41})$$

with  $\Sigma_r \equiv \text{Re}(\Sigma)$ ,  $\Sigma_i \equiv i \text{Im}(\Sigma)$  and the relativistic energy  $p_0^r$ .

Now, we transition to the non-relativistic limit (assume  $\Sigma_r, |\Sigma_i| \ll m$  and keep the first order only)

$$\begin{aligned} t_1 &= p_0^r - \left[ (m + \Sigma_r)^2 - \Sigma_r^2 + p^2 + 2m\Sigma_i \right]^{\frac{1}{2}} + i\epsilon \\ &\approx p_0^r - (m + \Sigma_r) \left[ 1 + \frac{p^2 + 2m\Sigma_i}{2(m + \Sigma_r)^2} - \frac{\Sigma_r^2}{2(m + \Sigma_r)^2} \right] + i\epsilon \\ &\approx p_0^r - (m + \Sigma_r) - \frac{p^2}{2(m + \Sigma_r)} - \Sigma_i + i\epsilon. \end{aligned} \quad (\text{A.42})$$

We define the non-relativistic energy to be  $p_0^{nr} \equiv p_0^r - (m + \Sigma_r)$  and similar to Eq. (A.42) follows

$$t_2 \approx 2(m + \Sigma_r). \quad (\text{A.43})$$

We eventually obtain

$$iG^r \approx \frac{1}{2(m + \Sigma_r)} iG^{nr} \equiv \frac{1}{2(m + \Sigma_r)} \frac{i}{p_0^{nr} - \frac{p^2}{2(m + \Sigma_r)} - \Sigma_i + i\epsilon}. \quad (\text{A.44})$$

Thus we identify  $\Sigma_r$  with a mass shift and  $2i\Sigma_i$  with a (partial) decay width. One could also apply all steps backwards, starting from the non-relativistic theory, by adding suppressed terms.



## B Dipole systems

### B.1 Fourier transform of the dipole-dipole potential

There are different approaches in order to calculate the Fourier transform of the potential in Eq. (4.3). At first we present an approach, rewriting the dipole potential with gradients acting on the Coulomb potential [83]

$$U_{dd}(\mathbf{r}) = -\mathbf{d} \cdot \nabla \left( \mathbf{d} \cdot \nabla \frac{1}{r} \right) - d^2 \frac{4\pi}{3} \delta(\mathbf{r}). \quad (\text{B.1})$$

The Fourier transform can be evaluated using partial integrations

$$\begin{aligned} V_{dd}(\mathbf{q}) &= - \int d^3r \left\{ e^{i\mathbf{q}\cdot\mathbf{r}} \mathbf{d} \cdot \nabla \left( \mathbf{d} \cdot \nabla \frac{1}{r} \right) \right\} - \frac{4\pi}{3} d^2 \\ &= (\mathbf{d} \cdot \mathbf{q})^2 \int d^3r \left\{ \frac{e^{i\mathbf{q}\cdot\mathbf{r}}}{r} \right\} - \frac{4\pi}{3} d^2 \\ &= \frac{4\pi}{3} \frac{-q^2 d^2 + 3(\mathbf{d} \cdot \mathbf{q})^2}{q^2}, \end{aligned} \quad (\text{B.2})$$

where we used the well known expression for the Fourier transform of the Coulomb potential from the second to the third line. The last line is proportional to the spherical harmonic  $Y_{20}(\Omega_q)$ . This dependence motivates a second ansatz which is particularly useful when regularizing the dipole potential, for example, with a Gaussian cutoff. Since we apply regulators in momentum space, we perform the Fourier transform backwards, i.e. from momentum to coordinate space. We begin with the regularized potential from Eqs. (4.5) and (4.7)

$$V_{dd}^{\text{reg}}(\mathbf{q}) = D \sqrt{\frac{16\pi}{5}} Y_{20}(\Omega_q) e^{-(\ell^2 + \ell'^2)/\lambda^2}. \quad (\text{B.3})$$

The regulator still depends on the relative in- and outgoing momenta  $\ell$  and  $\ell'$ . Thus, we rewrite the dependence using  $\mathbf{q} = \ell - \ell'$  and  $\mathbf{Q} = \ell + \ell'$ , so that  $\ell^2 + \ell'^2 = q^2/2 + Q^2/2$ . We factorize the exponential and focus on the  $\mathbf{q}$  dependence since the Fourier transform of the Gaussian of  $\mathbf{Q}$  is also in coordinate space a Gaussian and just an overall factor. In summary we have

$$U_{dd}^{\text{reg}}(\mathbf{r}) = \int \frac{d^3q}{(2\pi)^3} e^{-i\mathbf{q}\cdot\mathbf{r}} D \sqrt{\frac{16\pi}{5}} Y_{20}(\Omega_q) e^{-q^2/2\lambda^2}. \quad (\text{B.4})$$

To evaluate expression (B.4) we use the plane wave expansion

$$\begin{aligned} U_{dd}^{\text{reg}}(\mathbf{r}) &= D \sqrt{\frac{16\pi}{5}} \int \frac{d\Omega_q}{(2\pi)^3} \int_0^\infty dq q^2 4\pi \underbrace{\sum_{n=0}^\infty \sum_{m=-n}^n (-i)^n j_n(qr) Y_{nm}^*(\Omega_q) Y_{nm}(\Omega_r) Y_{20}(\Omega_q)}_{e^{-i\mathbf{q}\cdot\mathbf{r}}} e^{-q^2/2\lambda^2} \\ &= \underbrace{-D \sqrt{\frac{16\pi}{5}} \frac{Y_{20}(\Omega_r)}{r^3}}_{U_{dd}(\mathbf{r})} \cdot \underbrace{\frac{2}{3\pi} \int_0^\infty dy y^2 j_2(y) e^{-y^2/2(r\lambda)^2}}_{\hat{f}^R(r)}, \end{aligned} \quad (\text{B.5})$$

where we used the orthogonality of the spherical harmonics. The  $j_2(y)$  is the spherical Bessel function of first kind. We separated the expression to identify the unregularized dipole-dipole potential and correspondingly the regulator function in coordinate space. The integral can be evaluated explicitly to yield

$$\hat{f}^R(r) = 1 - \left[ \sqrt{\frac{2}{\pi}} \left( r\lambda + \frac{(r\lambda)^3}{3} \right) e^{-(r\lambda)^2/2} + \text{erfc} \left( \frac{r\lambda}{\sqrt{2}} \right) \right], \quad (\text{B.6})$$

with the complementary error function  $\text{erfc}$ . The regulator function is smooth, monotonic, positive definite and does not oscillate. Properties which are advantageous when treating the dipole-dipole problem numerically. It is depicted in Fig. B.1. For  $r \rightarrow \infty$ ,  $\hat{f}^R(r) \rightarrow 1$  and for  $r \rightarrow 0$ ,  $\hat{f}^R(r) \rightarrow 0$ . These limits imply that the regulator in coordinate space cuts off contributions from physics at short distances whereas long-distance physics remains unchanged. We show it for two different values of the momentum cutoff  $\lambda$ . It illustrates how short-distance cutoffs are connected with large-momentum cutoffs and vice versa. When increasing the cutoff, high-momentum, or equivalently short-distance degrees of freedom are brought back into the theory.

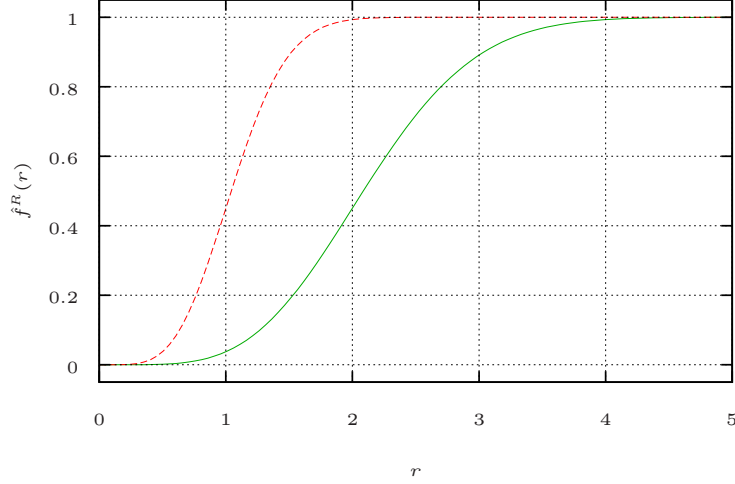


**Figure B.1.:** Gaussian regulator function in coordinate space. The momentum cutoff is set to  $\lambda = 1$  for the green, solid line and to  $\lambda = 2$  for the red, dashed line.

## B.2 Partial wave expansions

### B.2.1 Cylindrical coordinates

In this section we expand the (long-range) dipole-dipole potential in a cylindrical basis. The partial waves for the short-range interaction are derived in section Sec. B.2.3. To expand in cylindrical coordinates we define as basis functions

$$y_m(\phi) \equiv e^{im\phi} / \sqrt{2\pi}, \quad (\text{B.7})$$

with the azimuthal angle  $\phi$ . They are orthonormal and complete on  $\phi \in [0, 2\pi)$

$$\int_0^{2\pi} d\phi y_m(\phi) y_n^*(\phi) = \delta_{mn}, \quad (\text{B.8})$$

$$\sum_{m=-\infty}^{\infty} y_m(\phi) y_m^*(\phi') = \delta(\phi - \phi'). \quad (\text{B.9})$$

To expand, we rewrite the dipole-dipole potential using a cylindrical basis, i.e. using

$$\underline{\ell} = \begin{pmatrix} \ell_\rho \cos(\phi_\ell) \\ \ell_\rho \sin(\phi_\ell) \\ \ell_z \end{pmatrix}. \quad (\text{B.10})$$

We obtain

$$\begin{aligned} V_{dd}(\mathbf{q}) &= D \left( -1 + \frac{3(\ell_z - \ell'_z)^2}{(\ell_z - \ell'_z)^2 + \ell_\rho^2 + \ell'^2_\rho - 2\ell_\rho \ell'_\rho \cos(\phi_\ell - \phi_{\ell'})} \right) \\ &\equiv D \left( -1 + \frac{3c_2(\underline{\ell}, \underline{\ell}')}{1 - c_1(\underline{\ell}, \underline{\ell}') \cos(\phi_\ell - \phi_{\ell'})} \right), \end{aligned} \quad (\text{B.11})$$

where we defined the functions

$$c_1(\underline{\ell}, \underline{\ell}') \equiv \frac{2\ell_\rho \ell'_\rho}{(\ell_z - \ell'_z)^2 + \ell_\rho^2 + \ell'^2_\rho}, \quad c_2(\underline{\ell}, \underline{\ell}') \equiv \frac{(\ell_z - \ell'_z)^2}{(\ell_z - \ell'_z)^2 + \ell_\rho^2 + \ell'^2_\rho}. \quad (\text{B.12})$$

The quantities  $\underline{\ell} \equiv (\ell_\rho, \ell_z)$  ( $\underline{\ell}' \equiv (\ell'_\rho, \ell'_z)$ ) denote the radial- and z-component of  $\ell$  ( $\ell'$ ). We use the completeness relation (B.9) to expand the potential as

$$V_{dd}(\mathbf{q}) = \sum_{m=-\infty}^{\infty} v_m^{dd}(\underline{\ell}, \underline{\ell}') y_m(\phi_\ell) y_m^*(\phi_{\ell'}). \quad (\text{B.13})$$

To extract the partial waves we use the orthogonality relation (B.8)

$$v_m^{dd}(\underline{\ell}, \underline{\ell}') = \int_0^{2\pi} d\phi_\ell d\phi_{\ell'} y_m^*(\phi_\ell) y_m(\phi_{\ell'}) V_{dd}(\mathbf{q}) = \int_0^{2\pi} d\phi \cos(m\phi) D \left( -1 + \frac{3c_2(\underline{\ell}, \underline{\ell}')}{1 - c_1(\underline{\ell}, \underline{\ell}') \cos(\phi)} \right). \quad (\text{B.14})$$

Note that the potential depends on the cosine of the relative angle  $\phi \equiv \phi_\ell - \phi_{\ell'}$  only. Therefore, the sine proportion of the exponential yields zero, implying that the partial waves are real valued. The first,  $\phi$ -independent term contributes for  $m = 0$  only. For the second term we use that  $v_m(\underline{\ell}, \underline{\ell}') = v_{-m}(\underline{\ell}, \underline{\ell}')$ . Hence, it is sufficient to evaluate Eq. (B.14) for  $m \geq 0$ . Omitting the factor of  $3c_2(\underline{\ell}, \underline{\ell}')$  and the momentum dependence of  $c_1$ , we show by induction

$$f_m \equiv \int_0^{2\pi} d\phi \frac{e^{im\phi}}{1 - c_1 \cos(\phi)} = \frac{2\pi}{\sqrt{1 - c_1^2}} \frac{1}{c_1^{|m|}} \left( 1 - \sqrt{1 - c_1^2} \right)^{|m|}. \quad (\text{B.15})$$

For  $m = 0$  and  $m = 1$ , expression (B.15) is a standard integral, which can be found in the literature [142].<sup>1</sup> For  $m \rightarrow m+1$  we factorize the exponential and use

$$e^{i\phi} = -\frac{2}{c_1} (1 - c_1 \cos(\phi)) + \frac{2}{c_1} - e^{-i\phi}, \quad (\text{B.16})$$

to obtain the recursive relation

$$f_{m+1} = \frac{2}{c_1} f_m - f_{m-1}, \quad (\text{B.17})$$

completing the induction step together with relation (B.15). In summary we have for the partial wave projected potential

$$v_m^{dd}(\underline{\ell}, \underline{\ell}') = 2\pi D \left( -\delta_{m0} + \frac{3c_2(\underline{\ell}, \underline{\ell}')}{\sqrt{1 - c_1^2(\underline{\ell}, \underline{\ell}')}} \frac{1}{c_1^{|m|}(\underline{\ell}, \underline{\ell}')} \left( 1 - \sqrt{1 - c_1^2(\underline{\ell}, \underline{\ell}')} \right)^{|m|} \right). \quad (\text{B.18})$$

The full potential is the sum of the short-range and the long-range part. We derive the partial wave projection of the short-range part in Sec. B.2.3 and use as the full, partial wave projected and regularized potential  $v_m$  for now. Further, we expand the scattering amplitude

$$T(E, \ell, \ell') = \sum_{m=-\infty}^{\infty} t_m(E, \ell, \ell') y_m(\phi_\ell) y_m^*(\phi_{\ell'}) \quad (\text{B.19})$$

and perform the angular integrations in the LS equation, again using the orthogonality relation (B.8). We obtain a system of fully decoupled integral equations in two dimensions

$$t_m(E, \underline{\ell}, \underline{\ell}') = -v_m(\underline{\ell}, \underline{\ell}') + \int d^2\mathbf{k} v_m(\underline{\ell}, \mathbf{k}) \frac{k_\rho}{E - k^2/M + i\epsilon} t_m(E, \mathbf{k}, \underline{\ell}'), \quad (\text{B.20})$$

where we used that  $\mathbf{k}^2 = k^2 = \underline{\mathbf{k}}^2$ .

---

## B.2.2 Spherical coordinates

---

For the spherical expansion we proceed in analogy to the cylindrical case. As orthonormal and complete set of basis functions we use spherical harmonics. We exploit the completeness of the spherical harmonics to expand the potential

$$V_{dd}(\mathbf{q}) = \sum_{l_1, l_2=0}^{\infty} \sum_m v_{dd}^{m, l_1, l_2}(\ell, \ell') Y_{l_1, m}(\Omega_\ell) Y_{l_2, m}^*(\Omega_{\ell'}). \quad (\text{B.21})$$

In spherical coordinates it is convenient to use the last expression for the potential in Eq. (4.5)

$$V_{dd}(\mathbf{q}) = D \sqrt{\frac{16\pi}{5}} Y_{20}(\Omega_q). \quad (\text{B.22})$$

<sup>1</sup> The use of the exponential instead of the cosine in Eq. (B.15) is convenient for the induction step.

At first we rewrite the potential employing the equality [143]

$$q^2 Y_{20}(\Omega_q) = \sqrt{4\pi \cdot 5!} \sum_{\substack{n_1, n_2=0 \\ n_1+n_2=2}}^2 (-1)^{n_2} \frac{\ell^{n_1} \ell'^{n_2}}{\sqrt{(2n_1+1)!(2n_2+1)!}} \sum_{\substack{n_1, n_2 \\ s_1=-n_1 \\ s_2=-n_2}} \begin{bmatrix} n_1 & n_2 & 2 \\ s_1 & s_2 & 0 \end{bmatrix} Y_{n_1 s_1}(\Omega_\ell) Y_{n_2 s_2}(\Omega_{\ell'}), \quad (\text{B.23})$$

with [...] being Clebsch-Gordan coefficients. To compensate for the additional factor of  $q^2$  we expand its inverse in a series of Legendre polynomials

$$\frac{1}{q^2} = \frac{1}{2\ell\ell'} \frac{1}{\frac{\ell^2+\ell'^2}{2\ell\ell'} - \cos(\theta_{\ell\ell'})} = \frac{1}{2\ell\ell'} \sum_{\sigma=0}^{\infty} \sum_{m_\sigma=-\sigma}^{\sigma} \frac{4\pi}{2\sigma+1} \alpha_\sigma(z) Y_{\sigma m_\sigma}(\Omega_\ell) Y_{\sigma m_\sigma}^*(\Omega_{\ell'}), \quad (\text{B.24})$$

with  $\theta_{\ell\ell'} = \angle(\ell, \ell')$ ,  $z \equiv \ell'/\ell$  and

$$\alpha_\sigma(z) \equiv \frac{2\sigma+1}{2} \int_{-1}^1 dx \frac{P_\sigma(x)}{\frac{1}{2}(z + \frac{1}{z}) - x}. \quad (\text{B.25})$$

Combining Eqs. (B.24) and (B.23), we can eventually project on the partial waves using for the integral over three spherical harmonics [143]

$$\int d\Omega_\ell Y_{n_1 s_1}(\Omega_\ell) Y_{\sigma m_\sigma}(\Omega_\ell) Y_{l_1 m}(\Omega_\ell) = \sqrt{\frac{(2n_1+1)(2\sigma+1)}{4\pi(2l_1+1)}} \begin{bmatrix} n_1 & \sigma & l_1 \\ 0 & 0 & 0 \end{bmatrix} \begin{bmatrix} n_1 & \sigma & l_1 \\ s_1 & m_\sigma & m \end{bmatrix} \quad (\text{B.26})$$

and analogous for  $\Omega_{\ell'}$ . The partial waves are thus given as

$$v_{dd}^{m, l_1, l_2}(\ell, \ell') = 4\pi D \sqrt{24} \sum_{n=0}^2 \sum_{s=-n}^n \sum_{\sigma=0}^{\infty} \frac{(-1)^{n+s}}{\sqrt{(2n)!(4-2n)!}} \frac{1}{\sqrt{(2l_1+1)(2l_2+1)}} z^{1-n} \alpha_\sigma(z) \\ \times \begin{bmatrix} n & 2-n & 2 \\ s & -s & 0 \end{bmatrix} \begin{bmatrix} n & \sigma & l_1 \\ 0 & 0 & 0 \end{bmatrix} \begin{bmatrix} n & \sigma & l_1 \\ s & m-s & m \end{bmatrix} \begin{bmatrix} 2-n & \sigma & l_2 \\ 0 & 0 & 0 \end{bmatrix} \begin{bmatrix} 2-n & \sigma & l_2 \\ s & m-s & m \end{bmatrix}. \quad (\text{B.27})$$

We show the partial waves for  $m=0$  for even  $l_1$  and  $l_2$ , i.e. for positive parity, in Fig. 4.1. Figure B.2 shows the partial waves for  $m=1$  and even parity.

In analogy to the cylindrical case, we expand the scattering amplitude

$$T(E, \ell, \ell') = \sum_{l_1, l_2=0}^{\infty} \sum_m t_m^{l_1, l_2}(E, \ell, \ell') Y_{l_1, m}(\Omega_\ell) Y_{l_2, m}^*(\Omega_{\ell'}) \quad (\text{B.28})$$

where  $m$  runs from minus to plus  $\min(l_1, l_2)$ . We obtain for the partial waves, using as full, partial wave projected and regularized potential  $v_m^{l_1, l_2}$

$$t_m^{l_1, l_2}(E, \ell, \ell') = -v_m^{l_1, l_2}(\ell, \ell') + \int dk \frac{k^2}{E - k^2/M + i\epsilon} \sum_{n=0}^{\infty} v_m^{l_1, n}(\ell, k) t_m^{n, l_2}(E, k, \ell'). \quad (\text{B.29})$$

Expression (B.29) is a system of coupled, one-dimensional integral equations. To numerically solve the system, the sum is truncated at  $L_{\max}$  (cf. Sec. B.5).

### B.2.3 Relation between spherical and cylindrical partial waves

Here, we give a relation between the partial waves in cylindrical and spherical coordinates. Further, the results of this section can be used to embed the anisotropic short-range interaction in the cylindrical partial waves. The expansions in cylindrical and spherical coordinates are directly related by the orthogonality relations of the  $y_m$  and  $Y_{l, m}$ , respectively. We use for the spherical harmonics

$$Y_{lm}(\theta, \phi) = \sqrt{\frac{2l+1}{2} \frac{(l-m)!}{(l+m)!}} P_l^m(\cos(\theta)) \underbrace{\frac{1}{\sqrt{2\pi}} e^{im\phi}}_{y_m(\phi)} \quad (\text{B.30})$$

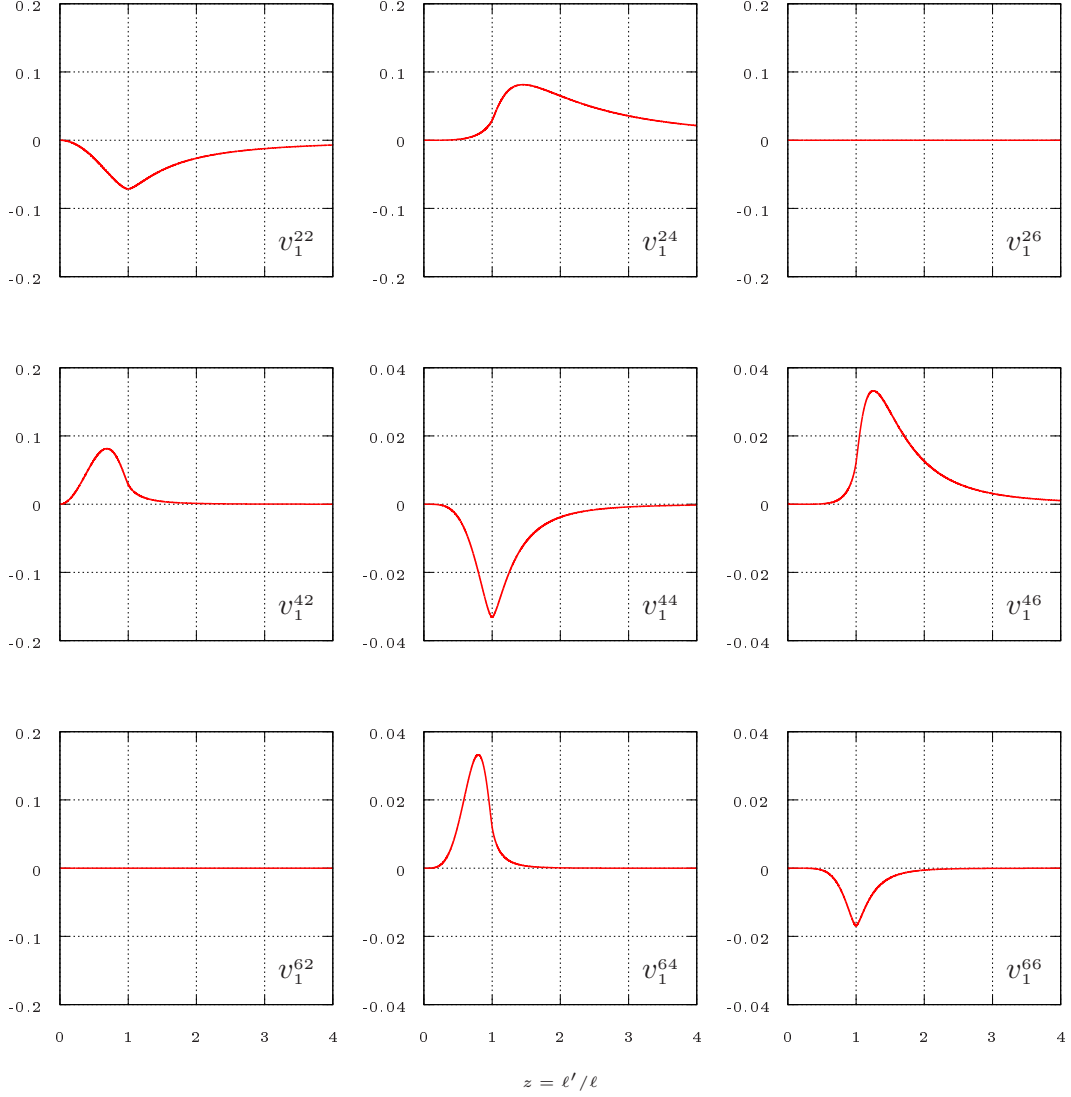


**Figure B.2.:** Partial wave projections for the long-range dipole-dipole potential for  $m = 1$  in dependence on the momentum ratio  $z \equiv \ell'/\ell$ . From left to right we increase  $l_1$  and from top to bottom  $l_2$  for  $v_1^{l_1 l_2}(z)$ . Note the different co-domain for higher partial waves.

with the associated Legendre polynomials  $P_l^m(\cos(\theta))$ . It follows for the scattering amplitudes

$$t_m(E, \underline{\ell}, \underline{\ell}') = \sum_{l_1, l_2=|m|}^{\infty} t_m^{l_1, l_2}(E, \ell, \ell') \xi_m^{l_1, l_2} P_{l_1}^m(\ell_z/\ell) P_{l_2}^m(\ell'_z/\ell'), \quad (\text{B.31a})$$

$$t_m^{l_1, l_2}(E, \ell, \ell') = \xi_m^{l_1, l_2} \int \frac{d\ell_z}{\ell} \int \frac{d\ell'_z}{\ell'} t_m(E, \underline{\ell}, \underline{\ell}') P_{l_1}^m(\ell_z/\ell) P_{l_2}^m(\ell'_z/\ell'), \quad (\text{B.31b})$$

where

$$\xi_m^{l_1, l_2} \equiv \sqrt{\frac{(2l_1 + 1)(2l_2 + 1)(l_1 - m)!(l_2 - m)!}{2 \cdot 2 \cdot (l_1 + m)!(l_2 + m)!}}. \quad (\text{B.31c})$$

and analogously for the dipole-dipole potential. Accordingly follows for the partial waves of the short-range potential (4.6)

$$v_m^s(\underline{\ell}, \underline{\ell}') = \sum_l g_{lm} \frac{2l + 1}{2} \frac{(l - m)!}{(l + m)!} P_l^m(\ell_z/\ell) P_l^m(\ell'_z/\ell'). \quad (\text{B.32})$$

Using spherical basis functions, the short-range partial waves can be read off immediately

$$v_s^{m, l_1, l_2} = \delta_{l_1, l_2} g_{l_1 m}. \quad (\text{B.33})$$

### B.3 Numerical implementation

We search for non-perturbative solutions to the LS Eqs. (4.14) and (4.24) and further to the bound-state Eqs. (4.18) and (4.26). In order to determine binding energies and scattering lengths, a numerical approach is employed. For  $E < 0$ , we can set  $\epsilon = 0$  in the denominator of the reduced propagator in Eqs. (4.14) and (4.24). Note that if the effective range expansion is applicable, it can be analytically continued to negative energies since it is analytic at threshold [102]. By implication, we can evaluate the scattering amplitude for negative energies and obtain the scattering length as the left-hand zero energy limit. If one is interested in the evaluation for positive energies the well-known formula

$$\frac{1}{x \pm i\epsilon} = \mathcal{P} \left( \frac{1}{x} \right) \mp i\pi\delta(x), \quad (\text{B.34})$$

can be employed to reduce the integrals occurring in Eqs. (4.14) and (4.24) to principal value integrals.

We begin with the spherical LS equation since it is an integral equation in just one variable. We discretize the integrals, e.g., using a Gauß-Legendre quadrature. In analogy to Sec. 2.3.1 we use weights  $\{w_i\}$  and sampling points  $\{y_i\} \in [0, \Lambda]$ . The momentum scale  $\Lambda$  ( $\Lambda \gg \lambda$ ), is a sharp cutoff introduced to obtain finite integration ranges.<sup>2</sup> We get for the spherical LS equation

$$t_m^{l_1, l_2}(E, y_i, y_j) = -v_m^{l_1, l_2}(y_i, y_j) + \sum_{k=0}^{N-1} w_k \frac{y_k^2}{E - y_k^2/M} \sum_{n=0}^{L_{\max}} v_m^{l_1, n}(y_i, y_k) t_m^{n, l_2}(E, y_k, y_j), \quad (\text{B.35})$$

where we already introduced the truncation parameter  $L_{\max}$ . Left to solve is a  $N \cdot L_{\max}$ -dimensional system of linear equations.

The bound-state equation (4.26) can be discretized in complete analogy. We obtain, similar to Eq. (2.44),

$$\chi_m^l(E, y_i) = \sum_{k=0}^{N-1} w_k \frac{y_k^2}{E - y_k^2/M} \sum_{n=0}^{L_{\max}} v_m^{l, n}(y_i, y_k) \chi_m^n(E, y_k) \equiv \sum_{k=0}^{N-1} \sum_{n=0}^{L_{\max}} K_{ik}^{ln, m} \chi_m^n(E, y_k). \quad (\text{B.36})$$

Again, we search for eigenvalues equals one for the kernel matrix ( $K_{ik}^{ln, m}$ ). Negative energies fulfilling this criteria are binding energies of the potential. Depending on the desired precision and the condition of the kernel matrix, eigenvalues have to be determined numerously.

It is possible to significantly improve numerical performance by rewriting Eq. (B.36) and, in particular, the bound-state wave function

$$\chi_m^l(E, y_i) \equiv (E - y_i^2/M) \bar{\chi}_m^l(E, y_i). \quad (\text{B.37})$$

The bound-state equation for  $\bar{\chi}$  reads

$$E \bar{\chi}_m^l(E, y_i) = \sum_{k=0}^{N-1} \sum_{n=0}^{L_{\max}} \left( w_k v_m^{l, n}(y_i, y_k) + \frac{\delta_{ik} \delta_{ln}}{M} \right) y_k^2 \bar{\chi}_m^n(E, y_k) \equiv \sum_{k=0}^{N-1} \sum_{n=0}^{L_{\max}} \bar{K}_{ik}^{ln, m} \bar{\chi}_m^n(E, y_k) \quad (\text{B.38})$$

and the negative eigenvalues of the modified kernel matrix ( $\bar{K}_{ij}^{ln, m}$ ) are the bound states for the potential  $V$ . For the functions  $\bar{\chi}_m^l$ , the energy is now rather a label than a variable, tagging the eigenstate belonging to energy  $E$ . Note that there might be positive energies fulfilling Eq. (B.38), being formal solutions to the bound-state equation. These do not belong to physical states since the bound-state equation is explicitly formulated for negative energies.

For the cylindrical system, the LS equation (4.14) is discretized with respect to the  $\rho$ - and  $z$ -component of the momenta. Sampling points and weights for the components are generated independently. For the radial component we use  $\{y_i^\rho\} \in [0, \Lambda]$  and corresponding weights  $\{w_i^\rho\}$ . For the  $z$ -component the sampling points are denoted by  $\{y_i^z\} \in [-\Lambda, \Lambda]$  with weights  $\{w_i^z\}$ . For shorthand notation we use  $\underline{y}_i \equiv (y_{i_\rho}^\rho, y_{i_z}^z)$  and  $w_i \equiv w_{i_\rho}^\rho w_{i_z}^z$ . The discretized LS equation reads

$$t_m(E, \underline{y}_i, \underline{y}_j) = -v_m(\underline{y}_i, \underline{y}_j) + \sum_{k_\rho=0}^{N-1} \sum_{k_z=-(N-1)}^{N-1} w_i v_m(\underline{y}_i, \underline{y}_k) \frac{y_{k_\rho}^\rho}{E - \underline{y}_k^2/M} t_m(E, \underline{y}_k, \underline{y}_j) \quad (\text{B.39})$$

<sup>2</sup> Note that it is also possible to substitute the integration measure in order to obtain a compact domain to integrate over. This substitution might also increase numerical performance. A sharp cutoff, however, is more intuitive and convergence within the ratio of the sharp over the Gauss cutoff can be controlled systematically. To achieve a similar decrease of computational costs, we utilize the inverse transformation method [144] to distribute sampling points non-homogeneously.

and we are left with an  $N \cdot (2N - 1)$ -dimensional system of linear equations. The bound-state equation for the rewritten bound-state wave function

$$\bar{\chi}_m(E, \underline{\ell}) \equiv (E - \ell^2/M)\chi_m(E, \underline{\ell}), \quad (\text{B.40})$$

reads after discretization

$$E\bar{\chi}_m(E, \underline{y}_i) = \sum_{\underline{k}} \left( w_{\underline{k}} y_{k\rho}^\rho v_m(\underline{y}_i, \underline{y}_{\underline{k}}) + \frac{\delta_{i\underline{k}}^{(2)}}{M} \underline{y}_{\underline{k}}^2 \right) \bar{\chi}_m(E, \underline{y}_{\underline{k}}). \quad (\text{B.41})$$

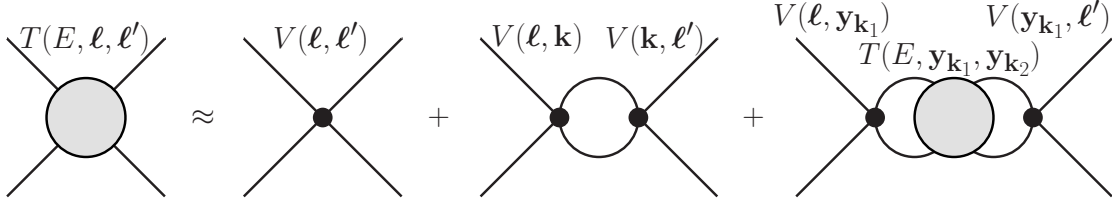


**Figure B.3.:** Two-loop representation of the LS equation used to interpolate the transition matrix with discretized in- and outgoing momenta to arbitrary on-shell energies.

To evaluate on-shell amplitudes for arbitrary, finite energies the amplitude has to be extrapolated. We use the Nyström method. For convenience we use a formulation for which only the fully discretized transition matrix is required, schematically depicted in Fig. B.3. The transition amplitude then has to be determined only once. We obtain for the on-shell transition matrix

$$T(E, \ell, \ell') \approx -V(\ell, \ell') - \int d^3k V(\ell, \mathbf{k}) \frac{1}{E - k^2/M} V(\mathbf{k}, \ell') + \sum_{\mathbf{k}_1} \sum_{\mathbf{k}_2} w_{\mathbf{k}_1} w_{\mathbf{k}_2} V(\ell, \mathbf{y}_{\mathbf{k}_1}) \frac{1}{E - \mathbf{y}_{\mathbf{k}_1}^2/M} T(E, \mathbf{y}_{\mathbf{k}_1}, \mathbf{y}_{\mathbf{k}_2}) \frac{1}{E - \mathbf{y}_{\mathbf{k}_2}^2/M} V(\mathbf{y}_{\mathbf{k}_2}, \ell'). \quad (\text{B.42})$$

Depending on the coordinate system chosen, projection operators have to be applied to Eq. (B.42).

## B.4 Further unrenormalized two-dipole spectra

In Sec. 4.1.4 we discussed spectra for even orbital angular momentum and positive parity. Here we present our findings for  $m = 0, P = -$  and  $m = 1, P = +$ . As described in Sec. 4.1.4, it is possible to classify sets of orbital angular momentum which present an almost conserved quantum number. It works particularly well for  $m = 0$  and  $P = +$  since the partial waves  $v_{20}(\ell, \ell')$  and  $v_{02}(\ell, \ell')$  contribute and dominate. For the here given examples no partial waves have a constant proportion and coupling between different sets of states is expected to be stronger.

### B.4.1 Cutoff dependence for $m = 0, P = -$

We show the cutoff dependence of the unrenormalized spectrum in Fig. B.4 for  $m = 0$  and  $P = -$ . The lowest partial wave contributing is  $v_0^{11}(\ell, \ell')$  and correspondingly we show the scattering length  $a_0^{11}$  below. However, peaks of the scattering length are extremely narrow and we need to keep the energy at which the on-shell scattering amplitude is evaluated finite in order to resolve the poles of the scattering length. This feature was already observed in Ref. [134] for  $a_0^{20}$ . It applies to all examined scattering lengths but  $a_0^{00}$ .

Wherever a new bound state appears, the scattering length possesses a pole. It is particularly sensitive to the lowest set of bound states but also couples to higher partial wave channels. In Fig. B.4 the latter dependence manifests itself only by a few scattered points due to the limited resolution.

We also performed an analysis in the truncation parameter  $L_{\max}$  to identify the different angular momentum sets. As discussed above, due to the absence of the dominating partial waves  $v_0^{20}(\ell, \ell')$  and  $v_0^{02}(\ell, \ell')$ , states are less distinct in angular momentum. Nonetheless, we can assign approximate sets. We identify the first set of bound states with  $\{l\} = \{1, 3\}$  and the second set with  $\{l\} = \{5, 7\}$ . The third set has not converged yet for  $L_{\max} = 9$  but presumably has a significant  $\{l\} = \{9\}$  proportion. The analysis is shown in App. B.5 in Fig. B.12.

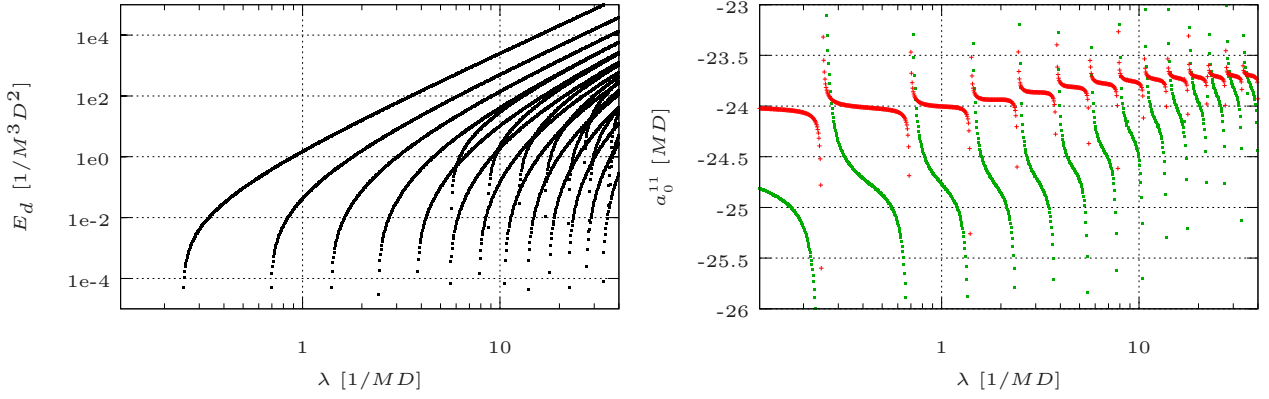


**Figure B.4.:** Unrenormalized spectrum of bound states and the scattering length  $a_0^{11}$  for  $D > 0$ ,  $m = 0$  and  $P = -$ . The unrenormalized spectrum of bound states and the scattering length  $a_0^{11}$  are shown on the left and on the right, respectively. The deepest bound state is of comparable magnitude as for positive parity but states appear less frequent and the spectrum is less dense. The shape of individual bound states is similar. The scattering length is not converged yet. The green squares show the on-shell, elastic scattering amplitude for  $E = -10^{-5}/M^3 D^2$ . The red crosses belong to an energy of  $E = -10^{-6}/M^3 D^2$ . For much smaller absolute values of the energy no structure could be resolved. Poles at cutoffs where new bound states appear are evident, though the shape and width can not be resolved.

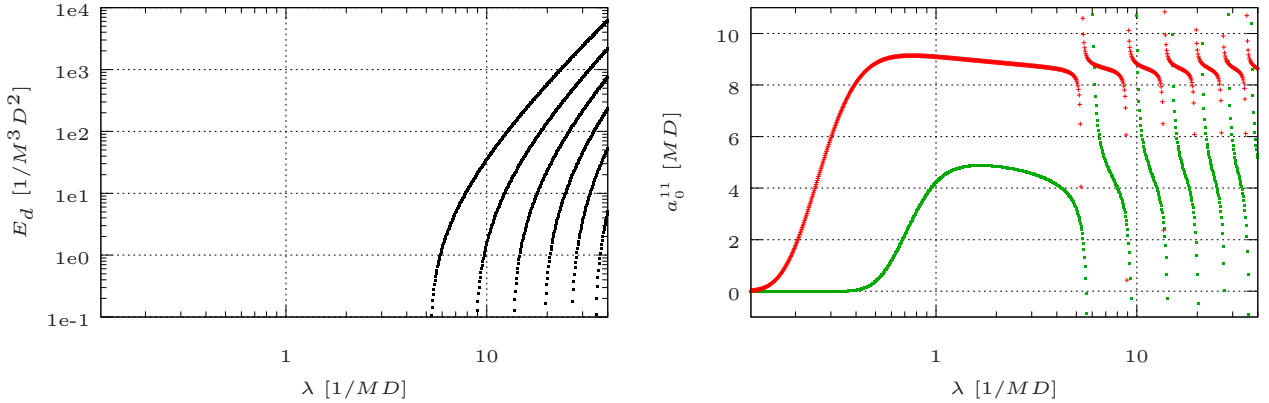


**Figure B.5.:** Unrenormalized spectrum of bound states and the scattering length  $a_0^{11}$  for  $D < 0$ ,  $m = 0$  and  $P = -$ . The unrenormalized spectrum of bound states and the scattering length  $a_0^{11}$  are shown on the left and on the right, respectively. The notation is the same as for parallel dipoles in Fig. B.4. However, in order to resolve the poles of the scattering length, we evaluate the on-shell scattering amplitude at much larger energies than before. We use  $E = -1/M^3 D^2$  for the green squares and  $E = -10^{-1}/M^3 D^2$  for the red crosses.

The spectrum for antiparallel dipoles is depicted in Fig. B.5. Only one set of bound states is present. Since its deepest bound state emerges for a much larger cutoff and is significantly weaker bound, we anticipate that it belongs to higher orbital angular momentum. An analysis in the truncation parameter can be found in Fig. B.13 in App. B.5 and confirms this expectation. Bound states do not show up for  $L_{\max} < 3$ . The set probably is best described with  $\{l\} = \{3, 5\}$ , but its coupling to  $\{l\} = \{7\}$  is large, indicated by a significant shift of binding energies when increasing  $L_{\max}$  from 5 to 7. We do not expect that the scattering length is precisely determined since we need to use energies as large as  $E = -1/M^3 D^2$  and  $E = -10^{-1}/M^3 D^2$  in order to resolve the structure and poles of the binding energy. Note that the finite energies imply a shift of the poles away from the cutoff where bound states first appear. It is of qualitative interest to illustrate that the lowest order scattering length with  $l_1 = l_2 = 1$  is sensitive to the bound states even though the observed set does not appear unless  $L_{\max} \geq 3$ . This behavior is similar to the earlier observation with  $P = +$  since the off-diagonal elements  $v_0^{13}(l, l')$  and  $v_0^{31}(l, l')$  couple both channels.

Moreover, we plot higher-order scattering lengths for the case of antiparallel dipoles. The dependence of the spectrum on the cutoff for antiparallel dipoles in a cutoff range of  $4/MD \leq \lambda \leq 120/MD$  and a truncation parameter  $L_{\max} = 9$  is plotted in Fig. B.6. We show the scattering lengths  $a_0^{33}$  for  $E = -1/M^3 D^2$  and  $E = -10^{-1}/M^3 D^2$  and  $a_0^{55}$  for  $E = -1/M^3 D^2$ . As expected from the partial wave analysis in App. B.5, the investigated scattering lengths are sensitive to the bound states and possess poles whenever a new state occurs.

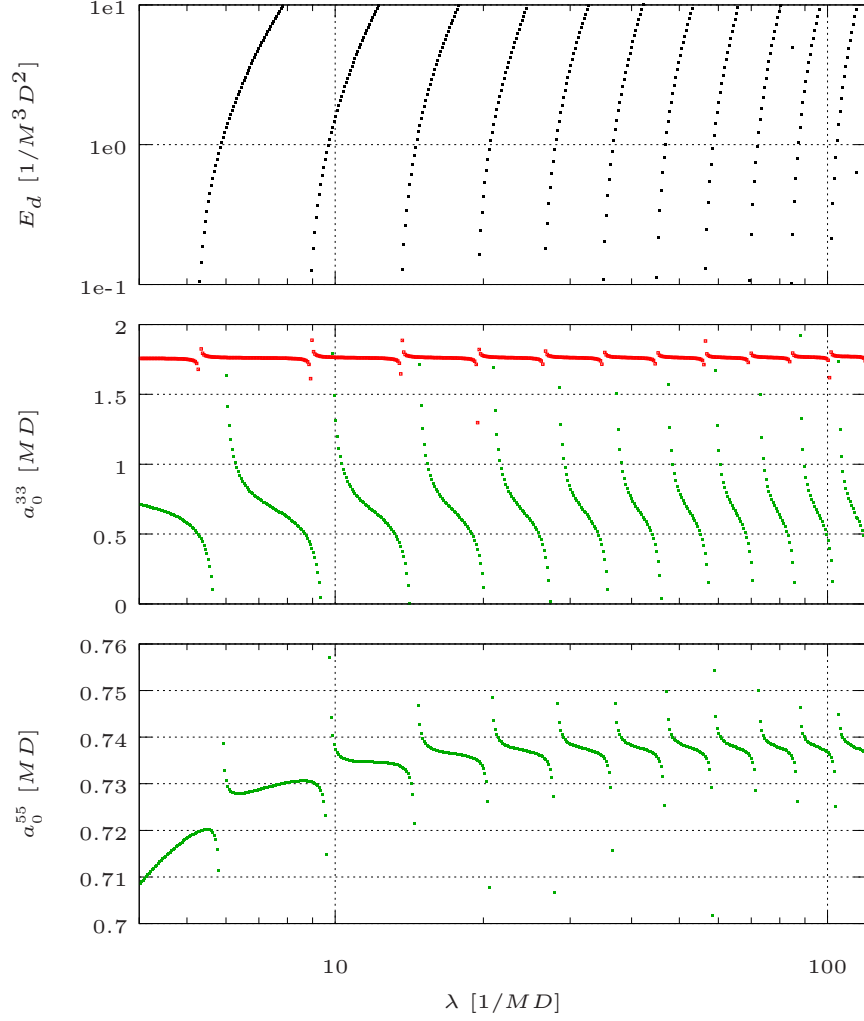


**Figure B.6.:** Unrenormalized spectrum of bound states and the scattering lengths  $a_0^{33}$  and  $a_0^{55}$  for  $D < 0$ ,  $m = 0$  and  $P = -$ . The notation is the same as in Fig. B.5. The cutoff scale is varied between  $4/MD \leq \lambda \leq 120/MD$ . The scattering length  $a_0^{33}$  is plotted for  $E = -1/M^3 D^2$  (green squares) and  $E = -10^{-1}/M^3 D^2$  (red crosses) and  $a_0^{55}$  for  $E = -1/M^3 D^2$  (green squares).

---

#### Cutoff dependence for $m = 1, P = +$

---

We further investigate spectra for non-vanishing orbital angular momentum projection  $m$ . Here, we briefly want to discuss the spectra for parallel and antiparallel dipoles for the next higher projection of  $m = 1$  and positive parity. We begin with the cutoff dependence of the binding energies for parallel dipoles, shown in Fig. B.7. A corresponding partial wave analysis in the truncation parameter is depicted in Fig. B.14 in App. B.5. We identify the states with  $\{l\} = \{2, 4\}$  and  $\{l\} = \{6, 8\}$ . The lowest partial wave contributing is  $v_1^{22}(\ell, \ell')$ . The spectrum is shallower and the deepest bound state is about one order of magnitude weaker bound than for  $m = 0$ . We point out that the spectrum is not renormalized and due to a fine tuning of coupling constants, the spectrum for  $m = 1$  can, in principle, possess deeper bound states than for  $m = 0$ . This scenario, however, is less likely and we anticipate that bound-state spectra as in Fig. B.7 represent a reasonable estimate for the strength of the interaction in the corresponding scattering channel.

For negative  $D$ , no bound states appear unless  $L_{\max} \geq 4$  and we assign  $\{l\} = \{4, 6\}$  to the set shown in Fig. B.8. In both cases, for parallel and antiparallel dipoles, the scattering length  $a_1^{22}$  is sensitive to the bound states. As soon as multiple sets of bound states exist, the scattering length is mainly sensitive to the bound states dominated by the lower orbital angular momentum. Note that for  $D < 0$ , the scattering length  $a_1^{22}$  has much more developed poles whenever a new state appears than for parallel dipoles.

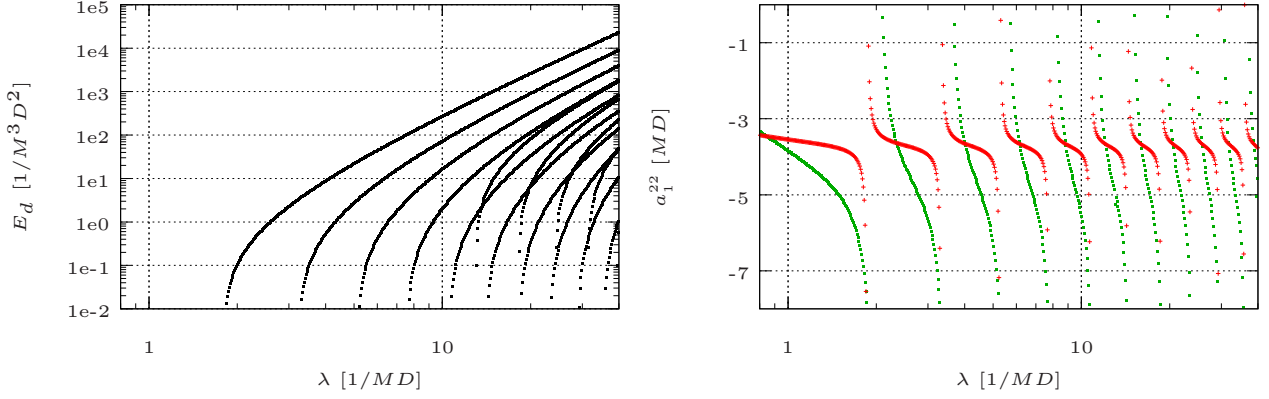


**Figure B.7.:** Unrenormalized spectrum of bound states and the scattering length  $a_1^{22}$  for  $D > 0$ ,  $m = 1$  and  $P = +$ . The unrenormalized spectrum of bound states and the scattering length  $a_1^{22}$  are shown on the left and on the right, respectively. The notation is the same as in Fig. B.4. Again, the scattering length is not converged yet. In order to resolve details of the scattering length, we evaluate the on-shell scattering amplitude at finite energies of  $E = -10^{-1}/M^3 D^2$  (green squares) and  $E = -2 \cdot 10^{-2}/M^3 D^2$  (red crosses).

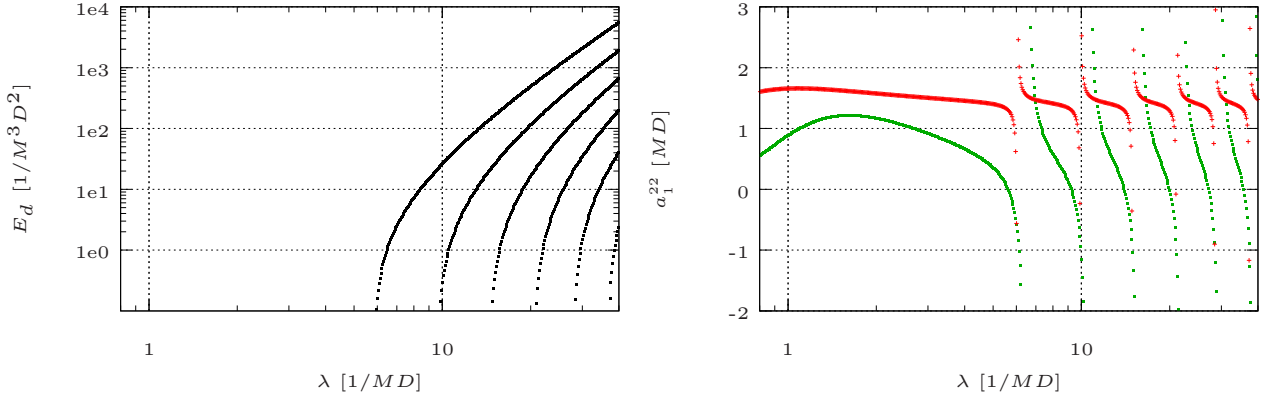


**Figure B.8.:** Unrenormalized spectrum of bound states and the scattering length  $a_1^{22}$  for  $D < 0$ ,  $m = 1$  and  $P = +$ . The unrenormalized spectrum of bound states and the scattering length  $a_1^{22}$  are shown on the left and on the right, respectively. The notation is the same as in Fig. B.7. The energies at which the on-shell, elastic scattering amplitude is evaluated are  $E = -10^{-1}/M^3 D^2$  for the green squares and  $E = -2 \cdot 10^{-1}/M^3 D^2$  for the red crosses.

## B.5 Convergence of the partial wave expansion

Here, we demonstrate how to determine a) the minimum  $L_{\max}$  to truncate at and b) the dominating orbital angular momentum quantum numbers for different sets of bound states, i.e.  $\{l\}$ . Since the spectrum for antiparallel dipoles is less complex than for parallel dipoles, we begin with  $D < 0$ . To carry out the analysis we vary the cutoff between  $10/MD$  and  $300/MD$  for  $m = 0$  and  $P = +1$ . Note that the minimum value of  $L_{\max}$  for which bound states first appear strongly depends on the range for the cutoff and the quantum numbers. From the upper left to the lower right, we show the spectrum for  $L_{\max} = 2, 6, 8$  and  $10$ . The results for a cylindrical coordinate system belong to the red circles whereas black squares show the outcome using a spherical basis to expand. The first set of bound states appears already for  $L_{\max} = 2$ , but spacings between states are clearly larger than found by the cylindrical algorithm. For  $L_{\max} = 4$  (not shown), the lowest order states have been fully converged and no new states show up. We conclude that this set is dominated by orbital angular momenta  $\{l\} = \{0, 2\}$ . The first states for the next set of bound states appear for  $L_{\max} = 6$  but the spectrum is still incomplete. For  $L_{\max} = 8$  the spacing is larger than suggested by expanding in cylindrical waves. Full convergence is finally achieved for  $L_{\max} = 10$ . In analogy to before, we determine  $\{l\} = \{6, 8\}$ . Deviations between both approaches in the low-energy regime come from numerical uncertainties, which are in the same order but do not have a one-to-one correspondence in both algorithms.

Although the spectrum for the chosen quantum numbers and range of cutoff does not converge unless  $L_{\max} \geq 10$ , shapes of individual bound states might be converged much earlier, demonstrated in Fig. B.10. There, the binding energy of the first (left plot) and the second (right plot) bound state of the  $\{0, 2\}$ -set of bound states is plotted against the scattering length  $a_0^{00}$ . For the red circles  $L_{\max} = 10$  whereas the black squares belong to  $L_{\max} = 2$ . Within numerical

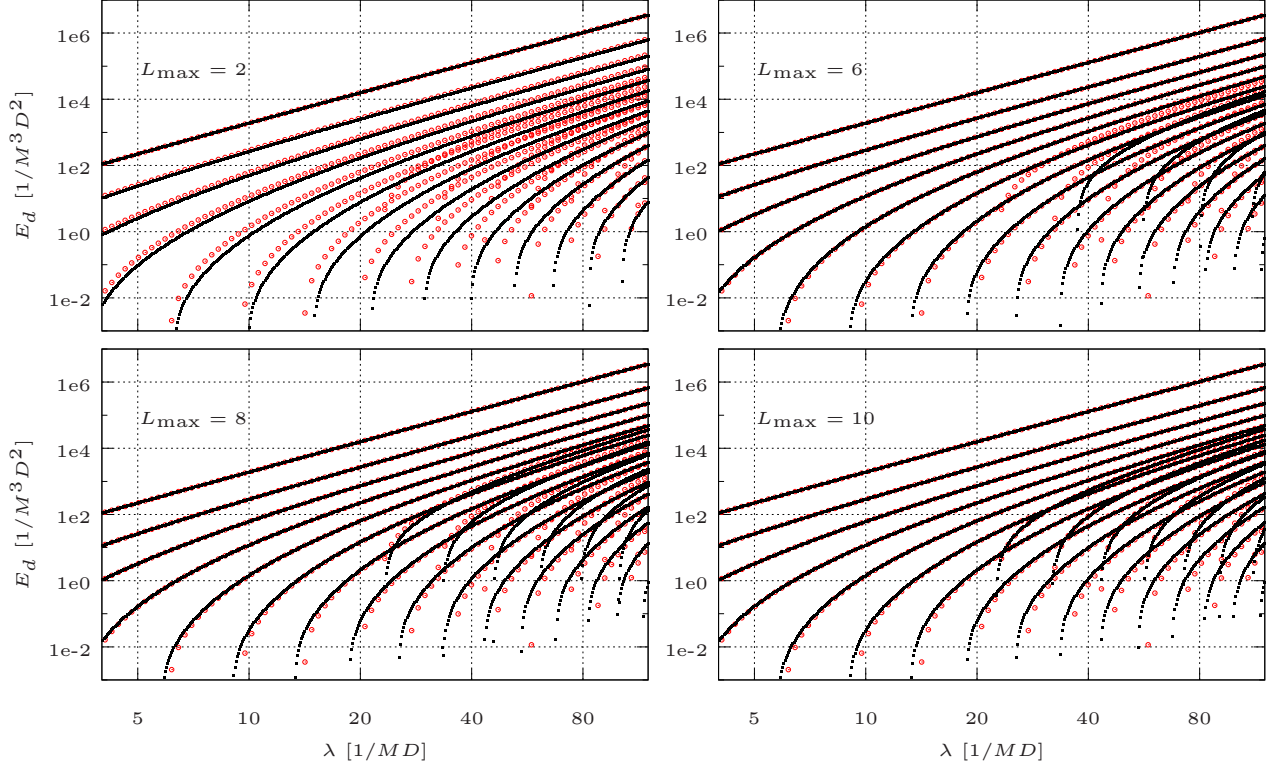


**Figure B.9:** Convergence in the truncation parameter used for the spherical algorithm (black squares) for  $D < 0$ ,  $m = 0$  and  $P = +$ . We show the unrenormalized spectrum and plot against the cutoff  $\lambda$ . The values for the truncation parameter are  $L_{\max} = 2, 6, 8, 10$  from top left to bottom right. The outcome of a cylindrical algorithm belongs to red circles and serves as an estimate how well the partial wave expansion converged. Deviations in the infrared occur since the algorithms can not be related exactly. Numerical precision, however, is of the same order.

precision, both curves coincide. So depending on the observable of interest,  $L_{\max}$  can be adjusted in order to simplify calculations and decrease computational expenses.

We further examined the dependence on the truncation parameter for other sets of quantum numbers and parallel and antiparallel dipoles, respectively. The analyses shown in Figs. B.11 to B.15 serve to check for convergence in the truncation parameter and to assign sets of orbital angular momentum  $\{l\}$  to different sets of bound states.

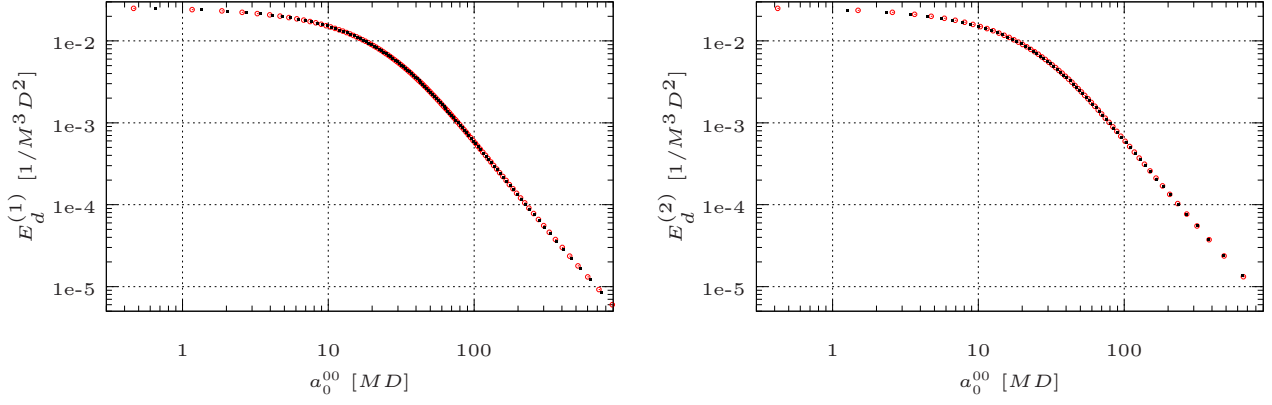


**Figure B.10.:** Binding energy of the first (left) and second (right) state of the  $\{0, 2\}$ -set in dependence on the scattering length  $a_0^{00}$ . The plot shows the independence of the shapes of the bound states on the truncation parameter  $L_{\max}$ . Though, the spectrum did not converge for the chosen range of cutoff and quantum numbers, the shapes coincide within numerical precision for  $L_{\max} = 2$  (black squares) and  $L_{\max} = 10$  (red circles).

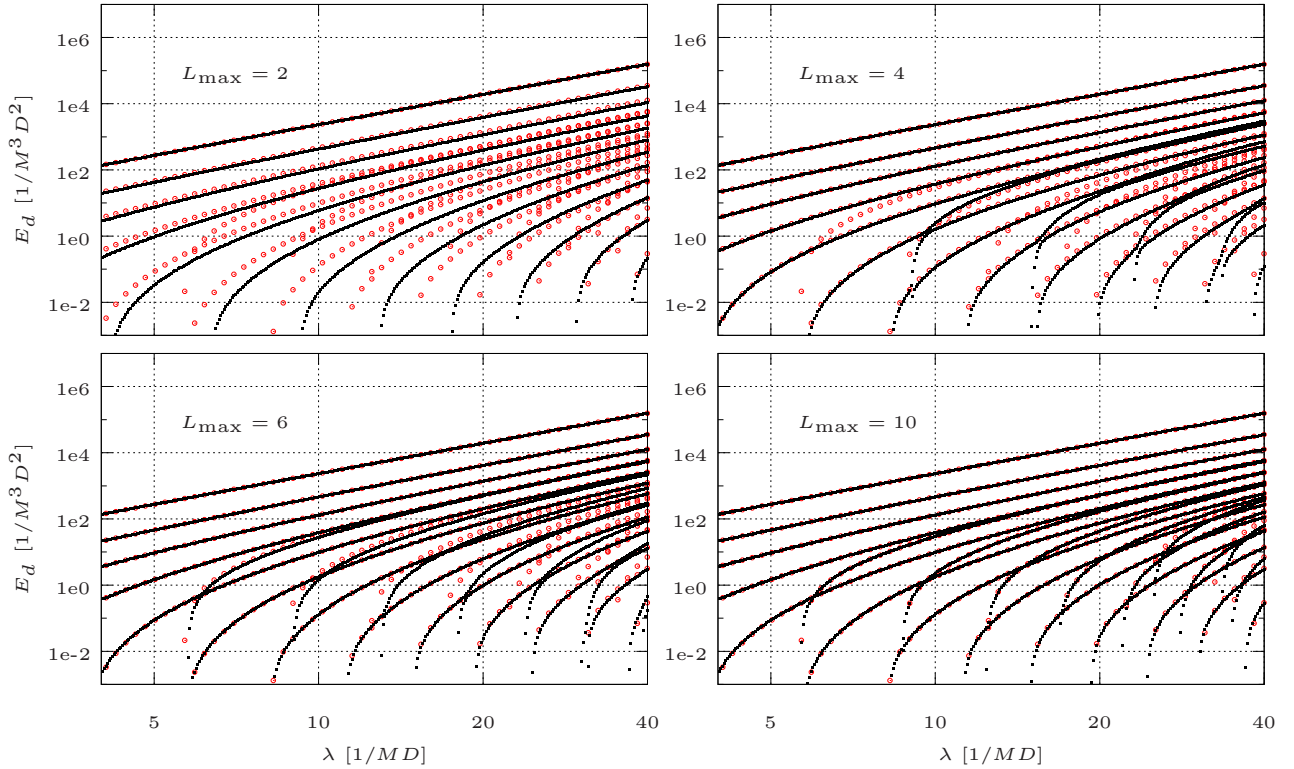


**Figure B.11.:** Convergence in the truncation parameter used for the spherical algorithm (black squares) for  $D > 0$ ,  $m = 0$  and  $P = +$ . The values for the truncation parameter are  $L_{\max} = 2, 4, 6, 10$  from top left to bottom right. The notation is the same as in Fig. B.9.

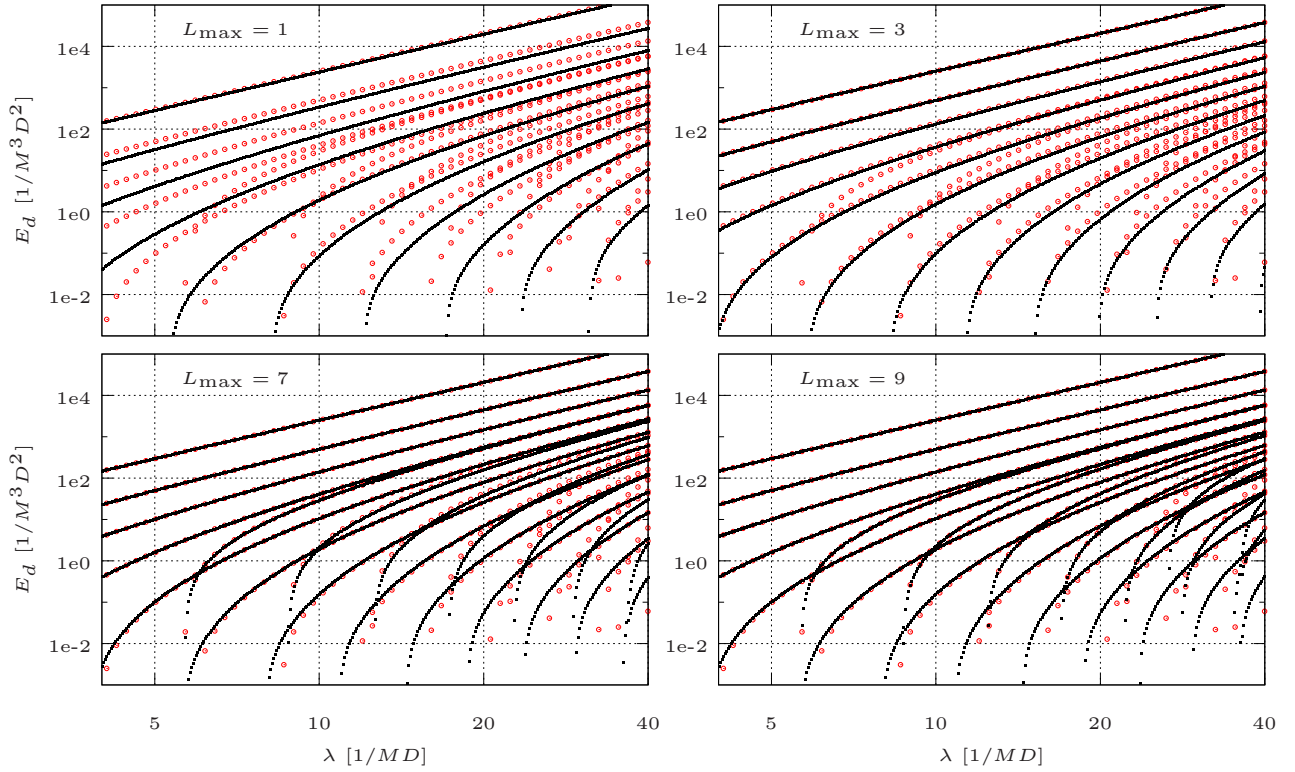


**Figure B.12.:** Convergence in the truncation parameter used for the spherical algorithm (black squares) for  $D > 0$ ,  $m = 0$  and  $P = -$ . The values for the truncation parameter are  $L_{\max} = 1, 3, 7, 9$  from top left to bottom right. The notation is the same as in Fig. B.9.

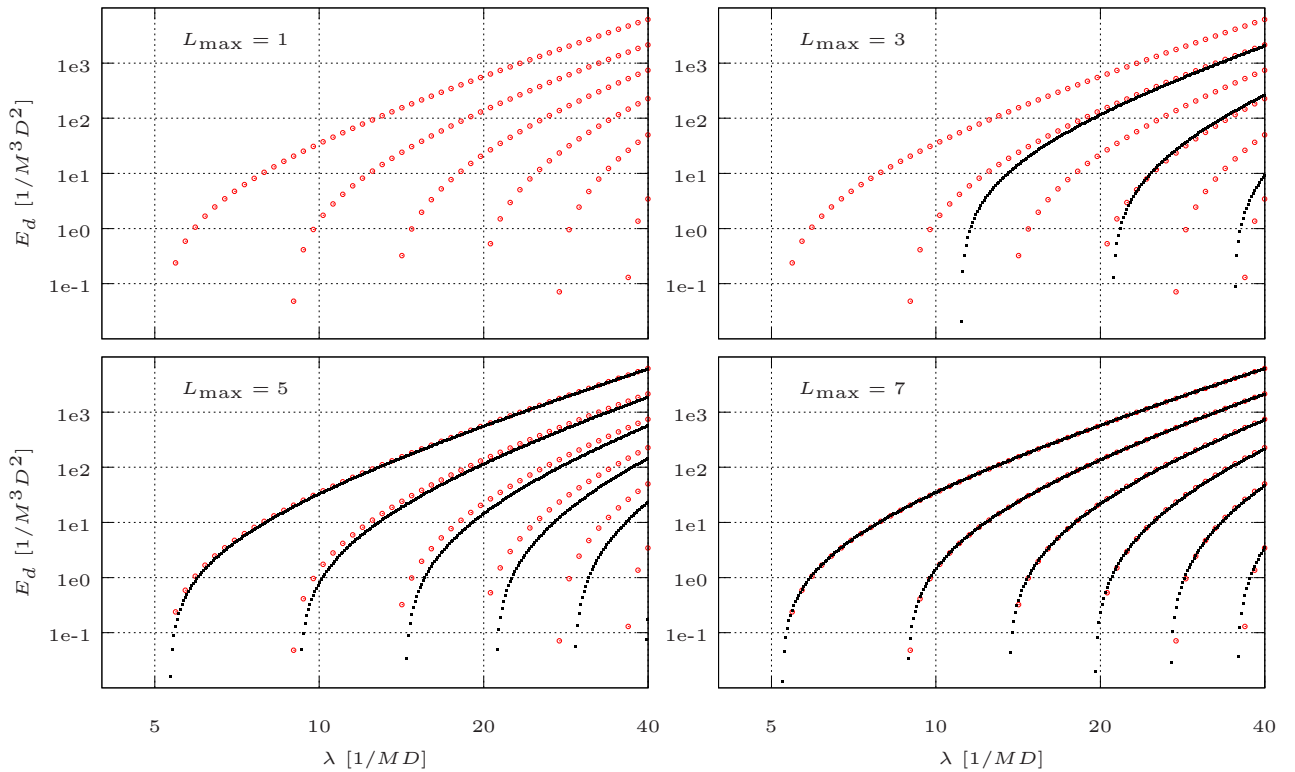


**Figure B.13.:** Convergence in the truncation parameter used for the spherical algorithm (black squares) for  $D < 0$ ,  $m = 0$  and  $P = -$ . The values for the truncation parameter are  $L_{\max} = 1, 3, 5, 7$  from top left to bottom right. The notation is the same as in Fig. B.9.

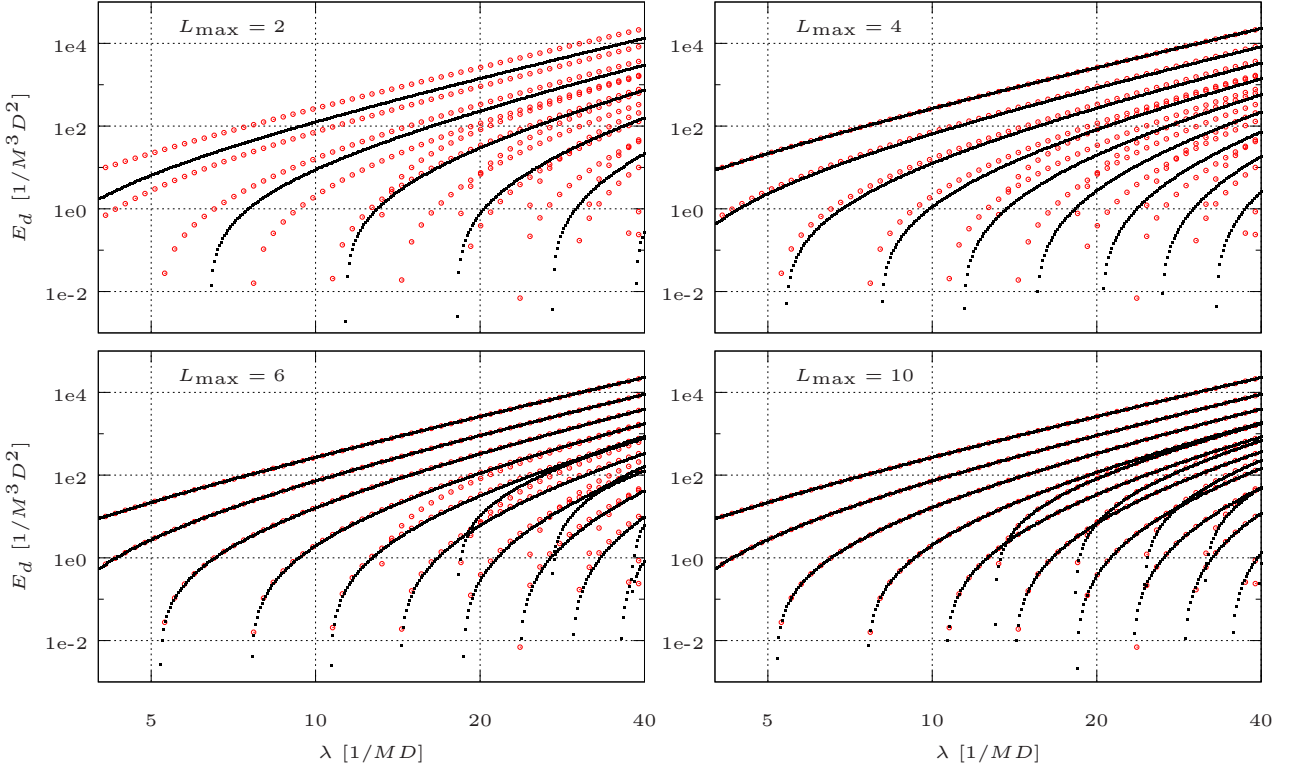


**Figure B.14.:** Convergence in the truncation parameter used for the spherical algorithm (black squares) for  $D > 0$ ,  $m = 1$  and  $P = +$ . The values for the truncation parameter are  $L_{\max} = 2, 4, 6, 10$  from top left to bottom right. The notation is the same as in Fig. B.9.

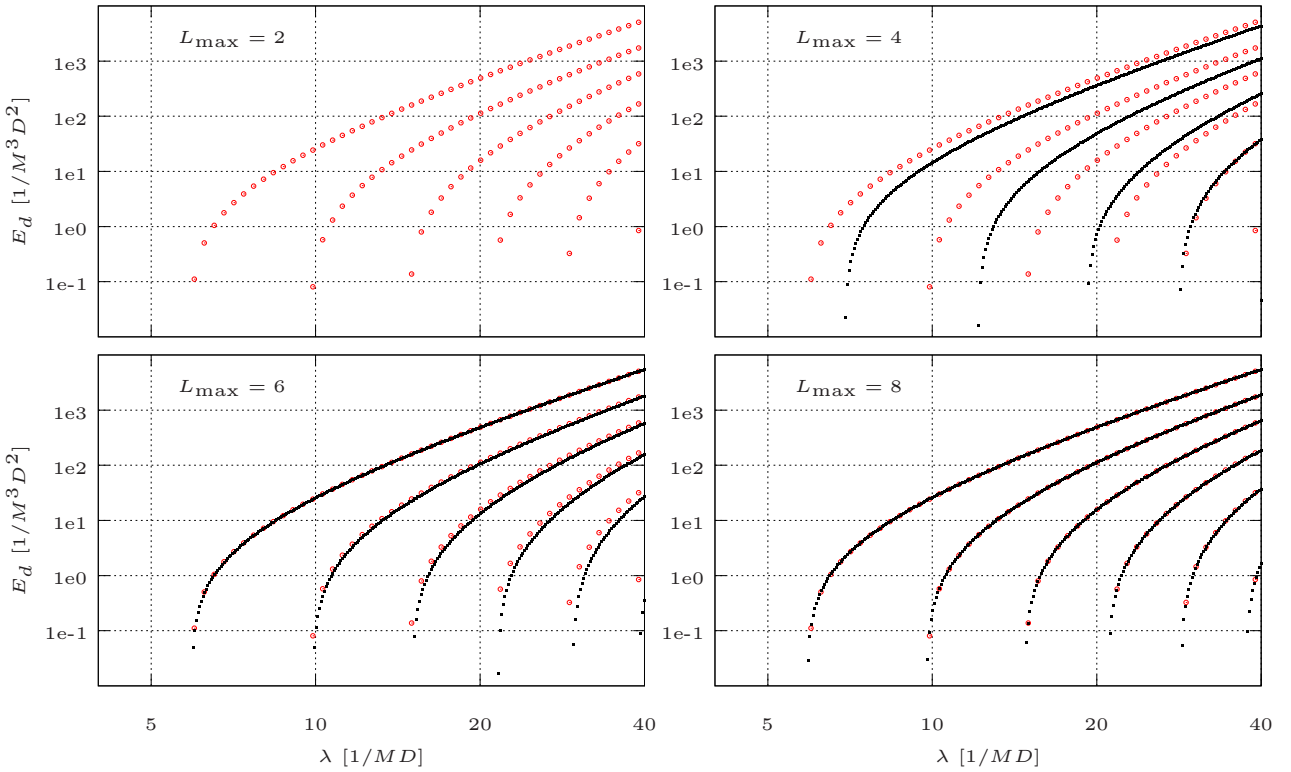


**Figure B.15.:** Convergence in the truncation parameter used for the spherical algorithm (black squares) for  $D < 0$ ,  $m = 1$  and  $P = +$ . The values for the truncation parameter are  $L_{\max} = 2, 4, 6, 8$  from top left to bottom right. The notation is the same as in Fig. B.9.

## B.6 Partial wave projection of the Faddeev equation

We show how to project the Faddeev equation (4.33) on cylindrical partial waves. We expand the transition amplitude according to Eq. (4.40) and use for the Faddeev components Eq. (4.41) to obtain

$$\begin{aligned}\psi(\mathbf{p}, \mathbf{q}) &= \sum_{m_1, m_2} \psi_{m_1 m_2}(\mathbf{p}, \mathbf{q}) y_{m_1}(\phi_p) y_{m_2}^*(\phi_q) \\ &= -g_0(p^2, q^2) \int d^2k \int d\phi_k \left\{ \sum_{m_1} t_{m_1}(E - \frac{3}{4}q^2/M, \mathbf{p}, \underline{\pi}_1) y_{m_1}(\phi_p) y_{m_1}^*(\phi_{\pi_1}) \right. \\ &\quad \left. \times \sum_{m_3, m_4} \psi_{m_3, m_4}(-\underline{\pi}_2, \mathbf{k}) y_{m_3}(\phi_{-\pi_2}) y_{m_4}^*(\phi_k) + \pi_{1,2} \leftrightarrow -\pi_{1,2} \right\}.\end{aligned}\quad (\text{B.43})$$

Here the sums over the  $m_i$  run from minus to plus infinity. Note that  $\underline{\pi}_1$  and  $\underline{\pi}_2$  depend on the relative azimuthal angle between  $\mathbf{k}$  and  $\mathbf{p}$  (cf. Eqs. (4.44)). We express the  $y_m(\phi_{\pi_{1,2}})$  in terms of  $y_m(\phi_k)$  and  $y_m(\phi_q)$ . The azimuthal angle of the negative of a vector is given as  $\phi_{-\pi_2} = \phi_{\pi_2} + \pi$  and thus,  $y_m(\phi_{-\pi_2}) = (-1)^m y_m(\phi_{\pi_2})$ . With aid of the binomial series, we obtain the identities

$$y_{m_1}^*(\phi_{\pi_1}) = \sqrt{2\pi} \sum_{n_1=0}^{m_1} \binom{|m_1|}{|n_1|} \frac{(k_\rho)^{|n_1|} (\frac{1}{2}q_\rho)^{|m_1|-|n_1|}}{(\pi_1^\rho)^{|m_1|}} y_{n_1}^*(\phi_k) y_{m_1-n_1}^*(\phi_q), \quad (\text{B.44a})$$

$$y_{m_3}(\phi_{-\pi_2}) = (-1)^{m_3} \sqrt{2\pi} \sum_{n_3=0}^{m_3} \binom{|m_3|}{|n_3|} \frac{(\frac{1}{2}k_\rho)^{|n_3|} (q_\rho)^{|m_3|-|n_3|}}{(\pi_2^\rho)^{|m_3|}} y_{n_3}(\phi_k) y_{m_3-n_3}(\phi_q), \quad (\text{B.44b})$$

with the binomial coefficients  $\binom{|m_1|}{|n_1|}$  and  $\binom{|m_3|}{|n_3|}$ . Identities (B.44a) and (B.44b) hold for positive and negative  $m$ . For the product follows

$$\begin{aligned}y_{m_1}^*(\phi_{\pi_1}) y_{m_3}(\phi_{-\pi_2}) &= \\ (-1)^{m_3} \sum_{n_1, n_3=0}^{m_1, m_3} &\underbrace{\binom{|m_1|}{|n_1|} \binom{|m_3|}{|n_3|} \left(\frac{1}{2}\right)^{|m_1|-|n_1|+|n_3|} \frac{(k_\rho)^{|n_1|+|n_3|} (q_\rho)^{|m_1|+|m_3|-(|n_1|+|n_3|)}}{(\pi_1^\rho)^{|m_1|} (\pi_2^\rho)^{|m_3|}}}_{\equiv D_{n_1 n_3}^{m_1 m_3}(q_\rho, k_\rho, \phi_k - \phi_q)} y_{n_3-n_1}(\phi_k - \phi_q) y_{m_1-m_3}^*(\phi_q).\end{aligned}\quad (\text{B.45})$$

Using expression (B.45), the left and right-hand side of Eq. (B.43) depend on  $\phi_p$ ,  $\phi_k$  and  $\phi_q$  only and we are in place to use the orthogonality relations for the  $y_m$  in order to project on partial waves

$$\begin{aligned}\psi_{m_1 m_2}(\mathbf{p}, \mathbf{q}) &= -g_0(p^2, q^2) \int d^2k \int_0^{2\pi} d\phi \left\{ t_{m_1}(E - \frac{3}{4}q^2/M, \mathbf{p}, \underline{\pi}_1(\phi)) \right. \\ &\quad \left. \times \sum_{m_3, m_4} \sum_{n_1, n_3} (-1)^{m_3} D_{n_1 n_3}^{m_1 m_3}(q_\rho, k_\rho, \phi) \delta_{m_1-m_3, m_2-m_4} y_{m_4}^*(\phi) y_{n_3-n_1}(\phi) \psi_{m_3 m_4}(-\underline{\pi}_2(\phi), \mathbf{k}) \right\}.\end{aligned}\quad (\text{B.46})$$

The dependence on  $\phi$  occurs on the one hand in the analytically known functions  $D_{n_1 n_3}^{m_1 m_3}(q_\rho, k_\rho, \phi)$  and  $y_{m_4}^*(\phi) y_{n_3-n_1}(\phi)$  and on the other hand in the shifted momenta, appearing in the transition matrix and the Faddeev component. The discretization is thus not as straightforward as for the two-body problem. We will address the numerical approach to solve Eq. (B.46) in the next section. Furthermore, Eq. (B.46) is a coupled integral equation. But we can apply a significant simplification, if the deepest two-body bound state belonging to a particular  $\bar{m}_1$  is clearly separated from bound states with different angular momentum projection. Then, close to the two-body threshold, the partial wave  $t_{\bar{m}_1}$  dominates the transition amplitude and we may assume

$$T(E, \underline{\ell}, \underline{\ell}') \approx t_{\bar{m}_1}(E, \underline{\ell}, \underline{\ell}') y_{\bar{m}_1}(\phi_\ell) y_{\bar{m}_1}^*(\phi_{\ell'}). \quad (\text{B.47})$$

The two-body partial wave amplitudes can then be replaced with

$$t_m(E, \underline{\ell}, \underline{\ell}') = \delta_{m \bar{m}_1} t_{\bar{m}_1}(E, \underline{\ell}, \underline{\ell}') \quad (\text{B.48})$$

and we obtain for the Faddeev equation

$$\begin{aligned}\psi_{\bar{m}_1 m_2}(\mathbf{p}, \mathbf{q}) &= -g_0(p^2, q^2) \int d^2k \int_0^{2\pi} d\phi \left\{ t_{\bar{m}_1}(E - \frac{3}{4}q^2/M, \mathbf{p}, \underline{\pi}_1(\phi)) \right. \\ &\quad \left. \times \sum_{n_1, n_3=0}^{\bar{m}_1} (-1)^{\bar{m}_1} D_{n_1 n_3}^{\bar{m}_1 \bar{m}_1}(q_\rho, k_\rho, \phi) y_{m_2}^*(\phi) y_{n_3-n_1}(\phi) \psi_{\bar{m}_1 m_2}(-\underline{\pi}_2(\phi), \mathbf{k}) \right\}.\end{aligned}\quad (\text{B.49})$$

Expression (B.49) is a completely decoupled integral equation which we expect to work particularly well for three-body binding energies close to the two-body threshold.

## B.7 Numerical implementation

To obtain binding energies, we solve Eq. (4.47) numerically. Since the Faddeev component depends on the shifted momenta, we can not simply discretize the system and reduce the integral equation to a system of linear equations as in Sec. B.3. Further, the shifted momenta still depend on the relative angle  $\phi_k - \phi_q$  and we can not analytically perform the angular integration. Therefore, we interpolate the Faddeev components under the integral. We use a spline interpolation as suggested by Glöckle et al. in Ref. [145]. The idea is to introduce spline elements  $S_k(y)$  with which a function  $f(y)$  can be interpolated

$$f(y) \approx \sum_k S_k(y) f(y_k), \quad (\text{B.50})$$

with sampling points  $\{y_k\}$  chosen such that  $y$  is always between two sampling points. In Eq. (4.47) we want to interpolate the transition matrix as well as the Faddeev components depending on the shifted momenta. In order to assure that the shifted momenta never exceed the range of the sampling points we use two different sets  $\{\underline{y}_i\}$  and  $\{\underline{z}_i\}$ <sup>3</sup>

$$y_{i\rho}^\rho \in [0, \Lambda], \quad (\text{B.51a})$$

$$y_{i_z}^z \in [-\Lambda, \Lambda], \quad (\text{B.51b})$$

$$z_{i\rho}^\rho \in [0, \frac{3}{2}\Lambda], \quad (\text{B.51c})$$

$$z_{i_z}^z \in [-\frac{3}{2}\Lambda, \frac{3}{2}\Lambda]. \quad (\text{B.51d})$$

For  $\underline{q}$  and  $\underline{k}$  we use the set  $\{\underline{y}_i\}$  with weights  $w_{\underline{k}} \equiv w_{k_\rho}^\rho w_{k_z}^z$  and for  $\underline{p}$   $\{\underline{z}_i\}$ . Since we are in a cylindrical basis, we need spline functions for the  $\rho$ - and the  $z$ -component. We abbreviate  $S_s(\underline{y}) \equiv S_{s_\rho}^\rho(y^\rho) \cdot S_{s_z}^z(y^z)$  and find after discretizing the integral in Eq. (4.47)

$$\begin{aligned} \psi_{\bar{m}_1 m_2}(E, \underline{z}_i, \underline{y}_j) = & -g_0(\underline{z}_i^2, \underline{y}_j^2) \sum_{\underline{k}} w_{\underline{k}} \mathcal{Y}_{k_\rho}^\rho \int_0^{2\pi} d\phi \left\{ \sum_{s_1} \mathbf{s}_{s_1}(\underline{\pi}_1(\phi)) t_{\bar{m}_1}(E - \frac{3}{4}\underline{y}_j^2/M, \underline{z}_i, \underline{z}_{s_1}) \right. \\ & \left. \times \sum_{n_1, n_3=0}^{\bar{m}_1} D_{n_1 n_3}^{\bar{m}_1 \bar{m}_1}(y_{j_\rho}^\rho, y_{k_\rho}^\rho, \phi) \frac{y_{m_2+n_1-n_3}^*(\phi)}{\sqrt{2\pi}} (-1)^{\bar{m}_1} \sum_{s_2} \mathbf{s}_{s_2}(-\underline{\pi}_2(\phi)) \psi_{\bar{m}_1 m_2}(\underline{z}_{s_2}, \underline{y}_k) + \pi_{1,2} \leftrightarrow -\pi_{1,2} \right\}. \end{aligned} \quad (\text{B.52})$$

All quantities depending on  $\phi$  are analytically known, allowing for a quick computation of the angular integration. For  $\bar{m}_1 = m_2 = 0$  Eq. (B.52) simplifies to

$$\begin{aligned} \psi_{00}(E, \underline{z}_i, \underline{y}_j) = & \\ & -g_0(\underline{z}_i^2, \underline{y}_j^2) \sum_{\underline{k}} w_{\underline{k}} \mathcal{Y}_{k_\rho}^\rho \int_0^{2\pi} \frac{d\phi}{2\pi} \left\{ \sum_{s_1} \mathbf{s}_{s_1}(\underline{\pi}_1(\phi)) t_0(E - \frac{3}{4}\underline{y}_j^2/M, \underline{z}_i, \underline{z}_{s_1}) \sum_{s_2} \mathbf{s}_{s_2}(-\underline{\pi}_2(\phi)) \psi_{00}(\underline{z}_{s_2}, \underline{y}_k) + \pi_{1,2} \leftrightarrow -\pi_{1,2} \right\}. \end{aligned} \quad (\text{B.53})$$

Equations (B.52) and (B.53) are systems of linear equations. We can write them symbolically as

$$\psi_{\bar{m}_1 m_2}(E, \underline{z}_i, \underline{y}_j) = \sum_{\underline{k}} \sum_{s_2} K_{\bar{m}_1 m_2}(E; \underline{z}_i, \underline{y}_j; \underline{z}_{s_2}, \underline{y}_k) \psi_{\bar{m}_1 m_2}(E, \underline{z}_{s_2}, \underline{y}_k), \quad (\text{B.54})$$

with a kernel matrix  $K_{\bar{m}_1 m_2}(E; \underline{z}_i, \underline{y}_j; \underline{z}_{s_2}, \underline{y}_k)$ . Using  $N$  sampling points for all  $\rho$ -components and  $2N - 1$  for all  $z$ -components, a  $N^2(2N - 1)^2$  dimensional system of equations is left to solve. Already for a small number of sampling points, the capability of, e.g., a QR algorithm is exceeded. However, the kernel matrix is sparse and hence, matrix vector multiplications can be implemented cost-efficiently. Thus we use a Lanczos type algorithm to solve Eq. (B.53) (cf., e.g., Ref. [146]).

Negative energies  $E$ , for which Eq. (B.52) has a solution, are binding energies for three bosonic dipoles. More specifically, a negative energy for which the kernel matrix has eigenvalue 1 is a binding energy of the three-boson system. Left to solve is a root-finding problem. For robustness, we employ a bisection method which constrains the three-body spectrum to a finite domain.

<sup>3</sup> The cutoff which regularizes ultraviolet divergences is the Gaussian cutoff scale  $\lambda$ , similar to Sec. B.3

## B.8 Derivation of the modified Faddeev equation

We present our derivation of the modified Faddeev equation with an energy independent kernel which is numerically favorable for non-separable potentials. We start from the modified transition matrix

$$\bar{T}(E, \ell, \ell') \equiv T(E, \ell, \ell') / (E - \ell^2 / M), \quad (\text{B.55})$$

which obeys the LS equation

$$(E - \ell^2 / M) \bar{T}(E, \ell, \ell') = -V(\ell, \ell') + \int d^3 k V(\ell, \mathbf{k}) \bar{T}(E, \mathbf{k}, \ell'), \quad (\text{B.56})$$

following straightforwardly from Eq. (4.1). We further define the inverse, modified transition matrix,  $\bar{T}^{-1}(E, \ell, \ell')$  to obey

$$\int d^3 k \bar{T}(E, \ell, \mathbf{k}) \bar{T}^{-1}(E, \mathbf{k}, \ell') \equiv \delta^{(3)}(\ell - \ell'), \quad (\text{B.57})$$

which we need in a next step. We can also derive an LS equation for  $\bar{T}^{-1}(E, \ell, \ell')$

$$\int d^3 k V(\ell, \mathbf{k}) \bar{T}^{-1}(E, \mathbf{k}, \ell') = V(\ell, \ell') - (E - \ell^2 / M) \delta^{(3)}(\ell - \ell'), \quad (\text{B.58})$$

which follows, when multiplying Eq. (B.56) for  $\bar{T}(E, \ell, \mathbf{k}')$  with  $\bar{T}^{-1}(E, \mathbf{k}', \ell')$  from the right and integrating over  $d^3 k'$  subsequently. Further, a similar, but weaker relation holds, when interchanging  $\bar{T}$  and  $\bar{T}^{-1}$  in Eq. (B.57). Using the LS Eq. for  $\bar{T}$  and  $\bar{T}^{-1}$  we find

$$\int d^3 k \int d^3 k' V(\ell, \mathbf{k}) \bar{T}^{-1}(E, \mathbf{k}, \mathbf{k}') \bar{T}(E, \mathbf{k}', \ell') = V(\ell, \ell'). \quad (\text{B.59})$$

We remark that Eq. (B.59) does not imply that the integral over  $\bar{T}^{-1} \bar{T}$  is proportional to a delta distribution like in Eq. (B.57) but just holds in combination with the potential  $V$ .

We take the Faddeev equation from Ref. [135]

$$\begin{aligned} \psi(E, \mathbf{p}', \mathbf{q}) = & \quad (\text{B.60}) \\ -g_0(p'^2, q^2) \int d^3 k d^3 k' d^3 q' T(E - \frac{3}{4}q^2 / M, \mathbf{p}', \mathbf{k}) \{ \mathcal{P}(\mathbf{k}, \mathbf{q}; \mathbf{k}', \mathbf{q}') + g_0(k^2, q^2) T_{3c}(E) [\mathbb{1} + \mathcal{P}](\mathbf{k}, \mathbf{q}; \mathbf{k}', \mathbf{q}') \} \psi(E, \mathbf{k}', \mathbf{q}'), \end{aligned}$$

with the permutation operator

$$\mathcal{P}(\mathbf{k}, \mathbf{q}; \mathbf{k}', \mathbf{q}') \equiv \delta^{(3)}(\mathbf{k} - \frac{1}{2}\mathbf{q} - \mathbf{q}') \delta^{(3)}(\mathbf{q} + \mathbf{k}' + \frac{1}{2}\mathbf{q}') + \delta^{(3)}(\mathbf{k} + \frac{1}{2}\mathbf{q} + \mathbf{q}') \delta^{(3)}(\mathbf{q} - \mathbf{k}' + \frac{1}{2}\mathbf{q}'), \quad (\text{B.61})$$

$$[\mathbb{1} + \mathcal{P}](\mathbf{k}, \mathbf{q}; \mathbf{k}', \mathbf{q}') \equiv \delta^{(3)}(\mathbf{k} - \mathbf{k}') \delta^{(3)}(\mathbf{q} - \mathbf{q}') + \mathcal{P}(\mathbf{k}, \mathbf{q}; \mathbf{k}', \mathbf{q}') \quad (\text{B.62})$$

and the three-body transition amplitude  $T_{3c}(E)$ . We use that

$$g_0(p'^2, q^2) T(E - \frac{3}{4}q^2 / M, \mathbf{p}', \mathbf{k}) = \frac{1}{E - \frac{3}{4}q^2 / M - p'^2 / M} T(E - \frac{3}{4}q^2 / M, \mathbf{p}', \mathbf{k}) \stackrel{\text{def}}{=} \bar{T}(E - \frac{3}{4}q^2 / M, \mathbf{p}', \mathbf{k}) \quad (\text{B.63})$$

and act from left with (cf. Eq. (B.58))

$$\int d^3 p' \{ V(\mathbf{p}, \mathbf{p}') - (E - (p^2 + \frac{3}{4}q^2) / M) \delta^{(3)}(\mathbf{p} - \mathbf{p}') \} = \int d^3 p' d^3 p'' V(\mathbf{p}, \mathbf{p}'') \bar{T}^{-1}(E - \frac{3}{4}q^2 / M, \mathbf{p}'', \mathbf{p}'). \quad (\text{B.64})$$

We can then use Eq. (B.59) and perform the integrations over  $d^3 p'$  and  $d^3 p''$  to obtain

$$\begin{aligned} & - (E - (p^2 + \frac{3}{4}q^2) / M) \psi(\mathbf{p}, \mathbf{q}) + \int d^3 p' V(\mathbf{p}, \mathbf{p}') \psi(\mathbf{p}', \mathbf{q}) \\ & = - \int d^3 k d^3 k' d^3 q' V(\mathbf{p}, \mathbf{k}) \{ \mathcal{P}(\mathbf{k}, \mathbf{q}; \mathbf{k}', \mathbf{q}') + g_0(k^2, q^2) T_{3c}(E) [\mathbb{1} + \mathcal{P}](\mathbf{k}, \mathbf{q}; \mathbf{k}', \mathbf{q}') \} \psi(E, \mathbf{k}', \mathbf{q}'). \end{aligned} \quad (\text{B.65})$$

The integration over the permutation operators eliminates two of the three integrations on the right-hand side and can be solved similarly to Eq. (B.60). However, there is one essential difference which is of importance when numerically searching for binding energies fulfilling Eq. (B.65). The energy dependence of the integral kernels in Eq. (B.65) is analytically known.

When discretizing Eqs. (B.65) or (B.60), left to solve is an eigenproblem. The binding energies are then those energies for which discretized kernel matrix has an eigenvalue 1 or  $E$ , respectively. This criterion necessitates a root search in the eigenvalues. For the original Faddeev equation (B.60) many evaluations of the two-body transition matrix are possibly required. For non-separable potentials this might actually yield the dominating contribution to the numerical expenses. Employing the modified Faddeev equation it is usually much cheaper to obtain the kernel matrix.

In the particular case of just two-body interactions, i.e. for  $T_c^{(3)}(E) \equiv 0$ , the kernel is completely energy independent and after performing the integrations over the permutation operators Eq. (B.65) further simplifies to

$$E\psi(\mathbf{p}, \mathbf{q}) = \frac{1}{M} \left( \frac{3}{4}q^2 + p^2 \right) \psi(\mathbf{p}, \mathbf{q}) + \int d^3 p' V(\mathbf{p}, \mathbf{p}') \psi(\mathbf{p}', \mathbf{q}) + \int d^3 q' \{ V(\mathbf{p}, \pi_1) \psi(-\pi_2, \mathbf{q}') + V(\mathbf{p}, -\pi_1) \psi(\pi_2, \mathbf{q}') \}. \quad (\text{B.66})$$

For this scenario, the kernel matrix on the right-hand side of Eq. (B.66) is completely energy independent and has to be evaluated just once. The negative eigenvalues represent the whole spectrum of three-body binding energies.

## B.9 Partial wave projection of the modified Faddeev equation

We show how to project the modified Faddeev equation (4.49) (Eq. (B.66)) on spherical partial waves. We use bipolar spherical harmonics (BIPS), defined in Eq. (4.50). The first term immediately follows from the orthogonality relation for the BIPS [143]

$$\int d\Omega_p \int d\Omega_q \mathcal{Y}_{l\lambda}^{LM}(\Omega_p, \Omega_q) \mathcal{Y}_{l'\lambda'}^{L'M'}(\Omega_p, \Omega_q) = \delta_{LL'} \delta_{MM'} \delta_{ll'} \delta_{\lambda\lambda'} \equiv \delta_{\alpha\alpha'}. \quad (\text{B.67})$$

We used the shorthand notation from Eq. (4.52) in the last equality. For the second term, which we denote  $E\psi^{(2)}(\mathbf{p}, \mathbf{q})$ , we insert a delta distribution

$$E\psi^{(2)}(\mathbf{p}, \mathbf{q}) = \int d^3 p' \int d^3 q' V(\mathbf{p}, \mathbf{p}') \delta^{(3)}(\mathbf{q} - \mathbf{q}') \psi(\mathbf{p}', \mathbf{q}') \quad (\text{B.68})$$

and project the potential including the delta distribution on BIPS

$$\begin{aligned} & \int d\Omega_p \int d\Omega_q \int d\Omega_{p'} \int d\Omega_{q'} \mathcal{Y}_\alpha^*(\Omega_p, \Omega_q) \mathcal{Y}_{\alpha'}(\Omega_{p'}, \Omega_{q'}) V(\mathbf{p}, \mathbf{p}') \delta^{(3)}(\mathbf{q} - \mathbf{q}') \\ &= \int d\Omega_p \int d\Omega_{p'} \sum_{m,\mu} \sum_{m',\mu'} \begin{bmatrix} l & \lambda & L \\ m & \mu & M \end{bmatrix} \begin{bmatrix} l' & \lambda' & L' \\ m' & \mu' & M' \end{bmatrix} Y_{lm}^*(\Omega_p) Y_{l'm'}(\Omega_{p'}) V(\mathbf{p}, \mathbf{p}') \\ & \times \int d\Omega_q \int d\Omega_{q'} Y_{\lambda\mu}^*(\Omega_q) Y_{\lambda'\mu'}(\Omega_{q'}) \delta^{(2)}(\Omega_q - \Omega_{q'}) \frac{\delta(q - q')}{qq'} \\ &= \delta_{\lambda\lambda'} \delta_{MM'} \sum_{m=-M}^M \begin{bmatrix} l & \lambda & L \\ m & M-m & M \end{bmatrix} \begin{bmatrix} l' & \lambda & L' \\ m & M-m & M \end{bmatrix} v_m^{ll'}(p, p') \frac{\delta(q - q')}{qq'} \\ & \equiv \mathcal{V}_{\alpha\alpha'}(p, p') \frac{\delta(q - q')}{qq'}, \end{aligned} \quad (\text{B.69})$$

with the projected two-body potential,  $v_m^{ll'}(p, p')$ , from Eq. (4.20). In the second line, we plugged in the definition of the BIPS (4.50). For the potential holds

$$V(\mathbf{p}, \mathbf{p}') \delta^{(3)}(\mathbf{q} - \mathbf{q}') = \sum_{\alpha, \alpha'} \mathcal{V}_{\alpha\alpha'}(p, p') \frac{\delta(q - q')}{qq'} \mathcal{Y}_\alpha(\Omega_p, \Omega_q) \mathcal{Y}_\alpha^*(\Omega_{p'}, \Omega_{q'}), \quad (\text{B.70})$$

following from the completeness of the BIPS [143]. To project  $\psi^{(2)}$ , we act with the operator

$$\int d\Omega_p \int d\Omega_q \mathcal{Y}_\alpha^*(\Omega_p, \Omega_q) \quad (\text{B.71})$$

from the left and use the orthogonality relation (B.67) to obtain

$$E\psi_{\alpha}^{(2)}(p, q) = \sum_{\alpha'} \int d p' p'^2 \mathcal{V}_{\alpha\alpha'}(p, p') \psi_{\alpha'}(p', q), \quad (\text{B.72})$$

with

$$\psi(\mathbf{p}, \mathbf{q}) = \sum_{\alpha} \psi_{\alpha}(p, q) \mathcal{Y}_{\alpha}(\Omega_p, \Omega_q). \quad (\text{B.73})$$

The projection of the third term proceeds in analogy to the well known partial wave projection of the Faddeev equation (4.33), which can be found in the literature (e.g. [135]).



## List of Figures

1.1. Experimental evidence for a signal in the 3872 MeV region . . . . .	2
1.2. Distribution for $B^+ \rightarrow K^+(X(3872) \rightarrow \pi^+ \pi^- J/\psi)$ decays . . . . .	3
1.3. Experimental evidence for a Bose-Einstein condensate of dysprosium . . . . .	5
2.1. Unrenormalized bound-state spectrum for the $1/r^2$ potential . . . . .	17
2.2. Renormalized bound-state spectrum and evolution of the coupling constant for the $1/r^2$ potential . . . . .	18
2.3. Unrenormalized bound-state spectrum for the $1/r^3$ potential . . . . .	20
2.4. Renormalized bound-state spectrum and evolution of the coupling constant for the $1/r^3$ potential . . . . .	20
3.1. Feynman rules for XEFT . . . . .	22
3.2. One-pion-exchange diagram . . . . .	23
3.3. Leading-order contribution to the $\bar{D}^0 D^{*0}$ scattering amplitude . . . . .	24
3.4. Next-to-leading-order contributions to the $\bar{D}^0 D^{*0}$ scattering amplitude . . . . .	25
3.5. Next-to-leading-order contribution from $D^{*0}$ self-energy . . . . .	25
3.6. Self-energy graph and counterterm for the $D^{*0}$ . . . . .	26
3.7. The full $D^{*0}$ propagator . . . . .	27
3.8. Scattering diagram for the asymptotic states $D^0 \bar{D}^0 \pi$ . . . . .	29
3.9. Scattering amplitudes shifting the coefficient $s_2$ at NNLO . . . . .	31
3.10. Example for a cut diagram, determining a contribution to the imaginary part of the pole position $B$ . . . . .	32
3.11. Expansion parameter for the perturbative inclusion of pions in XEFT . . . . .	33
3.12. Binding energy of the $X(3872)$ in dependence on the light quark masses . . . . .	34
3.13. Quark mass dependence of the real and imaginary part of the $X(3872)$ 's scattering length . . . . .	35
3.14. Quark mass dependence of the $X(3872)$ 's $S$ -wave effective range . . . . .	35
3.15. Density plot for the expansion parameter $\epsilon_{\pi}^L$ . . . . .	39
3.16. Volume dependence of the binding energy for stable $D^{*0}$ meson . . . . .	40
3.17. Volume dependence of the binding energy for physical quark masses . . . . .	41
3.18. Quark mass dependence of the binding energy for various box lengths . . . . .	42
4.1. Partial wave projections for the long-range dipole-dipole potential ( $m = 0$ ) . . . . .	47
4.2. Unrenormalized spectrum and the scattering length $a_0^{00}$ for $D > 0$ , $m = 0$ and $P = +$ . . . . .	49
4.3. Binding energies in dependence on the scattering length $a_0^{00}$ . . . . .	50
4.4. Unrenormalized spectrum and the scattering length $a_0^{00}$ for $D < 0$ , $m = 0$ and $P = +$ . . . . .	51
4.5. Partially renormalized spectrum for antiparallel dipoles ( $\{l\} = \{0, 2\}$ ) . . . . .	52
4.6. Partially renormalized spectrum for antiparallel dipoles ( $\{l\} = \{6, 8\}$ ) . . . . .	53
4.7. Fully renormalized spectrum for two antiparallel dipoles and evolution of coupling constants . . . . .	53
4.8. Binding energies for parallel and antiparallel dipoles in dependence on the scattering length $a_0^{00}$ . . . . .	54
4.9. Spectrum for three bosons acting via a two-body contact potential . . . . .	57
4.10. Bound-state spectrum for three bosonic dipoles . . . . .	58
4.11. Three-body bound-state spectrum and runtime comparison for the $1/r^3$ potential . . . . .	61
A.1. Momentum dependent NLO contact interaction . . . . .	68
A.2. Tree level OPE contribution to the NLO amplitude . . . . .	69
A.3. One-loop pion-exchange contribution to the NLO amplitude . . . . .	70
A.4. Two-loop pion-exchange contribution to the NLO amplitude . . . . .	71
A.5. Lowest-order self-energy insertion. . . . .	73
B.1. Gaussian regulator function in coordinate space . . . . .	76
B.2. Partial wave projections for the long-range dipole-dipole potential for $m = 1$ . . . . .	79
B.3. Two-loop representation of the LS equation . . . . .	81
B.4. Unrenormalized spectrum and the scattering length $a_0^{11}$ for $D > 0$ , $m = 0$ and $P = -$ . . . . .	82
B.5. Unrenormalized spectrum and the scattering length $a_0^{11}$ for $D < 0$ , $m = 0$ and $P = -$ . . . . .	82
B.6. Unrenormalized spectrum and the scattering lengths $a_0^{33}$ and $a_0^{55}$ for $D < 0$ , $m = 0$ and $P = -$ . . . . .	83
B.7. Unrenormalized spectrum and the scattering length $a_1^{22}$ for $D > 0$ , $m = 1$ and $P = +$ . . . . .	84
B.8. Unrenormalized spectrum and the scattering length $a_1^{22}$ for $D < 0$ , $m = 1$ and $P = +$ . . . . .	84

---

B.9. Convergence in the truncation parameter for $D < 0$ , $m = 0$ and $P = +$ . . . . .	85
B.10. Binding energy in dependence on the scattering length for different $L_{\max}$ . . . . .	86
B.11. Convergence in the truncation parameter for $D > 0$ , $m = 0$ and $P = +$ . . . . .	86
B.12. Convergence in the truncation parameter for $D > 0$ , $m = 0$ and $P = -$ . . . . .	87
B.13. Convergence in the truncation parameter for $D < 0$ , $m = 0$ and $P = -$ . . . . .	87
B.14. Convergence in the truncation parameter for $D > 0$ , $m = 1$ and $P = +$ . . . . .	88
B.15. Convergence in the truncation parameter for $D < 0$ , $m = 1$ and $P = +$ . . . . .	88

---

## Bibliography

---

- [1] H. D. Politzer. Reliable perturbative results for strong interactions? *Phys. Rev. Lett.*, 30:1346–1349, 1973.
- [2] D. J. Gross and F. Wilczek. Ultraviolet behavior of non-abelian gauge theories. *Phys. Rev. Lett.*, 30:1343–1346, 1973.
- [3] S. Bethke. Experimental tests of asymptotic freedom. *Prog. Part. Nucl. Phys.*, 58:351–386, 2007.
- [4] M. Gell-Mann. A schematic model of baryons and mesons. *Phys. Lett.*, 8:214–215, 1964.
- [5] K. G. Wilson. Confinement of quarks. *Phys. Rev.*, D10:2445–2459, 1974.
- [6] J. Gasser and H. Leutwyler. Chiral perturbation theory to one loop. *Ann. Phys.*, 158:142, 1984.
- [7] J. Gasser and H. Leutwyler. Chiral perturbation theory: expansions in the mass of the strange quark. *Nucl. Phys.*, B250:465–516, 1985.
- [8] E. Braaten and H. W. Hammer. Universality in few-body systems with large scattering length. *Phys. Rept.*, 428:259–390, 2006.
- [9] H. Metcalf and P. V. der Straten. *Laser cooling and trapping*. Springer, 1999.
- [10] M. A. Baranov, M. Dalmonte, G. Pupillo and P. Zoller. Condensed matter theory of dipolar quantum gases. *Chem. Rev.*, 112(9):5012–5061, 2012.
- [11] M. H. Anderson, J. R. Ensher, M. R. Matthews, C. E. Wieman and E. A. Cornell. Observation of Bose-Einstein condensation in a dilute atomic vapor. *Science*, 269(5221):198–201, 1995.
- [12] K. B. Davis et al. Bose-Einstein condensation in a gas of sodium atoms. *Phys. Rev. Lett.*, 75:3969–3973, 1995.
- [13] T. Kraemer et al. Evidence for Efimov quantum states in an ultracold gas of caesium atoms. 440:315–318, 2006.
- [14] S. Knoop et al. Observation of an Efimov-like trimer resonance in ultracold atom-dimer scattering. *Nature Physics*, 5:227–230, 2009.
- [15] N. Brambilla et al. Heavy quarkonium: progress, puzzles and opportunities. *Eur. Phys. J.*, C71:1534, 2011.
- [16] S. Fleming, M. Kusunoki, T. Mehen and U. van Kolck. Pion interactions in the  $X(3872)$ . *Phys. Rev.*, D76:034006, 2007.
- [17] S. Giovanazzi, A. Görlitz and T. Pfau. Tuning the dipolar interaction in quantum gases. *Phys. Rev. Lett.*, 89:130401, 2002.
- [18] M. B. Voloshin and L. B. Okun. Hadron molecules and charmonium atom. *JETP Lett.*, 23:333–336, 1976.
- [19] S. Choi et al. Observation of a narrow charmonium-like state in exclusive  $B^\pm \rightarrow K^\pm \pi^+ \pi^- J/\psi$  decays. *Phys. Rev. Lett.*, 91:262001, 2003.
- [20] T. Barnes and S. Godfrey. Charmonium options for the  $X(3872)$ . *Phys. Rev.*, D69:054008, 2004.
- [21] K. Abe et al. Evidence for  $X(3872) \rightarrow \gamma J/\psi$  and the sub-threshold decay  $X(3872) \rightarrow \omega J/\psi$ . In *Lepton and photon interactions at high energies. Proceedings, 22nd International Symposium, Uppsala, Sweden, 2005*.
- [22] E. Braaten and M. Kusunoki. Low-energy universality and the new charmonium resonance at 3870 MeV. *Phys. Rev.*, D69:074005, 2004.
- [23] M. Takizawa and S. Takeuchi.  $X(3872)$  as a hybrid state of the charmonium and the hadronic molecule. *PTEP*, 2013:0903D01, 2013.
- [24] R. D. Matheus, S. Narison, M. Nielsen and J. M. Richard. Can the  $X(3872)$  be a  $1^{++}$  four-quark state? *Phys. Rev.*, D75:014005, 2007.

- [25] Z.-G. Wang and T. Huang. Analysis of the  $X(3872)$ ,  $Z_c(3900)$  and  $Z_c(3885)$  as axial-vector tetraquark states with QCD sum rules. *Phys. Rev.*, D89(5):054019, 2014.
- [26] J. Ferretti, G. Galatà and E. Santopinto. Quark structure of the  $X(3872)$  and  $\chi_b(3P)$  resonances. *Phys. Rev.*, D90(5):054010, 2014.
- [27] N. A. Törnqvist. Possible large deuteronlike meson-meson states bound by pions. *Phys. Rev. Lett.*, 67:556–559, 1991.
- [28] E. S. Swanson. Diagnostic decays of the  $X(3872)$ . *Phys. Lett.*, B598(3-4):197–202, 2004.
- [29] M. Voloshin. Interference and binding effects in decays of possible molecular component of  $X(3872)$ . *Phys. Lett.*, B579(3-4):316–320, 2004.
- [30] E. S. Swanson. Short-range structure in the  $X(3872)$ . *Phys. Lett.*, B588:189–195, 2004.
- [31] F. E. Close and P. R. Page. The  $D^{*0}\bar{D}^0$  threshold resonance. *Phys. Lett.*, B578(1-2):119–123, 2004.
- [32] S. L. Olsen. A new hadron spectroscopy. *Front. Phys.*, 10:101401, 2015.
- [33] K. Olive et al. Review of particle physics. *Chin. Phys.*, C38:090001, 2014.
- [34] D. Acosta et al. Observation of the narrow state  $X(3872) \rightarrow J/\psi \pi^+ \pi^-$  in  $\bar{p}p$  collisions at  $\sqrt{s} = 1.96$  TeV. *Phys. Rev. Lett.*, 93:072001, 2004.
- [35] R. Aaij et al. Determination of the  $X(3872)$  meson quantum numbers. *Phys. Rev. Lett.*, 110:222001, 2013.
- [36] B. Aubert et al. Search for  $B^+ \rightarrow X(3872)K^+$ ,  $X(3872) \rightarrow J/\psi \gamma$ . *Phys. Rev.*, D74:071101, 2006.
- [37] A. Abulencia et al. Analysis of the quantum numbers  $J^{PC}$  of the  $X(3872)$ . *Phys. Rev. Lett.*, 98:132002, 2007.
- [38] P. del Amo Sanchez et al. Evidence for the decay  $X(3872) \rightarrow J/\psi \omega$ . *Phys. Rev.*, D82:011101, 2010.
- [39] K. Abe et al. Experimental constraints on the possible  $J^{PC}$  quantum numbers of the  $X(3872)$ . In *Lepton and photon interactions at high energies. Proceedings, 22nd International Symposium, Uppsala, Sweden, 2005*.
- [40] E. Braaten and D. Kang.  $J/\psi \omega$  decay channel of the  $X(3872)$  charm meson molecule. *Phys. Rev.*, D88:014028, 2013.
- [41] Y.-B. Yang et al. Lattice study on  $\eta_{c2}$  and  $X(3872)$ . *Phys. Rev.*, D87:014501, 2013.
- [42] S.-K. Choi et al. Bounds on the width, mass difference and other properties of  $X(3872) \rightarrow \pi^+ \pi^- J/\psi$  decays. *Phys. Rev.*, D84:052004, 2011.
- [43] D. Gamermann and E. Oset. Isospin breaking effects in the  $X(3872)$  resonance. *Phys. Rev.*, D80:014003, 2009.
- [44] J. J. Sakurai. *Modern quantum mechanics*. Addison Wesley, 1993.
- [45] R. A. Briceño, Z. Davoudi, T. Luu and M. J. Savage. Two-nucleon systems in a finite volume: (II)  ${}^3S_1 - {}^3D_1$  coupled channels and the deuteron. *Phys. Rev.*, D88(11):114507, 2013.
- [46] E. Garzon, R. Molina, A. Hosaka and E. Oset. Strategies for an accurate determination of the  $X(3872)$  energy from QCD lattice simulations. *Phys. Rev.*, D89(1):014504, 2014.
- [47] Efimov, V. Energy levels arising from resonant two-body forces in a three-body system. *Phys. Lett.*, B33(8):563 – 564, 1970.
- [48] V. Baru et al. Three-body  $D\bar{D}\pi$  dynamics for the  $X(3872)$ . *Phys. Rev.*, D84:074029, 2011.
- [49] V. Baru et al. Quark mass dependence of the  $X(3872)$  binding energy. *Phys. Lett.*, B726:537–543, 2013.
- [50] E. Braaten. Galilean-invariant effective field theory for the  $X(3872)$ . *Phys. Rev.*, D91(11):114007, 2015.
- [51] S. Fleming, T. Mehen and I. W. Stewart. NNLO corrections to nucleon-nucleon scattering and perturbative pions. *Nucl. Phys.*, A677:313–366, 2000.

- [52] S. Fleming and T. Mehen. The decay of the  $X(3872)$  into  $\chi_{cJ}$  and the operator product expansion in XEFT. *Phys. Rev.*, D85:014016, 2012.
- [53] E. Braaten, H.-W. Hammer and T. Mehen. Scattering of an ultrasoft pion and the  $X(3872)$ . *Phys. Rev.*, D82:034018, 2010.
- [54] S. Prelovsek and L. Leskovec. Evidence for  $X(3872)$  from  $DD^*$  scattering on the lattice. *Phys. Rev. Lett.*, 111:192001, 2013.
- [55] M. Padmanath, C. B. Lang and S. Prelovsek.  $X(3872)$  and  $Y(4140)$  using diquark-antidiquark operators with lattice QCD. *Phys. Rev.*, D92(3):034501, 2015.
- [56] S.-h. Lee, C. DeTar, H. Na and D. Mohler. Searching for the  $X(3872)$  and  $Z_c^+(3900)$  on HISQ lattices. 2014.
- [57] M. Lüscher. Volume dependence of the energy spectrum in massive quantum field theories. 1. stable particle states. *Commun. Math. Phys.*, 104:177, 1986.
- [58] M. Lüscher. Volume dependence of the energy spectrum in massive quantum field theories. 2. scattering states. *Commun. Math. Phys.*, 105:153–188, 1986.
- [59] S. Beane, P. Bedaque, A. Parreno and M. Savage. Two nucleons on a lattice. *Phys. Lett.*, B585:106–114, 2004.
- [60] K. Polejaeva and A. Rusetsky. Three particles in a finite volume. *Eur. Phys. J.*, A48:67, 2012.
- [61] R. A. Briceño and Z. Davoudi. Three-particle scattering amplitudes from a finite volume formalism. *Phys. Rev.*, D87(9):094507, 2013.
- [62] M. T. Hansen and S. R. Sharpe. Relativistic, model-independent, three-particle quantization condition. *Phys. Rev.*, D90(11):116003, 2014.
- [63] L. Roca and E. Oset. Scattering of unstable particles in a finite volume: the case of  $\pi\rho$  scattering and the  $a_1(1260)$  resonance. *Phys. Rev.*, D85:054507, 2012.
- [64] S. Kreuzer and H.-W. Hammer. The triton in a finite volume. *Phys. Lett.*, B694:424–429, 2011.
- [65] S. Kreuzer and H.-W. Hammer. On the modification of the Efimov spectrum in a finite cubic box. *Eur. Phys. J.*, A43:229–240, 2010.
- [66] S. Bour, S. Koenig, D. Lee, H.-W. Hammer and U.-G. Meißner. Topological phases for bound states moving in a finite volume. *Phys. Rev.*, D84:091503, 2011.
- [67] D. Agadjanov, M. Doring, M. Mai, U.-G. Meißner and A. Rusetsky. The optical potential on the lattice. *JHEP*, 06:043, 2016.
- [68] U.-G. Meißner, G. Ríos and A. Rusetsky. Spectrum of three-body bound states in a finite volume. *Phys. Rev. Lett.*, 114(9):091602, 2015.
- [69] H. Feshbach. Unified theory of nuclear reactions. *Ann. Phys.*, 5(4):357 – 390, 1958.
- [70] S. Inouye et al. Observation of Feshbach resonances in a Bose-Einstein condensate. *Nature*, 392(6672):151–154, 1998.
- [71] C. Chin et al. Precision Feshbach spectroscopy of ultracold  $\text{Cs}_2$ . *Phys. Rev.*, A70:032701, 2004.
- [72] K. Dieckmann et al. Decay of an ultracold fermionic lithium gas near a Feshbach resonance. *Phys. Rev. Lett.*, 89:203201, 2002.
- [73] M. W. Zwierlein et al. Condensation of pairs of fermionic atoms near a Feshbach resonance. *Phys. Rev. Lett.*, 92:120403, 2004.
- [74] J. Werner et al. Observation of Feshbach resonances in an ultracold gas of  $^{52}\text{Cr}$ . *Phys. Rev. Lett.*, 94:183201, 2005.
- [75] A. Griesmaier, J. Werner, S. Hensler, J. Stuhler and T. Pfau. Bose-Einstein condensation of chromium. *Phys. Rev. Lett.*, 94:160401, 2005.

- [76] T. Lahaye et al. Strong dipolar effects in a quantum ferrofluid. *Nature*, 448(7154):672–675, 2007.
- [77] M. Lu, N. Q. Burdick, S. H. Youn and B. L. Lev. Strongly dipolar Bose-Einstein condensate of dysprosium. *Phys. Rev. Lett.*, 107:190401, 2011.
- [78] W. C. Martin, R. Zalubas and L. Hagan. Atomic energy levels - The rare-earth elements. *National Bureau of Standards, US Department of Commerce*, 1978.
- [79] E. P. Gross. Structure of a quantized vortex in boson systems. *Il Nuovo Cimento*, 20(3):454–477, 1961.
- [80] L. Pitaevskii. Vortex line in an imperfect Bose gas. *Sov. Phys. JETP*, 13:451, 1961.
- [81] S. Yi and L. You. Trapped atomic condensates with anisotropic interactions. *Phys. Rev.*, A61:041604, 2000.
- [82] C. Eberlein, S. Giovanazzi and D. H. J. O'Dell. Exact solution of the Thomas-Fermi equation for a trapped Bose-Einstein condensate with dipole-dipole interactions. *Phys. Rev.*, A71:033618, 2005.
- [83] D. H. J. O'Dell, S. Giovanazzi and C. Eberlein. Exact hydrodynamics of a trapped dipolar Bose-Einstein condensate. *Phys. Rev. Lett.*, 92:250401, 2004.
- [84] B. Gadway and B. Yan. Strongly interacting ultracold polar molecules. *J. Phys.*, B49(15):152002, 2016.
- [85] S. Baier et al. Extended Bose-Hubbard models with ultracold magnetic atoms. *Science*, 352(6282):201–205, 2016.
- [86] G. Mazzarella, S. M. Giampaolo and F. Illuminati. Extended Bose-Hubbard model of interacting bosonic atoms in optical lattices: from superfluidity to density waves. *Phys. Rev.*, A73:013625, 2006.
- [87] K. R. A. Hazzard et al. Many-body dynamics of dipolar molecules in an optical lattice. *Phys. Rev. Lett.*, 113:195302, 2014.
- [88] V. Roudnev and M. Cavagnero. Universal resonant ultracold molecular scattering. *Phys. Rev.*, A79:014701, 2009.
- [89] C. Ticknor. Energy dependence of scattering ground-state polar molecules. *Phys. Rev.*, A76:052703, 2007.
- [90] C. Ticknor and S. T. Rittenhouse. Three-body recombination of ultracold dipoles to weakly bound dimers. *Phys. Rev. Lett.*, 105:013201, 2010.
- [91] Y. Wang, J. P. D'Incao and C. H. Greene. Efimov effect for three interacting bosonic dipoles. *Phys. Rev. Lett.*, 106:233201, 2011.
- [92] S. Ospelkaus et al. Controlling the hyperfine state of rovibronic ground-state polar molecules. *Phys. Rev. Lett.*, 104:030402, 2010.
- [93] S. A. Will, J. W. Park, Z. Z. Yan, H. Loh and M. W. Zwierlein. Coherent microwave control of ultracold  $^{23}\text{Na}^{40}\text{K}$  molecules. *Phys. Rev. Lett.*, 116:225306, Jun 2016.
- [94] D. B. Kaplan, M. J. Savage and M. B. Wise. A New expansion for nucleon-nucleon interactions. *Phys. Lett.*, B424:390–396, 1998.
- [95] H. Georgi. Effective field theory. *Ann. Rev. Nucl. Part. Sci.*, 43:209–252, 1993.
- [96] G. P. Lepage. How to renormalize the Schrödinger equation. In *Nuclear physics. Proceedings, 8th Jorge Andre Swieca summer school, Sao Jose dos Campos, Campos do Jordao, Brazil*, 1997.
- [97] F. Halzen and A. D. Martin. *Quarks and leptons: an introductory course in modern particle physics*. Wiley, 1984.
- [98] S. Weinberg. Phenomenological lagrangians. *Physica*, A96:327–340, 1979.
- [99] J. O. Andersen. Theory of the weakly interacting Bose gas. *Rev. Mod. Phys.*, 76:599, 2004.
- [100] J.-W. Chen, G. Rupak and M. J. Savage. Nucleon-nucleon effective field theory without pions. *Nucl. Phys.*, A653:386–412, 1999.
- [101] V. Baru et al. Heavy-quark spin symmetry partners of the  $X(3872)$  revisited. 2016.
- [102] H. A. Bethe. Theory of the effective range in nuclear scattering. *Phys. Rev.*, 76:38–50, 1949.

- [103] U. Kolck. *Chiral dynamics: theory and experiment: proceedings of the workshop held in Mainz, Germany*. Springer, 1998.
- [104] C. Bertulani, H.-W. Hammer and U. van Kolck. Effective field theory for halo nuclei: shallow p-wave states. *Nucl. Phys.*, A712(1-2):37 – 58, 2002.
- [105] M. E. Peskin and D. V. Schroeder. *An introduction to quantum field theory*. Westview Press, 1995.
- [106] S. König, D. Lee and H.-W. Hammer. Volume dependence of bound states with angular momentum. *Phys. Rev. Lett.*, 107:112001, 2011.
- [107] H.-W. Hammer and B. G. Swingle. On the limit cycle for the  $1/r^2$  potential in momentum space. *Ann. Phys.*, 321(2):306 – 317, 2006.
- [108] S. R. Beane et al. Singular potentials and limit cycles. *Phys. Rev.*, A64:042103, 2001.
- [109] J. D. Jackson. *Classical electrodynamics*. Wiley, 1999.
- [110] A. Nogga, R. G. E. Timmermans and U. van Kolck. Renormalization of one-pion exchange and power counting. *Phys. Rev.*, C72:054006, 2005.
- [111] G. F. Gribakin and V. V. Flambaum. Calculation of the scattering length in atomic collisions using the semiclassical approximation. *Phys. Rev.*, A48:546–553, 1993.
- [112] V. N. Efimov. Weakly-bound states of three resonantly-interacting particles. *Sov. J. Nucl. Phys.*, 12:589, 1971.
- [113] C. Cohen-Tannoudji, B. Diu, F. Laloe and B. Dui. *Quantum mechanics*. Wiley, 1977.
- [114] Lurié, D. *Particles and fields*. Wiley, 1968.
- [115] M. Jansen, H.-W. Hammer and Y. Jia. Light quark mass dependence of the  $X(3872)$  in an effective field theory. *Phys. Rev.*, D89(1):014033, 2014.
- [116] M. Jansen, H. W. Hammer and Y. Jia. Finite volume corrections to the binding energy of the  $X(3872)$ . *Phys. Rev.*, D92(11):114031, 2015.
- [117] M. Gell-Mann, R. Oakes and B. Renner. Behavior of current divergences under  $SU_3 \times SU_3$ . *Phys. Rev.*, 175:2195–2199, 1968.
- [118] C. McNeile et al. Direct determination of the strange and light quark condensates from full lattice QCD. *Phys. Rev.*, D87(3):034503, 2013.
- [119] E. Braaten and J. Stapleton. Analysis of  $J/\psi\pi^+\pi^-$  and  $D^0\bar{D}^0\pi^0$  decays of the  $X(3872)$ . *Phys. Rev.*, D81:014019, 2010.
- [120] A. Denner, S. Dittmaier, M. Roth and D. Wackerth. Predictions for all processes  $e^+e^- \rightarrow 4$  fermions +  $\gamma$ . *Nucl. Phys.*, B560:33–65, 1999.
- [121] A. Denner, S. Dittmaier, M. Roth and L. H. Wieders. Electroweak corrections to charged-current  $e^+e^- \rightarrow 4$  fermion processes: technical details and further results. *Nucl. Phys.*, B724:247–294, 2005.
- [122] M. Suzuki. The  $X(3872)$  boson: molecule or charmonium. *Phys. Rev.*, D72:114013, 2005.
- [123] A. R. Choudhary. Improved effective-range formula. *Phys. Rev.*, C27:398–404, 1983.
- [124] M. W. Kermode, L. J. Allen, J. P. McTavish and A. McKerrell. The effective-range function in the presence of a Yukawa potential. *J. Phys.*, G10(6):773, 1984.
- [125] T. Mehen and I. W. Stewart. Radiation pions in two-nucleon effective field theory. *Nucl. Phys.*, A665:164–182, 2000.
- [126] M. Voloshin. Interference and binding effects in decays of possible molecular component of  $X(3872)$ . *Phys. Lett.*, B579:316–320, 2004.
- [127] G. Colangelo, J. Gasser and H. Leutwyler.  $\pi\pi$  scattering. *Nucl. Phys.*, B603:125–179, 2001.

- 
- [128] D. Becirevic and F. Sanfilippo. Theoretical estimate of the  $D^* \rightarrow D\pi$  decay rate. *Phys. Lett.*, B721:94–100, 2013.
- [129] J. P. Lees et al. Measurement of the  $D^*(2010)^+$  meson width and the  $D^*(2010)^+ - D^0$  mass difference. *Phys. Rev. Lett.*, 111(11):111801, 2013.
- [130] F.-K. Guo, C. Hanhart and U.-G. Meißner. Interactions between heavy mesons and Goldstone bosons from chiral dynamics. *Eur. Phys. J.*, A40:171–179, 2009.
- [131] J. F. Ward. Calculation of nonlinear optical susceptibilities using diagrammatic perturbation theory. *Rev. Mod. Phys.*, 37:1–18, 1965.
- [132] J. Gasser and H. Leutwyler. Light quarks at low temperatures. *Phys. Lett.*, B184:83, 1987.
- [133] M. Jansen. Bound states of two and three bosonic dipoles. Master’s thesis, 2012.
- [134] K. Kanjilal and D. Blume. Low-energy resonances and bound states of aligned bosonic and fermionic dipoles. *Phys. Rev.*, A78:040703, 2008.
- [135] Glöckle, W. *The quantum mechanical few-body problem*. Springer, 1983.
- [136] L. Platter. *From cold atoms to light nuclei: the four-body problem in an effective theory with contact interactions*. PhD thesis, 2005.
- [137] P. F. Bedaque, H. W. Hammer and U. van Kolck. Renormalization of the three-body system with short-range interactions. *Phys. Rev. Lett.*, 82:463–467, 1999.
- [138] P. F. Bedaque, H. W. Hammer and U. van Kolck. The three-boson system with short-range interactions. *Nucl. Phys.*, A646:444–466, 1999.
- [139] W. ElKamhawy. Effective field theory for the  $X(3872)$  with explicit pions. Master’s thesis, 2016.
- [140] M. Schmidt. The  $X(3872)$  as  $D\bar{D}\pi$  resonance. Master’s thesis, 2016.
- [141] J. Messchendorp. The PANDA experiment at FAIR - Subatomic physics with antiprotons. 2016.
- [142] I. N. Bronstein and K. A. Semendjajew. *Taschenbuch der Mathematik*. Teubner, 1979.
- [143] D. A. Varshalovich, A. N. Moskalev and V. K. Khersonskii. *Quantum theory of angular momentum*. World Scientific, 1988.
- [144] L. Devroye. *Non-uniform random variate generation*. Springer, 1986.
- [145] W. Glöckle, G. Hasberg and A. R. Neghabian. Numerical treatment of few-body equations in momentum space by the spline method. *Z. Phys.*, A305(3):217–221, 1982.
- [146] A. Meister. *Numerik linearer Gleichungssysteme - Eine Einführung in moderne Verfahren*. Vieweg, 1999.

---

# Maximilian Jansen

## Curriculum vitae

### Personal details

Date of Birth        June 28, 1988  
Address              Luisenstraße 18  
                            64283 Darmstadt  
Email                 jansen@theorie.ikp.physik.tu-darmstadt.de

### Work experience

2014-present        Institut für Kernphysik der TU Darmstadt (Darmstadt, Germany)  
                            Scientific employee (May - present)  
2013                  Institute of High Energy Physics (Beijing, China)  
                            Visiting researcher (Apr. - Dec.)  
2012-2014          Helmholtz-Institut für Strahlen- und Kernphysik (Bonn, Germany)  
                            Scientific employee (Dec. - Apr.)  
2010-2012          University of Bonn (Bonn, Germany)  
                            Course instructor for physics (Oct. - Nov.)

### Education

2014-present        TU Darmstadt; Ph.D. student (May - present)  
2012-2014          University of Bonn; Ph.D. student (Dec. - Apr.)  
2010-2012          University of Bonn; M.Sc. in Physics (excellent, 1.0) (Oct. - Nov.)  
2010-2012          Bonn-Cologne Graduate School of Physics and Astronomy;  
                            Scholarship (Oct. - Sept.)  
2007-2010          University of Bonn; B.Sc. in Physics (very good, 1.4) (Oct. - Sept.)  
1998-2007          Rhein-Sieg-Gymnasium; Abitur (good, 1.9) (July - May)

---



---

## Danksagung

---

Abschließend möchte ich mich für die Unterstützung bedanken, die ich während der letzten Jahre von zahlreichen Seiten erfahren habe. Zunächst danke ich meinen Gutachtern, Prof. Dr. Hans-Werner Hammer und Prof. Dr. Jens Braun. Weiterhin bedanke ich mich besonders bei Prof. Dr. Hans-Werner Hammer für die durchgängig hervorragende Betreuung. Außerdem möchte ich Prof. Dr. Yu Jia danken, in dessen Arbeitsgruppe ich mich während meines Aufenthalts in Peking außerordentlich wohl gefühlt habe. Überdies danke ich Yu und Hans-Werner für die äußerst konstruktive Zusammenarbeit. Für wesentliche Hinweise und Anregungen gilt mein Dank Prof. Dr. Eric Braaten, PD Dr. Akaki Rusetsky und PD Dr. Bernard Metsch. Hilfreiche Denkanstöße erhielt ich in zahlreichen Diskussionen. Insbesondere danke ich hierfür Jonas Braun, Patrick Niemann, Artem Volosniev, Wael Elkamhawy und Marcel Schmidt. Für das gewissenhafte Korrekturlesen meiner Dissertation bedanke ich mich bei Jonas Braun, Julia Hartmann und Felix Jansen. Schließlich danke ich meinen Eltern, die mich unentwegt und bedingungslos unterstützen.

---